On the coupling between natural ventilation and sensible energy charge and discharge in buildings : an experimental and modeling approach

Miguel Chen Austin

▶ **To cite this version:**

Miguel Chen Austin. On the coupling between natural ventilation and sensible energy charge and discharge in buildings : an experimental and modeling approach. Mechanics [physics]. Université de Bordeaux, 2018. English. NNT : 2018BORD0150 . tel-01932939

HAL Id: tel-01932939
https://theses.hal.science/tel-01932939

Submitted on 23 Nov 2018

HAL is a multi-disciplinary open access archive for the deposit and dissemination of scientific research documents, whether they are published or not. The documents may come from teaching and research institutions in France or abroad, or from public or private research centers.

L'archive ouverte pluridisciplinaire **HAL**, est destinée au dépôt et à la diffusion de documents scientifiques de niveau recherche, publiés ou non, émanant des établissements d'enseignement et de recherche français ou étrangers, des laboratoires publics ou privés.

université de BORDEAUX

THÉSE PRÉSENTÉE

POUR OBTENIR LE GRADE DE

DOCTEUR DE

L'UNIVERSITÉ DE BORDEAUX

ÉCOLE DOCTORALE DES SCIENCES PHYSIQUES ET DE L'INGÉNIEUR

SPÉCIALITÉ MÉCANIQUE

PAR MIGUEL CHEN AUSTIN

Couplage entre ventilation naturelle et stockage-déstockage d'énergie sensible en bâtiment : approche expérimentale et modélisation

Sous la direction et l'encadrement de : Denis BRUNEAU, Alain SEMPEY et Laurent MORA

Soutenue le 20 septembre 2018

MEMBRES DU JURY:

M. SALAGNAC, Patrick	PU (HDR)	Université de La Rochelle	Président/Rapporteur
M. LASSUE, Stéphane	PU (HDR)	Université d'Artois	Rapporteur
M. BRUNEAU, Denis	PR des ENSA (HDR)	ENSAP Bordeaux	Directeur de thèse
M. SEMPEY, Alain	MCF	Université de Bordeaux	Co-encadrant
M. MORA, Laurent	MCF	Université de Bordeaux	Co-encadrant
M. RODRÍGUEZ, Julio	PU	Universidad Tecnológica de Panamá	Examinateur
Mme. VOGT-WU, Tingting	MCF	Université de Bordeaux	Invitée
M. SOMMIER, Alain	IR	CNRS	Invité
M. LAGIERE, Philippe	MCF	Université de Bordeaux	Invité

Abstract

Couplage entre ventilation naturelle et stockage-déstockage d'énergie sensible en bâtiments : approche expérimentale et modélisation

As part of the searching for solutions to reduce the energy consumption related to the cooling in buildings, a naturally ventilated test platform, located in Southwest France, has been heavily instrumented in terms of heat flux and temperature measurements.

Here, we are interested in contributing to the improvement of the passive management of the thermal comfort of an existing building during the summertime, by controlling the mobile elements of its envelope, that is to say, the solar protections and the opening natural ventilation. These two mobile elements allow a priori to control the radiative and convective contributions, respectively. Then, the control of these two mobile elements vis-à-vis the dynamics of the thermal mass of the building (which in particular is subject to the charge/discharge process), will make more appropriate selections of natural ventilation strategies, this which will also minimize the need for air conditioning. Thus, such type of control should have the characteristic of being in function of the meteorology and the instantaneous thermal state of the building in order to be able to envisage a control in real time. For this type of control, it is necessary to define the necessary metrology and the control variables, as well as to describe the system to be controlled. This description must be sufficiently simple and light to solve in order to consider the implementation of such type of control. Thus, in this context, this thesis aims first of all to comprehend and highlight the charge/discharge process and its coupling with natural ventilation, and then to construct a simple model to describe this coupling.

The test platform is a Plus Energy House prototype, called Sumbiosi, created to participate in the inter-university competition Solar Decathlon Europe 2012. It was designed in such a way as to promote the passive storage of daytime energy in the winter and the semi-passive night storage in summer. Three main elements allow a priori these functions of energy storage and discharge: a thermally heavy-weighted floor slab located behind of the South-facing glazed-facade, fixed or mobiles and programmable solar protections and openings on the South and North facades.

On the one hand, three measurement campaigns were carried out in the summertime to characterize the energy charge-discharge process and identify their nature. For this, a semi-empirical model is developed for decoupling the superficial heat transfer into its convective and radiative components, using couples of black and shiny heat flux meters. Correlation analysis is employed, to spot relevant heat-transfer couplings between the indoor and outdoor environment. On the other hand, the natural ventilation in the platform is characterized in terms of the airflow capacity of the openings and the natural airflow rate. The former is determined in situ by performing airtightness tests, and the latter, by transient airflow simulation using CONTAM software.

Finally, a thermal model is developed to describe the behavior of the platform, based on its thermal characterization. This model consists of representing the heat transfers in (1) the indoor air via a global

energy balance and in (2) the concrete slab by non-uniform heat conduction, as well as, of representing (3) the natural airflow rate accounting for wind and thermal buoyancy effects simultaneously via a semi-empirical model.

Keywords: Natural ventilation, heat flux measurement, sensible energy charge-discharge, airflow simulations, airtightness tests, superposition of wind and buoyancy effects.

Résumé

Couplage entre ventilation naturelle et stockage-déstockage d'énergie sensible en bâtiments : approche expérimentale et modélisation

Dans le cadre de la recherche de solutions visant à réduire la consommation d'énergie liée au rafraîchissement des bâtiments, une plateforme expérimentale, située dans le Sud-ouest de la France, a été fortement instrumentée en termes de flux thermique et de température.

Ici, on s'intéresse à contribuer à l'amélioration de la gestion passive du confort thermique d'un bâtiment existant en période estivale, par pilotage des éléments mobiles de son enveloppe, c'est-à-dire, les occultations solaires et les ouvrants de ventilation naturelle. Ces deux éléments mobiles permettent a priori de contrôler les apports radiatifs et convectifs, respectivement. Alors, le pilotage de ces deux éléments mobiles vis-à-vis de la dynamique de la masse thermique du bâtiment (qui notamment est soumise au processus de stockage/déstockage), permettra de faire des sélections plus adéquates des stratégies de ventilation naturelle, ce qui permettra aussi de minimiser le recours à la climatisation. Alors, un tel pilotage devrait avoir la caractéristique d'être en fonction de la météorologie et l'état thermique instantané du bâtiment afin de pouvoir envisager un contrôle en temps réel. Pour ce type de contrôle, il y a besoin de définir la métrologie nécessaire et les variables de contrôle, ainsi que de décrire le système à piloter. Cette description doit être suffisamment simple et légère à résoudre afin d'envisager de faire un tel type de contrôle. Ainsi, dans ce cadre, les travaux de cette thèse ont pour objectif tout d'abord de comprendre et mettre en évidence le processus de stockage/déstockage et son couplage avec la ventilation naturelle, et puis de modéliser ce couplage de façon simple.

La plate-forme d'essai est un prototype BEPos, appelé Sumbiosi, réalisée par un consortium rassemblé autour du campus de Bordeaux dans le cadre de sa participation à la compétition interuniversitaire Solar Decathlon Europe 2012. Elle a notamment été conçue de manière à favoriser le stockage passif de l'énergie diurne en hiver et le déstockage semi-passive nocturne en été. Trois éléments principaux permettent a priori ces fonctions de stockage et de déstockage d'énergie : une dalle à forte inertie thermique située derrière la façade vitrée orientée au Sud, des protections solaires fixes ou mobiles et programmables et des ouvertures mobiles et programmables en façades Sud et Nord.

D'une part, trois campagnes de mesures ont été réalisées en été pour caractériser le processus de charge-décharge et identifier sa nature. Pour cela, un modèle semi-empirique est développé pour découpler le transfert thermique superficiel dans ses composantes convectives et radiatives, en utilisant des couples de fluxmètres noirs et brillants. L'analyse de corrélation est utilisée pour repérer les couplages de transfert de chaleur pertinents entre l'environnement intérieur et extérieur du bâtiment. D'autre part, la ventilation naturelle dans la plate-forme est caractérisée en termes de l'aéraulique des ouvertures et le débit d'air. Le premier est déterminé in situ par des tests d'étanchéité à l'air, et le second par simulation de flux d'air transitoires à l'aide du logiciel CONTAM.

Enfin, un modèle thermique est développé pour décrire le comportement de la plate-forme, basé sur

sa caractérisation thermique. Ce modèle consiste à représenter les transferts de chaleur sur (1) l'air intérieur via un bilan énergétique global et sur (2) la dalle de béton par conduction thermique non-uniforme, ainsi qu'à représenter le débit d'air entrant en prenant en compte les effets de vent et du tirage thermique simultanément via une approche semi-empirique.

Mots-clés: Ventilation naturelle, mesure de flux thermique, stockage-déstockage d'énergie sensible, simulations aéraulique, essais d'étanchéité à l'air, superposition des effets du vent et du tirage thermique.

Unité de recherche

I2M-TREFLE, UMR CNRS 5295, Esplanade des Arts et Métiers 33405 Talence

Résumé détaillé

Couplage entre ventilation naturelle et stockage-déstockage d'énergie sensible en bâtiments : approche expérimentale et modélisation

L'augmentation de la consommation énergétique mondiale constitue aujourd'hui une préoccupation vitale puisque, en 2015, environ 82 % de la production d'énergie était encore basée sur des combustibles fossiles. Environ 22 % de cette consommation était due au secteur résidentiel. Ce 22 % était associé à 17 % des émissions de CO_2 [54]. La majorité de la demande en énergie pour ce secteur appartient aux applications de chauffage, de ventilation et de climatisation (CVC), ce qui en fait un contributeur important aux émissions mondiales de gaz à effet de serre. L'équilibre de la situation actuelle accentue la pression pour prendre des mesures, telles que celles mises en place récemment lors de la Conférence de Paris sur le climat (COP21). En conséquence, la réduction de la consommation d'énergie liée au système CVC et l'amélioration de l'efficacité des technologies utilisées dans ces applications, sont une tendance dominante de nos jours.

Sur ce sujet, dans le cadre de la recherche de solutions visant à réduire la consommation d'énergie dans les bâtiments, la réglementation thermique 2020 (RT 2020) vise à réduire cette consommation d'énergie de 50 $kW{\cdot}h{\cdot}m^{-2}{\cdot}an^{-1}$ en 2012 à 15 $kW{\cdot}h{\cdot}m^{-2}{\cdot}an^{-1}$ d'ici 2020 par le développement des systèmes énergétiques plus efficaces. Ces systèmes doivent être passifs ou semi-passifs, ce qui permet d'atteindre des bâtiments à énergie nulle ou à énergie positive. Ici, on s'intéresse à contribuer à l'amélioration de la gestion passive du confort thermique d'un bâtiment existant en période estivale, par pilotage des éléments mobiles de son enveloppe, c'est-à-dire, les occultations solaires et les ouvrants de ventilation naturelle. Ces deux éléments mobiles permettent a priori de contrôler les apports radiatifs et convectifs, respectivement. Alors, le pilotage de ces deux éléments mobiles vis-à-vis de la dynamique de la masse thermique du bâtiment (qui notamment est soumise au processus de stockage/déstockage), permettra de faire des sélections plus adéquates des stratégies de ventilation naturelle, ce qui permet aussi de minimiser le recours à la climatisation. Alors, un tel pilotage devrait avoir la caractéristique d'être en fonction de la météorologie et l'état thermique instantané du bâtiment afin de pouvoir envisager un contrôle en temps réel. Pour ce type de contrôle, il y a besoin de définir la métrologie nécessaire et les variables de contrôle, ainsi que de décrire le système à piloter. Cette description doit être suffisamment simple et légère à résoudre afin d'envisager de faire un tel type de contrôle.

Ainsi, dans ce cadre, les travaux de cette thèse ont pour objectif tout d'abord de comprendre et mettre en évidence le processus de stockage/déstockage et son couplage avec la ventilation naturelle, et puis de modéliser ce couplage de façon simple. Donc, la première partie du manuscrit est dédiée à décrire l'approche expérimentale employée afin d'accomplir ces objectifs.

La mise en œuvre d'études expérimentales permettant, en générale, d'améliorer la compréhension des phénomènes physiques, il est décidé de caractériser le transfert de chaleur dans le processus de stockage/déstockage de l'énergie sensible dans une plate-forme expérimentale à l'échelle 1 in situ. Cette

plateforme fait l'objet d'un prototype de bâtiment à énergie positive (BEPos), nommé Sumbiosi, construite par un consortium ressemblé autour du campus de l'Université de Bordeaux, dans le cadre de sa participation au concours interuniversitaire Solar Décathlon Europe 2012, qui est actuellement installée sur le site de l'IUT de Bordeaux (figures i-ii). Cette plateforme a été conçue de manière à favoriser le stockage passif diurne en hiver et le déstockage semi-passif nocturne en été. Elle présente trois caractéristiques architecturales principales qui favorisent ces fonctions de stockage et de déstockage, à savoir : une dalle de béton derrière la façade vitrée au Sud, des occultations solaires fixes et programmables, et des ouvrants de ventilation naturelle programmables au Sud, au Nord et au shed.

Figure i: Image of the experimental platform, Sumbiosi: South-facade view.

Figure ii: Image of the experimental platform, Sumbiosi: North-facade view.

Pour adopter une stratégie de recherche visant à atteindre les objectifs spécifiques mentionés, nous devons d'abord obtenir une meilleure compréhension des phénomènes physiques qui sous-tendent le comportement thermique des bâtiments et des processus de stockage/déstockage associés à une ventilation naturelle. De même, la compréhension du rôle de l'enveloppe et de la ventilation, ainsi que des techniques expérimentales d'identification concernant la modélisation pour la prévision, sont essentielles. Ainsi, le premier chapitre est consacré à l'exploration et à la détermination des approches expérimentales et de modélisation les mieux adaptées à notre cas. Comme un modèle physique est recherché, nous avons également ciblé cette étude bibliographique sur les approches de modélisation pour les modèles physiques détaillés. Cette étude comprendre : le comportement thermique des bâtiments, la ventilation naturelle et la métrologie de la mesure du flux thermique sur les surfaces rigides et les procédures pour leur étalonnage. L'intérêt de ce dernier sujet peut être justifié par le fait que la ventilation naturelle interagit avec le processus de déstockage d'énergie sous forme de transfert de chaleur par convection. Comme leur couplage direct est à étudier, les mesures directes du flux convectif semblent convenir, car elles permettent de quantifier et de mettre en évidence les processus de stockage et de déstockage.

Cette étude bibliographique a permis de noter les remarques suivantes : d'abord, le couplage entre la ventilation naturelle et la masse thermique d'un bâtiment peut être étudié en considérant seulement deux bilans énergétiques simples, l'un sur l'air intérieur et l'autre sur la masse thermique, et l'équation du débit d'air de ventilation. Deuxième, l'emplacement des infiltrations doit être analysé attentivement afin d'éviter une surestimation ou une sous-estimation du taux de fuite d'air. Et troisième, l'utilisation de fluxmètre à plaques plates (comme Captec®) est une bonne technique expérimentale pour estimer

les échanges convectifs sur des parois lourdes et les modules thermoélectriques sont beaucoup plus attractifs que les fluxmètres classiques en ce qui concerne leurs sensibilités et coûts.

En ce qui concerne les techniques expérimentales et de modélisation permettant d'estimer le débit d'air de ventilation naturelle, une limite s'applique à leur applicabilité à notre cas particulier : par rapport aux techniques expérimentales, qui notamment peuvent conduire à une meilleure compréhension des phénomènes impliqués, nécessitent une instrumentation lourde (souvent coûteuse) des ouvertures en termes de vitesse et de pression (locales). Et aussi, les techniques de modélisation telles que CFD nécessitent un temps de calcul important en fonction de la puissance de l'ordinateur et des modèles eux-mêmes. Les modèles basés sur des observations empiriques requièrent la connaissance des modèles de circulation d'air dans le bâtiment. Ainsi, la technique de modélisation plus adaptée à notre cas semble être l'implémentation de modèles de flux d'air réseau (network airflow models) via des simulations aérauliques directes effectuées par un logiciel tel que CONTAM, car la connaissance du parcour de circulation de l'air n'est pas requise. La technique expérimentale la plus appropriée semble être les tests d'étanchéité à l'air, car elle permet d'obtenir des expressions empiriques reliant directement le débit d'air de ventilation à la différence de pression dans le bâtiment dans les deux cas : infiltrations (ouvrants fermées) et ouvrants ouvertes. En outre, l'emplacement des infiltrations peut être identifié sans complications, et cette technique a le potentiel d'estimer in situ la capacité de flux d'air et les caractéristiques aérauliques ouvertures.

L'étude expérimentale réalisée dans la plate-forme pour caractériser les processus de stockage et de déstockage, et leur couplage aux sollicitations thermiques extérieures, en particulier la ventilation naturelle en été, est décrite au chapitre 2. La caractérisation du stockage/déstockage vise à comprendre le comportement thermique de la plate-forme et à déterminer les phénomènes de transfert de chaleur impliqués dans chaque processus. Ils conduiront finalement à construire un modèle physique de la plate-forme qui ne considère que les paramètres clés pour décrire le comportement thermique de l'environnement intérieur.

Dans le but d'estimer les échanges convectifs et radiatifs par expérimentation, nous proposons un simple dispositif de mesure, basé sur les travaux d'autres chercheurs concernant les approches expérimentales de découplage du transfert thermique superficiel. Ce dispositif comprend les éléments suivants : un couple noir/brillant de modules Peltier, un thermocouple type T pour la mesure de température d'air, et un thermocouple type T inséré dedans le module Peltier brillant pour mesurer la température de surface (figure iii).

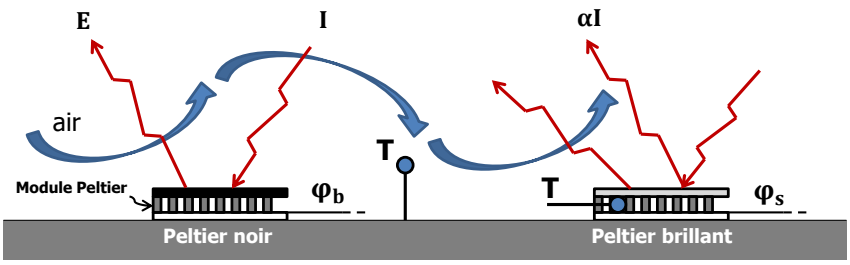

Figure iii: Echanges radiatifs et convectifs sur le dispositif de mesure destiné à observer et quantifier le stockage/déstockage.

Après un étalonnage judicieux des modules Peltier et thermocouples, plusieurs de ce dispositif de mesure ont été mis en place sur l'ensemble de la surface de dalle (figure iv), sur la surface du plafond et celle du vitrage en façade Sud.

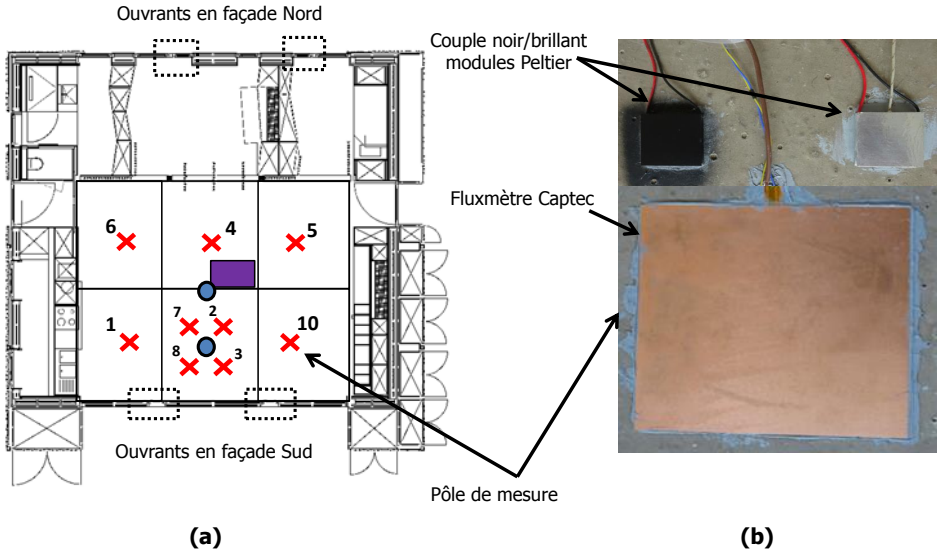

Figure iv: Instrumentation de l'ensemble de la surface de dalle : représentation schématique (a) et dispositif de mesure pour observer le stockage/déstockage (b).

Afin de quantifier les échanges convectifs et radiatifs, un modèle analytique a été mis en place pour exploiter les mesures de flux thermique. Ce modèle, basé aussi sur des travaux de recherche précédents, est composé d'un bilan de flux à la surface de chaque module Peltier et des hypothèses assez importantes retenues lors de notre cas particulier, issues des essais préliminaires et de l'étalonnage des thermocouples : les températures des modules Peltier noirs et brillants, ainsi que celle de la surface où ils sont disposés ont la même valeur ; d'autres hypothèses ont été retenues pour simplifier le découplage des parts convectifs et radiatifs : les capteurs dans un même « dispositif de mesure », sont soumis à la même densité de flux radiatif total incident et au même coefficient d'échange convectif. Ainsi, ces deux bilans et hypothèses, nous permettent de trouver des expressions à la fois pour la densité du flux radiatif incident (I) et le coefficient d'échange convectif (h_C), et à la fois pour les parts convectifs et radiatifs. Ces quatre expressions sont en fonction des mesures directes des capteurs, dont la densité du flux des modules Peltier noir (φ_b) et brillant (φ_s), température d'air (T_{ia}) et surface (T_b, T_s), et aussi des émissivités des surfaces noire (ε_b) et brillante (ε_s) :

$$I(t) = \frac{\varphi_s(t)}{\varepsilon_s - \varepsilon_b} - \frac{\varphi_b(t)}{\varepsilon_s - \varepsilon_b} + \frac{\sigma \cdot \left[\varepsilon_s \cdot T_s^4(t) - \varepsilon_b \cdot T_b^4(t)\right]}{\varepsilon_s - \varepsilon_b} \qquad \left[\mathrm{W{\cdot}m^{-2}}\right] \tag{1}$$

$$h_C(t) = \frac{\varepsilon_b}{\varepsilon_b - \varepsilon_s} \cdot \frac{\varphi_s(t)}{\Delta T_s(t)} - \frac{\varepsilon_s}{\varepsilon_b - \varepsilon_s} \cdot \frac{\varphi_b(t)}{\Delta T_s(t)} \qquad \left[\mathrm{W{\cdot}m^{-2}{\cdot}K^{-1}}\right] \tag{2}$$

$$\varphi_C(t) = \frac{\varepsilon_s}{\varepsilon_s - \varepsilon_b} \cdot \varphi_b(t) - \frac{\varepsilon_b}{\varepsilon_s - \varepsilon_b} \cdot \varphi_s(t) \qquad \left[\mathrm{W{\cdot}m^{-2}}\right] \tag{3}$$

$$\varphi_R(t) = \frac{\varepsilon_b}{\varepsilon_b - \varepsilon_s} \cdot \varphi_b(t) - \frac{\varepsilon_b}{\varepsilon_b - \varepsilon_s} \cdot \varphi_s(t) \qquad \left[\mathrm{W{\cdot}m^{-2}}\right] \tag{4}$$

où φ_C et φ_R représentent les densités du flux convectif et radiatif, respectivement, et ΔT est la différence de température entre l'air (T_{ia}) et la surface. Ce dispositif de mesure et hypothèses, permettent aussi la mise en place d'une autre expression qui relie la température des environs radiatifs (T_{surr}) aux mesures directes de flux (φ_b, φ_s) et de température de surface (T_s), donnant le suivant :

$$T_{surr}(t) = \sqrt[4]{\frac{\varphi_b(t) - \varphi_s(t)}{[\varepsilon_b - \varepsilon_s] \cdot \sigma} + T_s^4(t)} \qquad [\mathrm{K}]\,. \tag{5}$$

Afin d'estimer au mieu ces cinq grandeurs (eqs. 1-5), une étude de sensibilité par la méthode de dérivés a montré que la certitude dans la valeur d'émissivité de la surface brillante (ε_s) est la plus importante, ce qu'amène à la mesurer de façon très précise. Ce dernier fait l'objet d'un des travaux menés dans [113] ; les valeurs des émissivités ont été déterminées avec une certitude satisfaisante, donnant 0,069 ± 0,014 pour ε_s, et 0,953 ± 0,012 pour ε_b.

Une fois les trois surfaces instrumentées, trois campagnes de mesures ont été menées afin d'observer le comportement de la plateforme sous trois configurations (où scénarios) d'ouverture/fermeture des ouvrants de ventilation naturelle (ceux en façade Sud et en shed) : ouvrants fermés en permanence (configuration 1), ouvrants ouverts en permanence (configuration 3), et n'ouvrir les ouvrants que si la température d'air extérieur est inférieure à l'air intérieur (configuration 2). Les occultations solaires programmables sont restées fermées pendant toutes les campagnes de mesures. Les résultats de ces campagnes nous ont permis de mettre en évidence les processus de stockage et déstockage dans les différentes surfaces instrumentées, ainsi que de les qualifier en ses parts convectifs et radiatifs. Par exemple, pour la configuration 2, on a pu constater que le stockage en surface de dalle est dominé par des échanges radiatifs et que son déstockage est dominé par les échanges convectifs notamment lors des moments d'ouverture des ouvrants de ventilation naturelle (figure v). Au contraire, en surface de plafond, le stockage est dominé par les échanges convectifs et aucun déstockage a lieu vers l'ambiance intérieur.

Ces résultats de densité de flux convectif et radiatif ont été qualifiés à travers une comparaison avec des fluxmètres classiques du type Captec® qui ont été aussi recouverts avec de revêtements noir et brillant. Une particularité sur la densité du flux convectif estimée a été trouvée, il s'agit d'une différence récurrente de l'ordre de 2, entre la densité du flux convectif estimée à partir des mesures des modules Peltier et celle estimé à partir des mesures des fluxmètres Captec® (présenté aux annexes). Ensuite, une étude à l'aide d'une analyse statistique de corrélation et des nombres adimensionnels a été mise en place afin de déterminer la nature des échanges convectifs au niveau de la surface de dalle. Les résultats de cette étude montrent qu'il n'y a pas une affinité assez forte afin de spécifier cette nature en convection naturelle ou forcée, ce qui amène à conclure qu'une convection mixte a lieu. En fin, une analyse de confort thermique a été réalisée avec les données de mesures, afin de quantifier la performance de la plateforme sous une ventilation naturelle nocturne (configuration 2), à travers des indicateurs recommandés par la norme ISO 7730. Cette analyse a permis de constater que l'implémentation de cette stratégie a amené à maintenir le confort thermique d'une durée de 29 jours sur 34 journées.

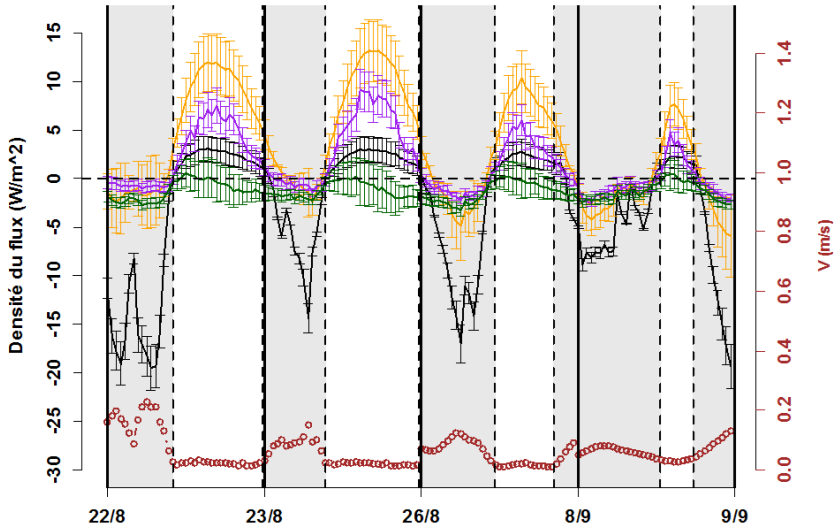

Figure v: Résultats de la densité du flux thermique pour la configuration 2. En surface de dalle : échanges radiatifs (orange) et convectifs (noir). En surface du plafond : échanges radiatifs (vert) et convectifs (violet). Vitesse d'air en surface de dalle (rouge foncé, axe à droite). Moments d'ouverture des ouvrants (zones grises).

Le troisième chapitre est consacré à la modélisation du débit d'air naturel dans la plateforme. En vue que cette plateforme est dotée d'une distribution non-standard des ouvrants de ventilation naturelle (ce que rendre difficile à déterminer les entrées ainsi que les sorties d'air), cette modélisation a été faite à l'aide du logiciel CONTAM. Ce choix était inspiré du fait que ce logiciel permet de faire des simulations aérauliques par modèle zonal, qui notamment n'a pas besoin effectivement de savoir le parcours de circulation d'air. Afin de construire le modèle zonal sur CONTAM, certains paramètres devraient être introduits au logiciel avant de simuler. Les plus importants d'entre ces paramètres sont les caractéristiques aérauliques des ouvrants de ventilation naturelle et des infiltrations (coefficient de décharge, coefficient du débit et l'exposant de l'écoulement), et les coefficients de pressions. Les valeurs de ces derniers ont été prises de la norme EN 1991-1-4 : 2005 (Euro code 1). Pour les caractéristiques aérauliques des infiltrations, des essais d'étanchéité à l'air ont été menés suivant la procédure recommandée par la norme NF EN 13829. Pour les caractéristiques des ouvrants de ventilation naturelle, ces essais ont été menés à l'aide de deux portes soufflantes. Dans ce cas, le coefficient de décharge de chaque ouvrant a été estimé par une égalisation de la définition théorique du débit d'air à travers une ouverture et des lois débit-pression obtenues des essais d'étanchéité. Puis, en vue que la valeur de ce coefficient varie pour de pressions assez faibles (notamment dans le cas où les mouvements d'air sont conduits par tirage thermique) et en attendant une valeur constante, la moyenne des valeurs résultantes pour ceux qui appartient aux pressions assez importantes a été prise. Ceci a donné : 0,40 $\pm$ 0,01 pour les ouvrants en façade Sud ; 0,31 $\pm$ 0,002 pour ceux en bas de façade Nord ; 0,28 $\pm$ 0,01 pour ceux en shed.

Une fois le modèle mono-zone construit et alimenté par les résultats de la caractérisation aéraulique expérimentale, l'emplacement des infiltrations a été défini. Pour cela, les simulations ont été réalisées avec deux emplacements différentes à la fois : infiltrations equitativement réparties à la mi-hauteur des

façades contenantes le plus d'ouvrants et portes (dans notre cas, les façades Sud et Nord), et infiltrations concentrées sur l'armoire technique en façade Ouest. Le premier emplacement est issu d'une hypothèse faite dans le cas où on ne connaît pas la distribution réelle (suivant difficile à déterminer [20, 32]). Le deuxième emplacement est issu des essais d'étanchéité, où en utilisant la poire à fumés, on a pu constater qu'y se concentrent la majorité d'infiltrations d'air.

A la fin de ce chapitre, se présentent les résultats des simulations distinctes qu'ont été réalisées d'une part pour déterminer séparément le taux du renouvellement de l'air (*ach*) en fonction des effets du tirage thermique et du vent, et d'autre part pour tester les deux emplacements différents d'infiltrations. Par rapport à ce dernier, les résultats ont montré que la valeur de *ach* est indistincte de l'emplacement des infiltrations dans notre cas. En ce qui concerne à la valeur de *ach* en fonction des effets du tirage thermique uniquement, les résultats ont été approximés par des régressions de loi de puissance, donnant l'expression générale suivante : $ach_{\Delta T} = \mathscr{A} \cdot [\Delta T/T]^x$ où les coefficients $\mathscr{A}$ et x ont de valeurs différentes pour les cas d'ouvrants seuls que pour le cas d'infiltrations. De même, en ce qui concerne à la valeur de *ach* en fonction des effets du vent uniquement, les résultats ont été aussi approximés par des régressions de loi de puissance, donnant l'expression générale suivante : $ach_W = \mathscr{B} \cdot [V_W]^y$ où les coefficients $\mathscr{B}$ et y ont aussi de valeurs différentes pour les cas d'ouvrants seuls que pour les infiltrations. En vue que la valeur du coefficient $\mathscr{B}$ dépende de la direction du vent (φ_W), cette valeur a été tracées en fonction de la direction du vent, et son comportement a pu être approximé par de séries de Fourier à 5 % près. La dernière partie de ce chapitre, se concentre sur le cas où les effets du tirage thermique et du vent se trouvent simultanément (cas de convection mixte). Dans ce cas, les résultats de simulations ont pu démontrer que la superposition de ces deux effets n'est pas définie par juste une addition ou reste des effets. Ce qui amène à rechercher puis à proposer de modèles de superposition, ceci fait l'objet du début du chapitre 4.

Ainsi, le quatrième chapitre est consacré à l'identification d'un modèle semi-empirique permettant de décrire le comportement thermique de l'environnement intérieur, en se concentrant tout d'abord sur le modèle de l'air intérieur et puis sur le choix d'un modèle pour la masse thermique (la dalle en béton). Ce chapitre commence par le choix d'un modèle d'entre plusieurs modèles de superposition reportés dans la littérature. Pour ceci, la « vraie » valeur de *ach* a été identifiée en utilisant un bilan sur l'air intérieur complété par une expression de la température moyenne radiative et alimenté par les mesures de la densité du flux convectif et de températures. En comparant cette identification avec les modèles proposés par la littérature, on a constaté que ces modèles sous-estiment souvent la valeur identifiée de *ach*. Ceci amène à proposer un autre modèle de superposition, dans notre cas on a choisi un modèle de superposition multiplicative de la forme : $ach = C \cdot ach_{\Delta T}^a \cdot ach_W^b$, inspiré d'après les travaux qui gèrent les nombres adimensionnels pour prendre en compte des phénomènes distincts sur une même grandeur. Dans notre cas, les termes $ach_{\Delta T}$ et ach_W représentent les phénomènes liés aux effets du tirage thermique et du vent ; leurs intensités ou bien leurs influences sur la valeur de *ach* est considéré à travers la valeur des exposants a et b, respectivement. Afin d'identifier les valeurs de ces trois coefficients, la méthode classique d'optimisation qui cherche à minimiser la valeur de RMSE entre le modèle et la mesure a été employée. Ici, on cherche à minimiser la valeur RMSE entre la mesure de la température d'air intérieur T_{ia} et son résultat numérique, en variant les valeurs des coefficients C, a et b, par « essais et erreur ». Après cette identification, on a pu constater qu'il semble exister une relation

forte entre les signes (positif ou négatif) des exposants et la direction du vent la plus fréquent (ou bien dominante).

La deuxième partie de ce chapitre 4 est dédiée au choix d'un modèle pour la dalle en béton. Après une évaluation avec le nombre de Biot et les résultats numériques pour un modèle 0D et un modèle 1D, un modèle de conduction unidirectionnelle qui discrétise cette dalle a été retenu, car ceci a donné une meilleure valeur RMSE respectant la température de surface de dalle (modèle et mesure). Enfin, ce deux modèles (air et dalle) ont été couplés faisant l'objet ultérieurement de notre modèle du coulage proposé (voir résultats en figure vi) :

$$
\begin{cases}
\textbf{1)} \quad \rho(T_{ia}) \cdot V_{ia} \cdot c_p(T_{ia}) \cdot \dfrac{\mathrm{d}T_{ia}(t)}{\mathrm{d}t} = h'_{C_D}(t) \cdot S_D \cdot \left[T_{S_D}(t) - T_{ia}(t)\right] \; + \; h'_{C_P}(t) \cdot S_P \cdot \left[T_{S_P}(t) - T_{ia}(t)\right] \\
\qquad\qquad\qquad\qquad\qquad\qquad\qquad\qquad + \; h'_{C_g}(t) \cdot S_g \cdot \left[T_{S_g}(t) - T_{ia}(t)\right] \\
\qquad\qquad\qquad\qquad\qquad\qquad\qquad\qquad + \; V_{ia} \cdot \dfrac{ach(t)}{3600} \cdot \left[\rho(T_{oa}) \cdot c_p(T_{oa}) \cdot T_{oa}(t) - \rho(T_{ia}) \cdot c_p(T_{ia}) \cdot T_{ia}(t)\right] \\
\textbf{2)} \quad \rho_D \cdot \Delta z \cdot c_{p_D} \cdot \dfrac{\mathrm{d}T_{D_N}(t)}{\mathrm{d}t} = \dfrac{T_{D_{N-1}}(t) - 2 \cdot T_{D_N}(t) + T_{D_{N+1}}(t)}{\Delta z} \\
\quad \text{with} \quad \rho_D \cdot \dfrac{\Delta z}{2} \cdot c_{p_D} \cdot \dfrac{\mathrm{d}T_{D_1}(t)}{\mathrm{d}t} = h'_{C_D}(t) \cdot \left[T_{ia}(t) - T_{D_1}(t)\right] + \varepsilon_D \cdot \sigma \cdot \left[T^4_{surr}(t) - T^4_{D_1}(t)\right] + \lambda_D \cdot \dfrac{T_{D_2} - T_{D_1}}{\Delta z} \\
\quad \text{and} \quad \rho_D \cdot \dfrac{\Delta z}{2} \cdot c_{p_D} \cdot \dfrac{\mathrm{d}T_{D_M}(t)}{\mathrm{d}t} = \lambda_D \cdot \dfrac{T_{D_{M-1}} - T_{D_M}}{\Delta z} \\
\textbf{3)} \quad T_{S_g}(t) = \frac{1}{\mathcal{F}_{g \to D}} \sqrt[4]{T^4_{surr}(t) - \mathcal{F}_{P \to D} \cdot T^4_{S_P}(t) - \left[1 - \mathcal{F}_{P \to D} - \mathcal{F}_{g \to D}\right] \cdot T^4_{ia}(t)} - 273,15 \\
\textbf{4)} \quad ach(t) = \begin{cases}
C_l \cdot \left[4 \cdot \left| \dfrac{T_{ia}(t) - T_{oa}(t)}{T_{oa}(t)} \right|^{0,58}\right]^{a_l} ; \text{when NV openings closed} \\
C_v \cdot \left[\mathcal{A} \cdot \left| \dfrac{T_{ia}(t) - T_{oa}(t)}{T_{oa}(t)} \right|^{1/2}\right]^{a_v} \cdot \left[\mathcal{B}_v(\phi) \cdot \mathcal{V}_{met}(t)\right]^{b_v} ; \text{when NV openings opened} \\
C_v \cdot \left[\mathcal{A} \cdot \left| \dfrac{T_{ia}(t) - T_{oa}(t)}{T_{oa}(t)} \right|^{1/2}\right]^{a_v} : \text{If } \mathcal{V}_{met}(t) = 0; \text{when NV openings opened}
\end{cases}
\end{cases}
\tag{6}
$$

En conclusion, ce modèle, basé sur la revue de la littérature concernant l'étude théorique du couplage entre ventilation naturelle et masse thermique, nous n'avons été intéressés que pour rendre compte du transfert de chaleur en deux éléments : l'air intérieur et la masse thermique (supposée être concentré dans le plancher dalle-béton). En plus de ces deux éléments, un troisième élément a été inclus : le débit d'air de ventilation naturelle. Une différence entre notre choix de modélisation et ceux trouvés dans la littérature, tient compte les aspects suivants, issus de la caractérisation des processus de stockage/déstockage d'énergie, ainsi que sur le débit d'air de ventilation naturelle au sein de la plate-forme :

- L'intégration de la température radiante moyenne de l'environnement intérieur de la plate-forme.
- La nécessité de comptabiliser séparément les échanges de chaleur par convection entre le volume d'air intérieur ventilé et les surfaces de la dalle de béton, du plafond et de la façade vitrée, dans la représentation du transfert de chaleur air intérieur en plus des termes de ventilation et de stockage d'énergie (première expression en eq. 6).

- La masse volumique (ρ) et la capacité thermique spécifique (c_p), sont dépendant de la température de l'air.
- La prise en compte des effets à la fois du vent et du tirage thermique via un modèle de superposition multiplicative pour le débit d'air de ventilation.
- Des coefficients de transfert de chaleur par convection qui varient dans le temps.

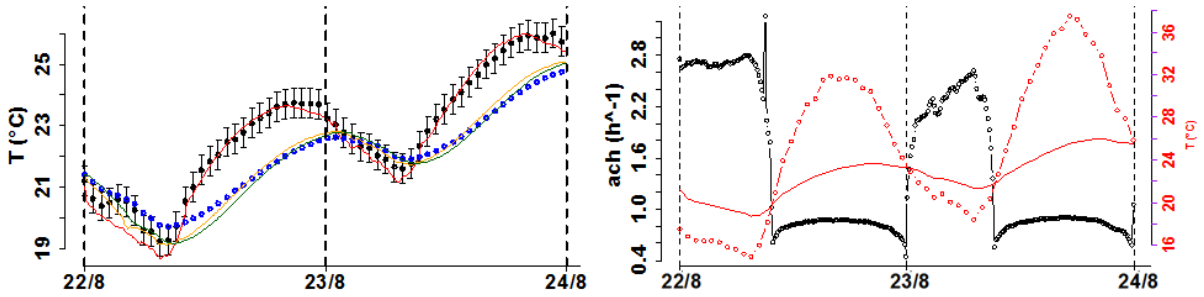

Figure vi: Résultats du modèle pour une configuration 2. A gauche : température d'air intérieur mesurée (noir) et simulée (rouge), température de surface de dalle mesurée (bleu) et simulée (orange premier nœud et vert dernier nœud). A droite : taux de renouvellement de l'air (noir) et températures d'air intérieur et extérieur (rouge).

Concernant le modèle de superposition multiplicative pour le débit d'air de ventilation, une particularité a été observée : le signe des exposants pourrait devoir être ajusté en fonction de la direction du vent. Cependant, la relation entre la valeur de ces coefficients et l'influence des effets du tirage thermique et du vent est encore inconnue. D'autres modèles de superposition trouvés dans la littérature se sont avérés inappropriés, car ils ont été développés pour des trajectoires de circulation d'air spécifiques, dans des stratégies de ventilation naturelle simples telles que la ventilation unilatérale, transversale et tirage assisté par le vent avec un nombre réduit d'ouvertures. Enfin, la caractérisation thermique de la plate-forme a contribué à promouvoir la mise en œuvre de modules thermoélectriques, en alternative aux fluxmètres classiques, pour estimer les échanges convectifs et radiatifs dans le domaine du bâtiment. Les caractéristiques les plus attrayantes à prendre en compte dans l'implémentation de ces derniers, sont les suivantes :

- Le budget nécessaire, puisque le coût des modules thermoélectriques, est environ dix fois inférieur à celui des fluxmètres classiques, tels que Captec®.
- Sensibilité/précision/taille, car les modules thermoélectriques génèrent un potentiel électrique plus élevé que les fluxmètres classiques, pour la même taille de surface. Ce potentiel plus élevé peut permettre une estimation plus précise du flux thermique mesuré avec la même chaîne de mesure (capteur + système d'acquisition). Cette estimation précise pourrait être essentielle pour mesurer les faibles niveaux de flux thermique dans les environnements passifs.

Mots-clés : Ventilation naturelle, mesure de flux thermique, stockage-déstockage d'énergie sensible, simulations aéraulique, CONTAM, essais d'étanchéité à l'air, superposition des effets du vent et du tirage thermique.

Acknowledgements

Je tiens à remercier tout d'abord mon directeur et mes encadrants de thèse qui m'ont toujours supporté et encouragé. Particulièrement, à **Denis**, tout d'abord pour m'encourager à apprendre très vite la langue afin de pouvoir mieux me communiquer/échanger. Aussi, pour me proposer ce parcours de recherche que j'ai bien trop aimé. À **Alain**, pour m'avoir fourni des outils bureau et expérimentales, et même aussi pour les conversations toujours remplies des nouveaux mots. À **Laurent**, même si on n'a pas pu trop échanger/discuter, ses conseils étaient toujours riche pour me faire avancer. À tous les trois, pour leur temps et pour me faire devenir plus rigoureux, plus exigeant avec mon travail. Je les remercie aussi pour vos conseils très avisés, et même aussi pour les phrases toujours encourageantes :

"Ça ne sera pas parfait, mais ça suffit (aux congrès)". "Il faut faire le mieux quand on peut, pas la moyenne".

D.B.

"Si tu perds ton chemin, reviens à ton but". "L'expérience, c'est ça que m'aide à encadrer des jeunes chercheurs comme toi".

A.S.

"En forme ?"

L.M.

Je remercie également aux membres du jury, pour avoir accepté de juger mon travail. À **M Salagnac** et à **M Lassue**, pour avoir accepté de rapporter ma thèse et me donner des remarques très riches, je vous remercie vivement. À **Julio Rodríguez** pour avoir accepté d'examiner et dirigé mon travail depuis le début de ma carrière comme ingénieur jusqu'au doctorat. À **Alain Sommier** pour l'aide apporté à la mise en place et mise en route de la métrologie, avec **Cédric**. À **Philippe** pour les échanges toujours très riches. À **Tingting** pour l'encadrement et l'encouragement apporté à mon travail (l'une de deux permanentes qui je suis arrivé à tutoyer).

"C'est comme ça la recherche".

T.W.

Je tiens à remercier également aux collègues du département TREFLE pour m'avoir bien accueilli au laboratoire I2M. En spécial à **Muriel** pour son aide à processus administratifs toujours très gentille. De même aux doctorants, postdoc que j'ai eu la belle opportunité de croisés dans mon séjour : **Paul-Antoine**, **Jérémy**, **Maïmouna**, **Tan** pour les conversations en français toujours très riches de nouveaux mots (mes camarades de bureau... Non, tu n'étais pas trop chiant sur la climatisation... C'est bien "loco" et "loca"... "un truc de con" et "une chose de connard") ; **Yibiao** (le porteur de la carte WE) ; **Tom, Xavi, Antonio, José, Lina, Jorge, Ulises, Yingying, Cécile, Mehrez, Paul, Youseff, Mehdi, Wen, Stéphanie, Antone, Sarah, Charlotte, Dung, Romain, Yajie, Tomas, Sébastien, Ludo, Terrence, Zakaria, Bauyrzhan (Bauka), Clément, Celia, Aslı, ...** ; **Hugo** pour les moments

d'échanges scientifique et ceux partagés aux Pyrénées. Je remercie aussi aux autres membres du département qui j'ai pu rencontrer **Jean-Rodolphe, Sandrine, Cyril, Audrey, Gérard, Fouzia, Marie, ...** Très particulièrement, à **Wahbi** pour toujours accepter de signer la demande WE.

Aux techniciens de l'IUT, **Martial Lyney, Jérôme Malvestio, Eric Marqueze**, pour avoir donné leur temps quand quelque chose était arrivé chez Sumbiosi. Au membre du CROUS, **M Proença**, ainsi qu'à **Mme Bordes** de l'école doctorale SPI, pour leur aide aux processus administratifs toujours très gentils.

Aux collègues de l'ENSAM pour m'avoir bien accueilli et me faire sentir partie de leurs environs : **Kiki**, **Baptiste**, **Dorian**, **Valérie**, **Pierre**, **Mickaël**, ... En spécial à **Mme Pernot** pour son aide aux processus administratifs toujours très gentille et pour son soutien, je vous remercie vivement. À mes profs de Master puis collègues au labo : **Batsale, Langla, Didier, Henri, Bonnet, Valat, Patrick, Perry**, en spécial à **Azita** pour son encouragement et sa disponibilité, toujours très gentille.

Ça m'a fait vraiment plaisir de vous avoir pu rencontrer à vous tous. Je serais très heureux de pouvoir continuer de travailler (soit du côté académique soit du côté académique/Enterprise) de près à mon retour.

Je remercie tout de même à l'institution panaméenne **IFARHU** et la **Universidad Tecnológica de Panamá**, pour leur disposition et support administratif comme financier au long de mon parcours en France.

Je remercie autant mes amis panaméens, **Marita, Shannon, Marcel, Stephanie, Eimy, ...** et même aussi **Dafni, Ezequiel, Lian** avec qui j'ai beaucoup partagé au Panama, en France et autour de l'Europe, et qui m'ont donnés leur soutien d'une façon ou d'une autre.

La fin serait pour remercier **ma mère** pour son soutien et l'éducation qu'elle m'a su donné, tout un modèle à suivre, toujours au courant de moi ; de même à mes frères **Daniel, Gabriel** et à ma famille, je vous remercie vivement.

'The call of the scientific pursue should not be only to make use of the world around us. It should be to understand it, fundamentally, no matter to what use it might be.'

Albert Einstein

Nomenclature

Latin Letters

$\dot{V}$	Airflow rate	$m^3 \cdot s^{-1}$
$\mathscr{A}$	Equivalent opening effective area related to stack forces	h^{-1}
$\mathscr{B}$	Equivalent opening effective area related to dynamic forces	$h^{-1} \cdot m^{-1} \cdot s$
$\mathscr{C}$	Airflow rate coefficient	$m^3 \cdot s^{-1} \cdot Pa^{-n}$
$\mathscr{E}$	Energy	J
$\mathscr{F}$	Diffuse view factor	–
$\mathscr{H}$	Enthalpy	J
$\mathscr{I}$	Electrical current	A
$\mathscr{K}$	Sensitivity of heat flux meters	$\mu V \cdot m^2 \cdot W^{-1}$
$\mathscr{U}$	Heat flux sensor response	V
$\mathscr{V}$	Velocity/speed	$m \cdot s^{-1}$
$\mathscr{L}$	Height	m
a	Seebeck coefficient	$V \cdot K^{-1}$
ach	Air change rate per hour	h^{-1}
C	Heat capacity	$J \cdot K^{-1}$
C_d	Discharge coefficient	–
C_p	Pressure coefficient	–
c_p	Specific heat capacity	$J \cdot kg^{-1} \cdot K^{-1}$
E	Emitted radiation heat flux	$W \cdot m^{-2}$
g	Acceleration due to Earth's gravity	$9{,}81\ m \cdot s^{-2}$
h	Convective coefficient	$W \cdot m^{-2} \cdot K^{-1}$
h'	Modified convective coefficient	$W \cdot m^{-2} \cdot K^{-1}$
I	Total incident radiation heat flux	$W \cdot m^{-2}$

L_c	Characteristic length	m
m	Mass	kg
N	Number of elements	–
n	Flow exponent	–
P	Pressure	Pa
Q	Heat	J
q	Heat per unit square	$J \cdot m^{-2}$
R	Global heat transfer coefficient/Correlation coefficient	–
S	Surface area	m^2
T	Temperature	K
t	Time	
U	Electrical potential	V
V	Volume	m^3
W	Work	J
w	Width	m
x	Length/x coordinate	m
y	y coordinate	
z	Height/z coordinate	m

Abbreviations

$RMSE$	Root mean square sum error
COC	Constant Odds Combination
CS	Control surfaces
CV	Control volume
FGT	Refers to conventional heat flux meters
LWL	Long wavelength
NPL	Neutral plane level
NV	Natural ventilation

SWL	Short wavelength	
TEM	Thermoelectric modules	
TTL	Thermal time constant	

Greek Letters

α	Thermal absorptivity	–
β	Thermal expansion coefficient	K^{-1}
δ	Represents the uncertainty	
λ	Thermal conductivity/conduction	$W \cdot m^{-1} \cdot K^{-1}$
μ	Viscosity	$Pa \cdot s^{-1}$
ω	Frequency	s^{-1}
Φ	Heat flow	W
ϕ	Angle	$^{\circ}$
ρ	Density	$kg \cdot m^{-3}$
σ	Stefan-Boltzmann constant	$(5{,}670373 \pm 0{,}0029) \times 10^{-8}$ $W \cdot m^{-2} \cdot K^{-4}$
ε	Thermal emissivity	–
φ	Heat flux	$W \cdot m^{-2}$
ξ	Friction factor	–
e	Thickness	m

Subscripts and Superscripts

50	Evaluated at a pressure difference of 50 Pa
ΔT	Thermal buoyancy
∞	Freestream region
$\mathfrak{b}$	Black coated sensor
$\mathfrak{s}$	Shiny coated sensor
a	Exponent in superposition model related to buoyancy effects
b	Exponent in superposition model related to wind effects
C	Convective/convection

D	Floor concrete-slab
dif	Diffuse
dir	Direct
eff	Effective
eq	Equivalent
f	Refers to facade height
fo	Full open
g	Glazed-facade
gen	Generation
i	Any surface
ia	Indoor air
in	Entering
ioa	average between indoor and outdoor
$iSWL$	Indoor solar radiation
$K-P$	Refers to K-P air-leakages model
L	Lower
l	Refers to air-leakages
$l+v$	Refers to air-leakages plus openings
M	Total number of nodes
met	Refers to meteorological station
$natural$	Evaluated at natural pressure levels
oa	Outdoor air
out	Leaving
P	Ceiling
R	Radiative/radiation
ref	Reflected
S	Surface

$surr$	Surrounding/for the mean radiant temperature
SWL	Refers to solar radiation
U	Upper
v	Refers to natural ventilation openings
W	Wind
w	Vertical walls other than the glazed-facade
x	Exponent in airflow rate due to buoyancy effects
y	Exponent in airflow rate due to wind effects
NPL	Neutral plane level

Other Symbols

$\cdot$	To express multiplication
Δ	Difference
$\dot{x}$	To express a change in time of a variable x
( )	To express dependence
[ ]	To group multiplication terms

Dimensionless numbers

$\mathcal{B}i$	Biot	$\frac{h_C \cdot L_c}{\lambda}$
$\mathcal{R}e$	Reynolds	$\frac{\rho \cdot \mathcal{V} \cdot L_c}{\mu}$
$\mathcal{G}r$	Grashof	$\frac{\rho^2 \cdot g \cdot \beta \cdot \Delta T \cdot L_c^3}{\mu^2}$
$\mathcal{N}u$	Nusselt	$\frac{h_C \cdot L_c}{\lambda}$
$\mathcal{P}r$	Prandlt	$\frac{c_p \cdot \mu}{\lambda}$
$\mathcal{R}a$	Rayleigh	$\mathcal{G}r \cdot \mathcal{P}r$
$\mathcal{R}i$	Richardson in thermal convection	$\frac{\mathcal{G}r}{\mathcal{R}e^2}$
$\mathcal{F}r$	Froude in natural ventilation	$\frac{\mathcal{V}_w}{\sqrt{g \cdot \frac{\Delta T}{T} \cdot \mathcal{L}}}$
$\mathcal{F}$	Flow rate	$\frac{\dot{V}}{S_{eff} \cdot \mathcal{V}_w}$

Contents

Abstract iii

Résumé v

Résumé détaillé vii

Acknowledgements xvii

Nomenclature xxi

Introduction 1

"The big picture" . . . 1
Thesis statement and specific objectives . . . 2
Charge and discharge processes and natural ventilation . . . 2
The test building . . . 3
Research strategy and organization of the manuscript . . . 5

1 Theoretical background and state of the art 7

1.1 Natural ventilation in buildings . . . 8
1.1.1 The role of natural ventilation . . . 9
1.1.2 The natural ventilation concept . . . 11
1.1.3 Assessment techniques for the natural ventilation airflow rate . . . 14
1.2 Thermal behavior modeling and identification approaches . . . 23
1.2.1 Thermal behavior of a passive building: the role of the envelope . . . 23
1.2.2 Modeling approaches for forecasting in buildings . . . 24
1.3 Coupling between natural ventilation and thermal mass . . . 25
1.4 Heat flux measurement techniques for rigid surfaces . . . 29
1.4.1 Principles of the heat flux measurement . . . 29
1.4.2 Implementation of heat flux meters for measuring the superficial heat exchanges 31
1.4.3 Perturbations and uncertainties introduced by the heat flux meter . . . 37
1.4.4 Calibration techniques for flat-plate type of heat flux sensors . . . 39
1.5 Concluding remarks and perspectives . . . 41

2 Characterization of the coupling of the energy charge-discharge process with natural ventilation 43

2.1 Description of the experimental platform . . . 44
2.1.1 Passive strategies for the charge-discharge process in summer . . . 44

2.1.2 Natural ventilation system and openings . . . 45
2.2 Experimental approach and protocol . . . 45
2.2.1 Instrumentation of the thermal mass domain . . . 47
2.2.2 Instrumentation of the building . . . 50
2.2.3 Measuring system and calibration . . . 52
2.3 Semi-empirical models for data processing . . . 58
2.3.1 Decoupling the convection and radiation heat exchanges . . . 58
2.3.2 Mean radiant temperature of surrounding surfaces . . . 63
2.4 Experimental plan implemented in the measurement campaigns . . . 64
2.5 Results and discussion on the coupling between the energy charge-discharge and natural ventilation . . . 65
2.5.1 Classification of the experimental data . . . 65
2.5.2 Thermal behavior of the platform under different opening configurations and outdoor conditions . . . 66
2.5.3 Coupling of the charge-discharge process with natural ventilation within the indoor environment . . . 69
2.6 Characterization of the energy charge and discharge processes . . . 75
2.6.1 Impact of the outdoor environment upon the indoor environment via correlation analysis . . . 75
2.6.2 Identification of the heat transfer phenomena involved . . . 83
2.7 Thermal comfort assessment of a simple opening-closing strategy . . . 93
2.7.1 Indicators employed in the assessment . . . 93
2.7.2 Impact of a passive night ventilation strategy on internal thermal comfort . . . 94
2.8 Concluding remarks . . . 97

3 Characterization of the natural ventilation airflow rate 99
3.1 Initial considerations and airflow pattern recognition . . . 100
3.2 Modeling of the natural airflow rate in the platform . . . 102
3.3 Airflow characteristics of the openings . . . 109
3.3.1 Recovery of the envelope tightness and airtightness tests . . . 109
3.3.2 Discharge coefficient of the openings . . . 111
3.3.3 Identification of $\mathscr{C}$ and n for each opening . . . 113
3.4 Results and analysis . . . 113
3.4.1 Airtightness tests and discharge coefficient identification . . . 113
3.4.2 Comparison of the air change rate per hour using airtightness tests . . . 116
3.4.3 Airflow simulation results . . . 117
3.5 Concluding remarks on the airflow characteristics of the platform and perspectives . . . 123

4 Identification of a thermal model to describe the behavior of the platform 125
4.1 Identification of a thermal behavior model for the indoor air using experimental data . . . 126
4.1.1 Energy balance for the indoor air . . . 126

4.1.2 Estimation of the natural airflow rate via heat flux and temperature measurements 131
4.1.3 Identification of Model A for all opening configuration 134
4.2 Choice of a thermal behavior model for the thermal mass 147
4.2.1 Lumped-capacitance approximation 147
4.2.2 Spatial discretization via finite differences 148
4.2.3 Choice of a Model B for all opening configuration 149
4.3 A complete model for describing the coupling between the energy charge-discharge of the thermal mass and natural ventilation 153
4.3.1 Evaluation of the model with data inside the identification process 153
4.3.2 Evaluation of the model with data outside the identification process 156
4.4 Concluding remarks 159

General conclusion and future work **161**

Associated publications **169**

Bibliography **181**

Appendices **197**
A Calibration and metrology 197
A.1 Experimental report: Calibration of thermocouples 197
A.2 Comparing the temperature of black and shiny thermoelectric modules 212
A.3 Assessment of thermoelectric modules as alternative to conventional heat flux meters for decoupling the superficial heat transfer 215
B Weather conditions from ENSAM meteorological station 220
C Reports of airtightness tests 221

Introduction

"The big picture"

The increase of the world energy consumption represents a vital concern nowadays since, in 2015, around 82% of the energy production was still based on fossil fuels (cf. fig. 1). Around 22% of this consumption was due to the residential sector. This 22% was associated with a 17% of CO_2 emissions [54]. The majority of the energy demand for this sector belongs to heating, ventilation and air-conditioning applications (HVAC), making them a significant contributor to global greenhouse gas emissions. The balance of the current situation increases the pressure to take action, such as those established recently at the Paris Climate Conference (COP21). They aim to restrict the increase of the greenhouse gas emissions, by holding the global average temperature rise to well below 2 °C [18]. Therefore, the reduction of energy consumption related to HVAC, and the improvement of the efficiency of technologies used in these applications is a prevailing trend nowadays.

In this matter, as part of the searching for solutions to reduce the energy consumption in buildings, in France, the 2020 Thermal Regulation (RT 2020) aims to reduce this energy consumption, from 50 $kWh \cdot m^{-2} \cdot an^{-1}$ in 2012 to 15 $kWh \cdot m^{-2} \cdot an^{-1}$ by 2020, through the development of more efficient energy systems (cf. fig. 2). These systems are required to be either passive or semi-passive, leading to attaining zero-energy or positive energy buildings. Here, it is intended to contribute to the improvement of the "passive" management of the summer thermal comfort in an existing building, by controlling the moving parts of its envelope: the programmable solar protections, e.g., window blinds, shutters, and natural ventilation openings, e.g., windows type. These moving parts allow, in principle, to control the radiative and convective interactions between the indoor and outdoor environments. If such control of these moving parts is wanted to be a real-time controller, the description of the system being controlled needs to be sufficiently simple and light

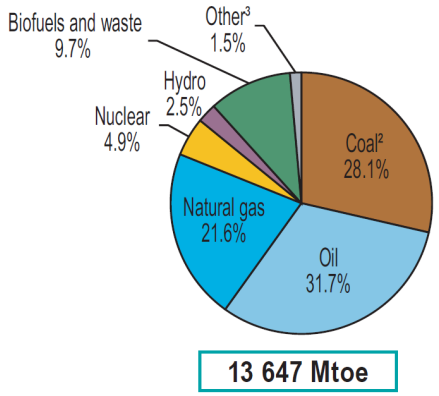

Figure 1: 2015 world total primary energy production according to IEA [54].

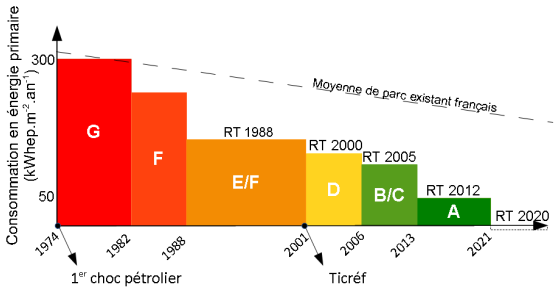

Figure 2: Objectives in energy consumption of the regulation RT 2020 in France.

Thesis statement and specific objectives

In this regard, we intend to verify that by performing a deep-comprehensive study of the physical phenomena regarding the coupling between the energy charge-discharge process and natural ventilation in a building, a suitable selection of a natural ventilation strategy leads to minimizing air conditioner usage regarding thermal comfort needs. This thesis focuses on first on the comprehension and highlighting of this coupling and after the construction of a simple physical model able to describe the thermal behavior of the building under different weather conditions and various natural ventilation strategies. We propose to address this statement by pursuing the following specific objectives:

1. To characterize (comprehension + highlighting) the coupling between the sensible energy charge-discharge process and natural ventilation.

2. To construct a model for describing the thermal behavior of the building considering the key parameters underlying this coupling, along with the outdoor conditions.

Since a better understanding of such coupling between these physical phenomena can be acquired by implementing experimental-based studies, it is decided to perform the characterization of the heat transfer, in the sensible energy charge-discharge process, in a full-scale test building under *in situ* conditions.

Charge and discharge processes and natural ventilation

So what do we call charge and discharge processes? In a 24h day-night cycle in the summertime, the building can be said to be submitted to different thermal stresses that are specially presented in two separate periods: the daytime and nighttime, in which the indoor environment of the building might behave differently.

During the daytime, the building experiences a "charge process" in which the principal heat source, or more accurately yet, the only source is the solar power; which manifests in the form of solar radiation (direct and diffuse) and is the leading cause of wind and the rising of the outdoor air temperature [14]. During this process, a passive building, a PEH, for instance, might choose to reduce the heat gains by closing the window openings and solar shades, in order to increase the total thermal resistance (and thus, increasing the building time constant), which may result in a sufficient attenuation of the outdoor "heat wave" (cf. fig. 3 (a)). In this case, such attenuation is primarily driven by the thermal mass of the envelope, where a poor attenuation will result in buildings with light-weight materials than in buildings with heavy-weight materials such as concrete.

During nighttime, the solar power "vanishes" causing a drop in the outdoor air temperature and the building experiences a "discharge process" (cf. fig. 3 (b)). During this process, the building might choose to evacuate, as much as possible, the heat stored during the previous charge process by cooling down the indoor environment, in order to provide suitable initial conditions to attenuate the incoming heat of the following charge process. Among passive buildings, a common way to evacuate the heat stored is through natural ventilation, which will successfully cool down the indoor air and the structure, if the

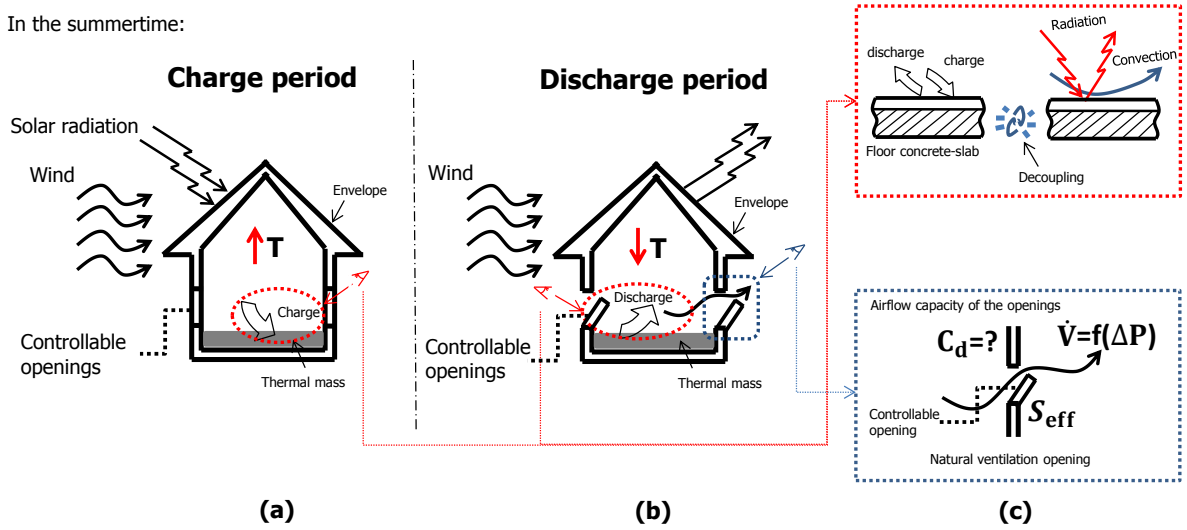

Figure 3: Overview of the physical phenomena: (a) charge process, (b) discharge process, and (c) physical phenomena.

outdoor conditions are suitable (windy nighttime, no rain, no unbearable noises) and the heavy-weight materials are correctly placed.

Natural ventilation in buildings is a subject that has been exhaustively studied over more than 50 years. Still, the mechanics of such physical problem hasn't been fully understood, despite the development of many descriptive models and software for airflow simulation coupled with heat transfer, to aid such an understanding. Many factors influence the adequate implementation of natural ventilation strategies regarding the occupant's comfort needs and thus affecting the energy consumption of the building. Among these factors, the behavior, knowledge, and tolerance of the occupants play an essential role.

In this regard, our starting hypothesis, is that the nature of these charge and discharge processes manifest in the form of convective and radiative heat transfer within the indoor environment of the building, and these processes can be decoupled into their convective and radiative parts (cf. fig. 3 (c) top). For instance, in the discharge period, since the outdoor air is usually colder than the indoor air, the implementation of natural ventilation might drag in denser air, and thus, this air will enter the building by the lower parts (near the floor). In cases where a concrete slab is part of the floor as shown in figure 3, the floor will experience a discharging in the form of convection when the outdoor air interacts with the floor surface.

The test building

The building employed for implementing the experimental-based study is a Plus Energy House (PEH) prototype, named Sumbiosi (cf. figs. 4-5), built by a consortium gathered around the campus of the University of Bordeaux, as part of its participation in the inter-university Solar Decathlon Europe 2012 competition. This prototype was designed in such a way as to promote the passive energy storage in winter daytime and the semi-passive energy discharge in summer nighttime. After the competi-

tion, Sumbiosi was installed in the campus of the University of Bordeaux; becoming an experimental platform for research purposes [72, 84, 85, 88, 91].

Figure 4: Image of the experimental platform, Sumbiosi: South-facade view.

Figure 5: Image of the experimental platform, Sumbiosi: North-facade view.

It has three main architectural features that aid to promote the strategies of passive energy storage and semi-passive energy discharge, namely: a concrete-slab behind the south glazed-facade, fixed and programmable solar shades, and programmable natural ventilation openings at the south and north facades, and at the Shed-roof.

The envelope consists of an external structure in maritime pine and an internal structure in wooden finishes. The internal structure of the North, East and West facades, as well as the ceiling and floor, include a thermal insulation layer of 32 cm thick. The external part of the east and west facades includes outdoor cabinets, as well as the South facade at its corners (cf. fig. 6 (b)).

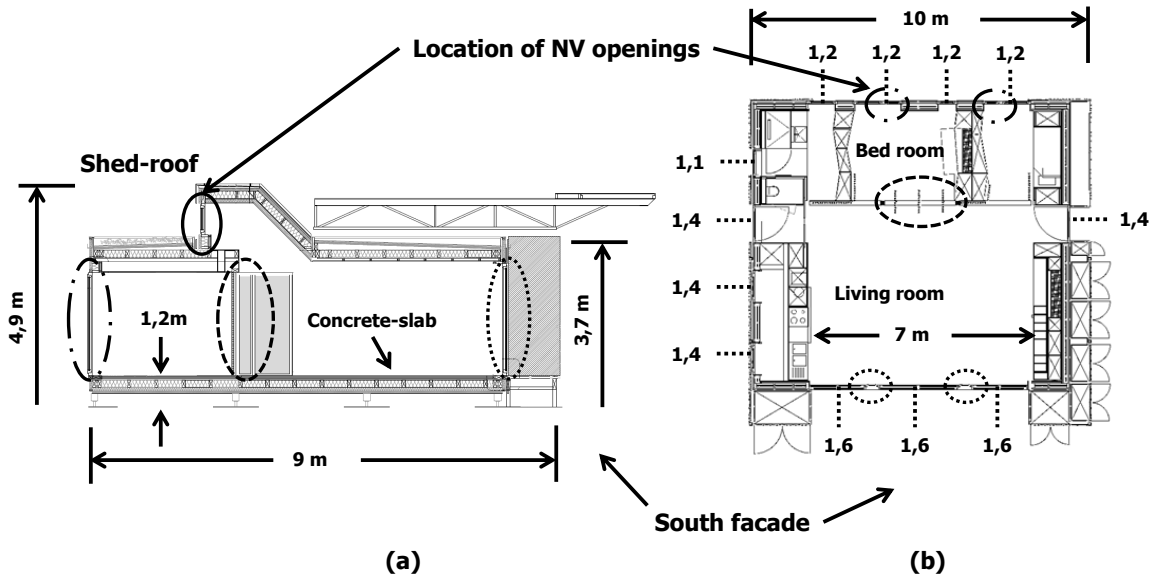

Figure 6: Schematic of the architectural plan of the experimental platform: (a) West view and (b) top view. Values of the global heat transfer coefficients for external walls of the platform (dotted lines).

The South and North facades include the natural ventilation openings, where the area of the openings in the South and North facades are 9,58% and 7,51%, respectively; apart from this, 90,42% of the total surface of the South facade consists of large double-glazed French-type windows. The platform enve-

lope encloses an air volume of about 211 m^3, with an envelope surface of about 226 m^2. The values of the global heat transfer coefficient for principal doors and windows, which are in direct contact with the indoor and outdoor environments.

The experimental platform is equipped with various systems helping to produce its own energy. The solar panels and collectors with position-tracking strategies, are some of the active systems. The natural ventilation openings, a PCM heat exchanger and solar shades, are some of the semi-passive systems. Also, these semi-passive energy storage systems are intended to be coupled with the platform thermal mass. Such coupling allows the platform to enabling energy storage and discharge strategies aiming to control the thermal comfort of the indoor environment. This strategies can be automatize thanks to the home automation system (KNX and Domovea), destined to continuously monitoring the indoor air quality, and the outdoor environment.

Research strategy and organization of the manuscript

To adopt a research strategy for accomplishing these specific objectives, we must first obtain a better understanding of the physical phenomena behind the thermal behavior of buildings, and they charge-discharge process coupled with natural ventilation. Also, the understanding of the role of the envelope and ventilation, as well as, the experimental techniques for identification regarding the modeling for forecasting and the natural airflow rate, is essential.

Thus, the first chapter is dedicated to explore and determine which experimental and modeling approaches are the more suitable for our case. Since a physical model is wanted, we also have focused this literature study on the modeling approaches for detailed physical models. This literature review will comprise: the thermal behavior of buildings, general aspects of natural ventilation, and the metrology in heat flux measurement on rigid surfaces and calibration procedures. The interest of this last topic can be justified by the fact that natural ventilation interacts with the energy discharge process in the form of convective heat transfer. Since their direct coupling is wanted to be studied, direct convective heat flux measurements appear to be suitable, because they allow to quantify and highlight the charge and discharge processes, as it will be shown later in this manuscript.

The second and third chapters involve an experimental part, regarding heat transfer and airflow, respectively. The second chapter is committed to characterizing the charge and discharge processes along with the phenomenology involved, within the test building, by implementing an experimental approach with heavy instrumentation in terms of heat flux and temperature. The third chapter is devoted to modeling the natural airflow rate in the test building.

Finally, the fourth chapter is dedicated to identifying a semi-empirical model for describing the thermal behavior of the indoor environment, by focusing only on the main elements of the building: the indoor air and the thermal mass.

Chapter 1

Theoretical background and state of the art

"... Une fenêtre n'est pas qu'une source de déperditions thermiques et la ventilation naturelle n'est pas simplement un courant d'air."

David Roditi

Scope

This chapter is devoted to comprehending the natural ventilation concept, and to assess the experimental and modeling techniques already implemented for past researchers, in the estimation of the ventilation airflow rate due to the wind and thermal buoyancy effects. This will provide a strong theoretical grasp of the natural ventilation process as part of the main elements in the thermal behavior of buildings. These bases will help to choose the most suitable techniques to estimate the natural ventilation airflow rate in our platform. Also, regarding the coupling between natural ventilation and the energy charge-discharge process presented earlier, the techniques for estimating the convective heat flux on rigid surfaces are also assessed. Then, this chapter consists of the following four main sections:

- Natural ventilation concept in buildings, including experimental and modeling techniques.
- Building thermal behavior modeling and identification approaches.
- Coupling between natural ventilation and thermal mass.
- Heat flux measurement techniques for rigid surfaces.

1.1 Natural ventilation in buildings

Natural ventilation is the process of renewing the air of a room by natural means by either from infiltrations (unavoidable) or window openings (on purpose). In general, there are three leading causes of air movements by natural means inside and around a building: (*i*) wind effects, (*ii*) air temperature and solar radiation, and (*iii*) concentration of moisture and pollutants [117]. A schematic showing the relation and influence factors, between these three causes and the air movements inside and around a building, is presented in figure 1.1:

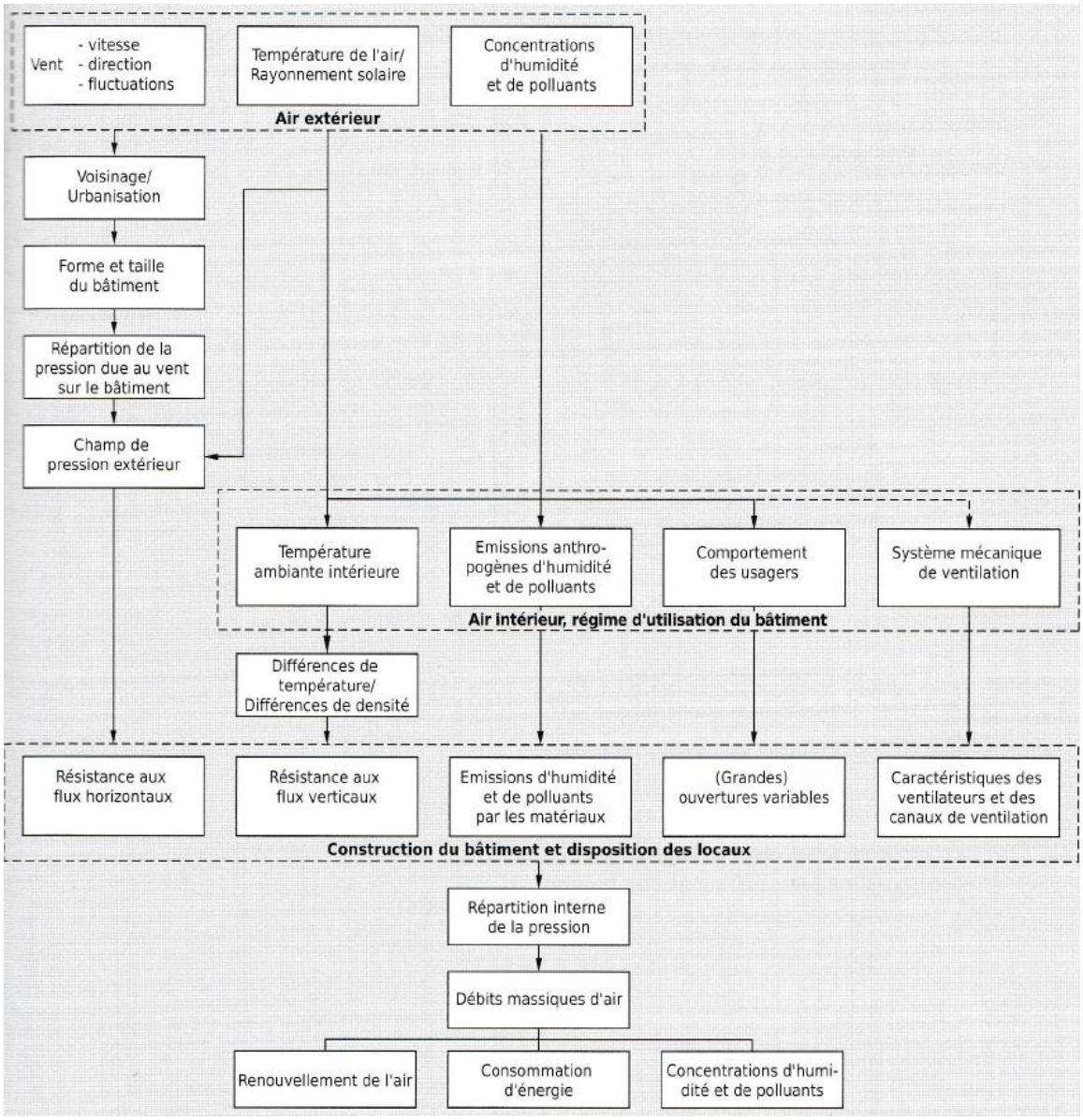

Figure 1.1: Influence factors and relations in the air movement domain inside and around the building [117].

1.1.1 The role of natural ventilation

In a building, the role of ventilation is crucial concerning two major points: the indoor air quality (comfort and minimum air renewal rate) and the energy consumption. In this regard, natural ventilation is wanted to efficiently provide a minimum air renewal rate to keep the air stale out from the room, and thus, avoiding the use of mechanical ventilation, leading to minimizing the energy consumption. In the present research work, we are only interested in the thermal aspects of comfort; no other aspect of comfort will be considered in further analysis.

(A) Thermal comfort:

The adequate implementation of natural ventilation in buildings strongly depends on the occupants' behavior, which is usually driven by their hygrothermal comfort needs. Many parameters influence these comfort needs, and can be classified into three categories: physical, physiological, and external; the indoor and outdoor conditions (air temperature, relative humidity, air currents), are among the physical parameters; the level of metabolic activity perform and the level of clothing, are some of the most important physiological parameters [2].

Thermal comfort indicators

Several comfort indicators can be found in the literature. In summer, the standard ISO 7730 recommend the use of the following values for comfortable indoor conditions:

- A room temperature between 23 and 26 °C,
- The difference in vertical temperature must be less than 3 °C,
- An average indoor air speed less than 0,25 $m \cdot s^{-1}$,
- The degree of discomfort that measures thermal dissatisfaction.

Another parameter very evoked in the literature, is the difference between the temperature of the interior air and the mean radiant temperature of the surrounding walls, that according to [83]: a feeling of discomfort can appear beyond a temperature difference higher than 2 °C, between the indoor air temperature and that of the ceiling, and 3 °C with that of the walls.

Nighttime ventilation as thermal comfort assistance

In regions with a significant temperature gradient between nighttime and daytime, night natural ventilation, if implemented adequately, arises as a good solution for the attenuation of the "heat wave" associated with the daytime period, leading to maintaining the thermal comfort for longer periods. Its application may be more attractive in office buildings, due to the absence of occupancy during nighttime.

Its principle consists of cooling down the structure of the building when it is not occupied (nighttime), providing a heat sink that is available during the occupancy period (daytime). This heat sink absorbs the heat gains related to occupancy or equipment and maintains acceptable indoor conditions

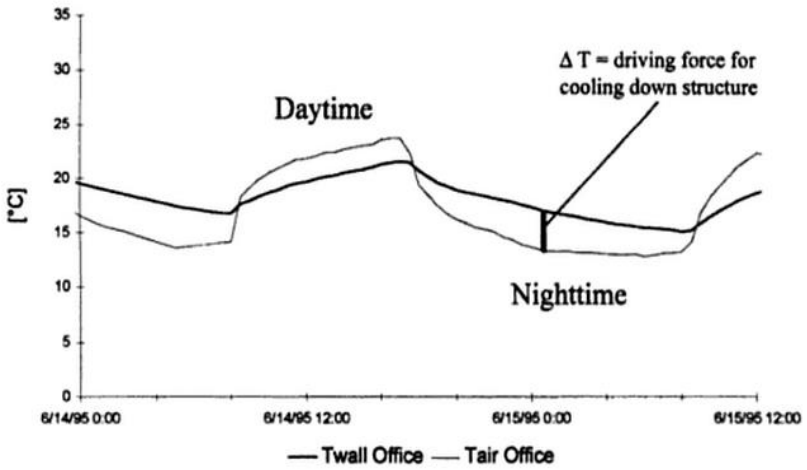

Figure 1.2: Cooling potential due to nighttime ventilation technique [2].

[2]. The cooling potential of nighttime ventilation can be assessed by the temperature difference between the indoor air and the surface of the wall (cf. fig. 1.2).

As observed in figure 1.2, during nighttime, the temperature of the walls is higher than the air inside the office; therefore heat transfer will occur outwardly (from the walls to the surrounding air), successfully cooling down the walls. In detail, the temperature difference between the indoor air and the wall surfaces is the consequence of the building interaction among other parameters, such as the outdoor air and the sky temperature, the surface temperature of the surrounding buildings, and wind effects. A review of the night natural ventilation strategies was recently published by Solgi *et al.* [94].

However, different limitations are encountered depending on the site where the building is located; urban or suburban. Also, depending, on the periods of occupancy in the building, implying that this strategy is useful for office buildings.

Limitations in applicability and usage

One of the most critical limitations of natural ventilation usage lays in its understanding. Some of the advantages (1-5) and limitations (6-9) regarding its applicability are [86]:

1. Well accepted by occupants who understand it and control it very easily.
2. The investment required is very low or zero.
3. The energy required for air transport is free.
4. It allows high flow rates, especially for passive cooling.
5. It does not crash or fail.
6. It doesn't work in noisy or polluted areas.
7. It doesn't work in places with a depth/height relation exceeds 2,5 (office landscape).
8. It hardly allows the heat recovery from exhaust air.
9. It provides a variable flow rate, which without proper controls, might not be necessary in relation to the needs.

(B) Air infiltrations and leakages:

Air infiltrations and leakages are the unavoidable part of the natural ventilation process, due to imperfections in the envelope or joinery. They are important for indoor air quality, but if not controlled properly they could become the leading cause of heating losses. Therefore, the quantification of the air-leakage rate represents an important issue for prediction of the heat losses. Also, regarding the nature of the air leakages, their distribution around the envelope is often complicated to be determined [20, 32].

(C) Impact in energy consumption and performance of natural ventilation strategies:

Despite it is known that the use of natural ventilation systems might reduce the overall power consumption if we applied them correctly, how much will it reduce, depends on many parameters. When applicable, natural ventilation can compensate cooling energy consumption and its energy costs and carbon dioxide emissions. The potential cooling energy that may be saved depends, of course, on the climate conditions of the building location and the internal and external heat gains [31].

When having not quite favorable climate conditions for the implementation of natural ventilation, coupling it to a mechanic system remains possible, which is accomplished in Hybrid Natural Ventilation systems. Among the performance indicators of natural ventilation strategies; a good indicator for evaluating the ventilation power is the level of air change per hour reached. Regarding the energy consumption, a good indicator is the percentage of occupied hours where minimum mechanical ventilation rates are met [13].

1.1.2 The natural ventilation concept

For a better understanding of the natural ventilation process, three essential aspects are introduced to define the concept of natural ventilation: How is it created? In which way it can be implemented in buildings? And, which architectural features can be employed? This can be illustrated in figure 1.3. Natural ventilation is created by either buoyancy forces, wind forces, or a combination of both. These two forces can be exploited to ventilate a space by "promoting" the implementation of some strategies: single-sided ventilation, cross ventilation, or stack ventilation; and this, through some architectural features such as wind towers, wind scoops, chimneys, double facades, atria, among others [58]. Finally, the determination of the natural airflow rate depends on the strategies implemented.

1.1.2.1 Driving forces

(A) Air flow due to wind forces:

In the case of wind driven ventilation, to benefit the most from this natural force, it is recommended that the facade with openings of a building located in a windy place must be oriented perpendicularly to the wind direction, although not strictly necessary [40]. When the wind currents find in their path a building, a high-pressure zone is created over the windward side (or upside) of the building, and the leeward side (or downside) experiences an under-pressure zone (cf. fig. 1.4 (a)). The other sides of the building (those in the wind direction) will also experience an under-pressure status (cf. fig. 1.4 (b)) [58].

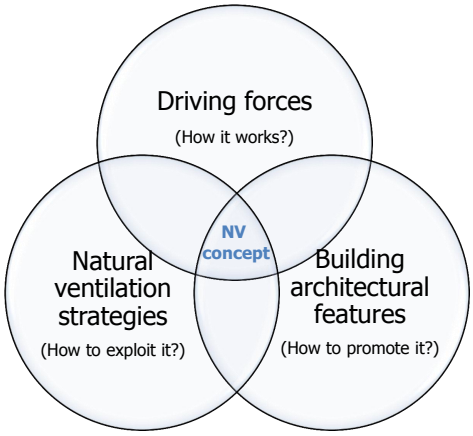

Figure 1.3: The natural ventilation concept.

In general, the resulting dynamic pressure over the windward facade can be defined as a function of the wind speed using Bernoulli's principle, as follows:

$$P_v(t) = \frac{1}{2} \cdot \rho \cdot \mathcal{V}_v^2(t) \qquad [\text{Pa}] \tag{1.1}$$

where ρ represents the air density at outdoor temperature, and $\mathcal{V}_v$ is the wind speed at the opening height on the windward side. The resulting airflow rate inside the building due to wind effects depends on the windward-leeward pressure difference, as follows:

$$\Delta P(t) = \frac{1}{2} \cdot C_p \cdot \rho \cdot \mathcal{V}^2(t) \qquad [\text{Pa}] \tag{1.2}$$

where C_p is known as the pressure coefficient.

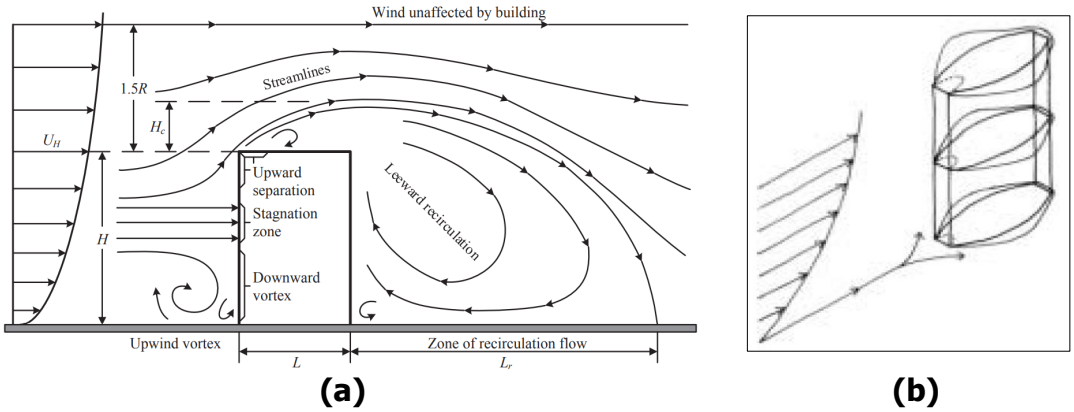

Figure 1.4: Representation of wind forces (a), and pressure distribution induced by wind (b) [58].

This pressure coefficient is introduced in the building domain to account for the pressure differences induced by the airflow over the building envelope. A simplified representation of these pressure differences is presented in figure 1.4 (a), where the windward facade of the building experiences an overpressure, while the leeward facade experiences a pressure drop with respect to the static pressure of the freestream, named dynamic pressure (P_∞), defined by equation 1.1. Thus, an expression for C_p

can be written as follows [56]:

$$C_p \equiv \frac{P - P_\infty}{\frac{1}{2} \cdot \rho_\infty \cdot \mathcal{V}_\infty^2} \qquad [-]$$

where P is the value of the pressure where the coefficient is being evaluated. ρ_∞ and $\mathcal{V}_\infty$ represent the density and velocity of the airflow on the freestream region, respectively. The windward facade will present positive values of C_p, while the leeward facade, negative values. An overview of acceptable models to predict C_p values in buildings are presented in §1.1.3.3.

(B) Air flow due to buoyancy forces:

A density gradient can induce air movement between two regions (buoyancy forces). This gradient can be created by either different gas concentrations, a temperature difference, a humidity difference, or a combination of these three. In buildings, this mentioned before can cause air movement within the same zone, between different zones within the building, between two facades [86], and between the inside and outside of the building (cf. fig. 1.5). The reason lays in that this density gradient creates a pressure difference between the zones, normally referred to as static pressure. In this case, the overall pressure difference can be defined as a function of the air density of two zones (indoor and outdoor air), by Bernoulli's principle as follows:

$$\Delta P(t) = \Delta\rho \cdot g \cdot \mathscr{Z} = [\rho_{oa} - \rho_{ia}] \cdot g \cdot \mathscr{Z} \qquad [\text{Pa}] \tag{1.3}$$

where g is the gravitational acceleration, and $\mathscr{Z}$ is the height between an upper and a lower openings (cf. fig. 1.5 (a)). Note that this expression is under the assumption that the air entering the building is at outdoor air density (ρ_{oa}) and the air leaving the building is at indoor air density (ρ_{ia}). Also, in equation 1.3 it is considered that the openings height is negligible with respect to their separation ($\mathscr{Z}$).

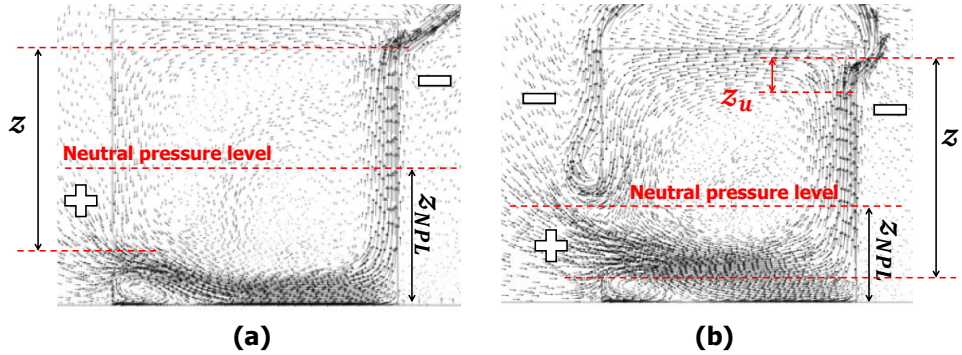

Figure 1.5: Air movement due to buoyancy forces: (a) small openings, (b) one large lower opening [70].

However, when the openings height is not negligible (case of large openings), the use of equation 1.3 might lead to either an underestimation or an overestimation of this overall pressure difference. In this case, the overall pressure difference can be defined as in equation 1.4, for the outgoing airflow [36, 70]:

$$\Delta P = \int_{Z-\mathscr{Z}_{NPL}-z_U}^{Z-\mathscr{Z}_{NPL}} \Delta\rho \cdot g \cdot dz \qquad [\text{Pa}] \tag{1.4}$$

where Z represents the vertical distance from the lower edge of the lower opening (L) to the upper edge of the upper opening (U); with height z_U (cf. fig. 1.5 (b)). The vertical distance $\mathscr{Z}_{NPL}$ represents the height of the "neutral pressure level" (NPL), where the indoor-outdoor pressure difference is equal to zero, with respect to the floor. Different ways to determine this height have been reported in the literature [3, 70, 86]. For instance, the value of $\mathscr{Z}_{NPL}$ can be determine by the following expression [70]:

$$\mathscr{Z}_{NPL} = \frac{\gamma^2}{1+\gamma^2} \cdot \mathscr{Z} \qquad [\mathrm{m}] \tag{1.5}$$

where γ is the opening ratio, as follows:

$$\gamma = \frac{C_{d_U} \cdot S_U}{C_{d_L} \cdot S_L} \qquad [-]$$

where C_d and S represent the discharge coefficient and the opening effective area, respectively. This vertical distance depends on the position and height of the openings. For an enclosure with a single opening, the NPL will established at half the height of this opening. For the same enclosure with another opening over the previous one at the same side, the NPL will established at half the distance between these openings, if they are of the same size. However, if they differ in size, the NPL will tend to get closer to the larger openings; and the height of the NPL is proportionally to the square of the opening surface [86].

(C) Air flow due to a combined effect:

If placing the openings at the correct location, wind effects will join the thermal buoyancy effect, reinforcing the ventilation airflow rate. On the contrary, not placing them correctly or if the building is not correctly oriented, the wind will mitigate the thermal buoyancy effect reducing the building ventilation. This can be observed in figure 1.6 (a), where the openings are correctly located improving the airflow traversing the building. However, in (b), the openings are not correctly located, causing zero airflow (neutralizing both effects) at a specific wind speed value [86].

In this interaction the wind turbulence effect is more important than in cross-ventilation configuration [44]. However, significant differences can be observed concerning the complexity of this interaction regarding theoretical or experimental approaches [107].

1.1.3 Assessment techniques for the natural ventilation airflow rate

Depending on the natural ventilation strategy implemented, the natural airflow rate can be assessed using different methods. Such methods can be grouped into two categories: Modeling and experimental techniques. For the determination of the airflow rate, all modeling techniques require the knowledge of the airflow capacity of the openings employed. Thus, hereafter, we address this matter in the following section.

1.1.3.1 Airflow capacity of an opening

(A) Theoretical and empirical airflow-pressure relation:

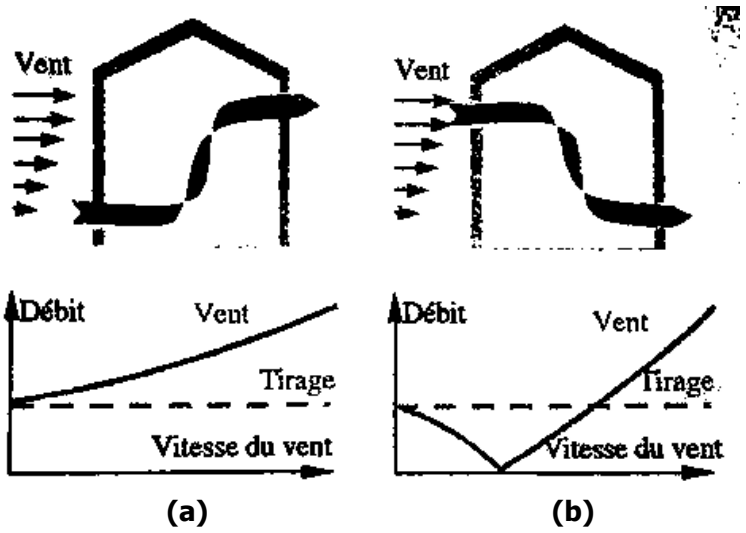

Figure 1.6: Stack ventilation with: (a) assisting winds, and (b) opposing winds [58].

A theoretical expression describing the airflow rate caused by a pressure difference between the upstream and downstream of an opening, can be written using Bernoulli's equation as follows:

$$\dot{V}(t) = S \cdot \sqrt{\frac{2 \cdot \Delta P(t)}{\rho}} \qquad \left[\mathrm{m}^3 \cdot \mathrm{s}^{-1}\right] \tag{1.6}$$

where $\dot{V}$ represents the airflow rate in $\mathrm{m}^3 \cdot \mathrm{s}^{-1}$ and S represents the area of free gap sections of the opening m^2 (usually called effective area S_{eff}). This expression considers a non-frictional fully developed turbulent fluid flow through the opening. If needed, the friction characteristics of the opening can be grouped in a single coefficient named the discharge coefficient (C_d) which multiples expression 1.6 here before.

For any type of fluid flow through an opening, the airflow rate caused by a pressure difference between the upstream and downstream of an opening, has been shown to follow expression 1.7:

$$\dot{V}(t) = \mathscr{C} \cdot [\Delta P(t)]^n \qquad \left[\mathrm{m}^3 \cdot \mathrm{s}^{-1}\right] \tag{1.7}$$

where $\mathscr{C}$ is called the airflow rate coefficient in $\mathrm{m}^3 \cdot \mathrm{s}^{-1} \cdot \mathrm{Pa}^{-n}$. Its value depends on the effective area of the opening, and also considers its friction characteristics. The exponent n is called the flow exponent: it takes the value of 0,5 for a fully developed turbulent flow and 1 for a laminar flow [93] ; for values in between, the flow is said to be partially developed. It has been shown that expression 1.7 describes the best, the air-leakages rate of a room or a building, where it can be small and big holes due to imperfections [39].

Daler *et al.* in 1982, as found in [57], reported the airflow capacity of bottom and side hung openings, for different opening degrees and as a function of a room indoor-outdoor temperature difference (cf. figs. 1.7-1.8). One of these types of openings, the bottom-hung window (also known as tilted window), is the same as the ones implemented in our test building.

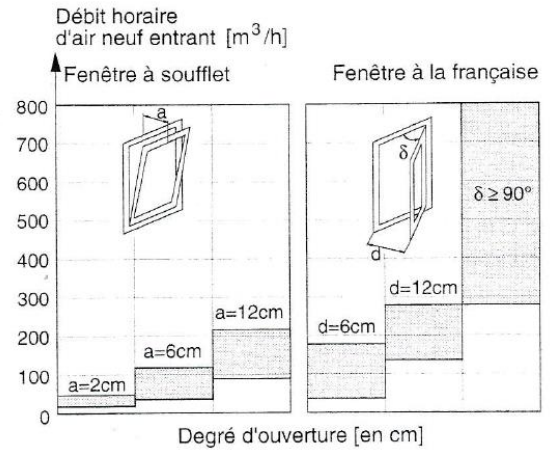

Figure 1.7: Airflow capacity of bottom and side hung windows depending on the opening degree [57].

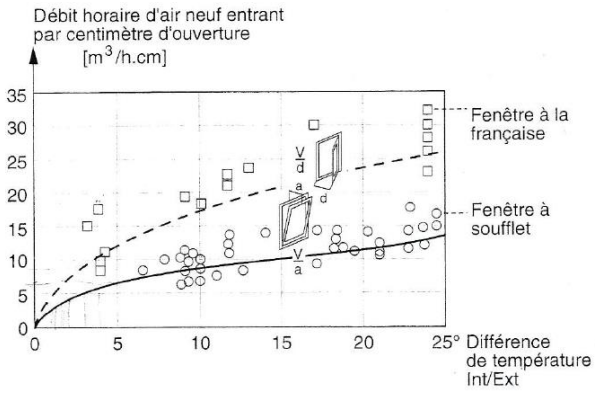

Figure 1.8: Variation of the airflow capacity of bottom and side hung windows as a function the indoor-outdoor temperature [57].

(B) The discharge coefficient and the effective area of an opening:

This coefficient can be defined as the ratio of the empirical (or real) airflow rate to the theoretical (or ideal) airflow rate, translating the fact that the free gap area (or jet section) is smaller than the total area of the opening [47]. Various experimental studies have been interested in the dependence the discharge coefficient presents when the pressure around the opening varies. Flourentzou *et al.* in 1998 [36] performed tracer gas and velocity measurements *in situ* in a three-level stack ventilated building to determine the C_d. A value of 0,6±0,1 was found, and thus, it was stated that: "the accepted value for the discharge coefficient was confirmed once again" (cf. fig. 1.9).

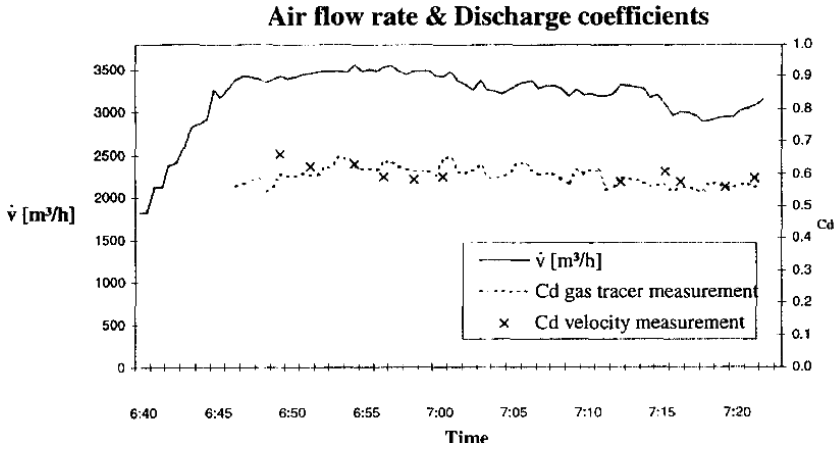

Figure 1.9: Values of discharge coefficient obtained by [36].

Heiselberg *et al.* in 2001 [49], performed airflow rate and pressure measurements at the opening in a laboratory set-up, and determined C_d values for openings similar to ours, using equation 1.6 (cf. fig. 1.10). It was concluded that "the use of a constant value could lead to serious errors in the prediction of airflow capacity", because their experimental results showed that the discharge coefficient changes with the effective area and the type of opening, as well as, with the temperature difference. Also, for

the three types of opening they tested, the value of the discharge coefficient slightly decreases as the pressure difference increases.

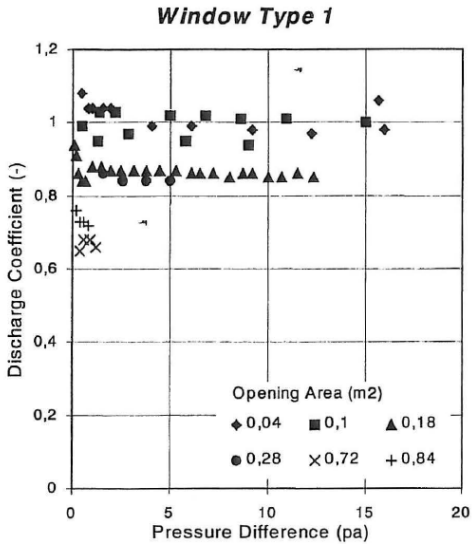

Figure 1.10: Values of discharge coefficient obtained by [49].

Costola and Etheridge in 2008 [25], performed pressure measurements in a scaled model in wind tunnel experiments, consisting of stack and wind-assisted strategies. The scaled model included one small orifice at ground level and one "stack opening" at the top. They reported C_d values (named C_z) for both the orifice and the stack opening, where the values of C_d for the former resulted around 0,7 for either still air, or wind-assisted (0° and 180°) strategies; similar to those in figures 1.10 and 1.9. However, for the stack opening, C_d values changed considerable depending on the Reynolds number as shown in figures 1.11 and 1.12, for still air and wind-assisted strategies, respectively. In the case of the still air strategy, the average C_d value was used, and in the case of the wind-assisted strategy, an average value from the constant region (from a $\mathcal{R}e$ of about 600) was taken.

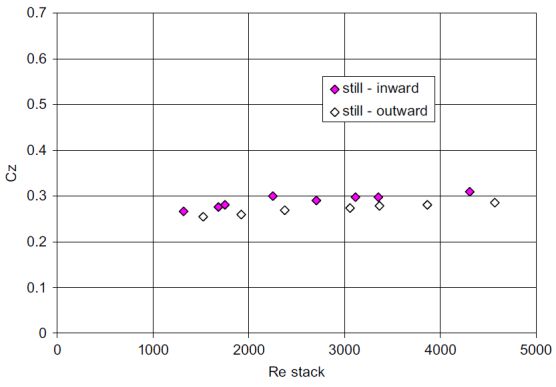

Figure 1.11: Values of stack discharge coefficients for inward and outward flow in still air [25].

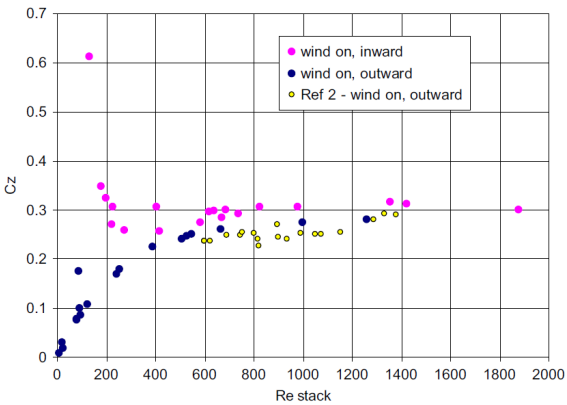

Figure 1.12: Values of stack discharge coefficients for inward and outward flow with wind [25].

Moreover, Teppner *et al.* in 2014 [98] performed an experimental study with wind tunnel using a

scaled room model with several bottom-hung windows, and CFD simulations.

By determining the friction factor ξ_v of the opening (S_{eff} = 0,377 m^2) to be equal to 28,9, a C_d value of 0,67 was determined using the following expression:

$$C_d = \frac{1}{\sqrt{1 + \xi_v \cdot \left(\frac{S_{eff}}{S_{fo}}\right)^2}} \qquad [-] \tag{1.8}$$

where S_{fo} stands for the area of the entire section of the opening (1,82 m^2). S_{eff} represents the effective area of the opening. Van Paassen *et al.* in 1998 [78] proposed the following expression to defined the effective area S_{eff} as a function of the opening angle, for tilted windows (bottom hung or side hung):

$$S_{eff} = \sqrt{\frac{1}{\frac{1}{(z \cdot w)^2} + \frac{1}{\left[2 \cdot z \cdot w \cdot \sin\left(\frac{\phi}{2}\right) + z^2 \cdot \sin\phi\right]^2}}} \qquad \left[\mathrm{m}^2\right] \tag{1.9}$$

where z and w represent the height and width of the opening, respectively, and ϕ represents the opening-angle (0 - 90°). The same expression was used latter by Krzaczek *et al.* in 2015 [60] for bottom hung openings. Other ways to calculate this area can be encountered in [19, 98].

Other models have been reported for the estimation of the discharge coefficient. Pelletret in 1991 [80], proposed an empirical model for C_d as a function of the ratio between the heights of the opening (z) and the room ($\mathscr{L}$), as follows:

$$C_d = 0{,}609 \cdot \frac{z}{\mathscr{L}} - 0{,}066 \qquad \text{if} \quad 0{,}2 \leq \frac{z}{\mathscr{L}} \leq 0{,}9 \tag{1.10}$$

On the contrary, Kiel and Wilson in 2009 [5], proposed another empirical model for C_d as a function of the indoor-outdoor temperature difference, accounting for thermal buoyancy effects, as follows:

$$C_d = 0{,}4 + 0{,}0045 \cdot |T_{ia} - T_{oa}| \qquad \text{for} \quad 0{,}5 \leq |T_{ia} - T_{oa}| \leq 40 \tag{1.11}$$

Moreover, a comparison of implementing these models, showing their impact on the natural airflow rate can be found in [96], concluding that the estimation of this coefficient should be performed attentively. Nevertheless, to determine either the airflow capacity or the discharge coefficient of an opening, experimental data is needed. Thus, hereafter the experimental and modeling techniques employed to determine such characteristics of the openings.

1.1.3.2 Experimental techniques and empirical correlations

Many experimental techniques have been developed/employed to determine the airflow rate in naturally ventilated buildings for the case of openings closed or opened. From the literature we can cite the well known and accepted methods with few reference work (since the list is very vast):

- Direct air velocity measurements [33, 98].
- Direct airflow rate measurements [50].
- Tracer gas method [33, 36].

- Particle image velocimetry [19, 49].
- Wind tunnel for scaled room models [98, 61].
- Saline solutions for scaled dimensional analysis [53].
- Blower door tests (or airtightness tests) [55].

In this section it is intended to present information about the airflow rate levels attained by implementing merely natural ventilation strategies. Thus, the following studies do not necessarily employ buildings and openings similar, in type and size, as our test building. Instead, we are interested in the reported airflow rate levels attained for given wind speed and direction, temperature difference, and the experimental technique employed. Nevertheless, we include the size and type of the building and openings. Finally, to determine the airflow rate, these experimental techniques are often complemented with empirical correlations or statistical methods, but they will not be presented here in detail.

Since the majority of the studies in the literature employed these techniques for cases with simple configurations, where the airflow path is well known (single-sided, cross or stack ventilation), and since our test building has a quite number of openings (rendering moot the assumption of a specific airflow path, with an inlet and outlet far away from each other), the same airflow rate levels reported might not be attained in our platform.

Kronvall and Persily between 1980 and 1985, developed the K-P model, as found in Sherman 1987 [93], to estimate the annual natural air-leakage rate of a building using airtightness tests as follows:

$$\overline{ach}_{natural} \equiv \frac{ach_{50}}{20} \qquad \left[\mathrm{h}^{-1}\right] \tag{1.12}$$

which later employed data from tests performed in more than 40 houses, and achieved the following linear regression:

$$\overline{ach}_{natural} \approx \frac{ach_{50}}{18} - 0,08 \qquad \left[\mathrm{h}^{-1}\right]$$

where ach_{50} referred to the value of ach at a pressure difference of 50 Pa measured via blower door tests.

Gładyszewska-Fiedoruk and Gajewski in 2012 [44], studied the effect of wind on the performance of stack ventilation by performing air speed measurements, proving that wind effects has a considerable influence that could change up to 350%. Figure 1.13 (a) shows the reported air change rate values, for stack and wind only. They also reported the variation of the air change rate, with respect to the wind speed (cf. fig.1.13 (b)).

Freire *et al.* in 2013 [37] (in an enclosure of 748 m^3) and Larsen *et al.* in 2003 [61] (in an enclosure of 93 m^3), compared measured data, from wind tunnel experiments, with different existing models, aiming to evaluate and improve the existing models for the case of single-sided ventilation (cf. figs. 1.14-1.15).

On the other hand, R. Jack *et al.* in 2015 [55], performed nine *in situ* airtightness tests (or blower door tests) for estimate the air change rate at natural pressure levels of a full-scale building of volume. The air infiltration rate, for either windows closed and opened, was determined using the K-P model in equation 1.12 (cf. fig. 1.16).

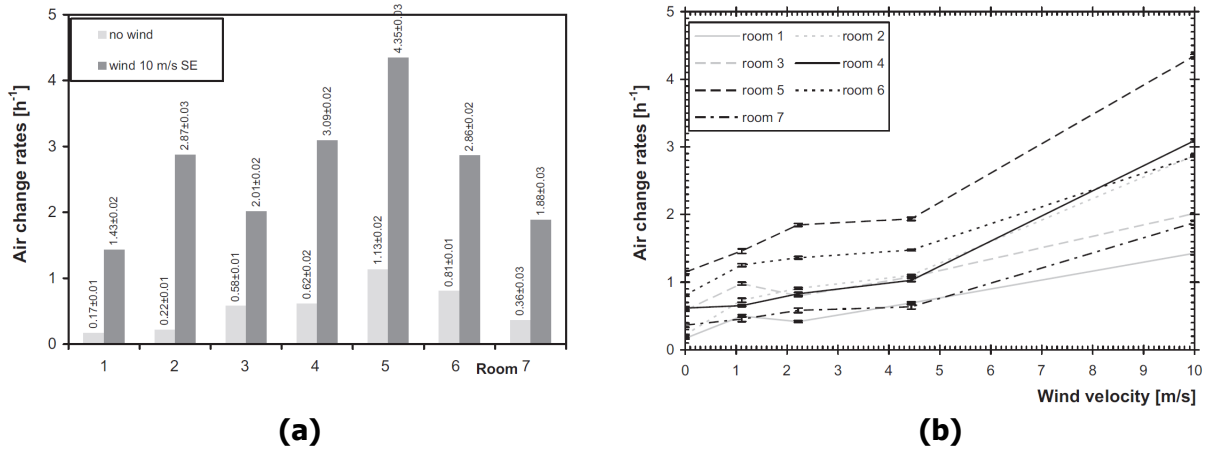

Figure 1.13: (a) Influence of wind on the efficiency of stack ventilation. (b) Air change rates in the investigated rooms as the function of the wind velocity [44].

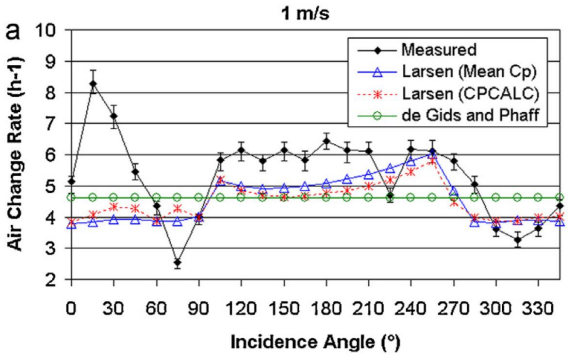

Figure 1.14: Comparisons between the experimental and simulation results performed into the PowerDomus software for the wind tunnel case [37].

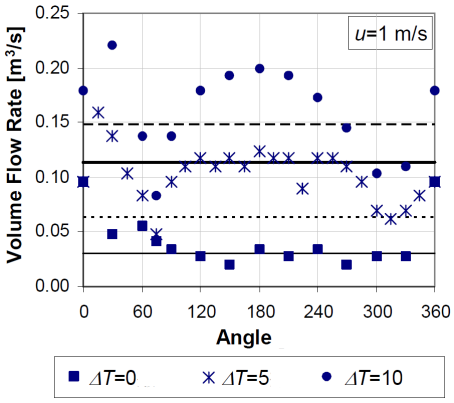

Figure 1.15: Measured and calculated volume flow rates: Warren & Parkins (black thin line), De Gids & Phaff (black dotted line, ΔT = 0 °C), and De Gids & Phaff (black thick line, ΔT = 5 °C) [61].

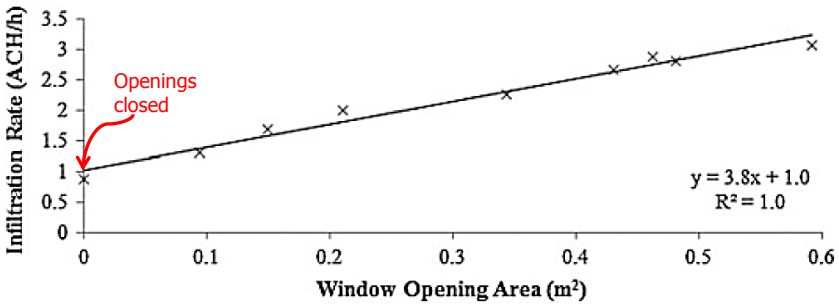

Figure 1.16: Results of the blower door tests with window opening from [55].

1.1.3.3 Models and numerical techniques

The local estimation of the impact of wind effects on the natural airflow rate remains complicated in buildings with "non-standard" architectural features. These devices, forming part of the building enve-

lope and being either openings or entire facades with a "non-standard" morphology, make it difficult to accurately take into account the effects of the wind on the instantaneous airflow rate. The reason lies in the needs to know the values of the external pressure coefficients and the discharge coefficients of its opening, which are not found always in the literature, for their consideration in the use of numerical airflow simulation tools.

Many researches have been undertaken for the estimation of this coefficient [26, 37]. Walton in 1982 [106], presented the following empirical models for the determination of this coefficient as a function of the wind direction (ϕ):

$$C_p = 0{,}75 - 1{,}05 \cdot \frac{\phi}{90} \qquad \text{if} \quad \phi \leq 90^\circ \tag{1.13}$$
$$C_p = -0{,}45 + 1{,}05 \cdot \frac{\phi}{90} \qquad \text{if} \quad \phi \geq 90^\circ.$$

On the other hand, Swami and Chandra in 1988 [97], and Grosso in 1992 [42], proposed guidelines to determine the model for this coefficient depending on various geometrical parameters of the building and the wind incident angle. Swami and Chandra reported the following model:

$$C_p = C_p(\phi = 0) \cdot ln \left[1{,}248 - 0{,}703 \cdot \sin\frac{\phi}{2} - 1{,}175 \cdot \sin^2\frac{\phi}{2} + 0{,}131 \cdot \sin^3(2 \cdot \phi \cdot G) \right.$$
$$\left. + 0{,}769 \cdot \cos\frac{\phi}{2} + 0{,}07 \cdot G^2 \cdot \sin^2\frac{\phi}{2} + 0{,}717 \cdot \cos^2\frac{\phi}{2} \right] \qquad [-] \tag{1.14}$$

where ϕ goes from 0 to 180°; for higher angles are obtained by symmetry. G corresponds to the natural logarithm of the side ratio (ratio of the lengths of adjacent walls). For vertical walls, Swami and Chandra recommend using a value of 0,6 for the pressure coefficient at zero incidence angle [37].

Mathews and Rousseau in 1996 [87], in their proposition for developing a new integrated design tool for naturally ventilated buildings, the wind effect on the proposed ventilation model took into consideration a fitted regression model for predicting C_p values for each angle (cf. fig. 1.17).

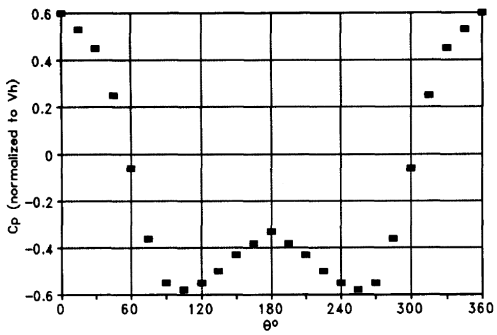

Figure 1.17: Averaged facade pressure coefficient as a function of azimuth angle [87].

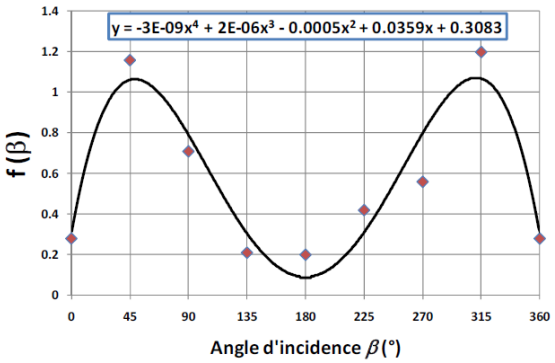

Figure 1.18: Fitted regression model over experimental data of a coefficient regarding wind effects as a function of the incident angle [62].

This regression model was fitted over C_p values computed using experimental data from pressure measurements and the expression for this coefficient presented in §1.1.2.1. This regression model is similar to equation 1.14, but without considering logarithms, the parameter G, and the whole angle was con-

sidered. Moreover, Larsen *et al.* in 2006 [62], developed an empirical model for the estimation of C_p as a function of the wind incident angle, by fitting regression models as shown in figure 1.18.

Nevertheless, all these models are applicable for buildings with simple rectangular geometries. For cases where other geometries should be taken into account, the standard EN 1991-1-4:2005 (Euro code 1) presents guidelines for the estimation of C_p values.

Different models have been developed and proposed for the determination of the natural airflow rate in terms of the driving forces, depending on the natural ventilation strategy implemented. Zhiqiang *et al.* in 2015 [114] and later in 2016 [115], reported a review of natural ventilation models for simple opening configurations, and classified them in two groups: analytical and empirical models, and network models. The analytical models are developed by applying the conservation equations to a specific configuration. According to the network modeling concept, a building is represented by a grid composed of several pressure nodes and flow paths (cf. fig. 1.19) [39]. These pressure nodes could represent the pressure of a single zone inside the building or the pressure of the exterior environment (cf. fig. 1.19 black ovals). The flow paths represent each opening in the building, e.g., windows, doors, etc. (cf. fig. 1.19 squares).

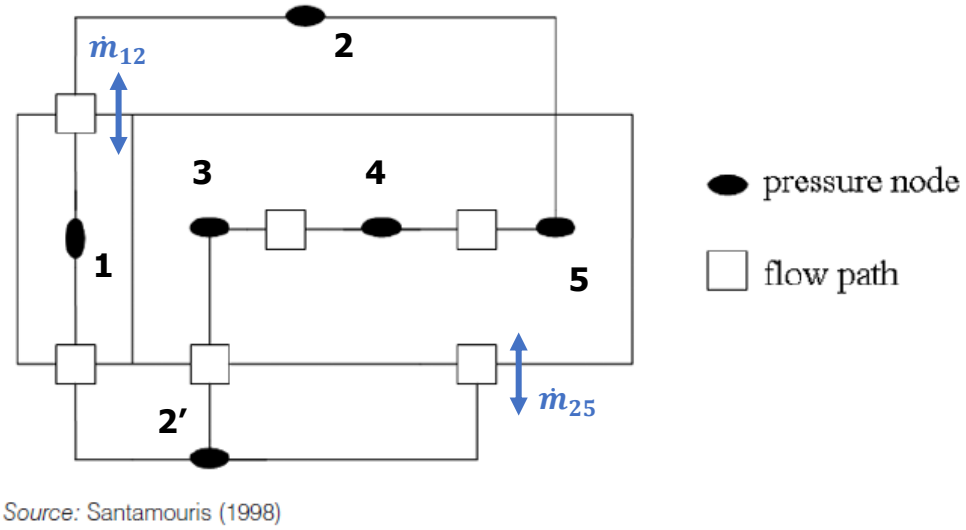

Figure 1.19: Example of a network airflow modeling applied to a multi-zone building [39].

Bernoulli's equation is then applied to relate every pressure node (taking into account a reference level). For instance, in the case of zone 1 (pressure node 1) assuming that the reference level is at the hight of the flow path between nodes 1 and 2′, and the pressure is constant on the zone of each node, Bernoulli's general equations yield:

$$P_{2'} + \frac{1}{2} \cdot \rho_{2'} \cdot \mathcal{V}_{2'}^2 = P_1 \qquad [\text{Pa}]$$

and in the case where the flow path between nodes 1 and 2 is located at a hight of $\mathcal{Z}_2$ with respect to the flow path between nodes 1 and 2′, then:

$$P_1 + g \cdot \rho_2 \cdot \mathcal{Z}_2 = P_2 + \frac{1}{2} \cdot \rho_2 \cdot \mathcal{V}_2^2 \qquad [\text{Pa}]$$

both expressions yield:

$$P_{2'} + \frac{1}{2} \cdot \rho_{2'} \cdot \mathcal{V}_{2'}^2 + g \cdot \rho_2 \cdot \mathcal{Z}_2 = P_2 + \frac{1}{2} \cdot \rho_2 \cdot \mathcal{V}_2^2 \qquad [\text{Pa}] \,.$$

Finally, all flow paths of one zone are related by writing the flow conservation equation. For instance, if a steady state is considered, for pressure node 1 results in:

$$\dot{m}_{12'} = \dot{m}_{12} \qquad \left[\text{kg}\cdot\text{s}^{-1}\right] .$$

The previous equation can be expressed in terms of pressure by using the expression relating the flow rate through an opening at the power of "n." The most common numerical method to solve the system of equations is Newton-Raphson's method. Various software implementing network airflow models exists, where the most commonly used are COMIS, CONTAM, EnergyPlus, and ESP-r [114].

1.2 Thermal behavior modeling and identification approaches

1.2.1 Thermal behavior of a passive building: the role of the envelope

The thermal behavior of a building can be defined as how the building indoor environment responses to the changes in the outdoor environment. This response is represented by the dynamics of the indoor environment temperature. The performance of a building can be characterized by the following parameters:

1.2.1.1 The thermal lag (TL)

The thermal lag (sometimes referred as time shift) is defined as the time between the maximum temperature value reached by the outdoor and indoor temperatures [38], as shown in figure 1.20. The building is characterized as to have good thermal inertia when presenting large TL values. This parameter is reported in over 24 h day-night cycle, and its values normally correspond to a few hours.

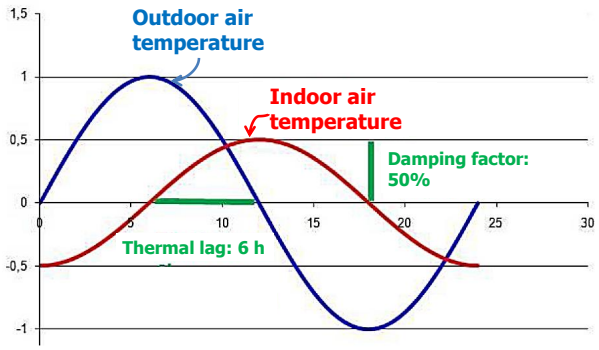

Figure 1.20: Comparison of the temperature of the outdoor and indoor environments: thermal lag and damping factor [43].

1.2.1.2 The damping factor (DF)

The damping factor is defined as the attenuation of the outdoor temperature amplitude reflected in the indoor temperature amplitude. For instance, a value of 0,7 for the damping factor can be interpreted as the 70% of the outdoor "heat wave" is transmitted to the indoor environment; the weaker the damping factor, the building structure performance is better for the thermal comfort in the summertime [43].

1.2.1.3 The time constant (TTL)

The time constant is defined as the product of the total heat storage capacity of the structure, and the global thermal resistance which accounts for transmission losses, i.e., ventilation and conduction through the envelope [48]. This before under the hypothesis that the building response is represented by the solution of a first order differential equation.

$$TTL = \frac{\sum m \cdot c_p}{1/R} \qquad [\text{h}] \tag{1.15}$$

where the heat storage capacity is represented by the product of the mass m and specific heat capacity c_p of the materials of the envelope. The magnitudes reported in the literature for this parameter, correspond to values larger than the thermal lag up to 100 h; about 147-184 h for thermally heavyweight houses, and about 20 h for light construction [4, 17, 48].

This parameter relates explicitly the thermal mass of the building envelope $m \cdot c_p$ and the heat losses by ventilation. Thus, if the heat storage capacity of a building is wanted to be increased, to attenuate the most the outdoor "heat wave", the time constant needs to be increased. Equation (1.15) indicates that this before can be accomplished by either increasing the thermal mass or limiting the heat losses by ventilation. In this matter and regarding the cooling in passive buildings, different strategies might be applied, to attenuate the outdoor "heat wave", when it is the most suitable period in the 24 h day-night cycle.

1.2.2 Modeling approaches for forecasting in buildings

Different approaches exists for the construction of models regarding the forecasting of the thermal behavior of a building. Depending on the level of physical phenomena considered, these approaches can be classified as: black, gray and white box models (cf. table 1.1). Where the physical sense is not taken into account whatsoever (black box models), is somewhat taken into account (gray box models), and is fully taken into account (white box models).

The most common modeling approaches in building thermal application are: thermal network models (or RC models, electrical analogy), and the use of thermal dynamic simulation tools such as TRNSYS, EnergyPlus, COMFIE, among others. These modeling approaches are often implemented with a sensibility analysis (such as Morris 1991 [73]) and optimization algorithms to identify the parameters of the model, such as the thermal capacities and thermal resistances. These parameters are estimated by fitting the numerical results over large sets of experimental data, minimizing the $RMSE$ value [15, 82, 102].

Table 1.1: Strengths and weaknesses of different forecasting model techniques [15].

Forecasting models	Physical model ("white box")	Inverse model ("black box")	Inverse model ("gray box")
Parametrization speed	-	++	+
Data access	-	++	+
Execution speed	-	+	+
Physical sense	++	-	+
Forecasting accuracy	++	?	?
Adaptability to changes in strategy	-	++	+

For the validation of such models, a set of experimental data other than the one used for identification, is employed to run the simulations again. The models are said to be validated if the numerical results meet certain criteria. For instance, on the deliverable n°3.3.2 [67], it is stated that the model must be met the criteria presented in table 1.2 in order to be eligible for control applications.

Table 1.2: Criteria for model validation [67].

N°	Quality	Observed/improved factors
1)	Fast when recalibration is needed	Uncomplicated models: choice of the number of parameters
2)	Reliability	Behavior of the error: Convergence to the same value at each identification
3)	Accuracy	Error values
4)	Prediction and adaptability	Observation of results for another dataset
5)	Robustness	Non-sensitivity to the set of parameters chosen

1.3 Coupling between natural ventilation and thermal mass

The coupling between natural ventilation and the thermal mass of the building, has been study for either design purposes [116], night ventilation assessment [16, 35], merely theoretical purposes on the thermal behavior [116, 112, 111], or a combination of these before [38].

From these studies we will detail those who aid to the understanding of such coupling since it is the primarily topic of our present work. As found in the literature, the study of such coupling is based mainly on three key elements: the heat transfer in the indoor air, the heat transfer in the thermal mass, and the ventilation airflow rate. In this regard, Feuermann and Hawthorne in 1991 [35], and Zhou *et al.* in 2008 [116], proposed a model where these key elements were taken into account by one thermal capacity and a constant ventilation airflow rate. The difference of these two studies lays in that, Feuermann and Hawthorne, only considered the thermal capacity of the thermal mass in a 1C3R model.

On the contrary, Zhou *et al.* only considered the thermal capacity of the indoor air and a constant ventilation flow rate, but also in a 1C3R model, as follows:

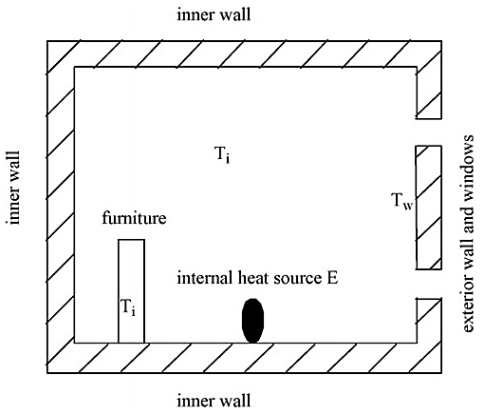

Figure 1.21: Schematic of the model [116].

Along with the following equation:

$$\rho \cdot c_p \cdot \dot{V} \cdot [T_o - T_i] + R_i \cdot S \cdot [T_W - T_i] + E = M \cdot \rho_M \cdot c_{p_M} \cdot \frac{\partial T_i}{\partial t} \qquad [\mathrm{W}]$$

where T_W corresponds to the inner surface temperature, expressed by:

$$T_W = \tilde{T}_W + \frac{S_{sol-air}}{v_e} \cdot \cos(\omega \cdot t - \phi_{sol-air} - \phi_e) + \frac{S_i}{v_f} \cdot \cos\big(\omega \cdot t - \phi_i - \phi_f\big) \qquad [^\circ\mathrm{C}]$$

where $\tilde{T}_W$ corresponds to the average inner surface temperature, the second term on the right refers to the fluctuation of the inner surface temperature caused by the variation of solar-air temperature under constant indoor air temperature conditions. The third is similar to the second term but induced by the variation of the indoor air temperature under constant outdoor air temperature conditions. The coefficients (v_e, v_f) and angles ($\phi_{sol-air}$, ϕ_e, ϕ_i, ϕ_f), refer to the damping factors and phase shift for the external walls respectively, with respect to the outdoor air temperature and indoor air temperature.

From this analysis, although theoretically, the latter developed a simple tool to estimate the amount of internal thermal mass needed, i.e., furniture, in order to maintain a desirable indoor air temperature by increasing the time constant.

On the other hand, Yam *et al.* in 2003 [111], by assuming a natural airflow rate only driven by thermal buoyancy forces, studied the nonlinear coupling between natural ventilation and the thermal mass by considering the main fluctuation frequency of the variables. The nonlinearity is due to the airflow rate dependence on the temperature difference at the power of 1/2. This research studied the behavior of the indoor air using indicators such as the phase shift, for two cases (cf. fig. 1.22): (*a*) the indoor thermal mass is not in equilibrium with the indoor air (2C2R), and (*b*) both are in equilibrium (1C2R).

For the case (a) where the thermal mass is not in equilibrium with the indoor air the equations employed were as follows:

$$\rho \cdot c_p \cdot \left|\dot{V}\right| \cdot [T_o - T_i] + h_M \cdot S_M \cdot [T_M - T_i] + E = 0 \qquad [\mathrm{W}]$$

$$M \cdot \rho \cdot c_p \cdot \frac{\partial T_M}{\partial t} + h_M \cdot S_M \cdot [T_M - T_i] = 0 \qquad [\mathrm{W}]$$

$$\dot{V} = C_d \cdot A^* \cdot sgn\,(T_i - T_o) \cdot \sqrt{\left|2 \cdot g \cdot h \cdot \frac{T_i - T_o}{\bar{T}_o}\right|} \qquad \left[\mathrm{m^3 \cdot s^{-1}}\right]$$

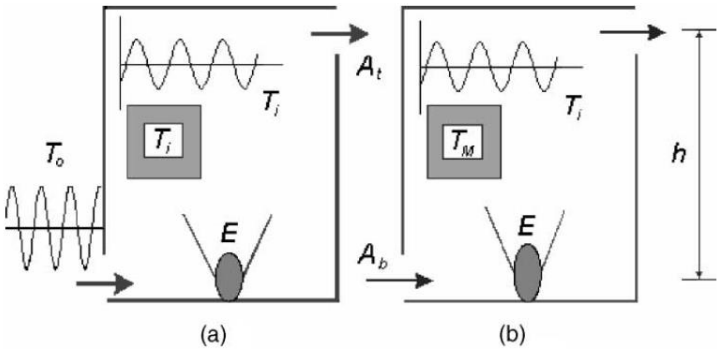

Figure 1.22: Schematic of the models for two cases: (*a*) the indoor thermal mass is not in equilibrium with the indoor air, and (*b*) both are in equilibrium [111].

where M represents the mass of the thermal mass, and A^* represents the equivalent free airstream area of the two-openings configuration. For the case (b) where the thermal mass is in equilibrium with the indoor air the equation employed was the following:

$$\omega \cdot M \cdot \rho \cdot c_p \cdot \frac{\partial T_i}{\partial(\omega t)} + \rho \cdot c_p \cdot \left|\dot{V}\right| \cdot [T_o - T_i] = E \qquad [\mathrm{W}]$$

where ω is the frequency of the outdoor temperature variation in h^{-1}. Finally, in each case, the solar radiation was not included because no heat transfer through the envelope was considered, and the outdoor temperature was assumed to be represented by the sum of sinusoidal components of a 24 hours period ($T_o = \tilde{T_o} + \Delta\tilde{T_o} \cdot \sin(\omega \cdot t)$). This analysis and numerical results showed that the consideration of the nonlinearity does neither change the behavior of the system, nor the behavior of the indoor air temperature phase shift, when a periodic (ideal) outdoor air temperature profile is considered.

Finally, the most recent theoretical study of such coupling was performed by Yang and Guo in 2016 [112]. This study was focused on the harmonically fluctuation introduced by natural ventilation into the thermal behavior of an enclosure experiencing ventilation by buoyancy forces only. The model considered an indoor air not in equilibrium with the internal thermal mass (2C4R).

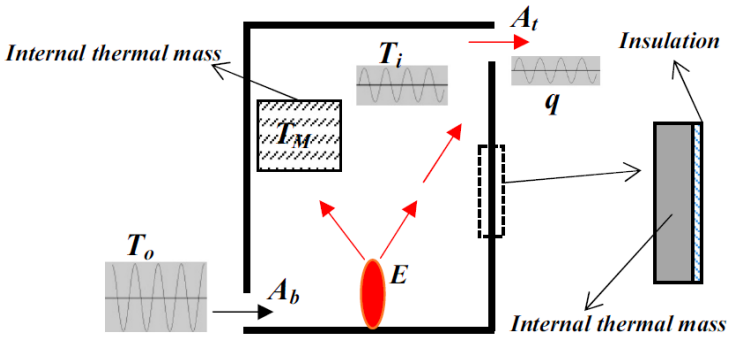

Figure 1.23: Schematic of the model [112].

In this case, where the thermal mass is not in equilibrium with the indoor air, the equations employed were as follows:

$$\rho \cdot c_p \cdot \dot{V} \cdot [T_o - T_i] + R_e \cdot S_e \cdot [T_o - T_i] + E = \rho \cdot c_p \cdot V \cdot \frac{\partial T_i}{\partial t} + h_M \cdot S_M \cdot [T_i - T_M] \qquad [\mathrm{W}]$$

$$M \cdot \rho \cdot c_p \cdot \frac{\partial T_M}{\partial t} + h_M \cdot S_M \cdot [T_M - T_i] = 0 \qquad [\mathrm{W}]$$

where the subscript e indicates "envelope." Here, it was assumed that the heat source is large enough as to avoid downward flows (inverse sense with respect to the one shown in figure 1.23); thus the airflow rate is expressed by:

$$\dot{V} = C_d \cdot A^* \cdot \sqrt{\left| 2 \cdot g \cdot h \cdot \frac{T_i - T_o}{\tilde{T}_o} \right|} \qquad \left[\mathrm{m}^3 \cdot \mathrm{s}^{-1}\right].$$

The nonlinear coupling was first decomposed into the corresponding multi-frequency fluctuations, decoupled and solved, and then, recomposed for the indoor air temperature and the resulting airflow rate. For this study, an experimental apparatus that fits the theoretical enclosure conditions was constructed to validate the theoretical analysis; air temperature and airspeed measurements were performed (cf. fig. 1.25).

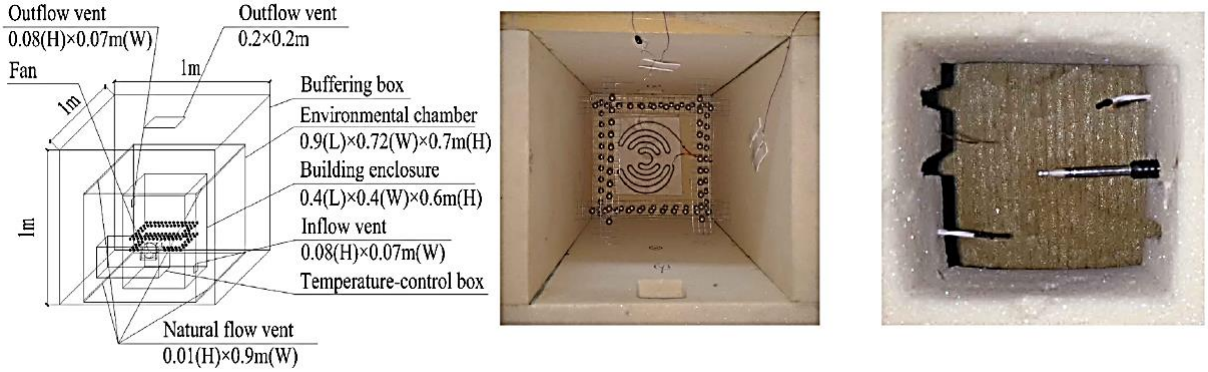

Figure 1.24: Experimental set-up: (*a*) Sketch, (*b*) inside the ventilated enclosure showing the heat source E and the thermal mass (steel balls), and (*c*) temperature and airspeed probes. [112].

Both analytical and experimental results showed that coupling between thermal mass and buoyancy inside a building could lead to multi-frequency (or an-harmonic) fluctuation of natural ventilation (cf. fig. 1.25). The phase shifts of the high-order indoor air temperature fluctuation terms (with respect to the 1st-order outdoor air temperature fluctuation term) can exceed $\pi/2$ [112].

Note that all these studies mentioned above, considered the lumped-capacitance approximation for the heat transfer in the thermal mass, i.e., null temperature gradients. In contrast, Holford and Woods in 2007 [52], considered uniform and non-uniform conduction heat transfer in the thermal mass in their study, and showed that the uniformity assumption could be very applicable to the fully-mixed spaces and thermal mass with thin layers. For thermally stratified spaces, this assumption may have limitations. For the thermal mass with thick layers, the temperature fluctuation could be only concentrated at the surface. However, the lumped-capacitance approximation is useful for fundamental investigation of the thermal balance in a naturally ventilated space [52].

In summary:
The coupling between natural ventilation and the thermal mass of a building can be studied by only considering two simple energy balances, one on the indoor air and another on the thermal mass, along with the equation for the ventilation airflow rate.

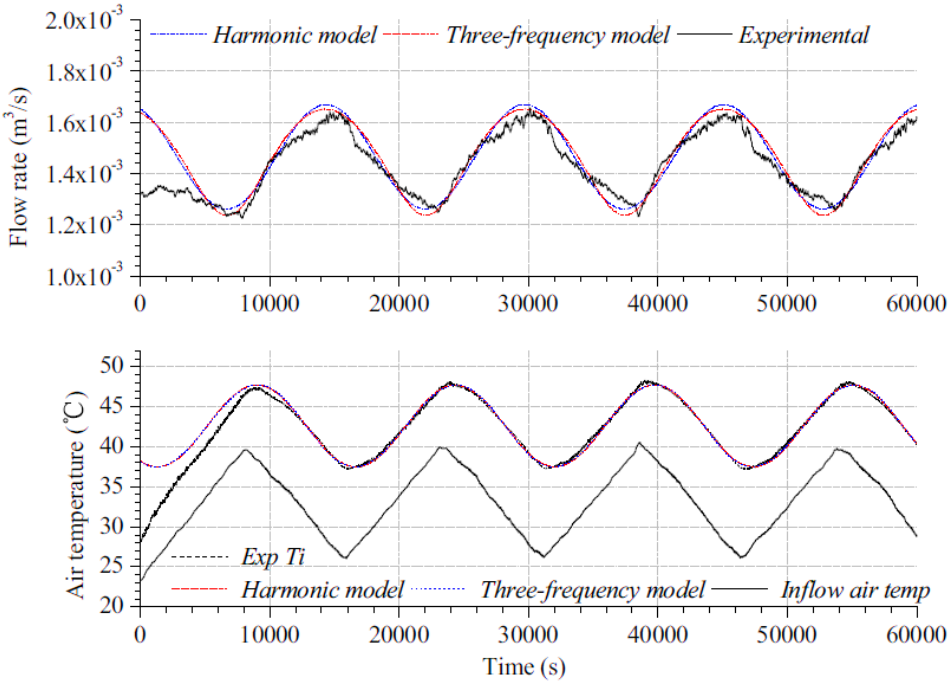

Figure 1.25: Experimental and theoretical results for the ventilation flow rate ($\dot{V}$) and the indoor air temperature (T_i) when $T_o = 33 + 7 \cdot \cos\left(4{,}09\text{x}10^{-4} \cdot t - \pi\right)$ [112].

1.4 Heat flux measurement techniques for rigid surfaces

This section first briefly describes the heat flux measurement theory for a flat-plate-type of heat flux sensor, the *Théry*-type (referred here as FGT), and for another kind of sensor, the thermoelectric module (also known as Peltier modules, referred here as TEM). Second, a brief review concerning experimental techniques that have been used for heat flux detection or measurement is presented along with proposed approaches for decoupling the convection and radiation parts of the heat flux measured. Third, the perturbations introduced by heat flux sensors, spotted by past researches, are discussed. Finally, experimental techniques for flat-plate heat flux sensors are described. The quantification of the heat flow rate is essential for a large variety of thermal applications, as it is for the presented work.

1.4.1 Principles of the heat flux measurement

1.4.1.1 *Théry*-type heat flux sensors

The measurement of this type of sensors is based on the Seebeck effect. Several and very small thermocouple junctions are connected in series, i.e., as a thermopile, distributed all over the surface of an insulated support (based on the printed circuit board technique). This support is then covered by two plates of copper, on each side. When both plates of this embedded element are submitted to different temperatures, each of the thermocouple junctions generates a potential difference due to the temperature gradient. This potential difference (U) is proportional to the heat flux traversing the sensor (φ), and they are related by a thermoelectric coefficient [23, 99, 110] (cf. fig. 1.26). These sensors are also able to measure the temperature of the surface where they are being placed.

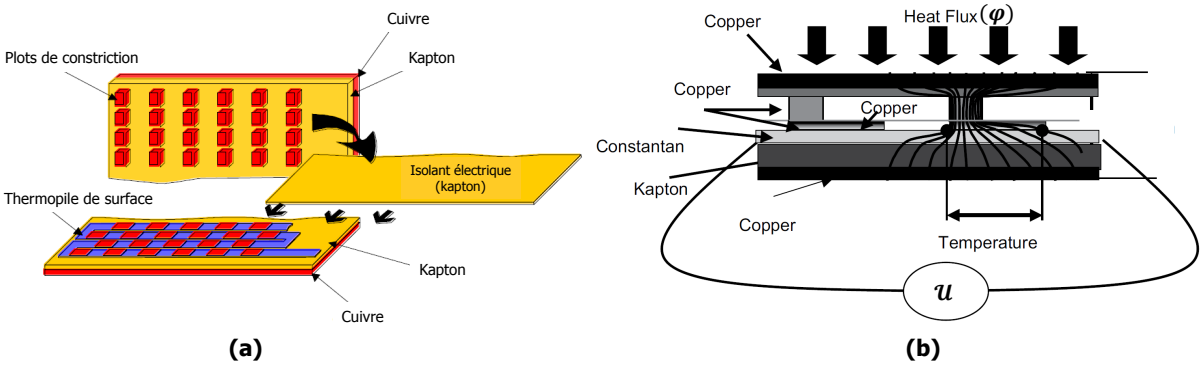

Figure 1.26: Structure of Captec® heat flux meter: (a) Composition, and (b) transversal side view with heat flux lines [23].

This before can be represented by a simple equation as follows:

$$\varphi(t) = \frac{U(t)}{\mathcal{K}} \qquad \left[\mathrm{W{\cdot}m^{-2}}\right] \tag{1.16}$$

where U is normally expressed in μV and φ is the heat flux measured or traversing the sensor. U can take positive and negative values, depending on the heat flux direction and on the polarity connection of the sensor. The coefficient $\mathcal{K}$ groups the thermoelectric properties of the sensor, e.g., the Seebeck coefficient, the total number of thermocouple junctions and the thermal conductivity, normally expressed in $\mu\mathrm{V{\cdot}m^2{\cdot}W^{-1}}$ and it is usually determined by calibration techniques. It could be demonstrated to be equal to the following expression:

$$\mathcal{K} = \frac{N \cdot a_{eq} \cdot e}{\lambda_{eq}} \qquad \left[\mu\mathrm{V{\cdot}m^2{\cdot}W^{-1}}\right] \tag{1.17}$$

where N corresponds to the number of thermocouples junctions, e the thickness of the active section of the sensor, a_{eq} the equivalent Seebeck coefficient, and λ_{eq} the equivalent thermal conductivity. Moreover, the coefficient $\mathcal{K}$ does not vary with temperature due to the thermoelectric properties of the materials used for this kind of sensors; their thickness is around a tenth of a millimeter. For example, the Captec® enterprise, offers square heat flux meters with a dimension range between 5x5 $\mathrm{mm^2}$ and 300x300 $\mathrm{mm^2}$ of surface area with a thickness of 0,5 mm. Depending on these dimensions, their sensibility value can vary from some $\mu\mathrm{V{\cdot}m^2{\cdot}W^{-1}}$ to a around a hundred of $\mu\mathrm{V{\cdot}m^2{\cdot}W^{-1}}$, for instance, a 50x50 $\mathrm{mm^2}$ presents a sensibility of around 20 $\mu\mathrm{V{\cdot}m^2{\cdot}W^{-1}}$, and a 150x150 $\mathrm{mm^2}$ presents a sensibility of around 120 $\mu\mathrm{V{\cdot}m^2{\cdot}W^{-1}}$; where the cost of the latter may reach the 400€ each.

1.4.1.2 Thermoelectric modules

The thermoelectric modules, also known as Peltier modules, are composed of several thermocouple junctions connected electrically in series and thermally in parallel, integrated between two ceramic plates [89] (cf. fig. 1.27). These thermocouple junctions consist of a n- and a p-type semiconductor materials connected by small and thin copper tabs. These modules are widely available in the market, normally used in electronics for cooling purposes, where the most common semiconductor materials

employed is a quaternary alloy of bismuth, tellurium, selenium, and antimony, e.g., Bi_2Te_3. In the case of cooling applications when higher performance is needed, multistage Peltier modules can be found in the market (cf. fig. 1.27 (b)).

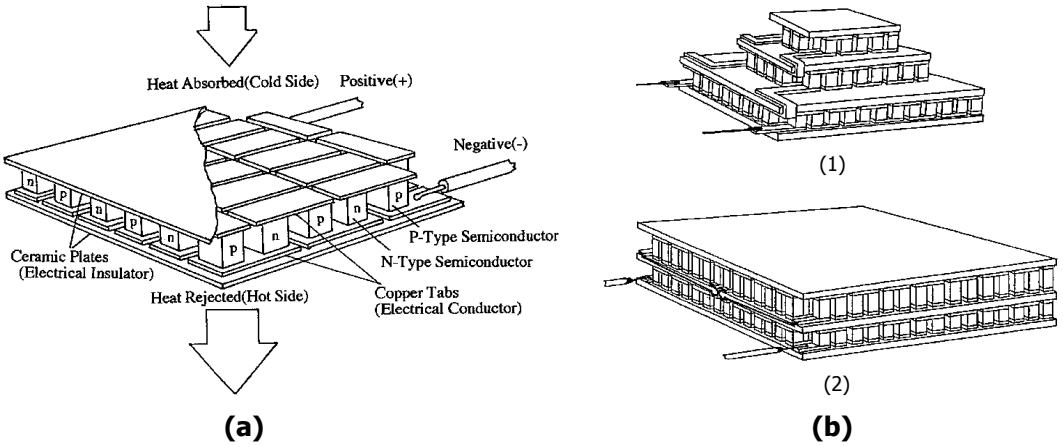

Figure 1.27: General structure of a Peltier module [89]: (a) a singular TEM, and (b) two multistage TEM configurations.

However, these modules can also be used for power generation [79]. For heat flux measurement or heat flux detection, they work in an open circuit configuration when connected to a multimeter or an acquisition system for data collection [68]. In this case, they follow a similar relation between the potential difference generated when a heat flux is traversing the module (cf. eq. 1.16). Even though they may have the particularity of a $\mathcal{K}$ coefficient dependent on temperature due to the semiconductor materials of the thermocouples junctions, and the time response is about one minute. The dimensions availability for this type of module is limited, but for the same dimensions a TEM presents a sensibility value of about a hundred times larger than the sensibility value of a conventional heat flux meter; their cost lays around the twentieth of euros.

1.4.2 Implementation of heat flux meters for measuring the superficial heat exchanges

1.4.2.1 Estimation of the convection and radiation heat exchanges

The measurement of superficial heat exchanges, i.e., convection and radiation, using FGT sensors and thermoelectric modules, have been a topic of interest of various researchers [103, 51, 66, 30, 29, 23, 110, 10, 113]. The interest lays in the possibility of splitting the convection and radiation parts from the heat flux measurement. This brings us to the question: can convection and radiation heat exchanges be separated from a heat flux measurement in a mixed environment? Thus, this review is focused on the implementation of such sensors for the estimation of both superficial heat exchanges; any other case was excluded. However, other research works have been found regarding the implementation of such sensors in the thermal characterization of walls, among which we have [65, 69, 103].

In the late 80s, a technique to estimate the convection and radiation heat exchanges on a surface was implemented, consisting of using two FGT sensors, where one was to be coated with a black surface and the other with a shiny surface. Then, under the premise that the black and shiny surfaces had

emissivities close to 1 and 0 respectively, the former was said to estimate the total heat flux (convection + radiation) and the latter to estimate the convection heat flux on the rigid surface where they installed the sensors, e.g., heavyweight and lightweight walls, and isolate-type wall. Herin in 1988 [51] worked on the design and characterization of convective and radiative heat flux meters applied to in situ measurements. The heat flux meters (25 x 25 x 0,02 cm and 30 $\mu V \cdot m^2 \cdot W^{-1}$), coated with foils with contrasted emissivities, were tested with the objective of separating the convective and radiative components when installed inside a climatic chamber (cf. fig. 1.28). The heat flux and temperature measurements were validated, allowing the separation of the convective and radiative components on heavyweight and lightweight walls, and also the determination of the thermophysical properties of such walls.

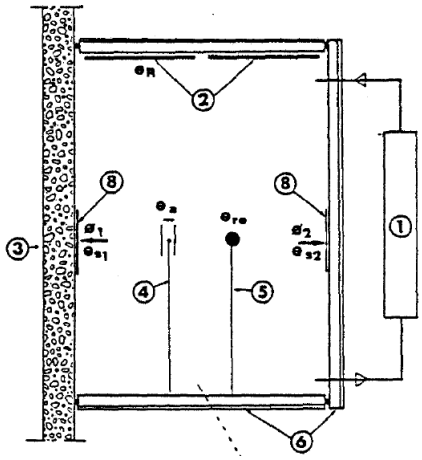

Figure 1.28: Experimental set-up in [51, 66]: (1) Air conditioning central, (2) Radiant panels, (3) a 12 cm heavyweight concrete wall, (4) air temperature probe, (5) room temperature probe, (6) a lightweight wall (isolation-wood), designed heat flux meters.

In the early 90s, Lassue *et al.* in 1992 [63], implemented the estimation of the convective and radiative heat flux, using flat-plate heat flux meters (0,01 cm thick and 20 $\mu V \cdot m^2 \cdot W^{-1}$), for the design of thermal comfort controllers (cf. fig. 1.29). These heat flux meters, coated with thin foils of contrasted emissivities (near 1 and near 0), were placed in the concrete wall of the enclosure (cf. fig. (b)).
In principle, the comfort control was proposed to be done by using the radiative heat flux as the control variable, in addition to the room temperature, for controlling four radiative panels installed on the ceiling, leading to achieve low cost controllers (taking into account the time delay of the room) with the permanent installation need of heat flux meters.

Moreover, Lassue *et al.* in 1993 [64], used heat flux meters (25 x 25 x 0,02 cm and $\sim$3 $\mu V \cdot m^2 \cdot W^{-1}$) coated with a thin polished aluminum foil and a prototype of airspeed/temperature sensor both based on the use of thermoelectric effects (designed to measure very small airspeeds), as to propose a new experimental approach for measuring the convective heat transfer coefficient on heavyweight walls. Results were found to agree with values reported in the literature for the case of laminar free convection along a vertical and isotherm heated plate.

One decade later or so, similar experiments were performed using FGT sensors: Douiri in 2007 [29, 95] (Captec®, 2 x 2 x 0,04 cm and $\sim$3 $\mu V \cdot m^2 \cdot W^{-1}$), for measuring the heat exchanges that an object will experience inside a particular type of oven for drying purposes (cf. fig. 1.30).

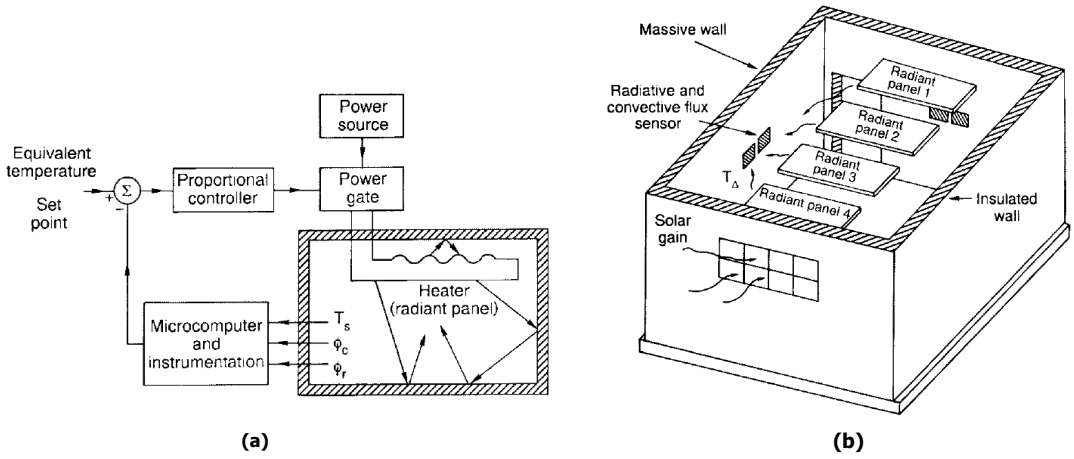

Figure 1.29: Proportional controller converted into a room temperature programmable device (a), and a schematic of the experimental room (b).

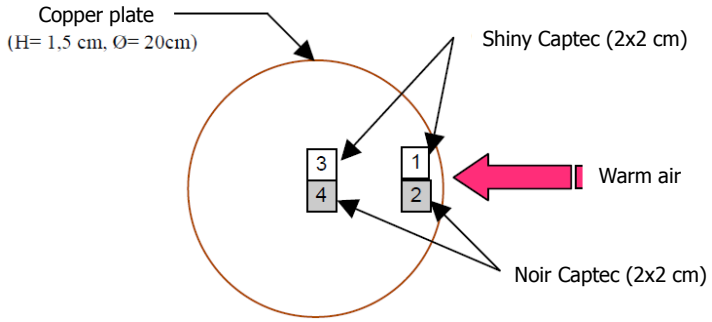

Figure 1.30: Experimental set-up in Douiri 2007 [29]: Heat flux meters installed inside the oven.

Cherif et al. in 2009 [23] (Captec®, 5 x 5 x 0,02 cm and $\sim$100 $\mu V \cdot m^2 \cdot W^{-1}$), to estimate the heat exchanges on the internal surface of a horizontal channel (cf. fig. 1.31(a)).

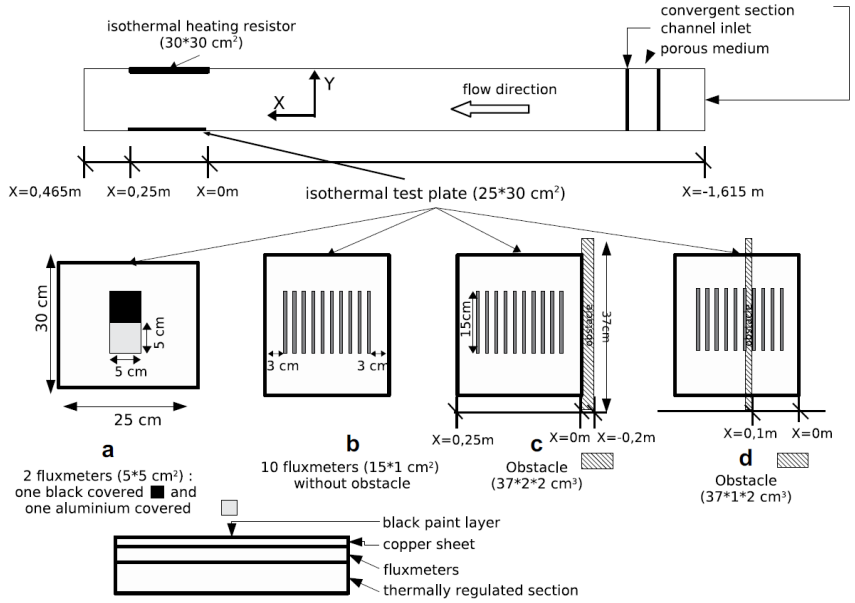

Figure 1.31: Experimental set-up in [23]: Heat flux meters black and shiny, installed inside the heat exchanger (a).

Vogt Wu in 2011 [109] used Captec® heat flux meters (20 x 20 x 0,03 cm and ~75 $\mu V \cdot m^2 \cdot W^{-1}$) for in situ characterization of the thermal properties of an external wall, but instead of coating the sensor with a shiny surface, it was coated with a material similar to the wall surface (cf. fig. 1.32).

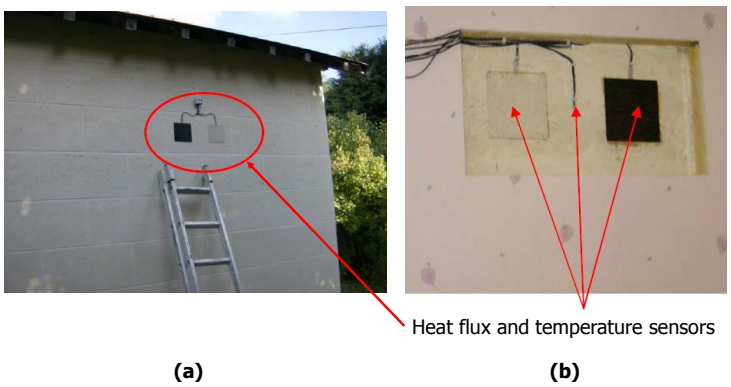

Figure 1.32: Experimental set-up in [109]: Heat flux meters installed at the (a) front and (b) rear faces of an external wall in a real residential building.

In 2012, Leephakpreeda [68] implemented thermoelectric modules only (4 x 4 x 0,09 cm and ~94 $\mu V \cdot m^2 \cdot W^{-1}$). The experiment procedure was quite different from the ones with the flat-plate sensors mentioned before. One of the experiments consisted in the detection, at the rear face, of the heat flow through an external wall of a building. Instead of placing the sensors in both, the front and rear faces of the wall, the sensors were only placed in the rear face (cf. fig. 1.33 (a)).

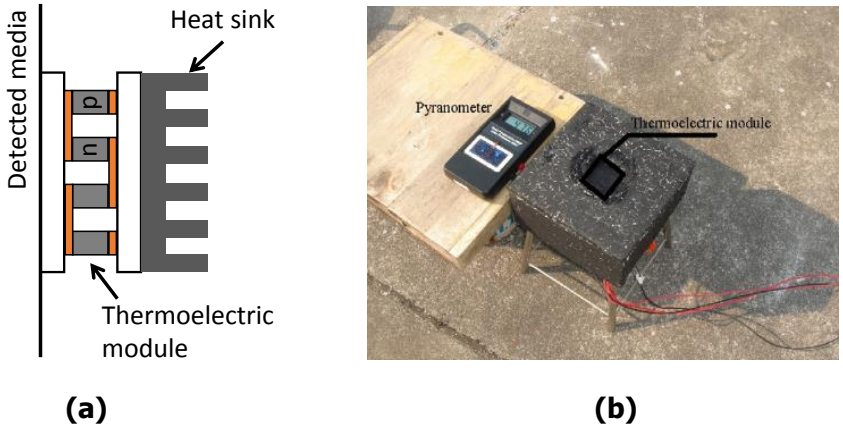

Figure 1.33: Experimental set-up in [68]: (a) installation on the rear face of a wall, and (b) for measuring solar radiation heat flux.

The front face of the wall was submitted to solar radiation heat flux and the rear face, to indoor air conditions. A heat dissipater (or heat sink) was installed on the sensor's surface in contact with the indoor air, to increase the heat flow rate through the sensor. Experimental results were compared with simulation, finding an average absolute difference of 6,7±2,7% with maximum and minimum values of 10,5% and 0,1%, respectively. The other experiment consisted of coating the thermoelectric module surface in black to measure solar radiation heat flux (cf. fig. 1.33 (b)); this was compared latter with a pyrometer. From this second experiment, it was pointed out that satisfactory results were encountered as the average of the absolute differences was 4,8±3,9%, which lead to conclude that the sensor

measurement can be used for radiation heat flux without knowing the exact emissivity value.

Recently, in 2017, Yang [113] used both types of sensors: Captec®, 5 x 5 x 0,04 cm and $\sim$18 $\mu V \cdot m^2 \cdot W^{-1}$, and thermoelectric modules, 3 x 3 x 0,35 cm and $\sim 0{,}39T + 139$ $\mu V \cdot m^2 \cdot W^{-1}$. The experiments were designed to characterize the thermal properties of a multilayer wall, placing a group of sensors on the front and rear faces, in two cases: in situ and under laboratory conditions (cf. fig. 1.34). In the laboratory case, a black and shiny pair of FGT and TEM were installed at the front face of the wall which was latter heated by 6 halogen lamps (cf. fig. 1.34 (a)); the rear face was maintained at room temperature. In the in situ case, only black and shiny FGT sensors were employed (cf. fig. 1.34 (b)) and installed on the front face heated by several solar like-type lamps; the rear face was exposed to outdoor conditions.

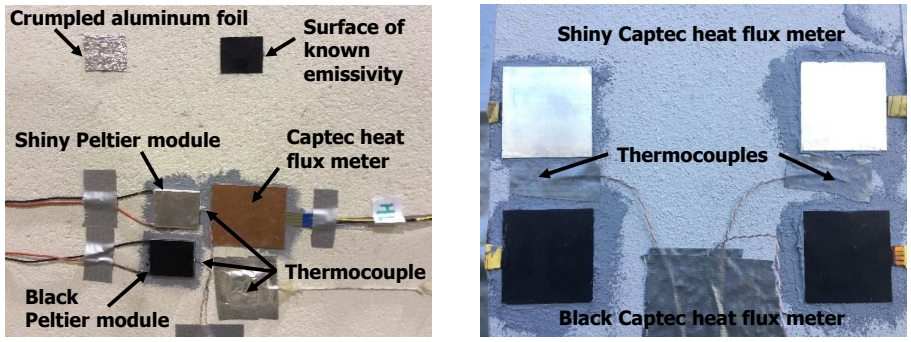

Figure 1.34: Experimental set-up in [113]: (a) heat flux (Peltier or TEM and Captec) and temperature sensors installed on the wall front face (laboratory case), and (b) heat flux (Captec) and temperature sensors installed on the wall front face (in situ case).

In summary:
The studies reviewed show that the implementation of the heat flux meters differed in geometry and arrangement, i.e., black and shiny sensors installed with one of their sides always in contact [23, 29] and installed with a separation between them [63, 109, 113]. The silicon thermal grease is used to reduce the contact thermal resistance when placing the heat flux sensors on walls. Also, the heat flux and temperature measurements when using conventional heat flux meters for estimating the convective heat transfer coefficient on non-isolated walls type, have been shown to be in strong accordance with the values reported in the literature.

1.4.2.2 Analytical approaches for splitting the convective and radiative heat exchanges

Cherif et al. [23] proposed a way to separate the convective and radiative parts from the heat flux measurement. The principle is based on a heat energy balance on the surface of the heat flux sensor, well-placed onto a wall surface, which is submitted to convection (φ_C) and radiation (φ_R) heat exchanges. The total heat flux (φ_T) on the sensor's surface is equal to the sum of φ_C and φ_R. Also, this is equal to the heat flux traversing the sensor (φ). This before could be expressed for any surface i as follows:

$$\varphi_i(t) = \varphi_{C_i}(t) + \varphi_{R_i}(t) \qquad \left[W \cdot m^{-2}\right] \tag{1.18}$$

It was stated that the heat flux measurement, on both sensors (black and shiny), would have a convection and radiation part, owing to the emissivity value of the black and shiny coating they used: a black paint (0,98) and a thin aluminum foil (0,1), respectively. Thus, the convection heat flux was determined by subtracting the radiation part from the shiny sensor measurement. This radiation part was computed using the "classical radiosity method" and also by numerical simulation on the Fluent software.

Going further on the emissivity issue, they analyzed numerically if the results depended on the emissivity value of the black coating. Changing the emissivity value from 0,9 to 1 (a perfect black body), it was found that increasing the emissivity yield to an increase in the total heat flux. Finally, it was concluded that the experimental procedure allows uncoupling the convection and radiation parts from the measurement since the relative error obtained was 5% maximum between the experimentation and numerical results. It is worth mentioning that the heat flux levels in this experiment reached up to 350 $\mathrm{W{\cdot}m^{-2}}$, as it will influence later the permissible error range for the present work.

Hereafter, we will referred to the measurement of the black and shiny heat flux meters as φ_b and φ_s, respectively. The heat balance on the black and shiny sensors, using equation 1.18, results in:

$$\varphi_b(t) = \varphi_{C_b}(t) + \varphi_{R_b}(t) \qquad \left[\mathrm{W{\cdot}m^{-2}}\right] \tag{1.19}$$

$$\varphi_s(t) = \varphi_{C_s}(t) + \varphi_{R_s}(t) \qquad \left[\mathrm{W{\cdot}m^{-2}}\right]. \tag{1.20}$$

Douiri [29] based the analysis in equations 1.19 and 1.20, but wanted to estimate the heat convection coefficient (h_C) and the mean radiant temperature (here referred as T_{surr}). This consisted of defining the convection part using Fourier's convection equation. For the radiation part, the Kirchhoff's hypothesis for radiation heat transfer was employed. This two magnitudes depended on several parameters, in which the temperatures (T_b, T_s) and emissivities (ε_b, ε_s: 0,93 and 0,1, respectively) of both sensors played an important role:

$$\varphi_b(t) = h_C(t) \cdot [T_{air}(t) - T_b(t)] + \varepsilon_b \cdot \sigma \cdot \left[T^4_{surr}(t) - T^4_b(t)\right] \qquad \left[\mathrm{W{\cdot}m^{-2}}\right] \tag{1.21}$$

$$\varphi_s(t) = h_C(t) \cdot [T_{air}(t) - T_s(t)] + \varepsilon_s \cdot \sigma \cdot \left[T^4_{surr}(t) - T^4_s(t)\right] \qquad \left[\mathrm{W{\cdot}m^{-2}}\right]. \tag{1.22}$$

It should be noted here, that this approach is under two hypotheses: (*i*) having only one convection coefficient for both sensors and (*ii*) the temperature measured by the sensor is that of its surface. The working heat flux ranges were of the order of 1500 $\mathrm{W{\cdot}m^{-2}}$ for the convection and 500 $\mathrm{W{\cdot}m^{-2}}$ for the radiation heat fluxes.

Yang [113], also based the analysis on the heat balance equations presented previously for determining the convective heat transfer coefficient (h_C), with the difference that the emissivity values of each coating were determined, with good precision, by using the emissivity measurement method proposed in the standard ISO 18434-1:2008(E). After separating the convection and radiation heat fluxes from sensors measurement, good concordance was found when comparing the estimated radiation heat flux with a pyrometer. Moreover, a significant difference was found between the convective coefficient h_C

estimated by the TEM and the FGT; the former was approximately two times greater than the latter (cf. fig. 1.35 (a), black and blue lines, respectively). The convective coefficient estimated with FGT measurements was verified with a well-known correlation for determining the convection coefficient on vertical walls under natural convection ([120] p.431) (cf. fig. 1.35 (a) red line).

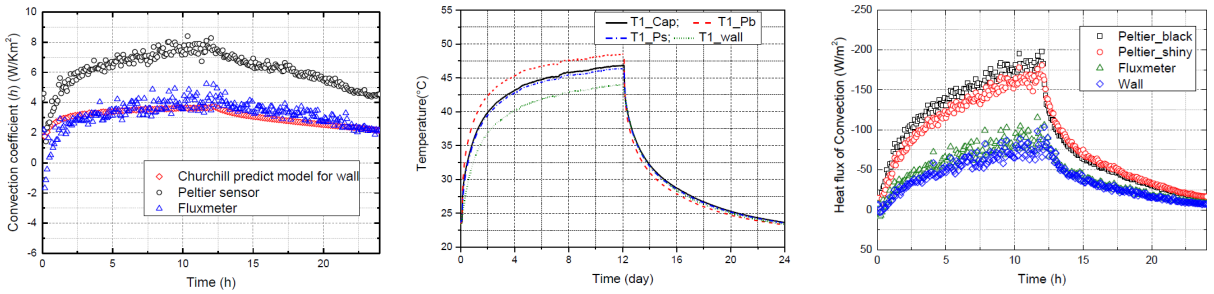

Figure 1.35: Results for laboratory case: (a) Convective coefficient estimated for the TEM (black) and FGT (blue); coefficient estimated by correlation (red). (b) Surface temperatures: FGT (black), black TEM (red), shiny (TEM) blue. (c) Resulting convective heat flux for the black TEM (black), shiny TEM (red), and FGT (green) [113].

Taking into account the estimated convective coefficient and the measured temperatures (cf. fig. 1.35 (b)), the convective heat flux was computed (cf. fig. 1.35 (c)). From this, it was inferred that the difference encountered was strongly related to the difference in the sensors thickness, but no further studies were reported (the thickness of the TEM was 8,75 times greater than the FGT thickness).

1.4.2.3 Radiative heat flux meters

More effort has been put into the estimation of the radiative heat flux. For instance, Herin in 1988 [51] and El Harzli in 1993 [30] worked in the development of a radiative heat flux sensor, based on the same reasoning mentioned in the previous paragraphs. In this case, several black and shiny strips are placed next to each other intercalated and carefully wired as to superposed the electric potential given by each strip (cf. fig. 1.36). One advantage of this type of sensor is that it allows to estimate the radiative heat flux directly from the sensor electrical response. This type of sensors is widely available in the market, e.g., Captec enterprises.

1.4.3 Perturbations and uncertainties introduced by the heat flux meter

Herin [51] compared its measurements with simulation results for two different cases, to estimate the errors in steady state: (*i*) the heat flux sensors (25 x 25 x 0,02 cm and $\sim$35 $\mu V \cdot m^2 \cdot W^{-1}$) placed on a vertical concrete wall (thermally heavyweight), (*ii*) the heat flux sensors placed on a polystyrene wall (thermal isolation). For the first case, the convection heat flux was encountered to be overestimated by near 26% and the radiation heat flux to be underestimated by practically 35% (cf. fig. 1.37 (a)). For the second case, the error on the radiation heat flux was around the -79% and on the convection heat flux was between 250 and 350% (cf. fig. 1.37 (b)). For the case of isolate wall types, it was concluded that the estimation of the convective and radiative components is complexed and a temperature correction under the sensors is needed (in the sensor-wall interface, T_s'), where errors were said to be mainly

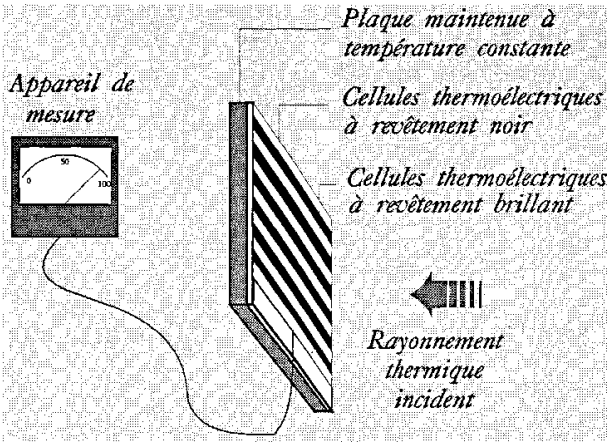

Figure 1.36: Schematic of the radiative heat flux designed by [30].

caused by the local temperature modifications on the wall surface, due to the presence of the sensors, which also modifies the heat flow distribution through the wall thickness (cf. figs. 1.37 (b) and 1.38); this was also pointed out in [99] and [66].

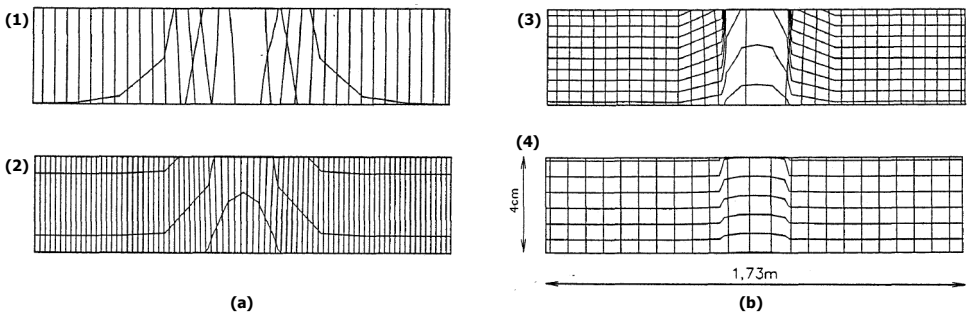

Figure 1.37: Simulation results in steady state conditions [51]. (a) In the case of a shiny heat flux meter place on a concrete wall submitted to: (1) $\varphi_R = 20\,\mathrm{W{\cdot}m^{-2}}$, (2) $\varphi_R = 20\,\mathrm{W{\cdot}m^{-2}}$ and $\varphi_C = 4 \cdot [20 - T_s]$ $\mathrm{W{\cdot}m^{-2}}$. (b) In the case of a shiny heat flux meter place on a polystyrene wall submitted to the same heat fluxes as in case (a): (3) and (4), respectively.

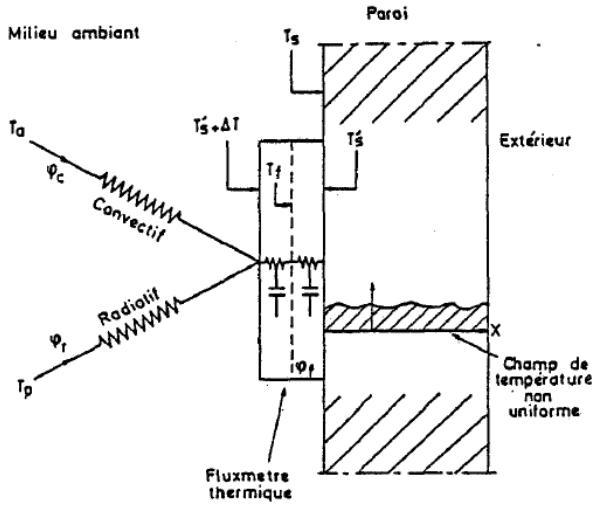

Figure 1.38: Schematic representation of the resistive circuit when a heat flux meter is installed [51].

For the case of errors caused by the local temperature modifications on the wall surface, a correction needed for the temperature of the shiny heat flux meter was also evoked in [66, 63], for cases when these sensors are placed onto an isolated-type wall.

In transient state, when a heat flux sensor is placed onto a surface, it will absorb the heat flow at the same rate as the wall if their thermal effusivities are the same. Also, the condition that the sensor's heat storage capacity is negligible concerning the heat flow traversing it must be verified to perform measurements in a transient state. Finally, he stated that the measurement error is proportional to the mismatching between the sensor and the wall, i.e., the difference between the effusivities $\sqrt{\lambda \cdot \rho \cdot c_p}$ and $\sqrt{C/R}$ of both, the sensor and the wall [51].

Leephakpreeda [68] pointed out that the amount of the detected heat flux through the wall was not identical to the amount that would be detected without the sensor. Two reasons were given to explain this difference: (*i*) the changes in the wall boundary conditions and (*ii*) the effect of the thermal contact resistance between the thermoelectric module and the wall. The same reasons were stated years before, for flat-plate sensors, by Thureau [99] in 1996 in a technical report describing first the theory of various types of heat flux sensors, a few calibrations methods and then giving various causes of perturbation introduced by the used of these sensors. Concerning the latter, one of them that haven't already be cited here, is the modification of the nature of the tested object surface: the thermal radiation properties, regarding the radiation heat transfer, and the roughness and thickness added to the tested surface, in regard of the convection heat transfer.

In summary:
From the aforementioned, it can be concluded that the scrupulously design and characterization of the conventional heat flux meters allow the estimation of the convective and radiative heat flux and the convective heat transfer coefficient, on heavyweight and lightweight walls, with great accuracy. The estimation of these parameters seems to be improved by the knowledge of the contrasted emissivity values, as the analytical approaches shown that the latter plays an important role in the accuracy of the estimated heat fluxes. However, for the case of Peltier modules, when used for heat flux measurement, a difficulty arises when trying to estimate the convective heat flux and convective coefficient. This might be strongly related to the very design of these devices (geometry and materials), which does not involve any problem for their natural application but seems to affect the estimation of such parameters as accurate as the conventional heat flux meters. Nevertheless, no other study has been encountered concerning this last remarked.

1.4.4 Calibration techniques for flat-plate type of heat flux sensors

The calibration process for heat flux sensors is usually employed to determine the sensor sensibility value $\mathcal{K}$ and the perturbations it introduces, regarding its equivalent specific thermal capacity C and its equivalent thermal resistance R [77]. The most common technique implemented for calibration has been the zero-flux method. Used by many researchers, some of them have been cited here before [77, 75, 103, 51, 66, 30, 29, 23, 110].

This technique consists, basically, in having the heat flux sensor inside a well-isolated-chamber

device, which contains (cf. fig. 1.39): two flat heater resistors (having the same surface area as the sensor), a second heat flux sensor (usually no necessarily calibrated) and two water-recirculation-plates connected to a thermostatically-controlled water bath (used as heat sink). The sensor to be calibrated is placed over one of the water-recirculation-plates, and one of the heaters is placed over the sensor. The second sensor is placed over the heater to detect heat dissipation in the opposite desired direction (towards the first sensor). The other heater is placed over the second sensor, serving as heat flux compensation, which power is regulated to maintain a null signal response from the second sensor, ergo, ensuring a zero heat flux through this sensor (wherefore the name zero-flux method).

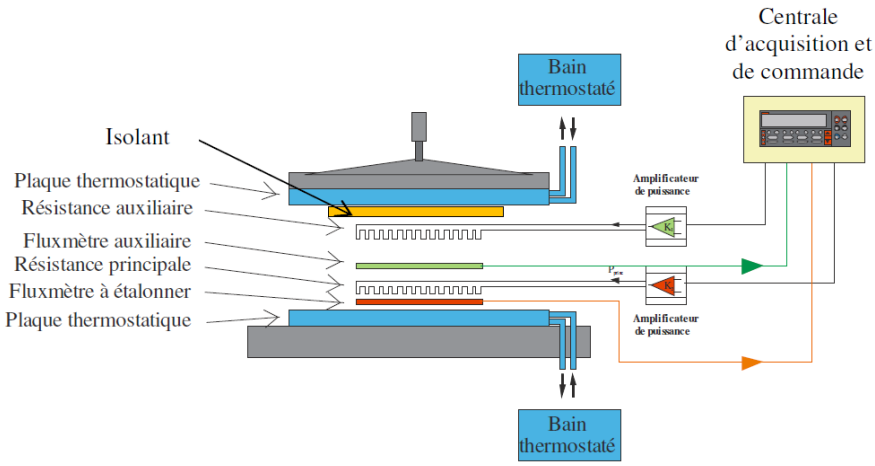

Figure 1.39: Schematic of the calibration apparatus employed for the zero-flux technique [110].

A profound study was conducted by Oiry [75] in 1985. This study aimed to verify the sensibility value K, estimated by this calibration procedure for the FGT, implementing two numerical models of the multilayer system using the governing equations of the physical phenomena that take place. By using this calibration technique, a sensibility value of 6,19 $\mu V \cdot m^2 \cdot W^{-1}$ and a contact resistance of 5,9x10^{-4} $K \cdot m^2 \cdot W^{-1}$ were found. The simulation results showed the following:

1. The influence of some parameters can be neglected (<7%) when confronted with the conduction heat flux.
2. Only 39% of the sensibility value could be explained when using the perfect thermal-contact hypothesis between the copper and constantan layers.
3. A value of the order of 1x10^{-6} $K \cdot m^2 \cdot W^{-1}$ for the latter was enough to obtain a sensibility value identical to the one obtained by calibration.
4. The value of the contact resistance between the copper and constantan layers had a small influence on the sensor internal resistance R calculated, being consistent with the value obtained by calibration.

On the other hand, [68] performed a different approach for the calibration of thermoelectric modules. The sensibility value was determined indirectly by estimating the total Seebeck coefficient and the equivalent thermal conductivity as in equation (1.17). For the total Seebeck coefficient, the module was energized with a DC power source. Then, the electrical response of the module and the temperature difference between its both sides, were measured after turning off the DC power; the Seebeck coefficient results from the slope of a fitted linear regression. The thermal conductivity was estimated by the

classical conductive methods.

1.5 Concluding remarks and perspectives

In this chapter, we have covered the basics for comprehending the natural ventilation concept. We have briefly reviewed the experimental and modeling techniques already implemented for past researchers, in the estimation of the ventilation airflow rate due to the wind and thermal buoyancy effects. Also, a brief reviewed of the experimental and modeling techniques concerning the heat flux measurement and the estimation of the convective and radiative heat flux, have been presented. These literature review has allowed noticing the following remarks:

- The coupling between natural ventilation and the thermal mass of a building can be studied by only considering two simple energy balances, one on the indoor air and another on the thermal mass, and the equation for the ventilation airflow rate.
- The location of the air-leakage/infiltrations must be analyzed attentively, to avoid overestimation or underestimation of the air-leakage rate.
- The use of flat-plate heat flux meters arises as a good experimental technique for estimating the convective heat exchanges, and more importantly, thermoelectric modules are considerably more attractive than conventional heat flux meters regarding their sensitivity.

Regarding this last remark, in the studies reviewed, the implementation of the heat flux meters differed in geometry and arrangement, i.e., black and shiny sensors installed with one of their sides always in contact [23, 29] and installed with a separation between them [63, 109, 113]. The selection of the heat flux meter depends mainly on the heat flux levels to be measured, the accuracy wanted in the heat flux measured and the measuring system employed in the measurement.

Regarding the experimental and modeling techniques for estimating the ventilation airflow rate, a limitation arises in their applicability to our specific case, since:

- The experimental techniques require heavy instrumentation (often expensive) of the openings in terms of airspeed and pressure measurements (local), being the ones that could lead to a better understanding of the phenomena involved in the ventilation process.
- The modeling techniques such as CFD requires large computation time depending on the computer power and the models itself. The models based on empirical observations require the knowledge of the airflow patterns within the building.

Thus, the modeling technique more suitable for our case seems to be the implementation of network airflow models via direct airflow simulations performed by software such as CONTAM, since the knowledge of the airflow patterns is not required.

The more suitable experimental technique seems to be the airtightness tests since it allows us to obtain empirical expressions relating the ventilation airflow directly to the pressure difference in the building for both cases: infiltrations (openings closed) and openings opened. Also, the location of the leakages can be identified without complications, and this technique has the potential to estimate *in situ* the airflow capacity and friction characteristics of the openings.

In summary, it has been highlighted that in the literature, the coupling between natural ventilation and the thermal mass can be considered by only two energy balances. Then, if we want to consider a

thermal behavior model as simple as those, a good characterization of the heat transfer within the test building is needed. With this, the key parameters in both the charge and discharge processes can be determined to later develop a model with the least quantity of parameters that accurately describe the thermal behavior of the building.

Chapter 2

Characterization of the coupling of the energy charge-discharge process with natural ventilation

Scope

This chapter describes the experimental study carried out on the platform for characterizing the energy charge and discharge processes, and their coupling to the outdoor thermal stresses, especially natural ventilation in the summertime. The characterization of both charge and discharge processes aims to understand the thermal behavior of the platform, and to determine the heat transfer phenomena involved in each process. They will ultimately, lead to construct a physical model of the platform that only considers the key parameters to describe the thermal behavior of the indoor environment. This chapter is organized as follows: first, a detailed description of the platform, the experimental approach and measuring systems implemented for data acquisition are presented. Second, an analytical model to qualify and quantify the charge and discharge processes in terms of convective and radiative heat fluxes is presented. Third, the protocol followed for implementing different configurations of the natural ventilation system during the measurement campaigns is presented. Finally, the experimental results showing the thermal behavior of the platform and the heat exchanges highlighted on the slab surface, as well as, evidence of the coupling between the energy charge-discharge process and the natural ventilation strategies implemented, are analyzed and discussed.

2.1 Description of the experimental platform

The current state of the experimental platform can be seen in figure 2.1 (a). As said before, the three main architectural features that aid to promote the strategies of passive energy storage and semi-passive energy discharge, are respectively in figure 2.1: a concrete-slab behind the South glazed-facade (b), fixed and programmable solar shades (c)-(f), and programmable natural ventilation openings (PNVO) at the South and North facades, and at the shed-roof (red, squares, (d)-(f)). In principle, these solar shades and PNVO permit the platform to control the heat loads, in the form of radiative and convective heat exchanges, from the outdoor environment.

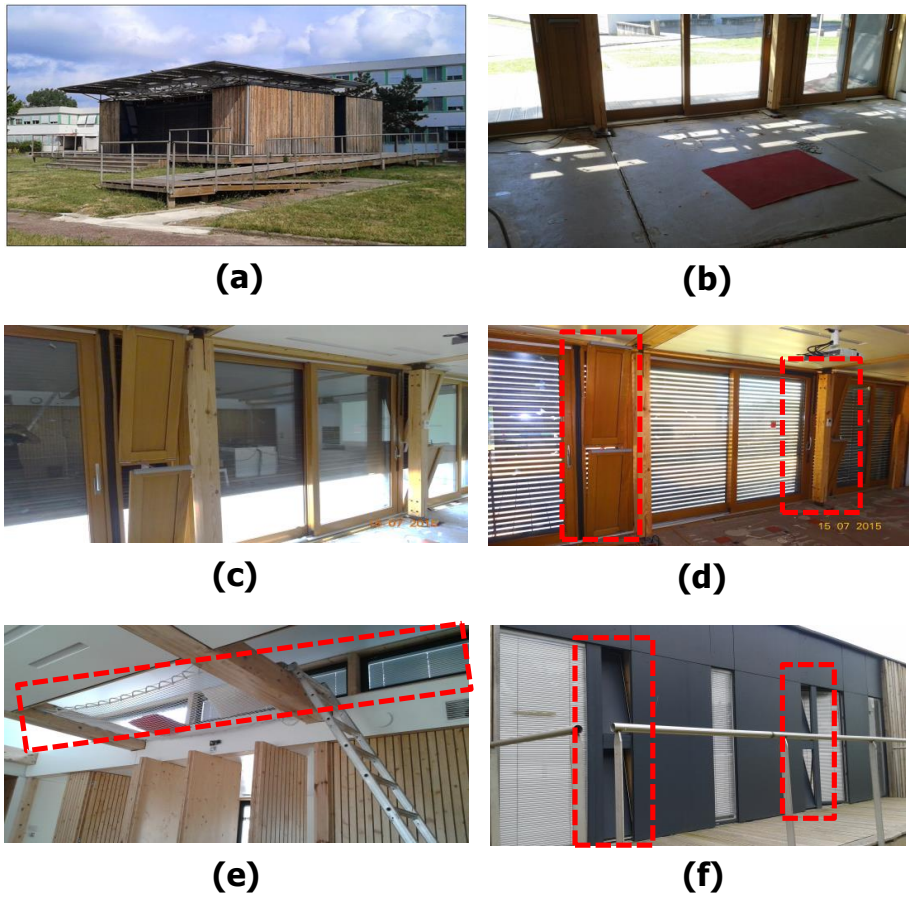

Figure 2.1: Image of Sumbiosi current state (a). Architectural features: floor concrete-slab (b), and programmable solar shades and natural ventilation openings (inside red squares) at the South glazed-facade (c)-(d), (e) at the shed-roof and (f) at the North facade.

2.1.1 Passive strategies for the charge-discharge process in summer

In summer daytime, the platform employs its three architectural features for attenuating the incoming heat, which can be presented in the form of convective and radiative heat exchanges due to solar gains, wind and air temperature, by closing both the solar shades and the natural ventilation openings. This attenuation of the incoming heat will results in, nonetheless, an indoor temperature rise (cf. fig. 2.2 (a)). Note here that the solar eave on the platform roof prevents solar rays from entering

the indoor environment, as the position of the sun is higher during the summer daytime. Then, in the summer nighttime, the platform configures its natural ventilation system as to promote the releasing (or discharging) of the heat stored during the daytime, depending on the weather conditions of wind, air temperature, and rain. This results in a decrease of the temperature of both the indoor air and indoor surface of the structure (cf. fig. 2.2 (b)). Given its characteristic and the intention of the platform design, the floor concrete-slab plays an important role in the energy charge-discharge process. Since this slab is the thermally heavier-weighted element in the platform envelope, it is considered as starting hypothesis, that majority of the thermal mass is concentrated in the concrete-slab.

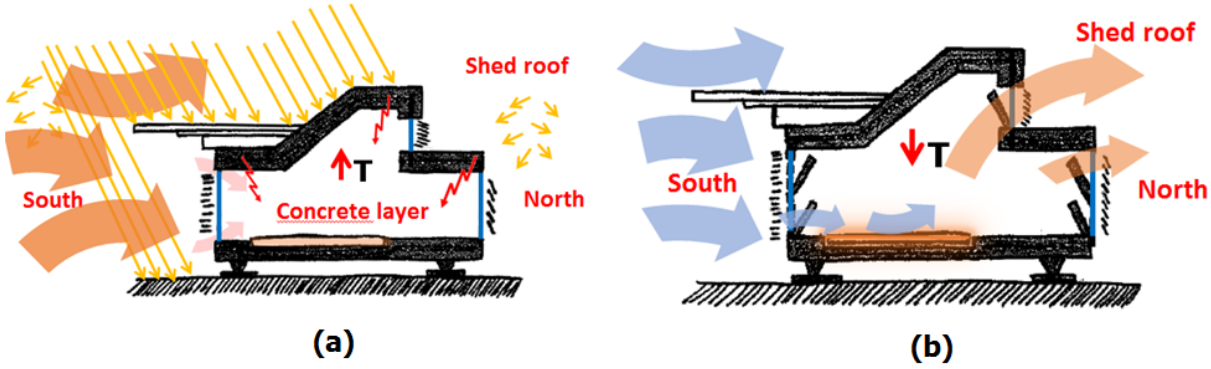

Figure 2.2: Illustration of the platform employing its architectural features: passive energy storage in summer daytime (a), and semi-passive energy discharge in summer nighttime (b).

2.1.2 Natural ventilation system and openings

The natural ventilation system of the platform controlled by the home automation system which allows automating the opening-closing configurations of the natural ventilation openings. This natural ventilation system is equipped with ten programmable openings of the type "horizontal-axis-tilted window" (also known as tilt windows or bottom-hung windows), restricted to a maximum inwardly opening-angle of 20°. They are distributed in the South and North facades, and three manual door-like openings located in an internal wall that separates the living room and the bedroom (cf. fig. 2.3 (a)-(d)).

The South facade has four natural ventilation openings of the same dimensions, being of 119 x 35 cm^2 (height x width) (cf. fig. 2.3 (a)), while the four openings in the North facade have different dimensions, all four being of 108 x 43 cm^2 (cf. fig. 2.3 (b)),. Finally, the shed-roof contains two window openings, having dimensions of 55 x 222 cm^2 (cf. fig. 2.3 (c)). A schematic of the west and top views of the platform architectural plans, showing the location of the natural ventilation openings and the floor concrete-slab, was presented earlier in figure 6 (p.4).

2.2 Experimental approach and protocol

In order to study the energy charge and discharge processes experienced by the platform, resulting of the outdoor thermal stresses (inputs) reflected in the indoor environment, the platform was instrumented in terms of temperature, heat flux and airspeed measurements. This experimental approach aims to observe, comprehend and quantify the thermal response of the platform and of its floor

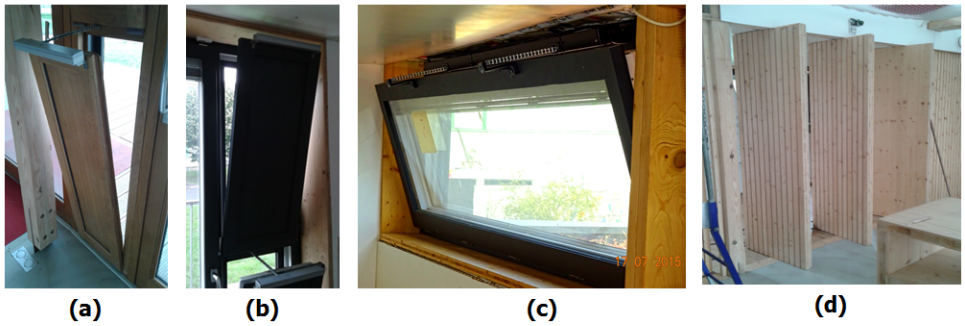

Figure 2.3: Images of the natural ventilation openings: (a) at the South facade, (b) at the North facade, (c) at the shed-roof, and (d) between the living room and bed room.

concrete-slab, under different inputs, especially, natural ventilation. These input-output relations is represented in figure 2.4 (top), where the thermal behavior of the platform (building domain) can be studied by the following outputs:

- Indoor air temperature
- Natural airflow rate
- Heat stored in the indoor air
- Mean radiant temperature.

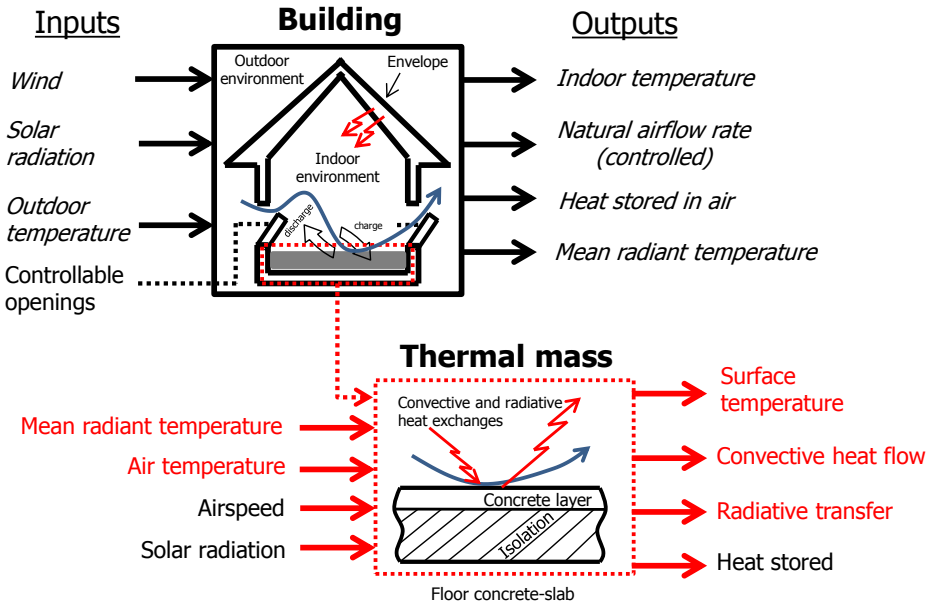

Figure 2.4: Domains and variables for the experimental approach. Top: inputs and outputs studied regarding the building domain (in italic letter). Bottom: inputs and outputs studied regarding the thermal mass domain (in red).

Similarly, the thermal response of the thermal mass domain (cf. fig. 2.4 (bottom)) can be studied by focusing on the convective and radiative heat exchanges, resulting of the interaction between the building domain and the outdoor thermal stresses. Thus, the thermal mass domain can be defined by the interactions between the floor concrete-slab (thermal mass) and the following inputs:

- the indoor air (in the form of convection due to air temperature and speed)

- the surrounding (in the form of radiation due to solar radiation and temperature of other surfaces).

Thus, its behavior can be studied by the following outputs (cf. fig. 2.4, outputs in red):

- the floor concrete-slab surface temperature
- the convective heat flux
- the radiative heat flux
- the heat stored in the slab.

Finally, this level of instrumentation leads to the possibility of relating the convective heat flux to the natural airflow, and the radiative heat flux to the surrounding surfaces of the indoor environment. In addition, regarding the radiative heat transfer between the floor and surrounding surfaces, the ceiling and glazed-facade surfaces have been also instrumented in terms of temperature and heat flux.

2.2.1 Instrumentation of the thermal mass domain

2.2.1.1 The "measurement device" for decoupling the convective and radiative parts

With the objective of estimating the convection and radiation heat exchanges through experimentation, in the present work, we propose a simple experimental set-up named "measurement device", based on the reported findings from past researchers concerning the experimental approaches for decoupling the superficial heat transfer (cf. §1.4.2). As this chapter develops, it will be show that such "device" allows to quantify directly the variables highlighted in red in figure 2.4. This "device" consists of the following:

A) A couple of black and shiny coated thermoelectric modules:

To measure the total heat flux and its convective part. These two modules were installed with a small separation between them (cf. fig. 2.5), as to expose all their sides to the air. These sensors were properly placed onto the surface studied using a silicon-based thermal grease with thermal conductivity of 5 $W{\cdot}m^{-1}{\cdot}K^{-1}$.

B) A type T thermocouple:

To measure the air temperature near the surface studied (without radiation shield); in each measurement zone, this thermocouple was installed as to measure the temperature at a distance of 10 cm over the surface studied.

C) A type T thermocouple inserted into the shiny thermoelectric module:

To measure the temperature of the surface studied. This thermocouple was coated with nail polish, for electrical insulation purposes, before inserting it into the shiny module. The decision of inserting a thermocouple only inside the shiny thermoelectric module was inspired and justified after conducting several preliminary experiments. This experiments showed that the difference between the temperature of the black and shiny thermoelectric modules lays inside the uncertainty interval of the instruments employed; thus leading to conclude that the temperature of the black and shiny modules cannot be experimentally distinguished when accounting for the measurement errors (cf. Appendix A.2).

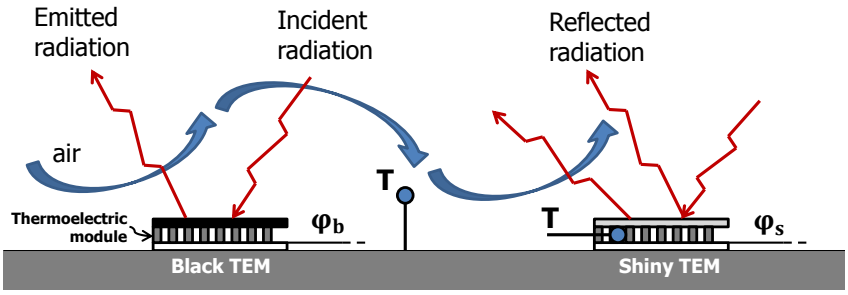

Figure 2.5: A representation of the convective and radiative heat exchanges over a "measurement device" containing a couple of black and shiny thermoelectric modules, and two thermocouples to measure the air and surface temperatures.

2.2.1.2 Floor concrete-slab surface

The floor surface of the platform consists of a concrete-slab located in the living room, behind the South-facing glazed-facade as presented in figure 2.1 (b). On the concrete-slab surface, nine "measurement devices" were installed as shown in figure 2.6. Here, to complement the main goal, the "measurement devices" were distributed all over the concrete-slab surface to also observe the local distribution of the convection and radiation heat fluxes.

Additionally, ten conventional heat flux meters of the type Captec®, were included for comparison purposes, since they have been validated (cf. §1.4.2.2), in the "measurement devices" close to the south-facing natural ventilation openings. Complementary experiments, to study the use of a couple of black and shiny thermoelectric modules instead of the use of a couple of black and shiny Captec®, were carried out later on (cf. Appendix A.3).

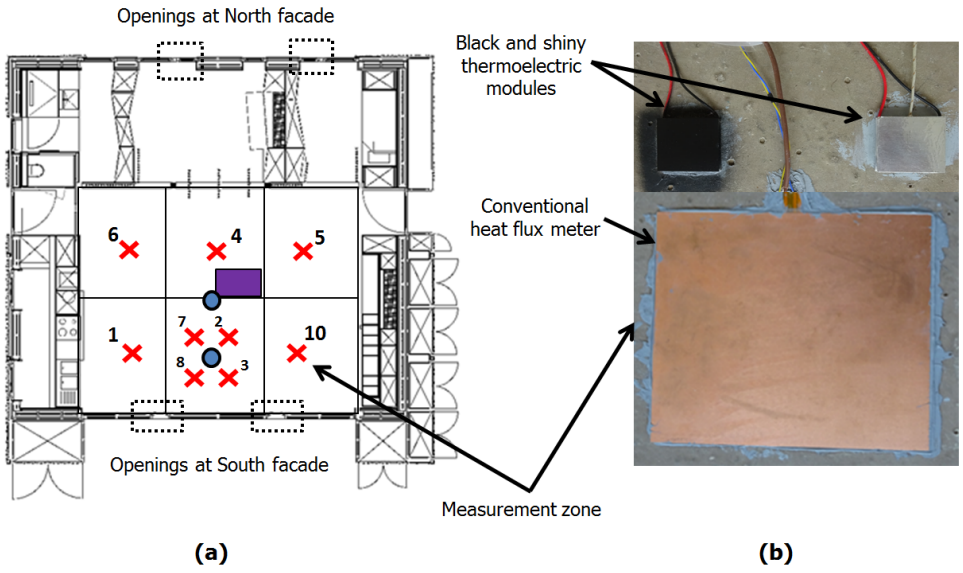

Figure 2.6: Instrumentation of the concrete-slab surface: (a) distribution of the "measurement devices", anemometers location (blue circles), and IR camera view section (purple square), (b) an image of the "measurement devices" near to the South facade openings.

2.2.1.3 Airspeed measurements

As complementary measurements, the airspeed were performed using omnidirectional hot-wire anemometers to monitor the air movement in two different locations in the platform (cf. fig. 2.6, blue circles). One anemometer was installed at 10 cm over the concrete-slab floor, as shown in figure 2.7. The other anemometer was installed at the same location where the indoor air temperature measurement was performed (cf. fig. 2.11 (a)).

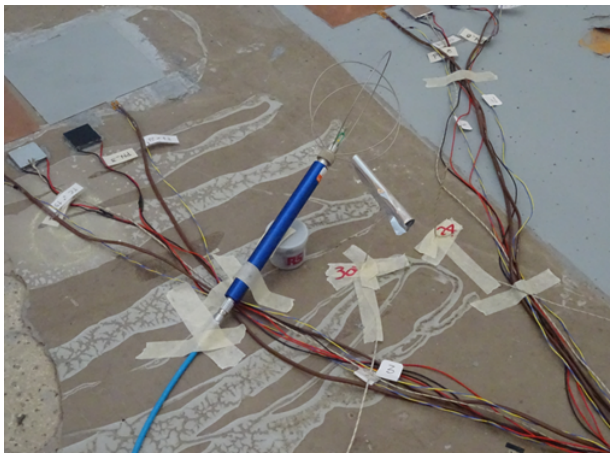

Figure 2.7: Image of the installation for airspeed measurement near the concrete-slab surface.

2.2.1.4 Ceiling and glazed-facade surfaces

As mentioned earlier, another "measurement device" was installed at the center of the ceiling and glazed-facade surfaces with the purpose of motorizing the convection and radiation heat exchanges, air temperature, and surface temperature. An image of both "measurement devices" and their location within the platform are presented in figures 2.8, 2.9, and 2.10, respectively. It is worth mentioning that the importance of having instrumented these two surfaces is highlighted in the results and analysis part.

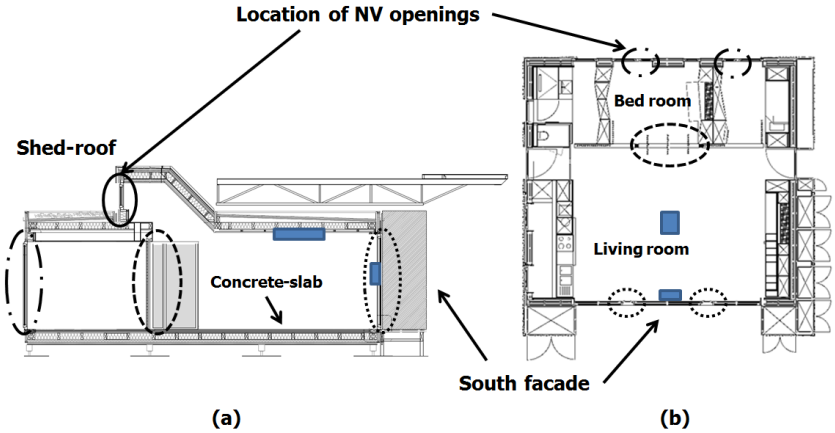

Figure 2.8: Location of the "measurement devices" at the ceiling and the glazed-facade (blue boxes): (a) West-side view and (b) top view.

Figure 2.9: Image of the measurement zone on the ceiling surface.

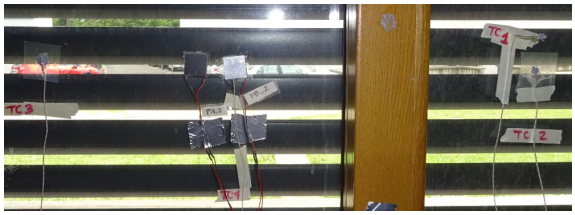

Figure 2.10: Image of the measurement zone on the glazed-facade surface.

2.2.2 Instrumentation of the building

The instrumentation of the building domain allows to quantify the variables in *italic font* in figure 2.4: (*i*) wind speed, (*ii*) direct solar radiation, (*iii*) outdoor air temperature, (*iv*) indoor air temperature, and (*v*) the mean radiant temperature.

2.2.2.1 Indoor and outdoor air temperature measurement

A type T thermocouple was installed at the center of the concrete-slab floor at 1,70 m height to measure the indoor air temperature (see location in fig. 2.6, middle blue circle and fig. 2.11, (a)). Its location was chosen, since it is the average height of the human body when standing up (ISO 7730, [117]). Another type T thermocouple was installed outside the south facade of the platform to measure the outdoor air temperature. An aluminum foil was placed over the thermocouple, as a sort of roof, to shield it from direct solar radiation (cf. fig. 2.11 (b)).

(a) **(b)**

Figure 2.11: Image of the installation for temperature measurement: (a) indoor air and (b) outdoor air.

2.2.2.2 Infrared measurements

The experimental set-up for infrared measurements is presented in figure 2.12. These measurements were performed during the main measurement campaign with the following objectives: (*i*) to measure the indoor mean radiant temperature, (*ii*) to measure the concrete-slab surface temperature, and (*iii*) to determine the concrete-slab surface emissivity value. These first two points were performed

for comparison purposes, to validate the surface temperature measurement performed inside the thermoelectric modules §2.2.1.1.**C)**, and to validate the estimation of the indoor mean radiant temperature obtained by heat flux measurement and an analytical model presented later in this chapter in §2.3.2.

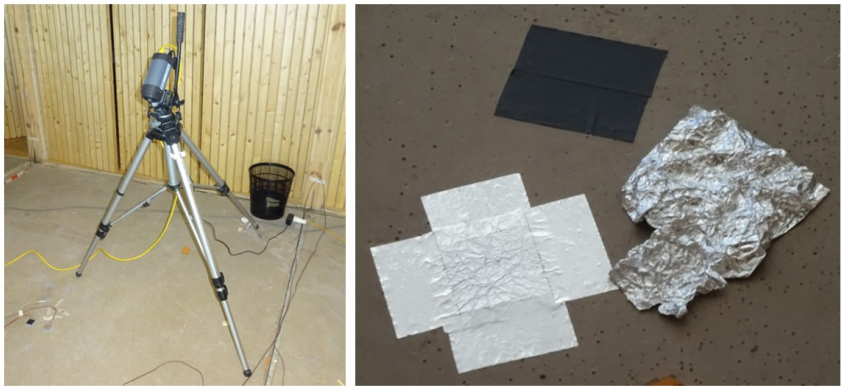

Figure 2.12: Experimental set-up for infrared measurements. On the left-hand side: Infrared camera. On the right-hand side: A fully crumbled aluminum foil (isotropic and diffuse reflector), a black foil placed on the concrete-slab surface (reference).

2.2.2.3 Wind and solar radiation measurements

Weather conditions data were obtained from a 10 m height meteorological station located near the platform at approximately 1,5 km (cf. fig.2.13), from which the direct solar radiation, wind speed and wind direction were recovered for the study. This meteorological data was continuously registered every 10 minutes.

Figure 2.13: Image of the meteorological station.

2.2.2.4 Supplementary indoor air temperature measurements

The vertical distribution of the air temperature inside a building is important when studying the natural airstreams due to thermal buoyancy. Therefore, supplementary type T thermocouples were distributed inside the platform at different heights for monitoring the vertical thermal stratification inside the platform. The location of all thermocouples is shown in figure 2.14.

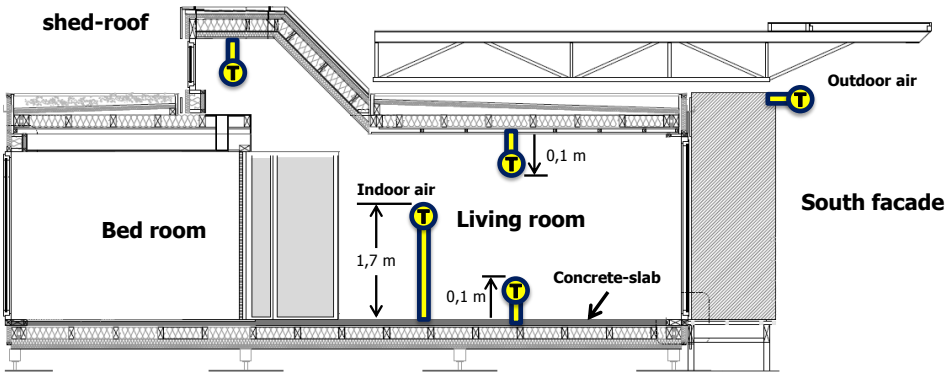

Figure 2.14: Distribution of supplementary thermocouples for air temperature measurements inside the platform (in yellow).

2.2.3 Measuring system and calibration

2.2.3.1 Measuring system for heat flux sensors

The two types of heat flux meters employed in this experimental study were thermoelectric modules and conventional heat flux meters. Both sensors were connected to the National Instrument acquisition board NI 9205, which is a very precise voltmeter with an uncertainty of ± 174 μV.

A) Conventional heat flux meters:

The conventional heat flux meters are from Captec® company; their surface area is 225 cm^2 (15 x 15 cm) and their thickness is 0,05 cm. Their response time is about 0,3 s, and they have an integrated type T thermocouple. These sensors were precalibrated by the company at room temperature, using a stationary conductivity measurement method, but with a very thin sample, and since the conductivity of the sample is known, the flux passing through the sensor can be deducted. The sensitivity value $\mathcal{K}$ does not change with the temperature of the sensor (cf. table 2.1) at $\pm 3\%$ of error. In table 2.1, the number of the Captec® sensors corresponds to their location on the concrete-slab surface (cf. fig. 2.6).

Table 2.1: Sensitivity values of Captec® heat flux meters.

N° Captec	1	2	3	4	5	6	7	8	9	10
$\mathcal{K}$ [μV·m^2·W^{-1}]	123	123	124	126	117	127	128	128	108	122

B) Thermoelectric modules:

The thermoelectric modules have a 9 cm^2 (3 x 3 cm) surface area and a 0,48 cm thickness (cf. fig.2.15). The surface of each thermoelectric module was covered with either black or shiny coatings, and their edge-sides were covered with concrete-colored silicon to isolate the semiconductor-joints from contact to surrounding air, before any implementation (cf. fig.2.15 (c)).

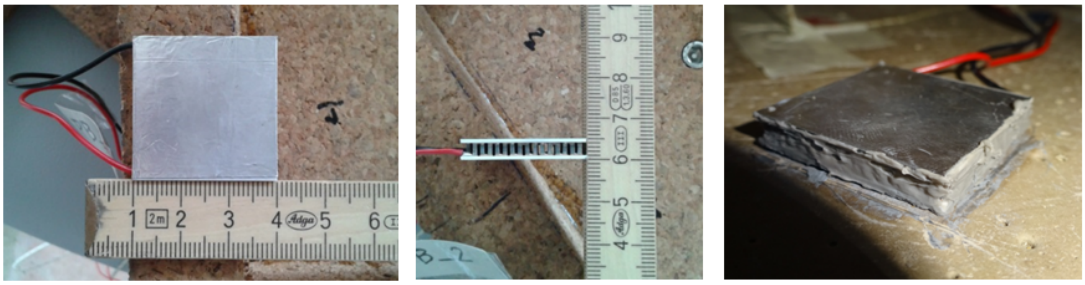

Figure 2.15: Images of a shiny thermoelectric module: (a) width, (b) thickness, and (c) a thermoelectric module installed with the silicon trail.

2.2.3.2 Calibration of the thermoelectric modules

A) Calibration set-up:

The experimental set-up depicted in figure 2.16 was implemented to determine the characteristics of the thermoelectric modules, such as the sensitivity value $\mathcal{K}$, the response time, and the thermal conductivity λ, along with the uncertainty in the heat flux measurement. This set-up consisted of the use of the following items:

1. A flat heating resistance of 20$\pm$0,05 Ω and a surface area of 1 cm^2 (1 x 1 cm): element number 1 in figure 2.16 (a), and in (b) at the top left square image. Note here that this surface area is smaller than the thermoelectric modules surface area.
2. Two flat thermocouples of type K: elements number 2 in figure 2.16 (a).
3. A thermoelectric module: number 3 in figure 2.16 (a).
4. A type T thermocouple inside the thermoelectric module: number 4 in figure 2.16 (a).
5. Two type of isolating materials of color black and white: number 5 in figure 2.16 (a), and also showed in (b). The white was used to isolate precisely the thermoelectric module, and the black was used to isolate the chamber.
6. A steel block that serves as a heat sink: number 6 in figure 2.16 (a).
7. A concrete block was used to keep the sensors steady inside the chamber: number 7 in figure 2.16 (a).

B) Calibration procedure:

The calibration procedure consisted of submitting the thermoelectric module to different constant heat loads and recording its thermal response, in steady state conditions. The heat loads were applied by the heating resistance and adjusted by a variable DC power source. Once the heating resistance was energized, approximately 20 minutes were awaited for the thermoelectric module response to stabilized (this time interval was chosen after previous observation of their behavior). After stabilization, the

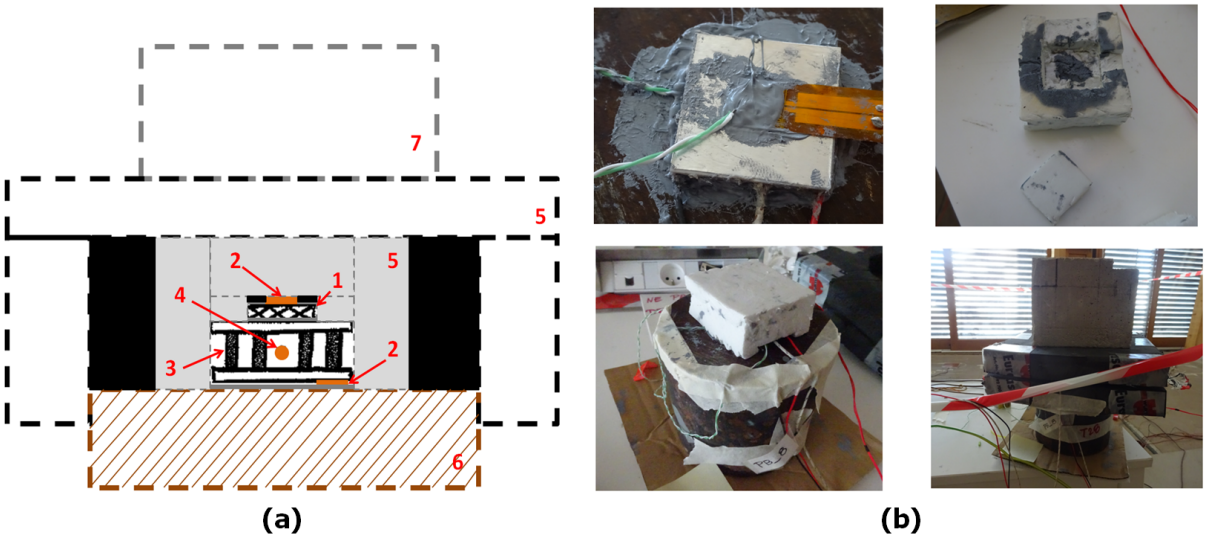

Figure 2.16: A cross-section schematic representation and images of the calibration set-up, (a) and (b) respectively.

heating resistance was de-energized for 5 minutes, waiting until the module reaches its equilibrium. The entire procedure was recorded, and the same process was performed for every heat load applied.

An example of the electrical response of the black coated thermoelectric module n^{o}8 measured when a heat load of 20 W·m^{-2} was applied, is presented in figure 2.17. After the electrical response was stabilized (at standard deviation of ± 20 μV), it can be observed that the time response is approximately 2 minutes (calculated at 90% of the maximum tension value).

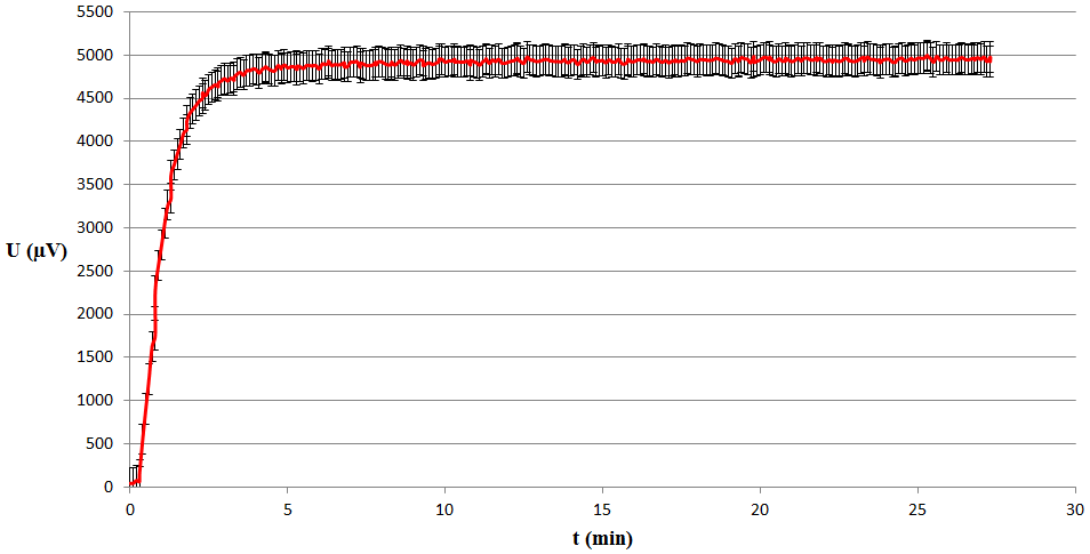

Figure 2.17: Electrical response of the black coated thermoelectric module N^{o}8 after correction, when applying a heat load of 20 W·m^{-2}, along with the uncertainty of the voltmeter NI 9205.

(C) Results and analysis:

The different heat loads applied in the calibration procedure and the electrical response of the Thermo-Electric Module (TEM) n°8 are presented in table 2.2. From left to right, table 2.2 presents the desired

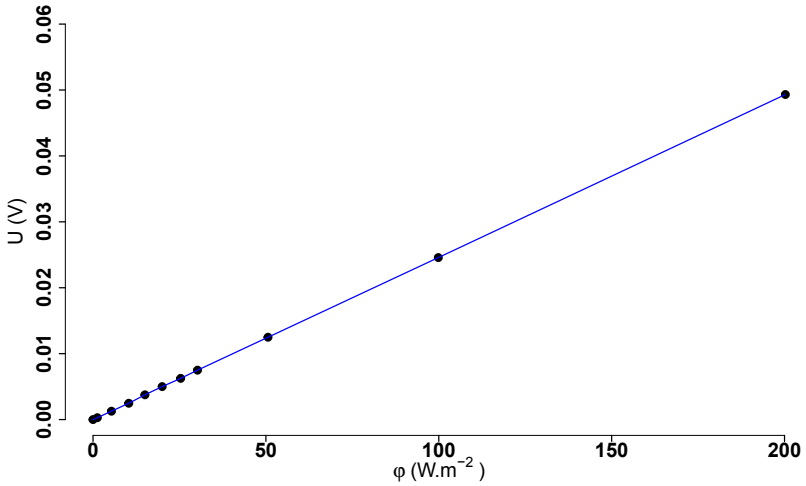

Figure 2.18: Linear regression fitted to the electrical response of the black coated thermoelectric module n°8, after correction, confronted with the heat loads applied, to determine the sensitivity value.

heat load or setpoint $\varphi_{setpoint}$, the voltage $\mathcal{U}$ and current $\mathcal{I}$ applied to the flat heating resistance, the resulting heat load applied φ_{real} by the flat heating resistance, the electrical response U of the thermoelectric module, and its corresponding corrected response $U_{corrected}$. The real heat loads applied φ_{real} were calculated by the following expression:

$$\varphi_{real} = \frac{\mathcal{U} \cdot \mathcal{I}}{S} \qquad \left[\mathrm{W{\cdot}m^{-2}}\right] \tag{2.1}$$

where S represents the surface area of the thermoelectric module.

Table 2.2: Response of the TEM N°8 to different heat loads.

$\varphi_{setpoint}$ [W·m^{-2}]	$\mathcal{U}$ [V]	$\mathcal{I}$ [A]	φ_{real} [W·m^{-2}]	U [μV]	$U_{corrected}$ [μV]
0	0	0	–	−59,61	–
1	0,141	0,008	1,25	225,71	285,32
5	0,300	0,016	5,33	1209,03	1268,64
10	0,424	0,022	10,34	2414,33	2473,94
15	0,520	0,026	15,02	3697,61	3757,22
20	0,600	0,030	20,00	4942,00	5001,61
25	0,671	0,034	25,35	6191,85	6251,46
30	0,735	0,037	30,22	7434,07	7493,68
50	0,949	0,048	50,61	12430,96	12490,57
100	1,342	0,067	99,87	24516,31	24575,92
200	1,897	0,095	200,24	49252,91	49312,52

In table 2.2, note that the first value in the column of the TEM response U, is negative (−59,61 μV). This may indicate two things:

- when no heat load was applied, the TEM response had an opposite direction in comparison when the heat loads were applied (positive),
- both sides of the thermoelectric module were not at the same temperature at the beginning of

the procedure.

This implies that when a heat load was applied, the latter must have been greater than the opposite heat flux created by the inequality in the temperature of the sensor sides, and a correction is required (cf. table 2.2, $U_{corrected}$ column). This correction can be generalized as follows: $U_{corrected}(\varphi_{setpoint}) = U(\varphi_{setpoint}) - U(\varphi_{setpoint} = 0)$.

For the calculation of the sensitivity value $\mathcal{K}$ of the thermoelectric module, the corrected electrical response $U_{corrected}$ was plotted against the applied heat load φ_{real}; the sensitivity value was determined then, by fitting a linear regression forced to cross the origin (see fig. 2.18 here above).

This calibration procedure was performed again for the black coated thermoelectric module n°4 on the same day, giving a $\mathcal{K}$ value of 247,91 $\mu V{\cdot}m^2{\cdot}W^{-1}$. It was also performed two times on July 8th, 2016 for the shiny coated thermoelectric module N°8, giving a $\mathcal{K}$ value of 267,53 $\mu V{\cdot}m^2{\cdot}W^{-1}$ the first time, and 267,14 $\mu V{\cdot}m^2{\cdot}W^{-1}$ the second time.

Apart from the fabrication errors, the only visible difference between the black and shiny modules is the type of coating used (texture and color). Not enough experiments have been performed to declare that these different coatings could explain the approximately 20 $\mu V{\cdot}m^2{\cdot}W^{-1}$ difference encountered between the $\mathcal{K}$ values: the uncertainty analysis has shown that this difference appears to be indistinguishable when accounting for the uncertainty of the instrument we have employed.

(D) Uncertainty in the heat flux measurement:

The uncertainty in the heat flux measurement of the black and shiny thermoelectric modules (δ_φ), was determined using the Constant Odds Combination (COC) method. Thus, to calculate the uncertainty in the heat flux measurement the COC method was applied to equation 1.16, as follows:

$$\delta_\varphi = \sqrt{\left[\frac{\delta_U}{\mathcal{K}}\right]^2 + \left[\frac{U \cdot \delta_\mathcal{K}}{\mathcal{K}^2}\right]^2} \qquad \left[W{\cdot}m^{-2}\right] \tag{2.2}$$

where δ_U is the uncertainty in the TEM response measured by the acquisition system and $\delta_\mathcal{K}$ is the uncertainty in the sensitivity of the TEM. For the latter, by equating expressions 1.16 and 2.1, an expression for the sensitivity value $\mathcal{K}$, yields

$$\mathcal{K} = \frac{U \cdot S}{\mathcal{U} \cdot \mathcal{I}} \qquad \left[\mu V{\cdot}m^2{\cdot}W^{-1}\right] \tag{2.3}$$

and thus, applying the COC method to the previous equation, results in:

$$\delta_\mathcal{K} = \sqrt{\left[\frac{S \cdot \delta_U}{\mathcal{U} \cdot \mathcal{I}}\right]^2 + \left[\frac{U \cdot \delta_S}{\mathcal{U} \cdot \mathcal{I}}\right]^2 + \left[\frac{U \cdot S \cdot \delta_\mathcal{U}}{\mathcal{U}^2 \cdot \mathcal{I}}\right]^2 + \left[\frac{U \cdot S \cdot \delta_\mathcal{I}}{\mathcal{U} \cdot \mathcal{I}^2}\right]^2} \qquad \left[\mu V{\cdot}m^2{\cdot}W^{-1}\right] \tag{2.4}$$

It can be observed from equation 2.4 that the uncertainties in $\mathcal{U}$ and S, being constant values depending on the instruments employed, could make vary the uncertainty in $\mathcal{K}$, depending on the value of the thermoelectric module response U, along with the value of the voltage and current applied to the heating resistance. The uncertainties of the instruments employed to measure each parameter are given in table 2.3.

Table 2.3: Uncertainties of the instruments for the calibration procedure.

Instrument	Parameter	Uncertainty δ
NI 9205	U	174 μV
Digital caliper	S	6,0x10^{-6} m^2
Digital DC power source	$\mathcal{U}$	10%
Digital DC power source	$\mathcal{I}$	10%

By evaluating equation 2.4 with the values in table 2.2 and those in table 2.3, the resulting uncertainties in $\mathcal{K}$ at each heat load applied are presented in table 2.4. Results showed that the uncertainty in $\mathcal{K}$ decreases when the heat load applied increases, resulting in an average value $\overline{\delta_{\mathcal{K}}}$ of 48,49 μV·m^2·W^{-1}.

Table 2.4: Components in the uncertainty of the sensitivity $\mathcal{K}$.

φ_{real}	U	$\frac{S}{\partial\mathcal{U}\cdot\mathcal{I}}$	$\frac{U}{\partial\mathcal{U}\cdot\mathcal{I}}$	$\frac{U\cdot S}{\partial\mathcal{U}^2\cdot\mathcal{I}}$	$\frac{U\cdot S}{\partial\mathcal{U}\cdot\mathcal{I}^2}$	$\delta_{\partial\mathcal{U}}$	$\delta_{\mathcal{I}}$	$\delta_{\mathcal{K}}$
0	0	–	–	–	–	–	–	–
1,25	285,32	0,798	0,253	-0,002	-0,028	0,014	0,001	142,72
5,33	1268,64	0,188	0,264	-0,001	-0,015	0,030	0,002	47,53
10,34	2473,94	0,096	0,265	-0,001	-0,011	0,042	0,002	38,53
15,02	3757,22	0,067	0,278	-0,0005	-0,010	0,052	0,003	38,14
20,00	5001,61	0,050	0,278	-0,0004	-0,008	0,060	0,003	37,36
25,35	6251,46	0,039	0,274	-0,0004	-0,007	0,067	0,003	36,48
30,22	7493,68	0,033	0,276	-0,0003	-0,007	0,074	0,004	36,49
50,61	12490,57	0,020	0,274	-0,0003	-0,005	0,095	0,005	36,02
99,87	24575,92	0,010	0,273	-0,0002	-0,004	0,134	0,007	35,80
200,24	49312,52	0,005	0,274	-0,0001	-0,003	0,190	0,010	35,79

In order to account for the uncertainty in the sensitivity $\mathcal{K}$, we have now to choose whether to consider $\delta_{\mathcal{K}}$ as an average value or as a value that varies with the heat flux applied. Thus, by evaluating equation (2.2), the difference between choosing one upon the other is presented graphically in figure 2.19. In this figure it is clear that larger uncertainties are obtained when using $\delta_{\mathcal{K}}$ as an average value (cf. fig. 2.19, color red), instead of using $\delta_{\mathcal{K}}$ as a heat-flux-applied dependent value (cf. fig. 2.19, color blue).

(E) Conclusion:

An estimation of the heat flux measured with the thermoelectric modules can be achieved, as precise as possible, by considering uncertainty values that depend on the heat flux measured instead of an average uncertainty value. Finally, the following expressions will be implemented when reporting the estimated heat flux measurement from the black and shiny thermoelectric modules, respectively:

$$\varphi_{\mathfrak{b}} = \frac{U_{\mathfrak{b}}}{247} \pm \delta_{\varphi_{\mathfrak{b}}} = \frac{U_{\mathfrak{b}}}{247} \pm \left[0{,}14 \cdot \frac{U_{\mathfrak{b}}}{247} + 0{,}35\right] \qquad \left[\mathrm{W{\cdot}m^{-2}}\right] \tag{2.5}$$

$$\varphi_{\mathfrak{s}} = \frac{U_{\mathfrak{s}}}{267} \pm \delta_{\varphi_{\mathfrak{s}}} = \frac{U_{\mathfrak{s}}}{267} \pm \left[0{,}14 \cdot \frac{U_{\mathfrak{s}}}{267} + 0{,}65\right] \qquad \left[\mathrm{W{\cdot}m^{-2}}\right] \tag{2.6}$$

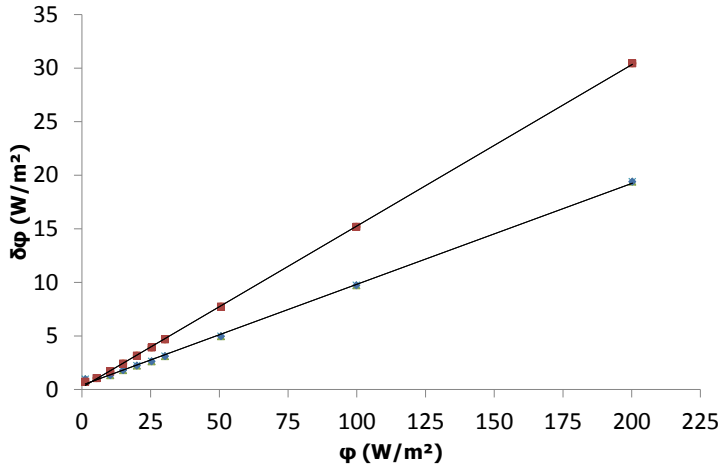

Figure 2.19: Variation in the uncertainty δ_φ in the heat flux measurement of the TEM N^{o}8: when using $\overline{\delta_\mathcal{K}}$ (in red) and when using $\delta_\mathcal{K}$ depending on the heat flux applied (in blue).

where φ_b and φ_s represent the heat flux measurement from the black and shiny thermoelectric modules, respectively.

2.2.3.3 Measuring system for thermocouples and calibration

Several type T thermocouples were calibrated using a thermostatic bath (LAUDA RE 415) with a temperature accuracy of $\pm$0,3 °C and $\pm$0,5% of the temperature value displayed, and a stability of $\pm$0,01 °C, assured by an integrated PT100. All thermocouples were connected to the NI 9213 acquisition card with a measurement sensitivity of $\pm$0,02 °C, and a measurement error of $\pm$0,8 °C for our temperature ranges.

The goal of the calibration procedure was to increase the accuracy of our thermocouples by correcting our measuring system (thermocouple + acquisition system) using a more accurate temperature measuring instrument as a reference; in this case, the thermostatic bath was used (see Appendix A.1 for full report).

Results showed that the maximum deviation between the thermocouples themselves before correction did not exceed the 0,3 °C when submerged in a stable medium (water in this case, cf. fig. 2.20). After correction, this maximum deviation was reduced to 0,07 °C (cf. fig. 2.21). Results also showed that the measurement stability of the thermocouples is $\pm$0,02 °C with a 95% of confidence.

2.3 Semi-empirical models for data processing

2.3.1 Decoupling the convection and radiation heat exchanges

A semi-empirical model is proposed here to distinguish the convection and radiation parts from the heat flux measurement. This model is based on a heat flux balance written for the considered surface i. A heat flux balance of the convective and radiative heat exchanges over this surface, as represented in

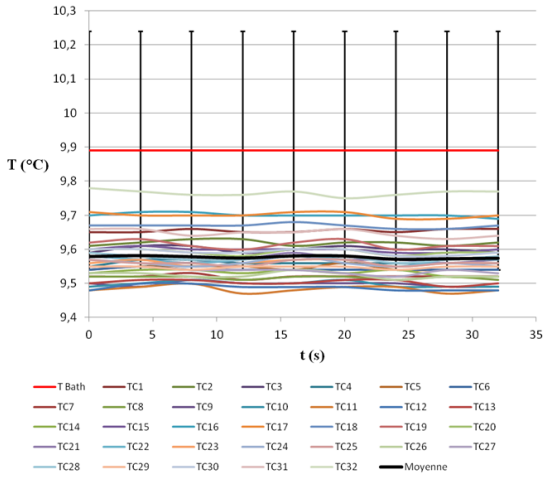

Figure 2.20: Thermocouples measurement when having the bath at 9, 89 °C, before correction.

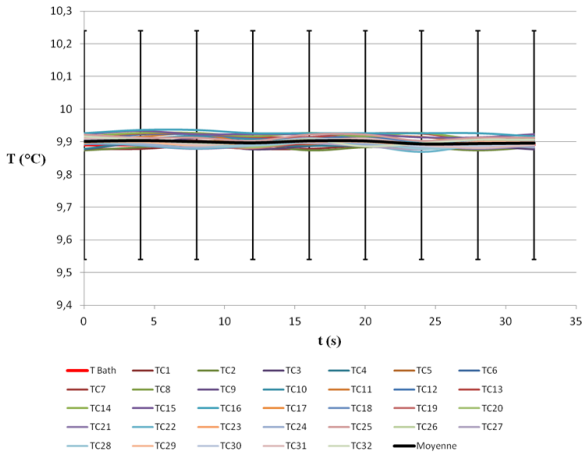

Figure 2.21: Thermocouples measurement when having the bath at 9, 89 °C, after correction.

figure 2.22, can be written as follows:

$$\varphi_i(t) = \varphi_{R_i}(t) + \varphi_{C_i}(t) = I(t) - I_{ref_i}(t) - E_i(t) + \varphi_{C_i}(t) \qquad \left[\mathrm{W{\cdot}m^{-2}}\right] \tag{2.7}$$

where φ_i is the total heat flux entering the surface i. Together I, I_{ref}, and E_i, represent the net radiation heat flux (φ_{R_i}) exchanged between the surface i and the surrounding environment, where I is the total incident radiation heat flux (short + long wavelength), I_{ref} is the reflected part of the total incident radiation, E_i is the emitted radiation heat flux, and φ_{C_i} is the convective heat flux.

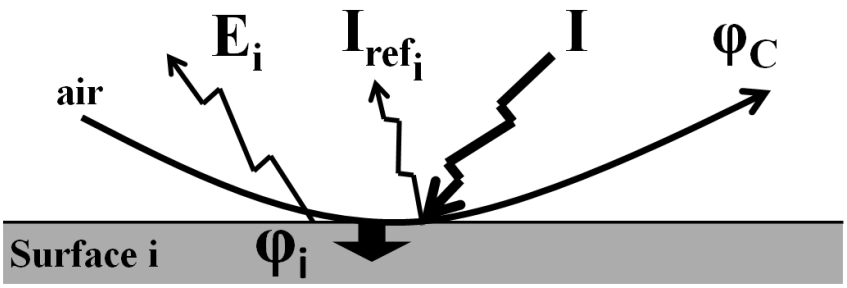

Figure 2.22: Schematic of a surface i submitted to superficial heat transfer.

The term $I - I_{ref}$ of equation 2.7 is equal to the absorbed part of the total incident radiation (I_{abs}), which also can be written as $\alpha_i \cdot I$, where α_i is the total thermal absorptivity. By considering the following four assumptions:

- In a single measurement zone, both black and shiny heat flux meters (and the surface they are placed on) are submitted to the same total incident radiation,
- he convective heat flux follows Fourier's law of convection and is different for each heat flux meter (accounting for any difference in their temperatures),
- the convective heat transfer coefficient is the same for both heat flux meters,
- the emitted radiation follows the Stefan-Boltzmann law for the radiative power emitted by a black body (supposing gray surfaces),

equation 2.7 can be rewritten as follows for the black and shiny heat flux meters, respectively:

$$\varphi_{\mathfrak{b}}(t) = \varphi_{R_{\mathfrak{b}}}(t) + \varphi_{C_{\mathfrak{b}}}(t) = \alpha_{\mathfrak{b}} \cdot I(t) - \varepsilon_{\mathfrak{b}} \cdot \sigma \cdot T_{\mathfrak{b}}^4(t) + h_C \cdot \Delta T_{\mathfrak{b}}(t) \qquad \left[\mathrm{W{\cdot}m^{-2}}\right] \tag{2.8}$$

$$\varphi_{\mathfrak{s}}(t) = \varphi_{R_{\mathfrak{s}}}(t) + \varphi_{C_{\mathfrak{s}}}(t) = \alpha_{\mathfrak{s}} \cdot I(t) - \varepsilon_{\mathfrak{s}} \cdot \sigma \cdot T_{\mathfrak{s}}^4(t) + h_C \cdot \Delta T_{\mathfrak{s}}(t) \qquad \left[\mathrm{W{\cdot}m^{-2}}\right] \tag{2.9}$$

where $\varphi_{\mathfrak{b}}$ and $\varphi_{\mathfrak{s}}$ represent the heat flux measurement of the black and shiny heat flux meters, respectively. The thermal emissivity is represented by ε, and σ represents the Stefan-Boltzmann constant in $W{\cdot}m^{-2}{\cdot}K^{-4}$. The convective coefficient is represented by h_C, and ΔT represents the temperature difference between the air and the heat flux meter.

Then, by solving together equations 2.8 and 2.9, for I and h_C yields:

$$I(t) = \frac{\Delta T_{\mathfrak{b}}(t) \cdot \left[\varphi_{\mathfrak{s}}(t) + \varepsilon_{\mathfrak{s}} \cdot \sigma \cdot T_{\mathfrak{s}}^4(t)\right] - \Delta T_{\mathfrak{s}}(t) \cdot \left[\varphi_{\mathfrak{b}}(t) + \varepsilon_{\mathfrak{b}} \cdot \sigma \cdot T_{\mathfrak{b}}^4(t)\right]}{\alpha_{\mathfrak{s}} \cdot \Delta T_{\mathfrak{b}}(t) - \alpha_{\mathfrak{b}} \cdot \Delta T_{\mathfrak{s}}(t)} \qquad \left[\mathrm{W{\cdot}m^{-2}}\right] \tag{2.10}$$

$$h_C(t) = \frac{\alpha_{\mathfrak{s}} \cdot \left[\varphi_{\mathfrak{b}}(t) + \varepsilon_{\mathfrak{b}} \cdot \sigma \cdot T_{\mathfrak{b}}^4(t)\right] - \alpha_{\mathfrak{b}} \cdot \left[\varphi_{\mathfrak{s}}(t) + \varepsilon_{\mathfrak{s}} \cdot \sigma \cdot T_{\mathfrak{s}}^4(t)\right]}{\alpha_{\mathfrak{s}} \cdot \Delta T_{\mathfrak{b}}(t) - \alpha_{\mathfrak{b}} \cdot \Delta T_{\mathfrak{s}}(t)} \qquad \left[\mathrm{W{\cdot}m^{-2}{\cdot}K^{-1}}\right]. \tag{2.11}$$

Note that in the previous equation, the estimation of the convective heat transfer coefficient does not, explicitly, depends on the roughness of the surface, the airspeed over the surface, the thickness of the sensors, or any other intrinsic characteristic regarding the convective coefficient as reported in the literature. In turn, the influence of all these characteristics are implicitly taken into account by the heat flux measurement itself from each heat flux meter.

Thus, by replacing equation 2.11 into Fourier's law of convection for the shiny heat flux meter, the convective heat flux $\varphi_{C_{\mathfrak{s}}}$, yields:

$$\begin{aligned} \varphi_{C_{\mathfrak{s}}}(t) = & \left[\frac{\alpha_{\mathfrak{b}} \cdot \Delta T_{\mathfrak{s}}(t)}{\alpha_{\mathfrak{b}} \cdot \Delta T_{\mathfrak{s}}(t) - \alpha_{\mathfrak{s}} \cdot \Delta T_{\mathfrak{b}}(t)}\right] \cdot \varphi_{\mathfrak{s}}(t) - \left[\frac{\alpha_{\mathfrak{s}} \cdot \Delta T_{\mathfrak{s}}(t)}{\alpha_{\mathfrak{b}} \cdot \Delta T_{\mathfrak{s}}(t) - \alpha_{\mathfrak{s}} \cdot \Delta T_{\mathfrak{b}}(t)}\right] \cdot \varphi_{\mathfrak{b}}(t) \\ & + \frac{\Delta T_{\mathfrak{s}}(t) \cdot \sigma \cdot \left[\alpha_{\mathfrak{b}} \cdot \varepsilon_{\mathfrak{s}} \cdot T_{\mathfrak{s}}^4(t) - \alpha_{\mathfrak{s}} \cdot \varepsilon_{\mathfrak{b}} \cdot T_{\mathfrak{b}}^4(t)\right]}{\alpha_{\mathfrak{b}} \cdot \Delta T_{\mathfrak{s}}(t) - \alpha_{\mathfrak{s}} \cdot \Delta T_{\mathfrak{b}}(t)} \qquad \left[\mathrm{W{\cdot}m^{-2}}\right]. \end{aligned} \tag{2.12}$$

A similar expression can be obtained for the convective heat flux for the black heat flux meter $\varphi_{C_{\mathfrak{b}}}$, just by replacing ΔT_s for ΔT_b in each numerator:

$$\begin{aligned} \varphi_{C_{\mathfrak{b}}}(t) = & \left[\frac{\alpha_{\mathfrak{b}} \cdot \Delta T_{\mathfrak{b}}(t)}{\alpha_{\mathfrak{b}} \cdot \Delta T_{\mathfrak{s}}(t) - \alpha_{\mathfrak{s}} \cdot \Delta T_{\mathfrak{b}}(t)}\right] \cdot \varphi_{\mathfrak{s}}(t) - \left[\frac{\alpha_{\mathfrak{s}} \cdot \Delta T_{\mathfrak{b}}(t)}{\alpha_{\mathfrak{b}} \cdot \Delta T_{\mathfrak{s}}(t) - \alpha_{\mathfrak{s}} \cdot \Delta T_{\mathfrak{b}}(t)}\right] \cdot \varphi_{\mathfrak{b}}(t) \\ & + \frac{\Delta T_{\mathfrak{b}}(t) \cdot \sigma \cdot \left[\alpha_{\mathfrak{b}} \cdot \varepsilon_{\mathfrak{s}} \cdot T_{\mathfrak{s}}^4(t) - \alpha_{\mathfrak{s}} \cdot \varepsilon_{\mathfrak{b}} \cdot T_{\mathfrak{b}}^4(t)\right]}{\alpha_{\mathfrak{b}} \cdot \Delta T_{\mathfrak{s}}(t) - \alpha_{\mathfrak{s}} \cdot \Delta T_{\mathfrak{b}}(t)} \qquad \left[\mathrm{W{\cdot}m^{-2}}\right]. \end{aligned} \tag{2.13}$$

It can be inferred from equation 2.12 that the assumption considering that the convective heat flux is entirely determined by the measurement of a heat flux meter coated with a shiny-foil ($\varphi_{\mathfrak{s}}$), might lead to an overestimation or an underestimation of this heat flux; depending on the radiative properties of the surface and the air-surface temperature difference for each sensor.

In turn, this equation implies that the convective heat flux would be determined by a shiny heat flux meter only if the following holds:

1. Both sensors are at the same temperature ($\Delta T_s = \Delta T_b$),
2. the shiny coating is a perfect reflector ($\varepsilon_{\mathfrak{s}} = 0, \alpha_{\mathfrak{s}} = 0$),
3. the emissivity values are considered to be equal to the absorptivity values ($\varepsilon = \alpha$), i.e., Kirchhoff's hypothesis for enclosures with non-participating medium.

Note here that if the latter holds, the knowledge of the radiative properties of the black coating is not important, which seems fairly straightforward to conceived, because in such case, a black heat flux meter would not be needed to measure the convective heat flux.

Now, if only item (1.) holds, the convective component for both heat flux meters would be the same (cf. eqs. 2.12-2.13), and if in addition to this, item (3.) holds, the last term of equation 2.12 would be null and the convective heat flux would only depend on the emissivity values.

Moreover, for surfaces with radiative properties similar to the black heat flux meter, an expression for the radiative heat flux ($\varphi_{R_{\mathfrak{b}}}$), can be obtained using the previous results, where $\varphi_{R_{\mathfrak{b}}}$ will result by subtracting $\varphi_{C_{\mathfrak{b}}}$ from $\varphi_{\mathfrak{b}}$ (because $\varphi_{\mathfrak{b}}$ accounts for the entire radiative heat flux with respect to $\varphi_{\mathfrak{s}}$, which only accounts for a small part of it), yields:

$$\begin{aligned}\varphi_{R_{\mathfrak{b}}}(t) = &\left[\frac{\alpha_{\mathfrak{b}} \cdot \Delta T_{\mathfrak{s}}(t)}{\alpha_{\mathfrak{b}} \cdot \Delta T_{\mathfrak{s}}(t) - \alpha_{\mathfrak{s}} \cdot \Delta T_{\mathfrak{b}}(t)}\right] \cdot \varphi_{\mathfrak{b}}(t) - \left[\frac{\alpha_{\mathfrak{b}} \cdot \Delta T_{\mathfrak{b}}(t)}{\alpha_{\mathfrak{b}} \cdot \Delta T_{\mathfrak{s}}(t) - \alpha_{\mathfrak{s}} \cdot \Delta T_{\mathfrak{b}}(t)}\right] \cdot \varphi_{\mathfrak{s}}(t) \\ &+ \frac{\Delta T_{\mathfrak{b}}(t) \cdot \sigma \cdot \left[\alpha_{\mathfrak{b}} \cdot \varepsilon_{\mathfrak{s}} \cdot T_{\mathfrak{s}}^4(t) - \alpha_{\mathfrak{s}} \cdot \varepsilon_{\mathfrak{b}} \cdot T_{\mathfrak{b}}^4(t)\right]}{\alpha_{\mathfrak{b}} \cdot \Delta T_{\mathfrak{s}}(t) - \alpha_{\mathfrak{s}} \cdot \Delta T_{\mathfrak{b}}(t)} \qquad \left[\mathrm{W{\cdot}m^{-2}}\right]\end{aligned} \tag{2.14}$$

Note that from expression 2.14, if item (2.) holds, it might be assumed that the value of the net radiation heat flux $\varphi_{R_{\mathfrak{b}}}$ would depend on the radiative properties of the black coating. However, in such case, it can be shown that the knowledge of the radiative properties of the black coating becomes unnecessary. In turn, the value of the net radiative heat flux would depend on the value of $\Delta T_{\mathfrak{b}}$ and $\Delta T_{\mathfrak{s}}$, resulting in: $\varphi_{R_{\mathfrak{b}}} = \varphi_{\mathfrak{b}} - \frac{\Delta T_{\mathfrak{b}}}{\Delta T_{\mathfrak{s}}} \cdot \varphi_{\mathfrak{s}}$.

This last remark is worth mentioning, in regard of the assumption made by former researchers before the 21$^{\text{st}}$ century (cf. §1.4.2): the shiny and black sensors measure the convective and total heat flux, respectively, and the radiative heat flux will result from a simple subtraction of both measurements. This assumption is proven to be only plausible, when $\Delta T_{\mathfrak{b}}$ is equal to $\Delta T_{\mathfrak{s}}$ or, in other words, $T_{\mathfrak{b}}$ is equal to $T_{\mathfrak{s}}$. Note here that this last remark refers to the inquiry of whether the temperature of both black and shiny heat flux meters is the same or not, and not whether the temperatures of the interface "sensor's upper surface - air" and of the interface "sensor's lower surface - wall" are the same or not. The inquiry regarding the difference between these two temperatures is not treated here, as in [66],p.38 or in [63],p.297.

Furthermore, for surfaces with radiative properties which values lay between $\varepsilon_{\mathfrak{s}}$ and $\varepsilon_{\mathfrak{b}}$, an expression for the net radiative heat flux can be determined by $\varphi_{R_i} = \alpha_i \cdot I - \varepsilon_i \cdot \sigma \cdot T_{S_i}^4$, using expression 2.10.

2.3.1.1 Experimental-based simplifications

Given that, during our experimental study, the temperature ranges encountered within the indoor environment were entirely in typical room temperature ranges, and since the window shades were kept always closed, Kirchhoff's hypothesis was admitted and retained (cf. Table 2.5, hyp. n°1 and n°2).

Table 2.5: Hypotheses and assumptions for data processing

N°	Hypotheses/assumptions	Notation	Justification
1)	LWL dominates indoor radiant environment	$\Phi_{SWL} = 0$	Window shades closed
2)	Kirchhoff's hypothesis	$\alpha = \varepsilon$	Experimentation-based simplification
3)	Couple black-shiny has the same temperature	$T_{\mathfrak{b}} = T_{\mathfrak{s}}$	Experimentation (cf. Appendix A.2)
4)	Temperature of shiny sensor has the same as the surface i	$T_{\mathfrak{b}} = T_{\mathfrak{s}} = T_{S_i}$	Simplification

Results from measurement campaigns carried out previously, allow us to establish that the temperature difference between the shiny and black thermoelectric modules always lays in 0,175±0,075 °C ($T_{\mathfrak{s}} - T_{\mathfrak{b}} = 0{,}175 \pm 0{,}075$ °C), and since the absolute uncertainty in our temperature measurements lays around ±0,4 °C, it was concluded that no significant difference can be detected, and thus, both heat flux meters are considered to have the same temperature (cf. Table 2.5, hyp. n°3). Therefore, equations 2.10 and 2.11 can be simplified as follows:

$$I(t) = \frac{1}{\varepsilon_{\mathfrak{s}} - \varepsilon_{\mathfrak{b}}} \cdot \varphi_{\mathfrak{s}}(t) - \frac{1}{\varepsilon_{\mathfrak{s}} - \varepsilon_{\mathfrak{b}}} \cdot \varphi_{\mathfrak{b}}(t) + \frac{\sigma \cdot \left[\varepsilon_{\mathfrak{s}} \cdot T_{\mathfrak{s}}^4(t) - \varepsilon_{\mathfrak{b}} \cdot T_{\mathfrak{b}}^4(t)\right]}{\varepsilon_{\mathfrak{s}} - \varepsilon_{\mathfrak{b}}} \qquad \left[\mathrm{W{\cdot}m^{-2}}\right] \tag{2.15}$$

$$h_C(t) = \frac{\varepsilon_{\mathfrak{b}}}{\varepsilon_{\mathfrak{b}} - \varepsilon_{\mathfrak{s}}} \cdot \frac{\varphi_{\mathfrak{s}}(t)}{\Delta T_{\mathfrak{s}}(t)} - \frac{\varepsilon_{\mathfrak{s}}}{\varepsilon_{\mathfrak{b}} - \varepsilon_{\mathfrak{s}}} \cdot \frac{\varphi_{\mathfrak{b}}(t)}{\Delta T_{\mathfrak{s}}(t)} \qquad \left[\mathrm{W{\cdot}m^{-2}{\cdot}K^{-1}}\right]. \tag{2.16}$$

Note that in equation 2.15 the temperatures at the power of fourth have not been simplified, because their difference becomes important in this case (around 5%), as encountered when using experimental results for computing the total incident radiation. However, for equation 2.16 when using experimental results no significant difference were encountered whether or not the temperatures at the power of fourth are removed.

Thus, the convective and radiative heat fluxes (cf. eqs. 2.12-2.14), after considering the previous hypotheses, result in the following:

$$\varphi_{C_{\mathfrak{s}}}(t) = \varphi_{C_{\mathfrak{b}}}(t) = \varphi_C(t) = \frac{\varepsilon_{\mathfrak{s}}}{\varepsilon_{\mathfrak{s}} - \varepsilon_{\mathfrak{b}}} \cdot \varphi_{\mathfrak{b}}(t) - \frac{\varepsilon_{\mathfrak{b}}}{\varepsilon_{\mathfrak{s}} - \varepsilon_{\mathfrak{b}}} \cdot \varphi_{\mathfrak{s}}(t) \qquad \left[\mathrm{W{\cdot}m^{-2}}\right] \tag{2.17}$$

$$\varphi_{R_{\mathfrak{b}}}(t) = \frac{\varepsilon_{\mathfrak{b}}}{\varepsilon_{\mathfrak{b}} - \varepsilon_{\mathfrak{s}}} \cdot \varphi_{\mathfrak{b}}(t) - \frac{\varepsilon_{\mathfrak{b}}}{\varepsilon_{\mathfrak{b}} - \varepsilon_{\mathfrak{s}}} \cdot \varphi_{\mathfrak{s}}(t) \qquad \left[\mathrm{W{\cdot}m^{-2}}\right]. \tag{2.18}$$

Finally, an expression for the net radiative heat exchange on a given surface i with an emissivity

value between ε_b and ε_s, can be obtained using the following definition where $\varphi_{R_i}(t)$ is equal to $\alpha_i \cdot I(t)$ minus $\varepsilon_i \cdot \sigma \cdot T_i^4(t)$. This before, along with Kirchhoff's hypothesis, results in:

$$\varphi_{R_i}(t) = \varepsilon_i \cdot \left\{ \frac{1}{\varepsilon_\mathfrak{b} - \varepsilon_\mathfrak{s}} \cdot \varphi_\mathfrak{b}(t) - \frac{1}{\varepsilon_\mathfrak{b} - \varepsilon_\mathfrak{s}} \cdot \varphi_\mathfrak{s}(t) + \sigma \cdot \left[T_\mathfrak{s}^4(t) - T_i^4(t) \right] \right\} \qquad \left[\mathrm{W{\cdot}m^{-2}} \right]. \tag{2.19}$$

Note here that if the surface studied i were to have the same emissivity value of the black coating, expression 2.19 would become the same as expression 2.18. Moreover, these simplifications have reduced the number of instruments needed in our experiments, along with the budget for instrumentation: ten thermocouples type T and another acquisition card NI 9213 have been saved. Thus, it is recommended to perform preliminary experiments with few instruments regarding the simplifications presented, before going further.

2.3.1.2 Determination of the emissivity

A sensitivity analysis showed that the estimation of the convective (cf. eq. 2.17) and radiative (cf. eq. 2.18) heat fluxes is strongly influenced by the uncertainty in the emissivity values of the shiny coating. Thus, a precise determination of the emissivity is required, with an uncertainty value around or smaller than $1\text{x}10^{-2}$.

The emissivity values for the black and shiny coatings used here were determined by following the methodology recommended in the standard ISO 18434-1:2008(E) for emissivity measurements. The emissivity values obtained for the black ($\varepsilon_\mathfrak{b}$) and shiny ($\varepsilon_\mathfrak{s}$) coatings were 0,953±0,012 and 0,069±0,014, respectively [113]. The hypotheses considered were: (*a*) the emissivity of the crumpled aluminum foil is zero and (*b*) the temperature of the reference is the same as the temperature of the object studied; hypothesis (*a*) is justified by the fact that a crumpled aluminum foil can be considered as a perfect reflector; hypothesis (*b*) was retained for simplification issues.

2.3.2 Mean radiant temperature of surrounding surfaces

A well estimation of the mean radiant temperature T_{surr} is needed when analyzing net radiative heat exchanges in buildings. Therefore, another way to estimate this temperature is proposed here by using the heat flux measurements, instead of an infrared camera. An expression to estimate the mean radiant temperature in terms of heat flux measurements in a measurement zone can be derived by subtracting equations 1.19 and 1.20 and assuming the same convection part for both sensors, results in:

$$\varphi_\mathfrak{b}(t) - \varphi_\mathfrak{s}(t) = \varphi_{R_\mathfrak{b}}(t) - \varphi_{R_\mathfrak{s}}(t) \qquad \left[\mathrm{W{\cdot}m^{-2}} \right] \tag{2.20}$$

Now, having these small heat flux meters enclosed by a bigger environment and a non radiation influence medium in between. The net radiation heat transfer φ_R for each sensor can be estimated by following Kirchhoff's hypothesis, resulting in:

$$\varphi_\mathfrak{b}(t) - \varphi_\mathfrak{s}(t) = \varepsilon_\mathfrak{b} \cdot \sigma \cdot \left[T_{surr}^4(t) - T_\mathfrak{b}^4(t) \right] - \varepsilon_\mathfrak{s} \cdot \sigma \cdot \left[T_{surr}^4(t) - T_\mathfrak{s}^4(t) \right] \qquad \left[\mathrm{W{\cdot}m^{-2}} \right] \tag{2.21}$$

By equating the previous equation, we obtain the following for T_{surr}:

$$T_{surr}(t) = \sqrt[4]{\frac{\varphi_b(t) - \varphi_s(t)}{[\varepsilon_b - \varepsilon_s] \cdot \sigma} + \frac{\varepsilon_b \cdot T_b^4(t) - \varepsilon_s \cdot T_s^4(t)}{\varepsilon_b - \varepsilon_s}} \qquad [\mathrm{K}]\,. \tag{2.22}$$

Finally, considering hypothesis n^{o}4 in table 2.5 (where T_b is considered as same as T_s), the following expression for the mean radiant temperature is obtained:

$$T_{surr}(t) = \sqrt[4]{\frac{\varphi_b(t) - \varphi_s(t)}{[\varepsilon_b - \varepsilon_s] \cdot \sigma} + T_s^4(t)} \qquad [\mathrm{K}]\,. \tag{2.23}$$

Smoothing of experimental data

All experimental data collected have been smoothed before implementation in the analytical models for data processing. Since all experimental data is processed using the software R, the function *smooth.spline*, with default smoothing parameters, is employed.

2.4 Experimental plan implemented in the measurement campaigns

Since the objective of the experimental approach is to highlight and to understand the energy charge and discharge processes of the platform submitted to the outdoor thermal stresses in the summertime, the experimental plan for the measurement campaign in 2016, consisted of the following points:

- All data from the instruments described before in §2.2.2, except for the IR camera, were set to be collected continuously at a sample time of one minute, regarding the acquisition systems limits in handling a significant amount of instruments and the time response of the sensors. This corresponds to a total of 63 observations registered each minute: 30 heat flux meters, 21 thermocouples for surface temperature, two anemometers, and ten thermocouples for air temperature. The data from the IR camera was set to be collected at a sample time of 30 minutes, regarding the computer storage limit.
- The solar shades were kept permanently closed during the entire measurement campaign, to filter the most of the solar radiation. The natural ventilation openings were programmed with the home automation system, by following the flowchart presented in figure 2.23: the openings will open when the indoor air temperature T_{ia} is higher than the outdoor air temperature T_{oa} and will close otherwise and when is raining. Only the openings at the South facade and shed-roof were functional, due to technical problems; the openings at the north facade have remained closed.
- The platform was unoccupied during the entire measurement campaign, and the lights remained turned off. On the contrary, two computers remained operational: one for data collection and one for controlling the platform home automation system.
- Since the inside of the platform is divided into four zones (the living room, bedroom, bathroom, and toilet), all doors dividing these zones were kept open, with the intention of mixing the air of all four zones.

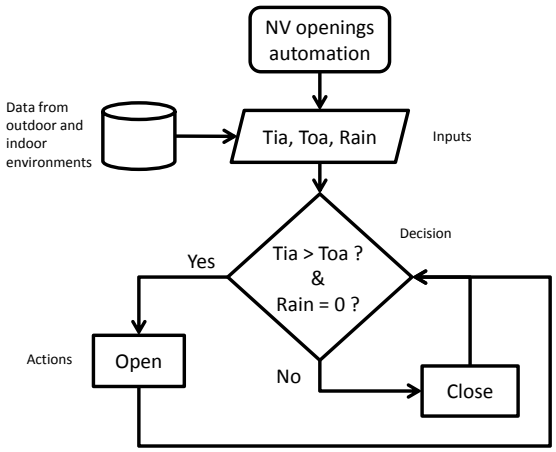

Figure 2.23: Flowchart of the automation strategy for the natural ventilation openings during the measurement campaign in 2016.

Another measurement campaign was performed in the summertime of 2017, in which the natural ventilation openings were programmed to implementing other configurations of the natural ventilation openings, where they were kept always opened and always closed during a short period. All measurement campaigns carried out during the summertime of 2016 and 2017 are summarized in table 2.6. It is worth mentioning that this experimental plan was also implemented in other measurement campaign carried out in the summertime in 2015. However, the data collected had only served for a qualitative study of the thermal behavior of the platform and the heat exchanges on the floor surface.

Table 2.6: Configurations of the openings on each measurement campaign in summertime.

		Openings configurations						
			Diurnal ($T_{ia} < T_{oa}$)			Nocturnal ($T_{ia} > T_{oa}$)		
	Dates	Duration	North	South	Shed-roof	North	South	Shed-roof
N°1)	23/5/17, 12/9 - 17/9 0h00 - 0h00	4 d	Closed	Closed	Closed	Closed	Closed	Closed
N°2)	27/7 - 12/9/16 0h00 - 0h00	35 d	Closed	Closed	Closed	Closed	Opened	Opened
N°3)	25/5 - 29/5/17 0h00 - 0h00	4 d	Closed	Opened	Opened	Closed	Opened	Opened

2.5 Results and discussion on the coupling between the energy charge-discharge and natural ventilation

2.5.1 Classification of the experimental data

The data collected from the measurement campaign in 2016 will be classified to analyze the thermal behavior of the indoor environment of the platform under different meteorological conditions. This classification organizes the ongoing meteorological conditions in terms of wind (windy and no-windy), and in terms of the sky state (clear and cloudy), in two distinguishable periods: when natural ventilation

openings are opened, which happened mostly during nighttime, and when natural ventilation openings remained closed, which happened mainly during the daytime. Most days have presented no-windy nighttime, as expected for summer periods. Various days had similar meteorological conditions; these days were grouped, for no windy nighttime, as follows:

- July 28th and 29th, with a cloudy and windy daytime, and a clear and no-windy nighttime.
- August 15th and 16th, with a sunny and windy daytime, and a cloudy and no-windy nighttime.
- August 19th and 20th, with a cloudy and windy daytime, and a cloudy and no-windy nighttime.
- August 22nd and 23rd, with a sunny and windy daytime, and a clear and no-windy nighttime.

and for windy nighttime:

- July 27th and August 17th, with a cloudy and windy daytime, and a cloudy and windy nighttime.
- August 26th and September 8th, with a cloudy and no windy and windy daytime, respectively, and a clear and windy nighttime.

Therefore, since eight days presented no-windy nighttime and only four presented windy nighttime, two days of each group will be chosen for further analysis. The most reasonable pair of days are those that presented typical summer weather conditions: sunny days and clear nights. On the other hand, the entire data collected from the measurement campaigns in 2017 will be used for the analysis, since it comprised a short period.

2.5.2 Thermal behavior of the platform under different opening configurations and outdoor conditions

Before going further in the analysis of the experimental results, the thermal behavior of the platform, under different meteorological conditions during the measurement campaigns, is presented and analyzed first, for the configurations presented in table 2.6. Figures 2.24 to 2.26, show the indoor temperatures and weather results for configurations n°1, n°2, and n°3, respectively.

Figure 2.24 shows the indoor temperatures and weather results for configuration n°1, which comprises May 23rd, September 12nd, and September 15th to 16th. Figures 2.25 shows the indoor temperatures and weather results for configuration n°2, in which, only two days with no windy nights (August 22nd and 23rd), and two days with windy nights (August 26th and September 8th) are presented. Figures 2.26 shows the indoor temperatures and weather results for configuration n°3 from May 25th to May 28th. The outdoor air temperature and solar radiation presented typical summertime values as expected. Wind speed and wind direction presented anticyclonic behavior and weak values, as also expected for this season.

Different behaviors of the indoor environment can be observed for each configuration. For instance, the lower day-night maximum indoor temperature gap is encountered for configuration n°1 (cf. fig. 2.24), which is also reasonable since both environments are, in principle, not allowed to interact with each other. Conversely, the higher day-night maximum indoor temperature gap is encountered during configuration n°3 (cf. fig. 2.26), which is reasonable since the indoor environment is permitted to interact the most with the outdoor environment.

Moreover, the mean radiant temperature (mean temperature of surrounding surfaces) appears to be very close to the indoor air temperature, which suggests that the LWL radiation heat transfer is weak

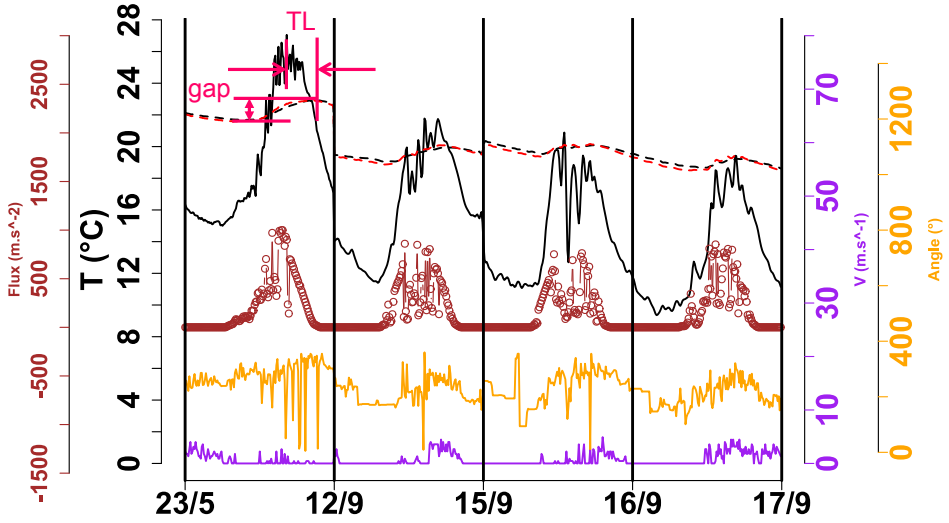

Figure 2.24: For config. n°1: Outdoor temperature (black solid line, left axis), indoor temperature (black dashed line, left axis), mean radiant temperature (red dashed line, left axis), wind direction (yellow, right axis), wind speed (purple, right axis), direct solar radiation (brown circles, left axis). Moments where openings remained opened (gray zones).

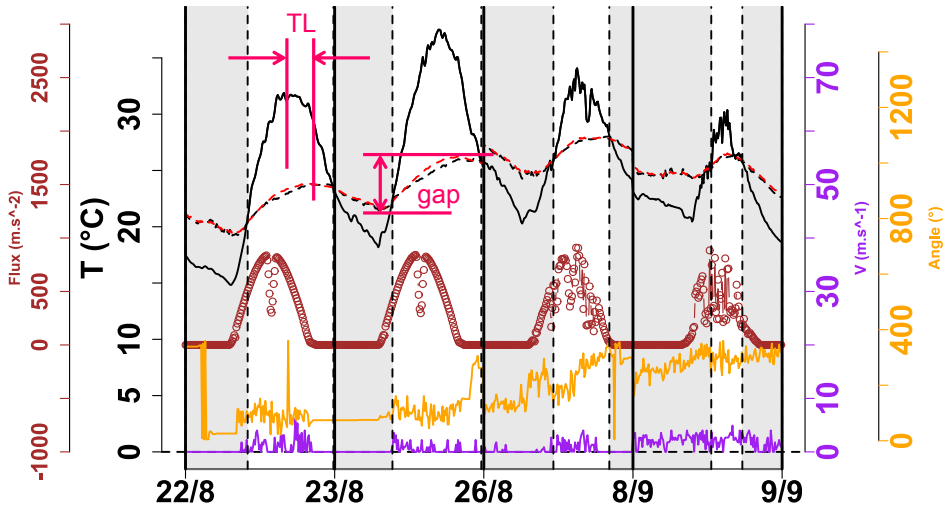

Figure 2.25: For config. n°2: Outdoor temperature (black solid line, left axis), indoor temperature (black dashed line, left axis), mean radiant temperature (red dashed line, left axis), wind direction (yellow, right axis), wind speed (purple, right axis), direct solar radiation (brown circles, left axis). Moments where openings remained opened (gray zones).

in the indoor environment. Depending on the configuration, the mean radiant temperature appears to be slightly higher or slightly lower than the indoor air temperature as follows:

- In configuration n°1, the indoor air is hotter than the surrounding surfaces during nighttime (cf. fig. 2.24); the opposite is encountered during the daytime.
- In configuration n°2, the indoor air appear to be slightly colder than the surrounding surfaces during nighttime, as expected; during the daytime, the indoor air is hotter than the surrounding

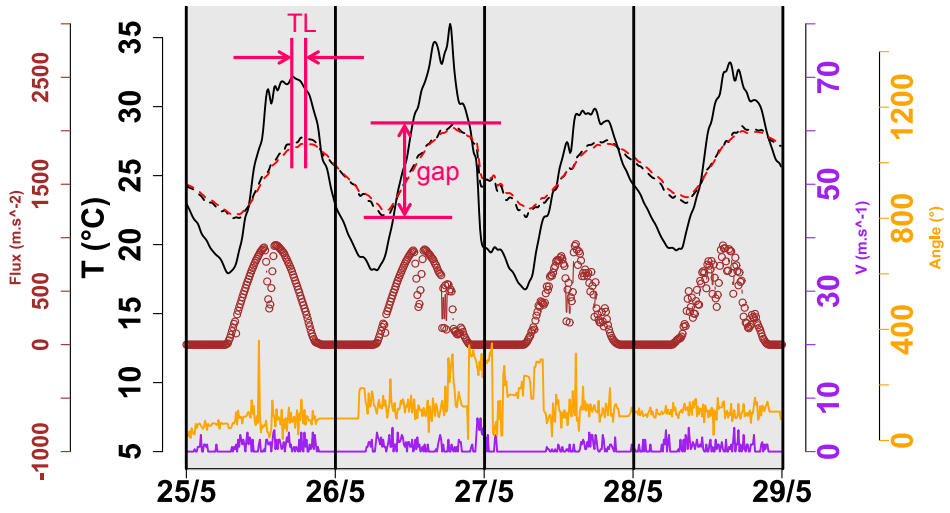

Figure 2.26: For config. n°3: Outdoor temperature (black solid line, left axis), indoor temperature (black dashed line, left axis), mean radiant temperature (red dashed line, left axis), wind direction (yellow, right axis), wind speed (purple, right axis), direct solar radiation (brown circles, left axis). Moments where openings remained opened (gray zones).

surfaces, as in agreement with configuration n°1 for this period (cf. fig. 2.25).

- In configuration n°3, the indoor air is slightly colder than the surrounding surfaces during nighttime, which agrees with what has been encountered for configuration n°2; the opposite is encountered during the daytime, as expected since the openings remained open (cf. fig. 2.26).

These last three remarks are rendered moot when accounting for the uncertainties of our instruments in the temperature measurement since both temperatures became indistinguishable. In other words, the difference between the temperature of the indoor air and surrounding surfaces lays within the uncertainty interval of the instruments employed. Nevertheless, these remarks are worth mentioning since the results encountered agree with the expected behavior of both temperatures for each configuration.

Regarding the thermal inertia of the platform, the indoor environment presents a higher thermal lag TL (or temporal phase shift) with respect to the outdoor air temperature during the daytime in increasing order as follows: configurations n°2, n°1 and n°3. This behavior can be simply explained by the fact that the platform attenuates the outdoor thermal stresses when the openings and solar shades are closed (config. n°1), and the platform attenuates them the most, when its indoor environment is cooldown the night before (config. n°2). As the openings remained open during the day for configuration n°3, the indoor environment of the platform opposes the least to the outdoor thermal stresses. On the other hand, during nighttime the platform presents a thermal lag (TL) in decreasing order as follows: n°1, and n°2/n°3 with slightly the same values, which is also expected.

In summary:
The previous analysis highlights the effects of the coupling between natural ventilation and the energy charge-discharge process by focusing only on the outdoor and indoor environments temperatures.

2.5.3 Coupling of the charge-discharge process with natural ventilation within the indoor environment

Now let us focus on the charge-discharge process in the indoor environment (thermal mass domain). The first evidence of the coupling is merely qualitative, and it can be observed at a glance since the behavior of the convective heat flux on each surface (floor and ceiling) is different depending on which opening configuration is being implemented. Here, we speak about the convective heat flux, because it is directly related to the energy flow caused by air movement.

In order to verify that the changes in the behavior of the convective heat flux are caused by the opening and closing of the natural ventilation openings, we take the behavior encountered in config. n°1 as a reference since the openings remained close. In this way, when the convective heat flux reaches significant values (with respect to config. n°1), it will be considered directly as a consequence of natural ventilation, and thus, highlighting the coupling between the latter and the charge-discharge process in the form of convection. This charge-discharge process is analyzed individually by focusing first on the convective heat flux, and after on the radiative heat flux. Also, sometimes its more accessible to referrer to these processes as charge and discharge period, and thus, the reader is wanted to note that both terms will be used interchangeably.

2.5.3.1 Charge and discharge by convection

The results of the convective heat flux and the corresponding air-surface temperatures for configurations n°1, n°2, n°3 are presented in figures 2.27-2.32. For visual purposes, the uncertainties are only presented for convective heat flux, since the temperature range is very narrow. Also, for the graphics where heat fluxes are presented, a horizontal dashed line will be drawn on zero to well separate the charge period, i.e., positive values (mostly during the daytime), and the discharge period, i.e., negative values (mostly during nighttime). These positive or negative values can also be regarded as if the heat flux is entering or leaving the surface, respectively.

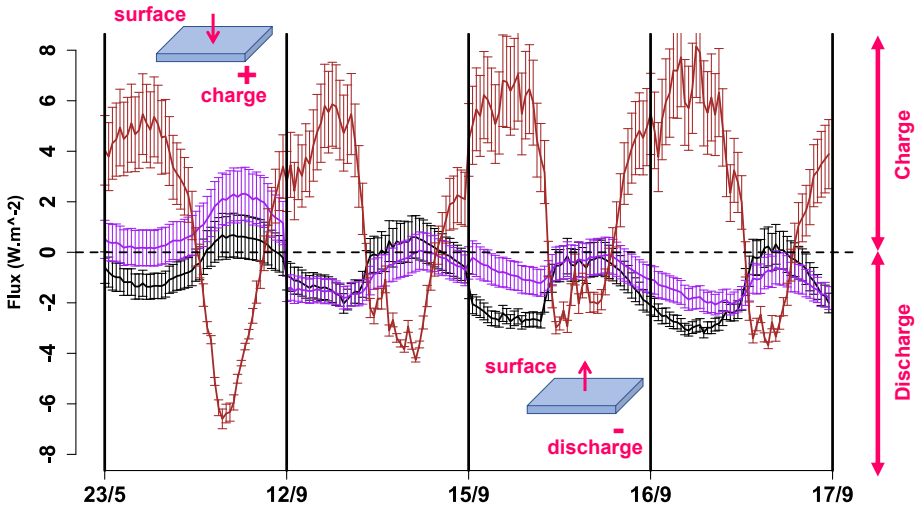

Figure 2.27: For config. n°1: Convective heat flux for the floor (black line), the ceiling (purple line), and for the glazed-facade (brown line). Moments where openings remained opened (gray zones).

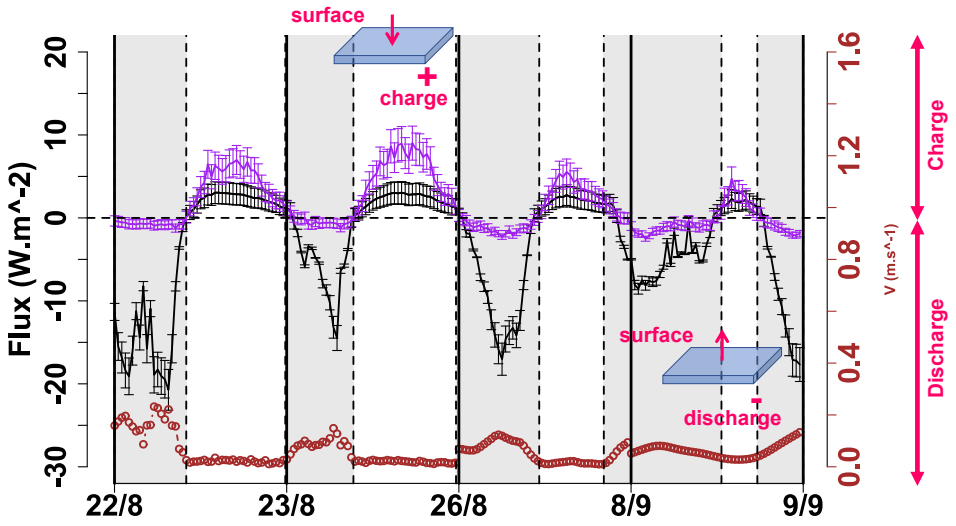

Figure 2.28: For config. n°2: Convective heat flux for the floor (black line), and the ceiling (purple line). Moments where openings remained opened (gray zones).

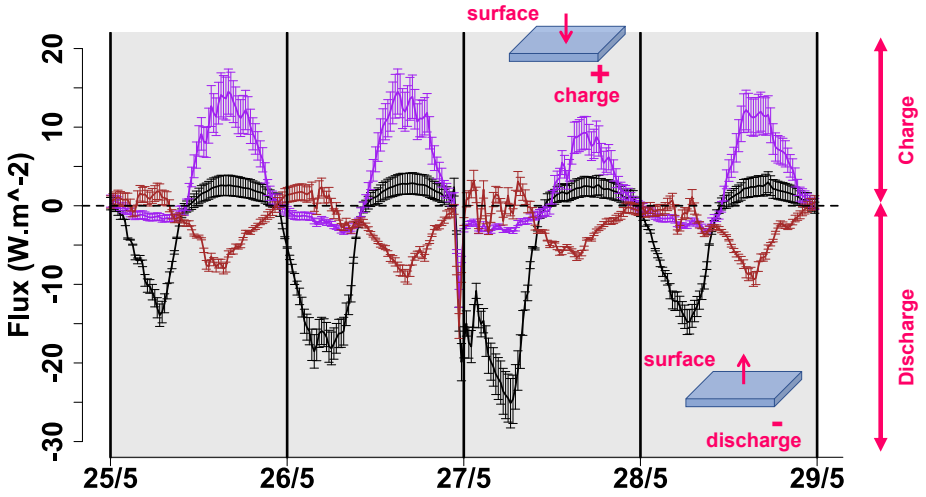

Figure 2.29: For config. n°3: Convective heat flux for the floor (black line), the ceiling (purple line), and for the glazed-facade (brown line). Moments where openings remained opened (gray zones).

Note that, as a convective heat flux presenting positive values indicates that the surface is being charged, this also indicates that the air near this surface is experimenting a "discharging." Conversely, if the heat flux presents negative values (indicating that the surface is being discharged), the air near this surface is experimenting a "charging." With this in mind, during the charge period, the behavior observed in figures 2.27 and 2.29 indicates that the glazed-facade (brown line) contributes the most to the charging of the indoor air (by convection). On the other hand, in figures 2.27, 2.28 and 2.29, the behavior of both the floor (black line) and ceiling (purple line), during the charge period, indicates that they contribute to discharging the indoor air, while these two surfaces are being charged. This statement only appears to apply to the first day (23/5) in config. n°1, as expected, due to the outdoor conditions of the following days (cf. fig. 2.24).

During the discharge period, the behavior of the convective heat flux at each surface indicates that their role in the charge-discharge has changed. The glazed-facade (brown line) contributes to the discharging of the indoor air, while the floor (black line) contributes to its charging. The magnitudes of the convective heat flux encountered, when the openings remained open (gray zones), at the floor surface (cf. figs. 2.28 and 2.29), with respect to the magnitude encountered for this surface when the openings remained close (cf. fig. 2.27), clearly indicate that the increment is caused by the opening of the openings, and thus, a consequence of natural ventilation. Moreover, the heat flux at the ceiling surface (purple line) appears to not have a significant contribution neither to the charging nor the discharging of the indoor air during the discharge period, regardless of the opening configuration implemented (cf. fig. 2.29).

It seems that the magnitude of the convective heat flux on the floor surface is significantly higher when the openings were kept open (cf. fig. 2.28, gray zones), than when they were kept closed. The same can be said for the airspeed measurements (brown circled lines). On the other hand, the magnitude of the convective heat flux on the ceiling surface appears to be significantly lower (almost null) when the openings were kept opened than when they were kept closed (white zones). This can be explained by the fact that when the openings remained open (mostly in nighttime), the outdoor air temperature was lower than the indoor air (cf. fig. 2.24). And since cold air is denser than warm air, outdoor air was entering at the lower part of the platform through the lower openings, and thus air currents near the floor surface is stronger. It will be shown later, that this is an essential result regarding the nature and modeling of the convective heat transfer coefficient on both surfaces. The values and signs adopted by the convective heat flux on both surfaces imply that, during nighttime, the floor is vigorously discharged, while the ceiling presents a weak discharge or none at all.

Regarding the temperatures, it can be observed from figures 2.30 and 2.32 that the glazed-facade surface (brown line) always presents the highest temperature of these three surfaces and its behavior appears to be synchronized with the behavior of the outdoor air temperature (no temporal phase shift appears to be present between them). This is expected since the glazed-facade has a weak heat capacity, and might suggest that the influence of direct solar radiation, in the heating of this surface, can be neglected.

Finally, it can be observe that when the heat flux at the glazed-facade is positive, i.e., a heat flux entering this surface (cf. fig. 2.27, brown solid line), its temperature (cf. fig. 2.30, brown line) appears to be lower than the near air, which air temperature is measured at 0,1 m (cf. fig. 2.30, brown circles). This indicates that the air near the surface is charging it. This last remark is worth mentioning, since this behavior, as logic as it may seem, was encountered to correspond only between the temperatures of the surface and the air at 0,1 m, but not between this surface and the air temperature measured at 1,70 m (black dashed line). For instance, consider the first day (22/8) for configuration n°2 in figure 2.28, and the first day (25/5) for configuration n°3 in figure 2.27, and let us concentrate on the convective heat flux at the floor surface (black line): at 0,10 m the exact moment when the heat flux changes from positive to negative values, the air temperature (cf. figs. 2.31 and 2.32, black circles) goes from being higher than the surface temperature (black solid line) to being lower. It can be observed that this does not apply if we perform the same exercise with the air temperature at 1,70 m.

About this last remark, a temperature measurement was performed (after the measurement cam-

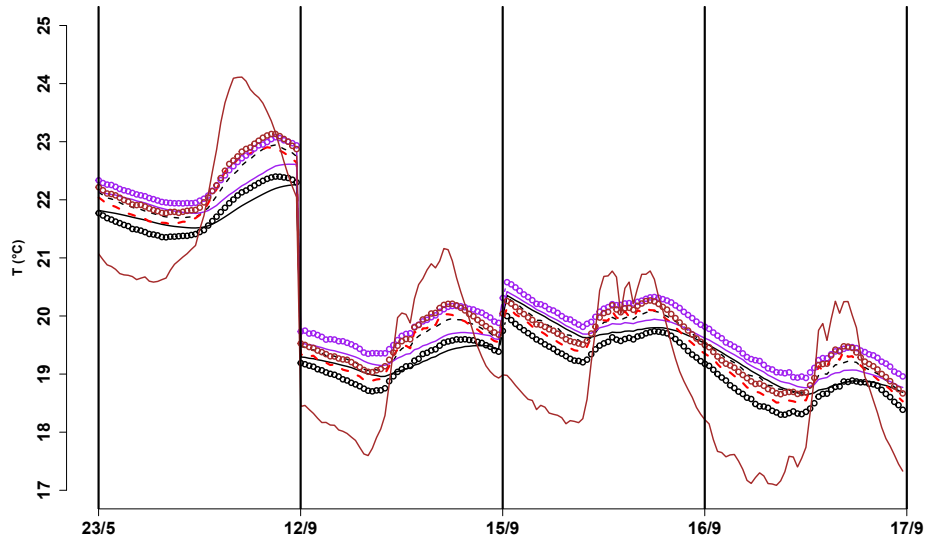

Figure 2.30: For config. n°1. Air temperatures (lines with small circles) measured at the: floor (black), ceiling (purple), and glazed-facade (brown). Indoor air (black dashed line) and mean radiant temperature (red dashed line). Surface temperatures (solid lines) measured at the: floor (black), ceiling (purple), and glazed-facade (brown). Moments where openings remained opened (gray zones).

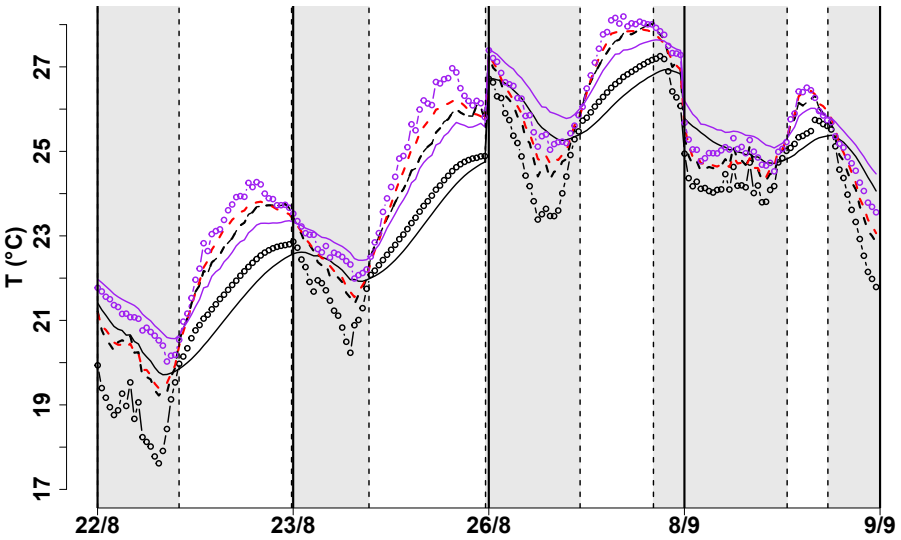

Figure 2.31: For config. n°2. Air temperatures (lines with small circles) measured at the: floor (black), and ceiling (purple). Indoor air (black dashed line) and mean radiant temperature (red dashed line). Surface temperatures (solid lines) measured at the: floor (black), and ceiling (purple). Moments where openings remained opened (gray zones).

paigns) at 0,02 m from the floor. This measurement presented lower values than the temperature measured at 0,10 m during nighttime. This before highlights the influence of the vertical thermal stratification of the indoor air, and also, that at the height of 0,10 m is the better location for measuring the air-surface temperature that better corresponds to the behavior of the convective heat flux.

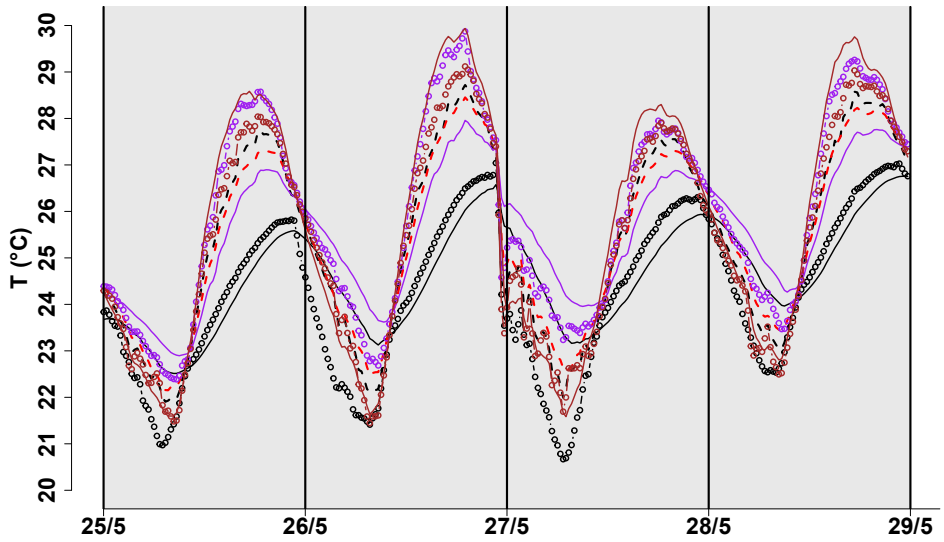

Figure 2.32: For config. n°3. Air temperatures (lines with small circles) measured at the: floor (black), ceiling (purple), and glazed-facade (brown). Indoor air (black dashed line) and mean radiant temperature (red dashed line). Surface temperatures (solid lines) measured at the: floor (black), ceiling (purple), and glazed-facade (brown). Moments where openings remained opened (gray zones).

2.5.3.2 Charge and discharge by radiation

The results of the radiative heat flux for configurations n°1, n°2, and n°3 are presented in figures 2.33-2.35, respectively. During the charge period, the radiative heat flux at the glazed-facade surface (brown line) also presents an opposite behavior, with respect to the other surfaces (cf. figs. 2.33 and 2.35), as seen earlier for the convective heat flux. Note that the magnitude and behavior of the convective and radiative heat fluxes at the glazed-facade surface appear to have the same values.

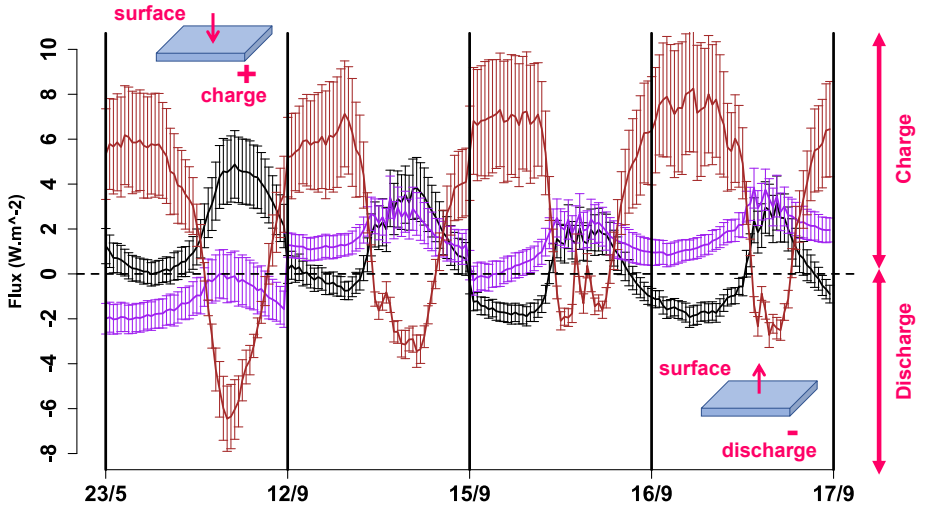

Figure 2.33: For config. n°1: Radiative heat flux for the floor (black line), the ceiling (purple line), and for the glazed-facade (brown line). Moments where openings remained opened (gray zones).

On the other hand, during the charge period, the radiative heat flux at the ceiling surface (purple line)

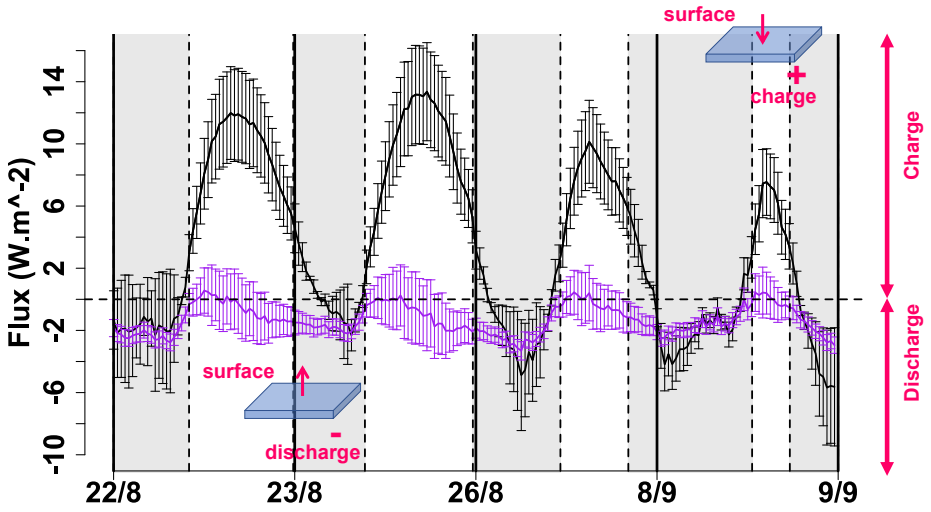

Figure 2.34: For config. n°2: Radiative heat flux for the floor (black line), and the ceiling (purple line). Moments where openings remained opened (gray zones).

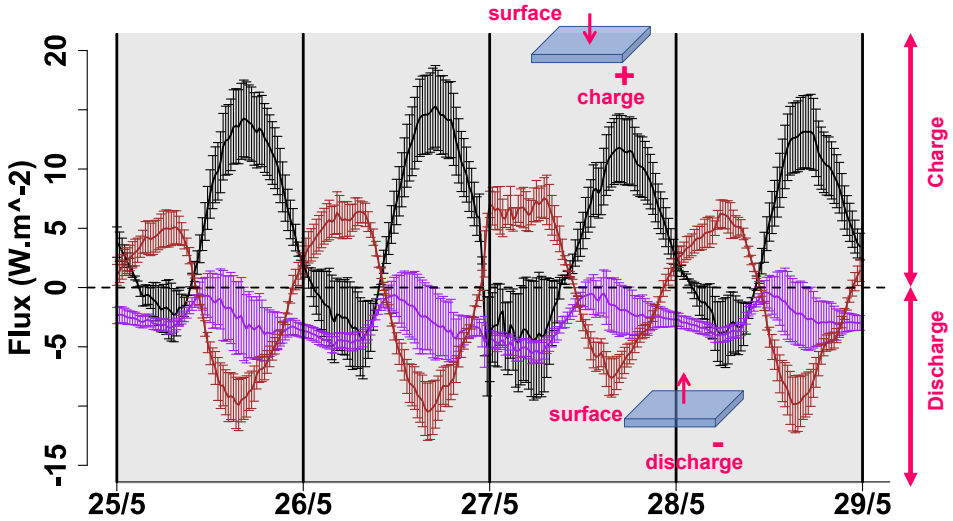

Figure 2.35: For config. n°3: Radiative heat flux for the floor (black line), the ceiling (purple line), and for the glazed-facade (brown line). Moments where openings remained opened (gray zones).

appears to be weak, with negative values, in comparison with the other surfaces. This might imply that the surrounding surfaces (as viewed from the ceiling: floor, glazed-facade, internal partitions, among others) are always at a temperature slightly lower than the ceiling surface. However, figures 2.30 and 2.32 show that the glazed-facade always presents higher temperatures than the ceiling, and the floor surface always presents a lower temperature. It can be inferred from this, that the radiative heat flux responds to a mean temperature of the surrounding surfaces (also depending on the corresponding view factors), as expected. Moreover, the radiative heat flux at the floor surface (black line) presents the largest values, during this period. This implies that the floor surface is the coldest surface, and thus, all surrounding surfaces are discharged towards it; indicating that the floor helps to attenuate the temperature rise of the other elements of the envelope.

During the discharge period, comparing figures 2.34 and 2.35 with 2.33, there appear to be no significant changes in the radiative heat flux between configurations n°1, n°2 and n°3, and therefore, the opening and closing of the natural ventilation openings do not seem to have a direct and explicit effect on the radiative environment. However, it is clear that if the floor surface has been cool down the night before (by leaving the openings opened), this surface will experience a stronger charging by radiation the following day, than if it was not cooled down the night before. This seems fairly straightforward to conceive since the concrete slab might be able to bear stronger heat loads the next daytime if it is cooling down enough the night before.

In summary:
The coupling between the charge-discharge and natural ventilation has been qualitatively highlighted by the behavior of the convective heat flux at each surface, for configuration. From the previous analysis it can be infer the following:

- The floor and ceiling play an essential role in the attenuation of the rising of the indoor air temperature, while the glazed-facade contributes the most to the heating of the indoor air.
- The role of the elements of the envelope appears to change places, depending on the periods of charge and discharge.
- The floor surface plays an essential role in the attenuation of the temperature rising of the elements of the envelope, since the latter discharge by radiation towards the floor.
- The opening and closing of the natural ventilation openings do not seem to have a direct effect on the radiative environment, since no changes in the radiative heat flux.

2.6 Characterization of the energy charge and discharge processes

The characterization of both energy charge and discharge processes aims to describe and determine the heat transfer phenomena involved in each process. This characterization will permit a full knowledge of the thermal behavior of the platform, which will ultimately, lead to construct a physical model that only considers the key parameters for the forecasting of the behavior of the indoor environment.

2.6.1 Impact of the outdoor environment upon the indoor environment via correlation analysis

To complement the characterization of both, the energy charge and discharge processes, we analyze the correlation between the data collected from the outdoor and indoor environments, to determine the relevance (or impact or influence) of the former over the latter via correlation analyses. Such analysis will allow us later in the modeling, whether to consider or not some parameters, for instance:

- Does the solar radiation reaching the platform indoor environment have a significant impact?
- Can the effect of solar radiation be neglected when modeling the heat transfer in the floor concrete-slab?

2.6.1.1 Data collection and sample rate

During the measurement campaign (34 days in the summertime), data were collected from the indoor environment (including the outdoor temperature) at a sample rate of an observation every one minute, equivalent to 1440 observations per day. From the outdoor environment, data were collected at a sample rate of an observation every ten minutes, equivalent to 144 observations per day. Here, a reduction for the indoor environment data was performed to be match with the outdoor environment sample rate: only 144 observations per day will be used for the indoor environment data.

2.6.1.2 Correlation analysis

A correlation analysis based on the Pearson correlation coefficient R was implemented to evaluate how strong is the relationship between indoor and outdoor variables, and also to understand better the coupling between the heat transfer and airflow effects in the platform.

Since the implementation of a correlation analysis of such physical problem via only the correlation coefficient may lead to subjective inferences, the statistical significance of the relationships between to variables is further analyzed using other approaches concerning its interpretation. To do this, we have implemented the following three approaches as presented in [90]:

1. The verification of the null and alternative hypothesis state via the $p\text{-}value$ (we will assume 0,95 as confidence level).
2. The explained variability of the data via the squared value of the Pearson's correlation coefficient R (R^2).
3. The visual trend that verifies the linear or curvilinear relationship via scattering plots.

Regarding the first approach (1.), the null hypothesis states, as default, that there is no significant relationship between the two variables studied (a $p\text{-}value$ greater than or equal to 0,05). Once the $p\text{-}value$ of the supposed correlated data is determined, if its value lays under 0,05, it is said that the null hypothesis is rejected and the alternative hypothesis holds: there is a significant correlation between the two variables studied.

Regarding the second approach (2.), as stated in [90], the value of R^2 indicates the percentage of the variability that can be explained by the knowledge of the correlated variables.

Regarding the third approach (3.), the visualization of the two correlated variables will verify their relationship subjected by R. In the case where values near zero are encountered (indicating no linear relationship exists), the visual trend can help us to determine whether to accept the "no correlation" implied by the value of or to consider the determination of another correlation coefficient that allows evaluating the strength in the trend encountered.

Finally, regarding this third approach, the Spearman's coefficient (or Spearman's rank-order correlation coefficient) will be determined, since it allows evaluating monotonic relationships. In such relationships, the variables tend to change together, but not necessarily at a constant rate. It is worth mentioning that it is possible to meet a situation where Pearson's coefficient is negative while Spearman's coefficient is positive or vice versa, which might lead to infer that such situation is an inconsistency. However, with a logical understanding of the difference between these two coefficients, such

"inconsistencies" are justified [46].

In addition to correlation plots, to present the results with Spearman's coefficient, we use correlation matrices using the software **R**, as they allow us to group the three approaches mentioned earlier.

2.6.1.3 Distinguishing strong from weak correlations

Here, we establish a threshold for the value of R that could help us to distinguish, as unbiased as possible, strong from weak correlations. This threshold is chosen based on the statistical interpretation of R^2, described earlier in §2.6.1.2.

As a value of R^2 greater than 0,51 indicates that the 51% of the variability of variable A is explained by a variable B, we extend this to the following: the variable B can explain the variability of variable A at least 51% of the times, which represents the majority. Thus, the threshold value for R results in 0,71 (the squared root of 0,51).

Then, a correlation will be classified as strong if the R value is greater than 0,71, and as weak if the R value is lower or equal to 0,71. Similar threshold or critical values were proposed by Cohen in 1988, as encountered in [81].

2.6.1.4 Day/nighttime criteria for data sorting

As the aspects we wish to analyze here are the impacts of external sources on the indoor environment and the impact of the night natural ventilation strategy implemented, the experimental data collected will be analyzed separately in the daytime and nighttime. To do this, we have sorted the data using the following criteria:

- Nighttime: Solar radiation $= 0$ & indoor-outdoor temperature difference > 0.
- Daytime: Solar radiation $\neq 0$ & indoor-outdoor temperature difference < 0.

Here, we have included the condition of the temperature difference, only for configuration n°2.

2.6.1.5 Classification of the correlation results as strong or weak

The results from the meteorological station have shown that the majority of days presented cloudy and windy daytime conditions, and clear and no-windy nighttime conditions. Nevertheless, first, we decided to apply the statistical approach to days with similar meteorological conditions: sunny and windy daytime and no-windy nighttime (August 15th, 16th, 22nd, and 23rd); a total sample size of 576: corresponding to 144 observations in four days. The correlation analysis results based on the Pearson's coefficient, are presented in figures 2.36 and 2.37, for no-windy nighttime (sample size of 196), and sunny and windy daytime (sample size of 271), respectively, using the criteria presented in §2.6.1.4. The missing 109 observations laid outside the day/nighttime criteria established.

The variables presented in figure 2.36 and 2.37 are: temperature of the (a) outdoor air, (b) indoor air, (c) floor surface, (d) ceiling surface, (e) averaged of surrounding surfaces and (f) air near floor surface. Also, the temperature difference between (g) the indoor and outdoor air, and (h) the air near the floor and the floor surface. The airspeed at (i) the location where the indoor air temperature was measured

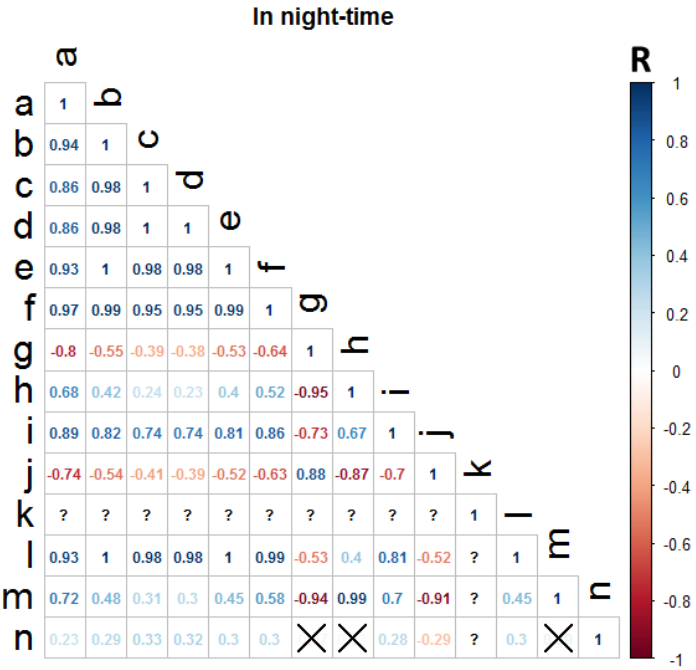

Figure 2.36: Correlation plot based on the Pearson coefficient for experimental results from no-windy nighttime: the sample size resulted in 196.

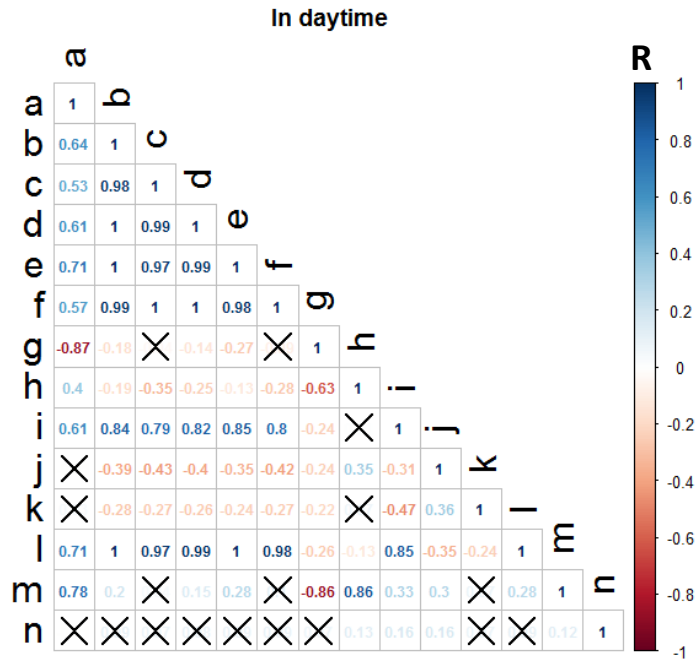

Figure 2.37: Correlation plot based on the Pearson coefficient for experimental results from windy and sunny daytime: the sample size resulted in 271.

and (j) near the floor. Additionally, the following heat fluxes: (k) outdoor direct solar radiation, (l) incident radiation on the floor surface, and (m) convection. And finally, (n) the external wind speed.

To read these graphs, we can assign to each segment (frames containing numbers) a pair of variables: (vertical-axis variable, "stairs"-axis variable). For example, in figure 2.37, the Pearson's coefficient

between indoor and outdoor air temperatures is the cross value between letter "b" in the vertical axis the letter "a" in the "stairs" axis, namely $R = 0{,}64$. Additionally, segments presenting an "X" indicates no significant statistical correlation, since the computed $p\text{-}values$ resulted in being greater than 0,05.

Before going further, to evaluate if the proposed correlation analysis can be considered as acceptable or not, it is applied to correlate variables that normally, in agreement with the physical laws, should present strong correlations coefficients. For instance, consider the convective heat flux (m) and the temperature difference between the air near the floor surface and the floor surface (h). Since these variables are known to be directly related, as stated by Fourier's law of convection, a strong R value should be expected; this can be observed in segment (m,h) in figures 2.36 and 2.37, which R values are 0,99 and 0,86. These values indicate that the correlation between m and h are both strong ($R > 0{,}71$) and positively correlated, as expected.

The difference in the previous R values for each period (daytime and nighttime), can be explained by the fact that convective heat flux values are stronger when the openings are opened than when they are closed. Another fair and obvious example can be the solar radiation heat flux (k) during nighttime. Since this variable usually is zero during this period, no correlation whatsoever should be encountered between this and other variables; this can be observed in figure 2.36, of which every R value related to the variable k resulted in a question mark (?) (in other words: "NA").

Moreover, other fair example, not as obvious as those presented before, is that all the temperatures from the indoor environment (b,c,d,e,f) should present strong correlations between one-another all the time. This can be observed in both figures 2.36 and 2.37, as expected. From those above, the statistical method proposed here, a priori, seems to be a reliable method to evaluate the strengths of correlated variables.

2.6.1.6 Correlation between the outdoor and indoor environments

The variables from the outdoor environment selected for the correlation analysis are the following: the air temperature (a), the direct solar radiation (k), and the wind speed (n). To evaluate the influence that these three variables have on the indoor environment, we choose the following variables for the indoor environment: the air temperature (b), the floor surface temperature (c), the total incident radiation on the floor surface (l), and the airspeed (i) and (j). In this way, we can evaluate, specifically, the contribution of the direct solar radiation to the thermal behavior of the floor surface temperature, and also the contribution of the wind speed to the air movement inside the platform.

First, from the variables mentioned here before we depurate by focusing on the R values greater than 0,71, and the "X" presented in both figures 2.36 and 2.37. Every segment presenting an R value lower or equal to 0,71 and an "X," is eliminated from the analysis. This allows us to obtain the relevant variables and to consider the third approach mentioned in §2.6.1.2, using correlation matrices with the Spearman's coefficient (cf. figs. 2.38 and 2.39). The correlation matrices include the following:

- The graphs of each pair of correlated variables, as well as their magnitudes (visual trends),
- the distribution of each corresponding sample (represented by histograms),
- The statistical significance due to the $p\text{-}value$ with red asterisks; where three asterisks ($***$) indicate that the $p\text{-}value$ is very close to zero, two asterisks ($**$) that are very close to 0,001, and

one asterisk (∗) that is very close to 0,01. A point (.) indicates that the *p-value* is very close to 0,1, and nothing ( ) indicates that is very close to 1.

The interest in using Spearman's coefficient is for comparison purposes as the Pearson's coefficient are already presented before. This type of graph (refer to Figs. 6 and 2.39) can be read in the same way as figures 2.36 and 2.37, but here the correlation coefficients of two correlated variables are presented above the diagonal with histograms; under this diagonal are the scatter plots of those variables showing their trend.

2.6.1.7 Wind speed and indoor air movements

In figures 2.38 and 2.39, for the wind speed (variable n), it is clear that there is no strong correlation presented between variable n and those representing the air movement in the indoor environment (i and j). This is fairly expected for the nighttime period (cf. fig. 2.38) since they presented no-windy conditions. In daytime (cf. fig. 2.39), the weak correlations encountered between variables n, i and j, might be explained by the fact that the openings remained closed; as a consequence, the air infiltrations are minimal. It is worth mentioning that for a no-windy nighttime, thermal buoyancy dominates the ventilation airflow in the platform.

Therefore, it can be inferred that the air movements in the indoor environment may be strongly correlated with a specific temperature difference. In this matter, figure 2.38 shows that there are strong correlations between the air movements (i and j), and the temperature differences: g and h. Between the segments (g,i), (g,j) and (h,j), which are the strongest ones, higher R values were encountered when using Spearman's coefficient (cf. fig. 2.38), than when using Pearson's (cf. fig. 2.36). This indicates that the relationship between these correlated variables is rather curvilinear than linear. In fact, based on the physical laws of natural convection and thermal buoyancy, relating the temperature difference and the resulting airspeed, a 1/2 power law trend is expected to be encountered (cf. fig. 2.38, visual trends).

2.6.1.8 Outdoor solar radiation and the indoor radiative environment

Results from correlation analysis showed that the direct solar radiation heat flux does not play an essential role in the indoor radiative environment, whether using the Pearson's coefficient (cf. fig. 2.37, segment (l,k): $R = 0{,}24$) or Spearman's (cf. fig. 2.39, segment (l,k): $R = -0{,}25$). In fact, the solar radiation heat flux (k) is not strongly correlated with any other variable, when considering the R threshold criterion proposed. This a priori means that the implemented double-glazed windows with blinds, reduce the incoming solar radiation heat flux, which lead to suspect that the indoor radiative environment is driven by internal long wavelength (LWL) radiation. This implies that the floor surface is heated by the surrounding surfaces, i.e., the glazed-facade and ceiling, among others.

However, the fact that no strong correlations have been encountered for the variable k can also be explained by the position of the Sun in the summertime and the solar eave facing south, on the ceiling. As the Sun position is higher, the solar eave prevents the sun rays from reaching the glazed-facade, and thus, the indoor floor surface. Also, a consequence of the orientation of the platform, the windows at the north facade will not be heated by direct solar radiation. It is worth mentioning that this analysis was first applied to data from only one day (sample size of 144), and greater correlation coefficient

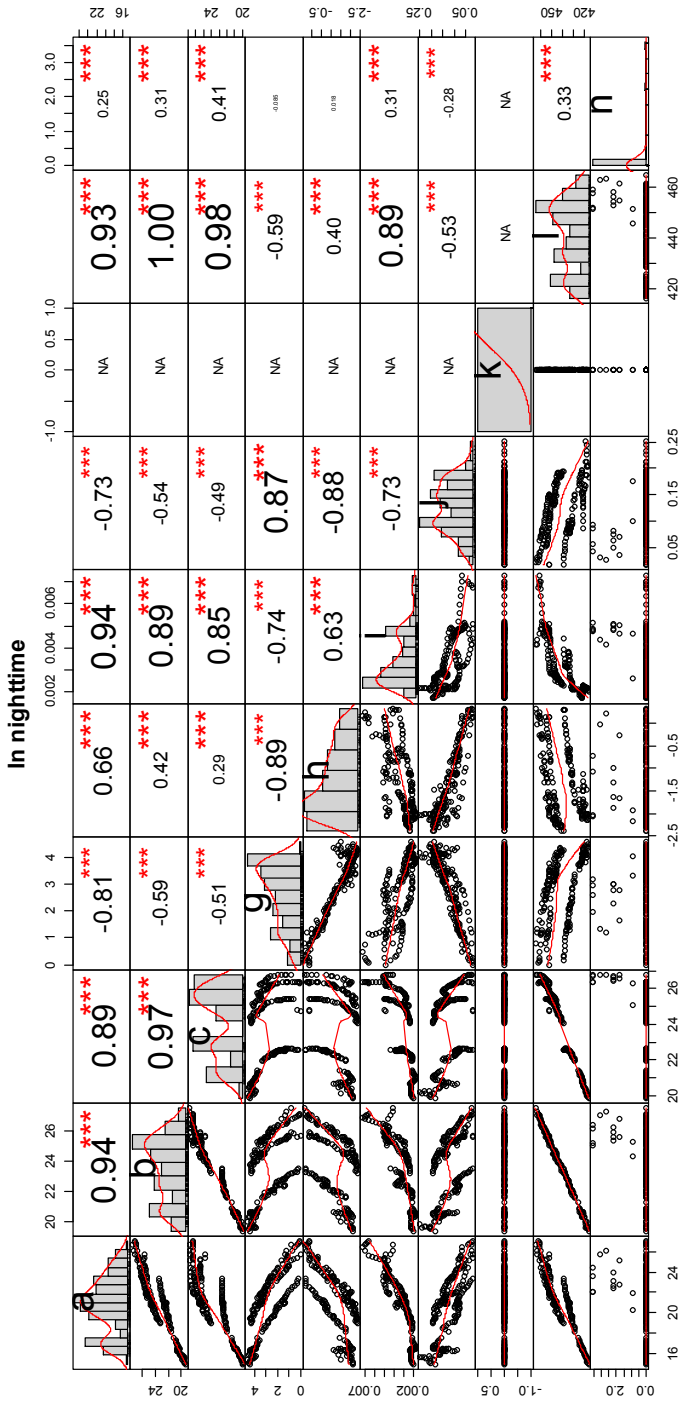

Figure 2.38: Correlation results for no-windy nighttime with Spearman's coefficient.

values have been encountered when larger sample size was used.

So far we have analyzed data from days with similar meteorological conditions. In addition to this, the same analysis was applied to days with mixed meteorological conditions, to observe if the correlation results hold: July 28th and 29th, and August 15th, 16th, 19th, 20th, 22nd, and 23rd. The R values were encountered to be lower than those found in the analysis presented before. This lead to conclude that

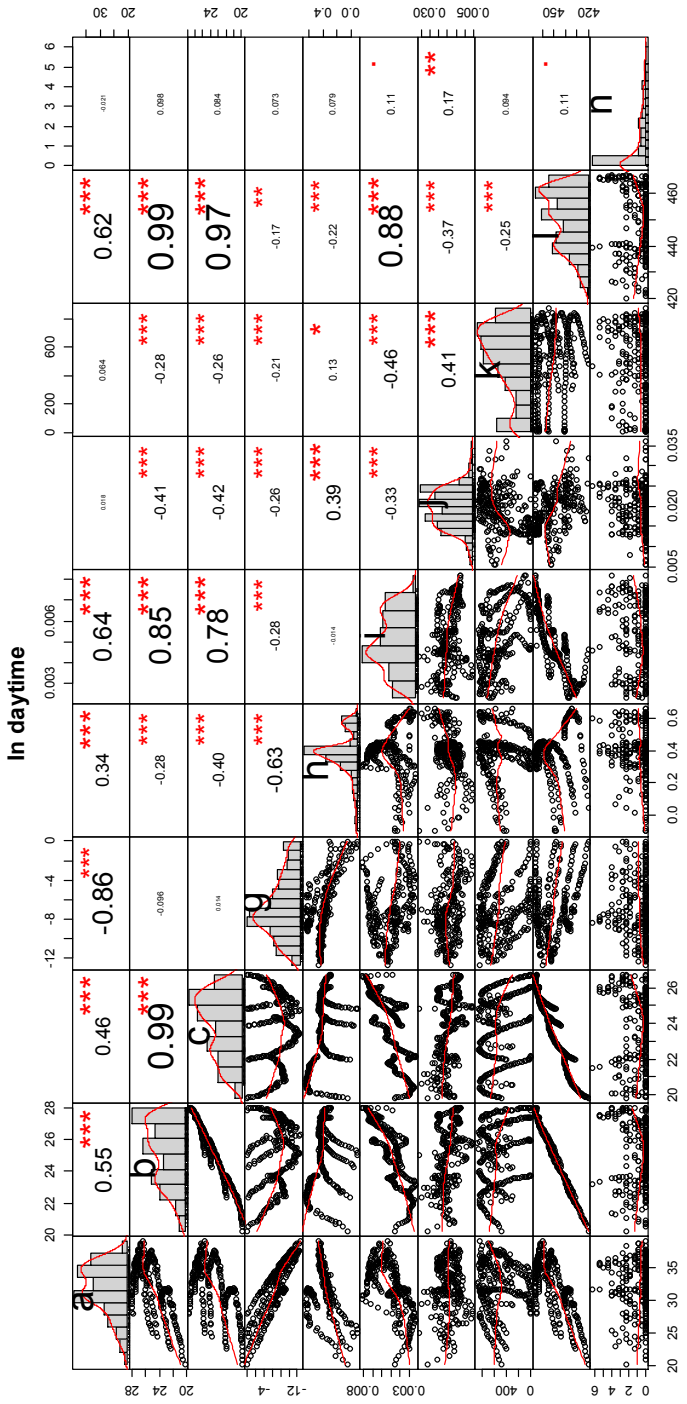

Figure 2.39: Correlation results for sunny and windy daytime with Spearman's coefficient.

if the variability of a variable "A" wants to be statistically studied regarding a variable "B", data from experiments with similar conditions should be used, rather than mixing data from experiments under different conditions together, as expected.

In summary:
The correlation analysis strongly suggests that indoor direct solar radiation is well attenuated by the double-glazed windows with blinds, which implies that the LWL radiation dominates the indoor radiative heat exchanges. Therefore, the direct solar radiation heat flux will be neglected in further analyses.

2.6.2 Identification of the heat transfer phenomena involved

2.6.2.1 Convective heat transfer coefficient in the charge and discharge

The periods of charge and discharge can also be highlighted by the behavior of the convective heat transfer coefficient. Since our experimental results allow us to determine this coefficient in two ways based on Fourier's law of convection:

- by confronting the convective heat flux with the corresponding air-surface temperature difference: $\varphi_C \propto \Delta T$ the resulting slope corresponds to the convective heat transfer coefficient (cf. figs. 2.40, 2.41 and 2.42).
- by dividing the convective heat flux ($\varphi_{C_{S_i}}$) with the corresponding air-surface temperature difference:

$$h_{C_{S_i}} = \frac{\varphi_{C_{S_i}}}{T_{ia_{S_i}} - T_{S_i}} \qquad \left[\mathrm{W{\cdot}m^{-2}{\cdot}K^{-1}}\right] \tag{2.24}$$

where S_i is the corresponding surface where the coefficient is been determined: concrete-slab (D), ceiling (P), glazed-facade (g). Note that the air temperature employed here (T_{ia}) is that measured at 0,1 m above the surface. In each figure, the colors black, purple and brown are assigned to the floor surface, ceiling surface, and glazed-facade, respectively.

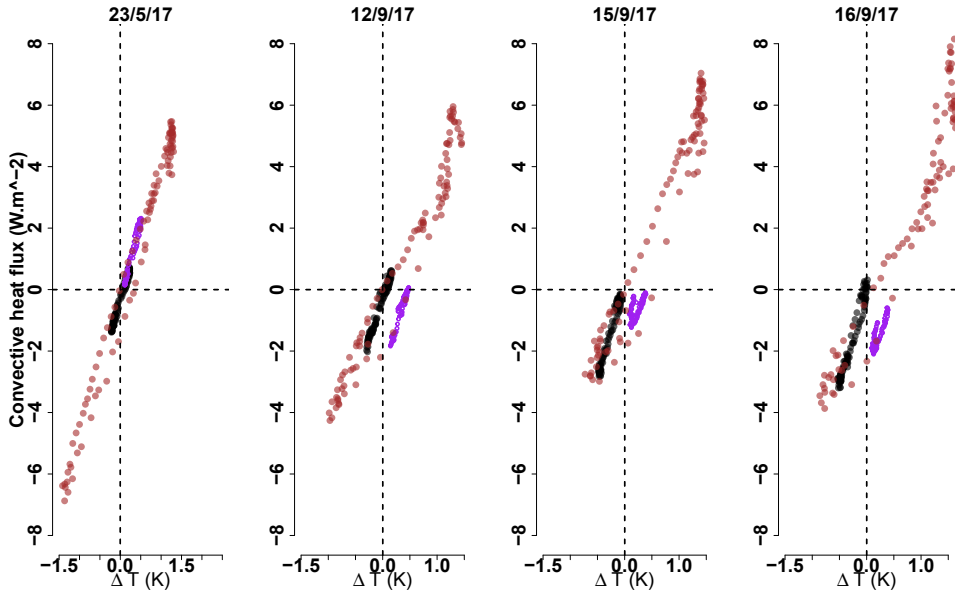

Figure 2.40: For each day in config. n°1, results of the convective heat flux vs air-surface temperature difference: floor (black), ceiling (purple), and glazed-facade (brown).

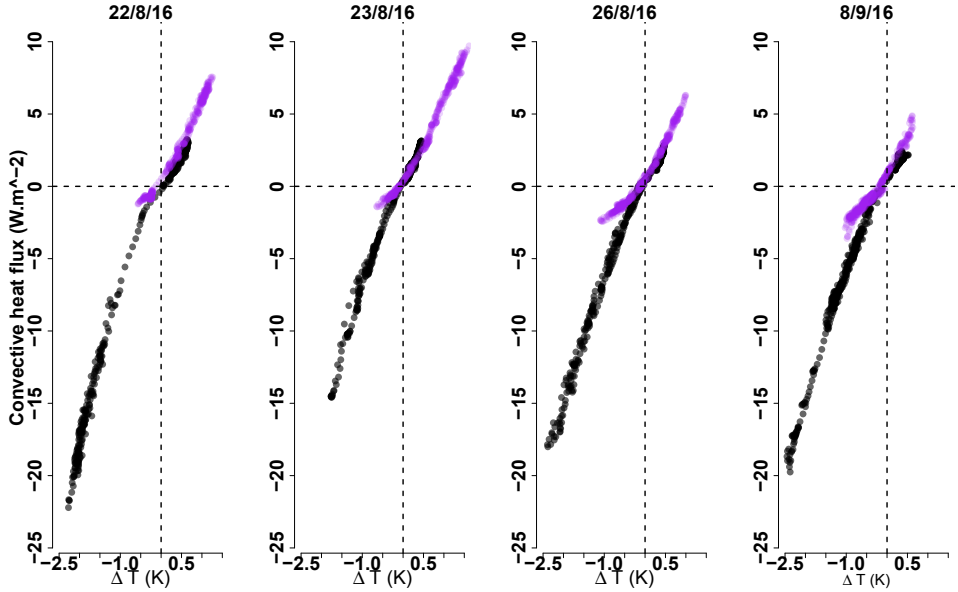

Figure 2.41: For each day in config. n°2, results of the convective heat flux vs air-surface temperature difference: floor (black), ceiling (purple), and glazed-facade (brown).

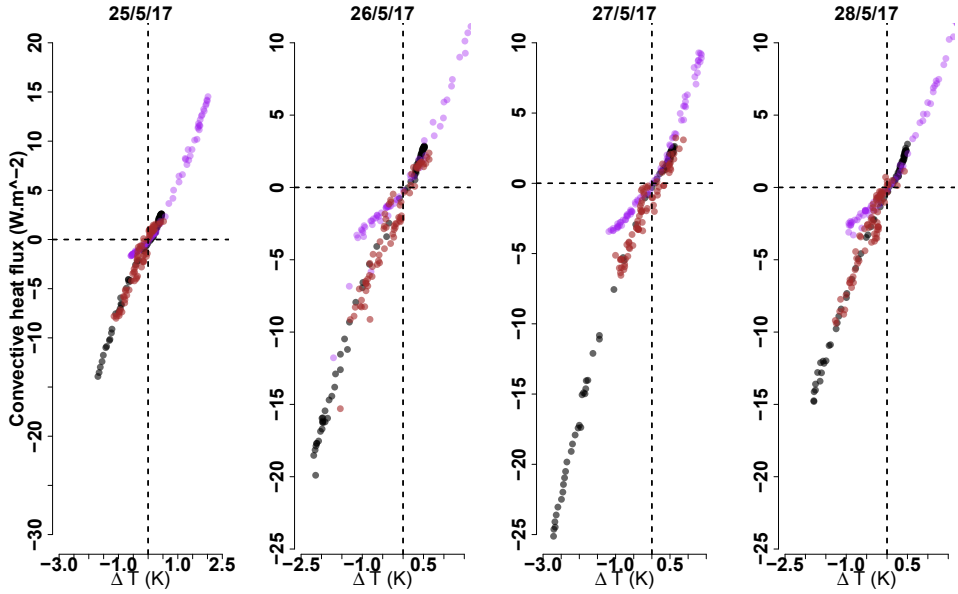

Figure 2.42: For each day in config. n°3, results of the convective heat flux vs air-surface temperature difference: floor (black), ceiling (purple), and glazed-facade (brown).

From figures 2.41 and 2.42, two different regions can be distinguished by the changes in the slopes. For instances, in figure 2.41 for the floor (black dotted line), the slope appears to have an inflection point around the origin ($\Delta T = 0$ and $\varphi_C = 0$); the ceiling (purple dotted line) appears to have the same inflection point. This before may imply that the convective heat transfer coefficient adopts different values in two different periods: the charge ($\varphi_C > 0$) and discharge ($\varphi_C < 0$). This remark can be confirmed by plotting the convective heat transfer coefficient with respect to time as in figures 2.44 and 2.45.

In these figures, the convective heat transfer coefficient for the floor (black circles) presents larger

values than for the ceiling, during the discharge period (nighttime). The opposite is observed during the charge period (daytime). This agrees with what was found for the case of their convective heat fluxes (cf. figs. 2.28 and 2.29).

Moreover, the value of the slope for either the floor or ceiling appears to be slightly different depending on the day, i.e., the slope for the 22/8 is not the same as for the 23/8 (cf. fig. 2.41). On the other hand, from figures 2.40 (23/5) and 2.42 for the glazed-facade (brown dotted line), the slope appears to remain the same for either the charge and discharge periods.

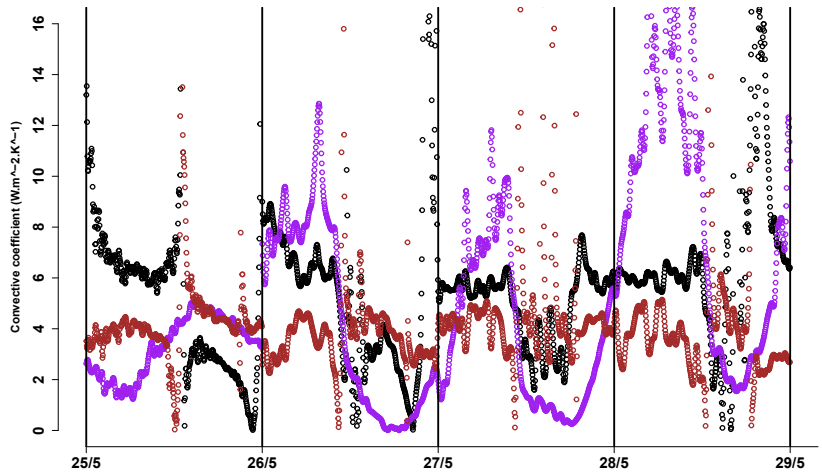

Figure 2.43: For each day in config. n°1, results of the convective heat transfer coefficient using equation 2.24: floor (black), ceiling (purple), and glazed-facade (brown).

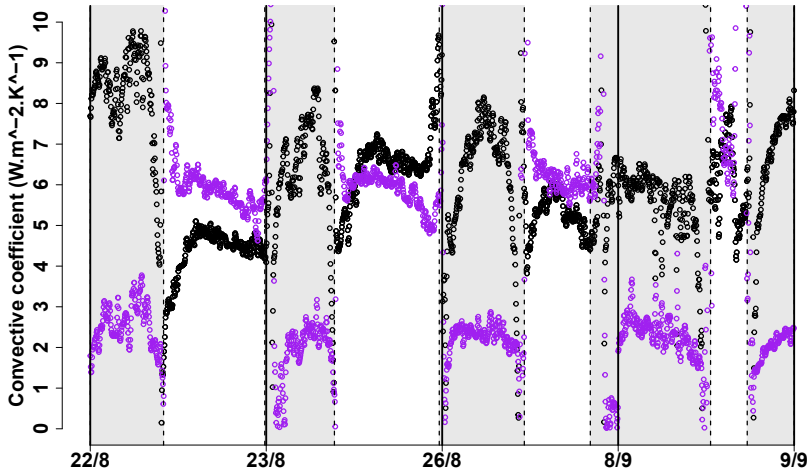

Figure 2.44: For each day in config. n°2, results of the convective heat transfer coefficient using equation 2.24: floor (black), and ceiling (purple).

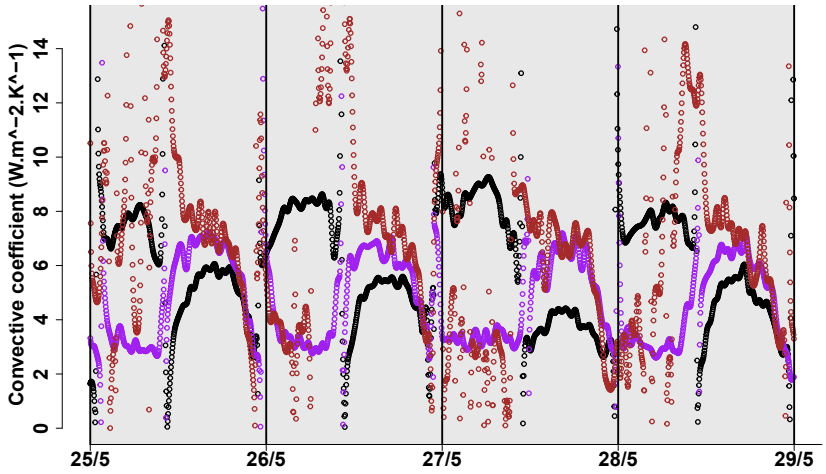

Figure 2.45: For each day in config. n°3, results of the convective heat transfer coefficient using equation 2.24: floor (black), ceiling (purple), and glazed-facade (brown).

In summary:
The implementation of a constant value might not be a suitable choice for modeling purposes, in order to enhance prediction accuracy. Thus, the determination of this coefficient as a function of other parameters might be necessary, for the case when the heat transfer phenomena involved is wanted to be taking into account explicitly. In this regard, the same statistical analysis performed earlier was employed here only for the floor concrete-slab surface, to determine the heat transfer phenomena involved in both charge and discharge periods.

2.6.2.2 Convection and conduction heat transfer phenomena at the floor concrete-slab surface

In order to determine the nature of the heat transfer phenomena involved in the most heavy-weighted element of the platform envelope, only the results for the floor concrete-slab are presented. In the case of convective heat transfer, we recur to the classic four dimensionless numbers frequently employed for this kind of analysis: $\mathcal{N}u$, $\mathcal{R}e$, $\mathcal{G}r$, $\mathcal{R}i$, $\mathcal{B}i$ and $\mathcal{F}r$ (referred to the last nomenclature page for mathematical definitions). $\mathcal{N}u$ number is employed to determine the strength of convective over conductive heat transfer, $\mathcal{R}e$ and $\mathcal{G}r$ are employed to associate the nature of the convective heat transfer to present more affinity to forced or natural convection. $\mathcal{R}i$ number is employed to determine the importance of either force or natural component that might be involved in the convective heat transfer. $\mathcal{B}i$ number is employed to determine if a uniform or non-uniform heat conduction occurs through the slab thickness. Finally, the $\mathcal{F}r$ number is employed in regard to natural ventilation forces to determine the importance of either the shear stress or thermal buoyancy.

The characteristic length L_c employed in $\mathcal{N}u$ number is the height at where the air temperature is measured above the floor surface 0,1 m. For $\mathcal{R}e$ number, the characteristic length is the horizontal distance between the openings at the glazed-facade and the location where the airspeed is measured at 0,1 m above the surface: 1 m. The same distance was employed for $\mathcal{G}r$ number to be in agree-

ment with $\mathcal{R}e$ number at the moment of comparison. Finally, for $\mathcal{B}i$ number, the slab slab thickness is used 0,068 m [118, 120]. The values implemented in all dimensionless number are presented in table 2.7.

Table 2.7: Constant parameters employed in the dimensionless numbers.

Parameter	Notation	Value
Concrete thermal conductivity	λ_D	1,8 $W{\cdot}m^{-1}{\cdot}K^{-1}$
Air thermal conductivity	λ_{ia}	0,024 $W{\cdot}m^{-1}{\cdot}K^{-1}$
Air density	ρ	1,2 $kg{\cdot}m^{-3}$
Dynamic viscosity	μ	1,81x10^{-5} $m^2{\cdot}s^{-1}$
Gravitational constant	g	9,81 $m{\cdot}s^{-2}$
Upper to lower openings height	$\mathcal{L}$	3,72 m
Parameter		**Critical range**
Biot number ($\mathcal{B}i$)		$\mathcal{B}i \ll 0{,}1$
Richardson number ($\mathcal{R}i$)		$0{,}1 < \mathcal{R}i < 10$
Froude number ($\mathcal{F}r$)		$0{,}3 < \mathcal{F}r < 3$

Table 2.8: Dimensionless numbers evaluated at the concrete-slab surface for each configuration.

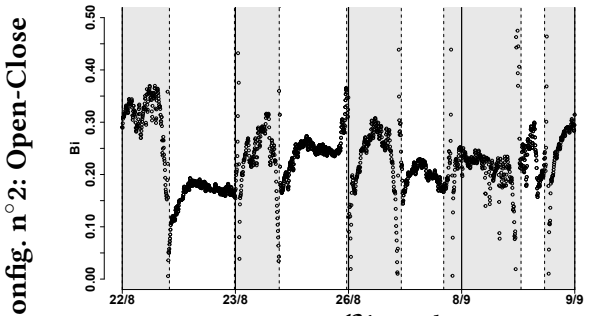

Figure 2.46: $\mathcal{B}i$ number.

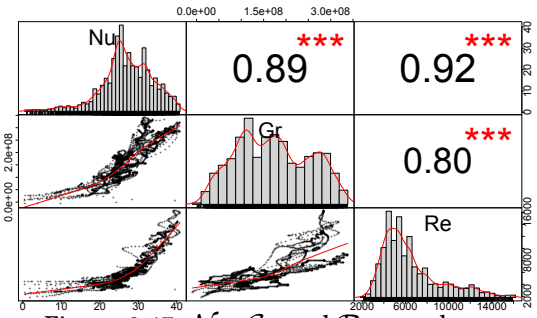

Figure 2.47: $\mathcal{N}u$, $\mathcal{G}r$ and $\mathcal{R}e$ numbers.

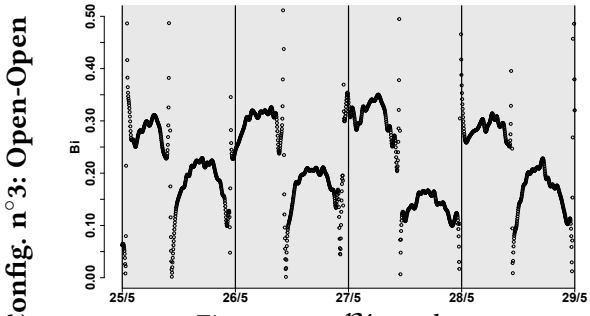

Figure 2.48: $\mathcal{B}i$ number.

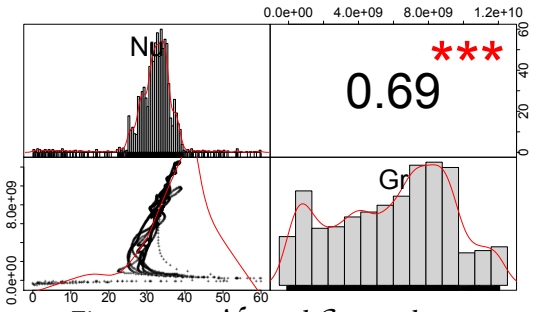

Figure 2.49: $\mathcal{N}u$ and $\mathcal{G}r$ numbers.

Color key: Moments where openings remained opened (gray zones). These results are from the thermoelectric modules.

The results for $\mathcal{B}i$, $\mathcal{N}u$, $\mathcal{R}e$ and $\mathcal{G}r$ for configurations n°2 and n°3, are presented in table 2.8. Despite the low values of $\mathcal{B}i$ number encountered for each configuration, they suggest that a non-uniform heat conduction is most likely to happen ($\mathcal{B}i > 0{,}1$) during both the charge and discharge periods (cf. figs. 2.46 and 2.48). As $\mathcal{B}i$ number presented in these figures accounts only for the convective heat

transfer coefficient, it is clear that the consideration of a modified $\mathcal{B}i$ number, including the radiative heat transfer coefficient, will also yield to the same conclusion.

A correlation matrix, with Spearman's coefficient, is employed here for the analysis of the convective heat transfer phenomena over the floor surface, during the discharge period only (cf. figs.2.47 and 2.49). By implementing the threshold value ($R > 0{,}71$) presented in earlier in §2.6.1.3 to distinguish strong from weak correlations between two variables, from figure 2.47 it can be observed that the $\mathcal{N}u$ number presents strong correlation with $\mathcal{G}r$ and $\mathcal{R}e$ numbers, in both correlation coefficient R (0,89 and 0,92, respectively), and in trend. This implies that a mixed convection takes place during the discharge period. The trend between both dimensionless numbers is expected since both $\mathcal{G}r$ and $\mathcal{R}e$, are related to the $\mathcal{N}u$ number by a power law [118, 120].

Moreover, a strong correlation ($R = 0{,}80$) is also encountered between $\mathcal{G}r$ and $\mathcal{R}e$ number. Since both numbers depend on different parameters from which may not have a direct relationship: temperature difference, and airspeed, respectively, the R value may be surprising at first sight. However, this might not be surprising at all, if we recall the pair (h,j) from figure 2.38 (p.81), where a strong correlation was encountered between the air-surface temperature difference at floor surface and the airspeed near it. This suggests that the airspeed detected is a consequence of the air movement caused by a temperature difference. In fact, by assuming Boussinesq approximation, an expression relating the airspeed ($\mathcal{V}$) with the air-surface temperature difference (ΔT) can be obtained as follows [34]:

$$\mathcal{V} = \sqrt{2 \cdot g \cdot L_c \cdot \beta \cdot \Delta T} \qquad \left[\mathrm{m{\cdot}s^{-1}}\right] \tag{2.25}$$

where β represents the expansion coefficient of the air. It can be inferred from this analysis, that the convective heat transfer has a dominant nature: natural convection.

On the other hand, the levels of the $\mathcal{R}i$ number encountered (cf. fig.2.50, black circles), suggest that mixed convection is most likely to happen during the discharge period (gray zones), as these values are between 0,1 and 10.

Regardless, the consideration of the uncertainty in this analysis might lead to different inferences. Also, in this figure, it can be observed that during the first three discharge periods the $\mathcal{F}r$ number presents a value of zero (brown circles) due to the absence of wind, suggesting that stack ventilation occurs [53, 71]. For the fourth day (8/9), an inconsistency appears to happen: as the $\mathcal{F}r$ number gets larger, the $\mathcal{R}i$ number also presents more significant values. The former indicates that wind effects are getting stronger, and the two-layer stratification established (stack ventilation) due to the absence of wind, is being disturbed, and mixing occurs. Values of $\mathcal{F}r$ number large enough indicates that wind effects dominate. On the contrary, large values of $\mathcal{R}i$ number indicates that natural convection dominates.

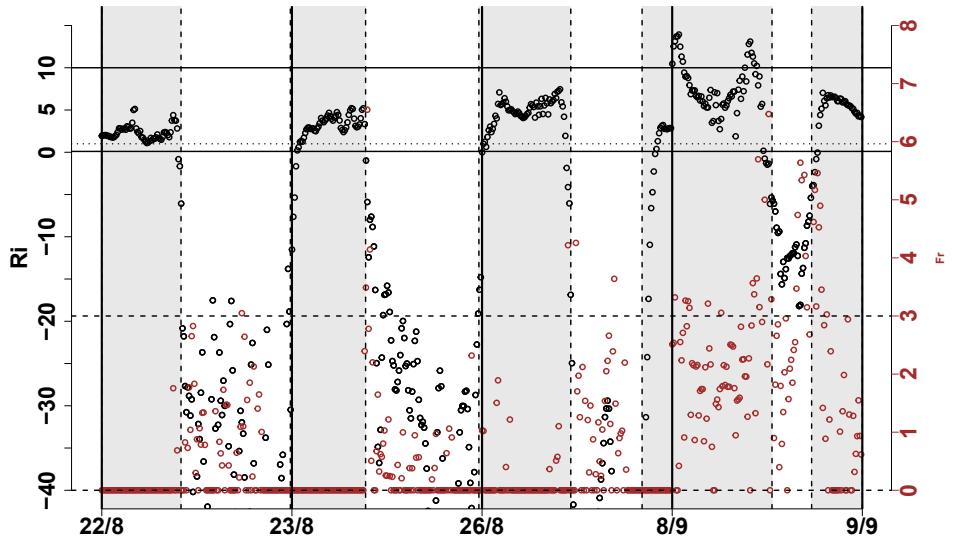

Figure 2.50: For config. n°2: $\mathcal{R}i$ number (black circles), and $\mathcal{F}r$ number (brown circles). Horizontal lines: both $\mathcal{R}i$ critical values (black solid lines), and both $\mathcal{F}r$ critical values (black dashed lines). $\mathcal{F}r = 0$: absence of wind.

In summary, we can retain the following:

- The heat conduction through the concrete-slab thickness might be best described when considering no-uniform heat conduction, for both charge and discharge periods.
- During the discharge period, it is strongly suggested that natural convection dominates the convective heat transfer at the floor surface. Regardless, there appear to be not enough evidence to completely neglect the forced convection component.

2.6.2.3 Air temperature distribution within the platform

Regarding the air thermal stratification within the platform, the air temperature measurements from configuration n°2 are presented in figure 2.51. From the point of view of thermal buoyancy or stack forces, the important gradients to analyze are: (*i*) between the air near the shed-roof and the air near the concrete slab (red solid line), and (*ii*) between the air near the ceiling and the air near the concrete slab (brown solid line).

Note that a maximum temperature difference of around 3 °C is encountered during the first discharge period (22/8 nighttime), and a decreasing trend is presented for the following days; indicating that thermal buoyancy gets weaker. This is in agreement with the behavior observed for the $\mathcal{F}r$ number in figure 2.50, which presents larger values for the following days; indicating that wind effects gets stronger, and thus, mixing occurs faster. The latter may also explain the fact that both temperature gradients (cf. fig.2.51, red and brown lines) appear to get similar values. However, during the entire measurement campaign (where only configuration n°2 was implemented) the most frequent air temperature difference between the shed and the floor (cf. fig. 2.51 A-D) was encountered to be 0,47 °C. This might indicates that a weak thermal stratification is more probably to happen (cf. fig. 2.52). However,

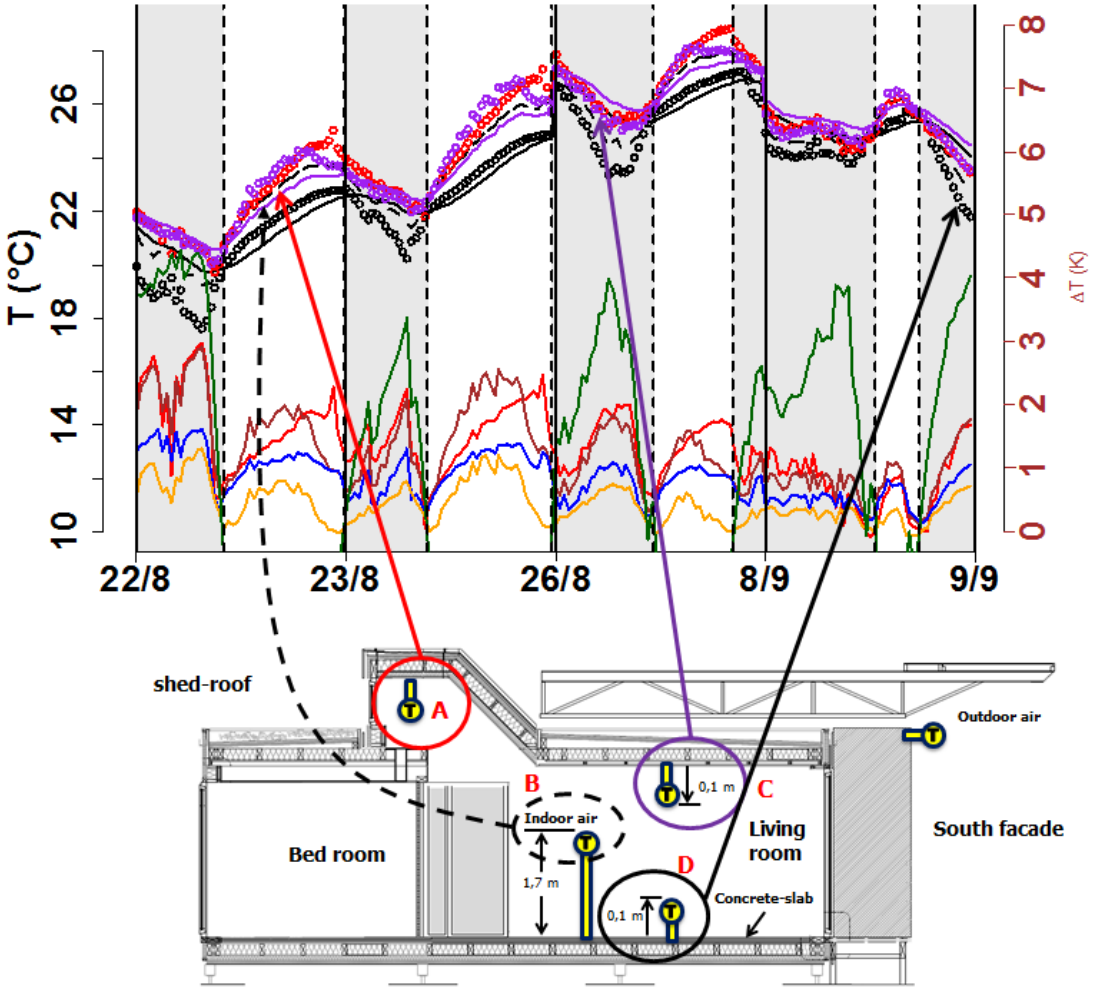

Figure 2.51: Air temperature vertical distribution within the platform. Air at the shed-roof (red circles). Indoor air (black dashed line). Floor: air (black circles), surface (black solid line). Ceiling: air (purple circles), surface (purple solid line). Air temperature differences: indoor-outdoor (green), ceiling-indoor (yellow), indoor-floor (blue), ceiling-floor (brown), and shed-floor (red).

this last remark is can be rendered moot since 0,47 °C falls inside the uncertainty in our temperature measurements (0,48 °C).

2.6.2.4 Distribution of the heat exchanges over the floor concrete-slab surface

Only as an illustrative mode, the experimental set-up implemented in the very first measurement campaign carried out in the summertime of 2015, is presented hereafter in figure 2.53, with the purpose of determining the locations where the total heat flux presents the most significant values over the floor concrete-slab. During this measurement campaign, all "measurement devices" were distributed to cover half of the concrete-slab surface near the glazed-facade.

Such "discrete" arrangement had allowed us to observe the distribution of the heat flux near the natural ventilation openings; an illustration of the total heat flux distribution results during the discharge period is presented in figure 2.54. It is worth recalling that since during this period, the radiative heat flux does not present significant values with respect to the convective heat flux, and thus, the most part

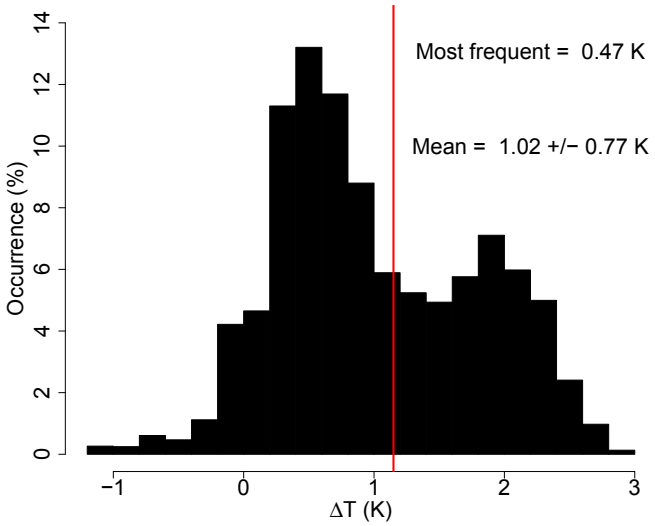

Figure 2.52: Occurrence distribution of the air temperature difference between the shed and the floor (a vertical distance of around 3,5 m). Data employed: measurement campaign carried out in 2016; a total of 51398 samples.

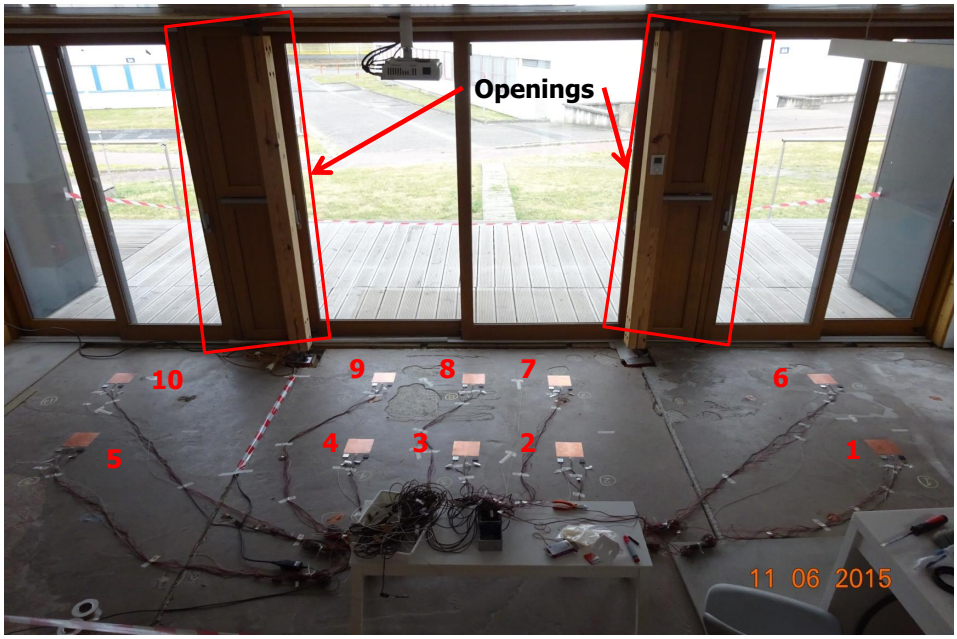

Figure 2.53: Experimental set-up implemented during the measurement campaign of 2015.

of the total heat flux measured is by convection.

In this figure 2.54, it can be observed that the total heat flux presents larger values near the openings, as expected. This heat flux appears to get smaller as we move away from the openings, which can be explained by the fact that after the air currents, at outdoor temperature, enter the platform and mixed with air, at indoor temperature (higher than the outdoor air), they reach the first row of "measurement devices" (10, 9, 8, 7, 6). Here, the air currents are heated as they get in contact with the concrete-slab surface between the first and second row of "measurement devices". Then, before reaching the second row (5, 4, 3, 2, 1): (*i*) some groups of air particles might get lighter enough, after heated, to detaching

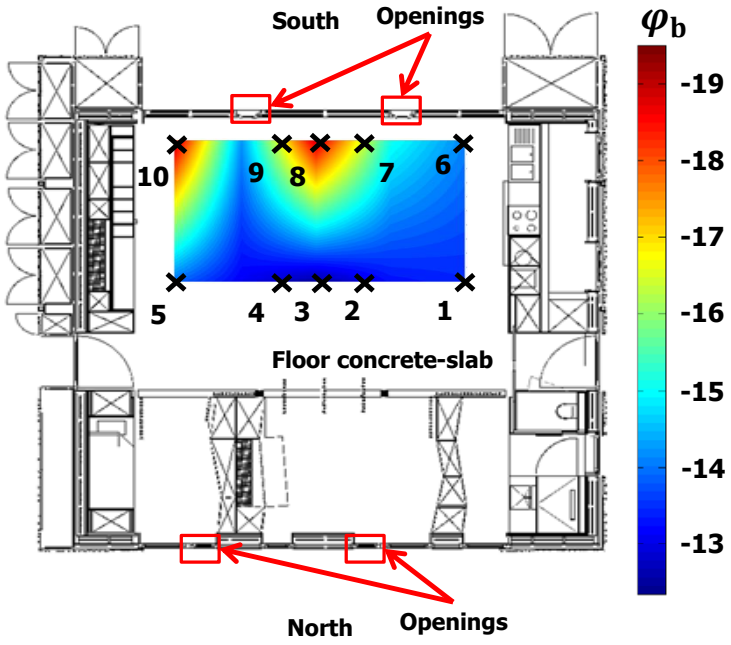

Figure 2.54: Total heat flux (φ_b) distribution over the floor concrete-slab surface during the discharge period from the measurement campaign of 2015.

from the rest of the groups towards the upper parts of the platform, weakening the air currents towards the second row, or (*ii*) the concrete-slab surface roughness (including the sensors) may be important enough as to weaken the air currents. This scenario might happen slowly since the airspeed detected were significantly low (cf. fig. 2.28, brown line, similar airspeed levels were encountered by [27]). This behavior was studied for a similar scenario (a buoyant cold flow dropping into the floor region), concluding, as expected, that it causes a radial air movement into the zone, and the airspeed is reduced as it moves away from the air jet from the opening [74].

Note that placing measurement devices exactly behind the openings results in an average underestimation of the total heat flux, and placing them too close to the glazed-facade, results in an average overestimation of this heat flux. This highlights the zones where the total heat flux distribution presents the most significant values, and this measurement point or zone will be employed for further analysis, regarding the modeling.

2.6.2.5 Contribution of the envelope to the charge process via infrared thermography

The impact that the outdoor environment has on the indoor environment can also be highlighted during the charging process using infrared thermography [11]. To illustrate this statement, thermograms of five elements of the platform envelope (viewed from the inside of the platform) are presented in figure 2.55: (*a*) the glazed-facade and concrete-slab, (*b*) the concrete-slab and surroundings surfaces via the crumbled aluminum foil, (*c*) the North facade, (*d*) the shed-roof, and (*e*) the East-side door. Since all thermograms were not all taken at the same moment, the color bar serves only to relatively distinguishing between "hot", and "not hot" surfaces, i.e., the color yellow might not indicate the same temperature level in all thermograms).

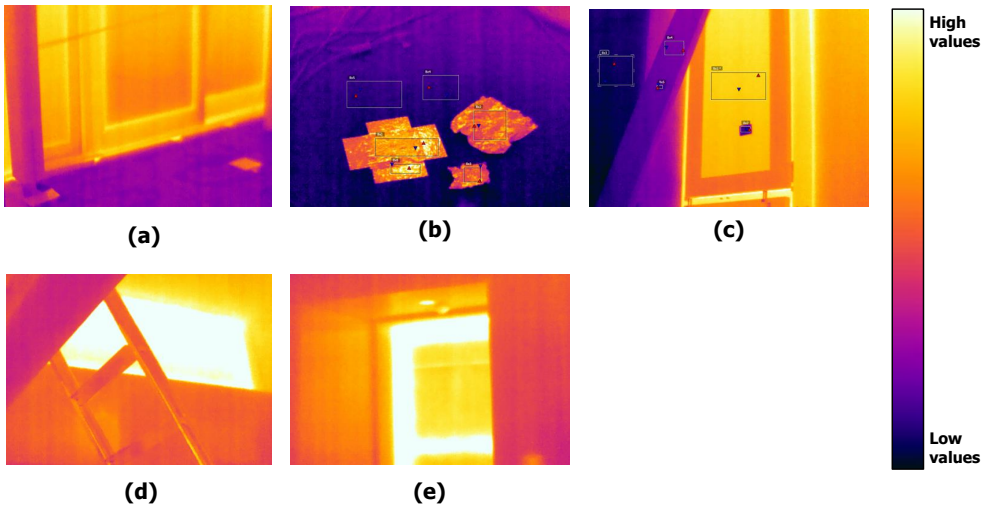

Figure 2.55: Thermograms of indoor surfaces of the envelope: (a) South facade, (b) concrete-slab and surroundings, (c) North facade, (d) shed-roof, (e) East door.

From thermogram (*a*) and (*b*) it can be observed that the concrete-slab surface appears to be less hot than the glazed-facade (*a*) and also less hot than the surrounding surfaces (*b*), which confirms the remark stated earlier in §2.5.3.2. Also, from the thermogram (*b*), it can be observed that the black foil placed on the concrete-slab surface (cf. fig.2.12) appears to banished from the view of the IR camera. This might indicate that the concrete-slab surface has similar emissivity value as the default set value of the camera, which resulted in being the case.

From thermogram (*c*), it can be observed that the opening (North facade) is hotter than the wall-facade (in purple). The little square stuck on the opening (a crumbled shiny foil), also indicates that the opening is hotter than the surrounding surfaces (partition-walls and doors separating the living room and the bedroom). This before may imply that, when in the modeling process, taking into account the entire surface of the north facade as to heat the indoor air, might yield to an overestimation of the heat gained by this air. A similar statement can be given by analyzing thermograms (*d*) and (*c*), regarding the shed-roof surface, and the East and West facades, respectively.

2.7 Thermal comfort assessment of a simple opening-closing strategy

Finally, since configuration n°2 was implemented during the entire measurement campaign in the summertime 2016, an evaluation of the impact of passive night natural ventilation, in maintaining the thermal comfort within the indoor environment, is performed hereafter based on the indicators recommended by the standard ISO 7730 (cf. §1.1.1**(A)**).

2.7.1 Indicators employed in the assessment

In order to estimate such indicators, we are interested in determining the following parameters: (*i*) the air temperature and (*ii*) air velocity at different heights, (*iii*) the mean radiant temperature, (*iv*) the room temperature, and (*v*) the degree of discomfort. The last three parameters are calculated from the

measurements; the others are directly measured.

For the calculation of the room temperature inside the platform, an expression given by ISO 7726 (1998) will be used. Regarding the estimation of discomfort, it is proposed to use the daily degree-hours of discomfort indicator (DDH). In addition, the difference between the temperature of the interior air and the mean radiant temperature of the surrounding walls, will be also evaluated (cf. §1.1.1**(A)**).

2.7.1.1 Room temperature according to the standard ISO7726

The room temperature takes into account both the temperature of the air, the average temperature of the walls, as well as the air velocity; all three being measured at the same location. It is described, according to ISO 7726 (1998), by the following equation:

$$T_{op}(t) = T_{ia}(t) + [1 - A_k(t)] \cdot [T_{surr}(t) - T_{ia}(t)] \qquad [^\circ\text{C}] \tag{2.26}$$

Where the parameter A_k is a function of the air velocity, $A_k(t) = 0{,}73V(t)^{0,2}$.

2.7.1.2 Daily degree-hour of discomfort (DDH)

Having chosen a comfort interval (23 - 26 °C), the degree-hour indicator (DH) is defined by the number of degrees exceeded by the room temperature, multiplied by the duration of this exceeding in hours. His expression is:

$$\text{DDH} = \int_{day} \left[T_{op}(t) - T_{comfort_{max}}(t)\right] \cdot \mathrm{d}t \qquad [^\circ\text{C·h}] \tag{2.27}$$

under the restriction that T_{op} is greater than $T_{comfort_{max}}$ ($T_{op} > T_{comfort_{max}}$).

2.7.2 Impact of a passive night ventilation strategy on internal thermal comfort

During this measurement campaign, the evolution of the outside air temperature (black line) and the internal room temperature (cf. eq. 23, red line) are shown in figure 2.56. Two horizontal dashed lines represent the chosen comfort range (23 - 26 °C).

Usually, the room temperature should be in the comfort range during the daytime period of a typical day. Thus we can see in figure 2.56 that the majority of the peaks of the room temperature were in agreement with the comfort interval.

Figure 2.57 shows the degree-hour of days with T_{op} (cf. eq. 24) greater than $T_{comfort_{max}}$ ($T_{op} > T_{comfort_{max}}$), and the difference in temperature maximum (ΔT_{max}) between these last two. There are also the maximum values of the outdoor temperature and room temperature.

In more detail, the comfort interval was exceeded by the room temperature 13% of the total duration of the measurement campaign (6862 times out of 51398 data). Here we observe that the more frequent exceeding degrees are less than 2 °C (6397 times out of 6862: 93,22% of the exceeding). This corresponds to a value of approximately 120 degree-hour of discomfort over the 34 days. In order to know if this value is significant, it should be compared with the results of degree-hour for similar weather days, without the implementation of night natural ventilation strategy.

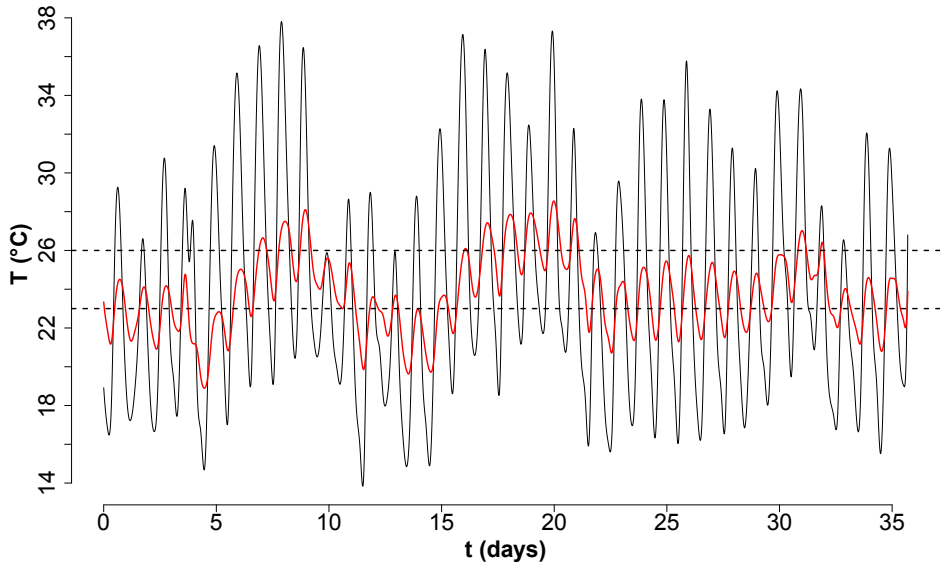

Figure 2.56: Outdoor (black line) and indoor (red line) air temperatures of the entire measurement campaign carried out during the summertime in 2016.

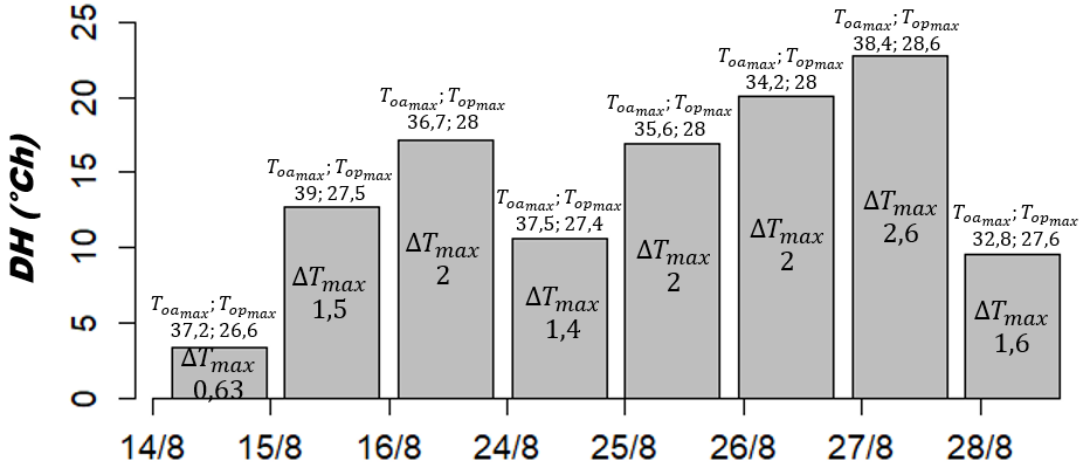

Figure 2.57: Degrees of discomfort time of days whose T_{op} is greater than $T_{comfort_{max}}$.

Part of the days in this measurement campaign, where the platform was in discomfort during the daytime period, is shown in figures 2.58 and 2.59. Figure 2.58 shows the other two indicators of comfort: the vertical air temperature difference and air currents. For the vertical differences in air temperature (temperature axis on the left of this figure), we find that the differences between an air temperature of 0,10 m (line with circles) and 1,70 m (black solid line) are less than 3 °C during the daytime period; being in agreement with the norm. For the air currents within the platform, figure 2.59 shows the airspeed levels at two different heights (right axis): at 0,10 m (black dotted line) and at 1,70 m (black solid line). In the daytime, we can observe that the speed levels are visibly lower than 25 cm·s^{-1}; which is also consistent with the norm.

In addition, figure 2.59 shows the resulting mean radiant temperature of the surrounding walls (black line with "+"). It can be observe that this temperature is confused with the line of the room temperature (blue dotted line) and likewise with that of the air temperature (black solid line). Among this results,

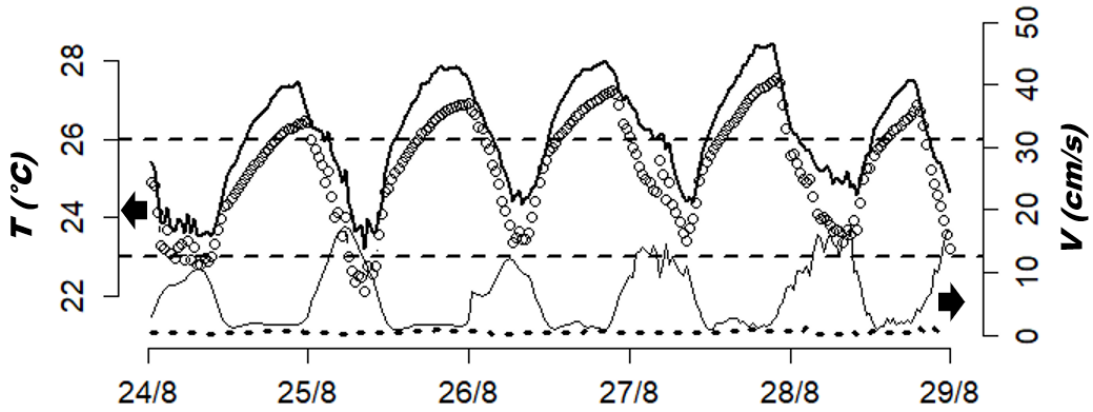

Figure 2.58: Left axis: T_{ia} to 1,70 m, black line. T_{ia} at 0,10 m, dotted with balls. Right axis: 1,70 m air velocity, black dotted line. Air velocity at 0,10 m, black line.

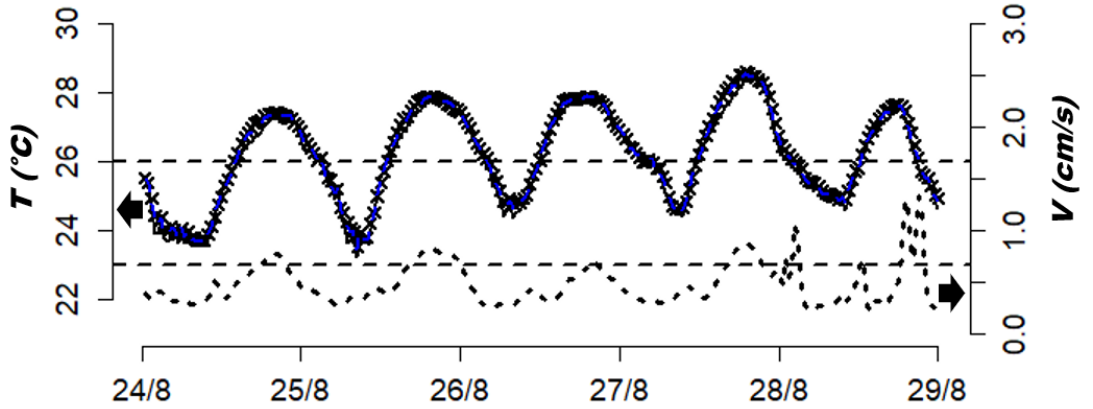

Figure 2.59: Left axis: T_{ia} black line. T_{surr} black line with "+". T_{op} dotted line in blue. Axis on the right: Air velocity, black dotted line. All measurements made at 1,70 m height.

the difference between the air temperature and the mean radiant temperature has never reached a gap as large as 3 °C. It can also be inferred that because the mean radiant temperature is very close to that of the indoor air, the level of radiation inside the platform is very low. This low level may be the result of good insulation of the building envelope and the fact that the solar shades always remained close.

In summary:
The results showed that this platform, under typical summer weather conditions, was able to maintain the comfort during the daytime of most days of this measurement campaign (87%, equivalent to 29 out of 34 days) this by allowing a night natural ventilation strategy and keeping the solar shades closed. This allows us to reaffirm that an adequate coupling between the thermal inertia of a building, programmable solar protection, and openings allowing natural night ventilation, can ensure an integral thermal comfort of the indoor environment during the period day of a typical day in the summer season. It should be noted that the natural ventilation strategy implemented throughout the campaign did not use all the openings of the platform; thus, implementing all the openings, for the days that have presented discomfort, might reduce the risk of discomfort.

2.8 Concluding remarks

The exhaustive experimental study presented in this chapter has allowed characterizing, in detail, the thermal aspects of the experimental platform, suggesting the following major points:

1. It is not enough to take the convective coefficients as constant values when the openings are open. It would be necessary to model or to identify them in another way.
2. The convection inside the platform does not appear to have a dominant nature, natural or forced, both may occur when the openings are open.
3. The direct solar radiation does not heat directly the indoor environment of the platform.
4. The most representative measuring location on the slab surface is between the two groups of openings and in the middle of the platform, close to the south facade.
5. It is necessary to take into account the convective effects on the slab surface, on the ceiling, and on the glazed-facade individually, due to their behavior.
6. It is clear that there are some vertical walls that contribute the most to the heating of the indoor air; taking them all when describing the indoor air heat gains might lead to overestimations.
7. The vertical thermal stratification of the indoor air within the platform, can be neglected regarding the thermal comfort of the indoor environment. However, regarding buoyancy driven ventilation, it is suggested that neglecting these thermal gradients may be a suitable choice for larger values of $\mathcal{F}r$ number, than the ones encountered.
8. The values of $\mathcal{B}i$ number encountered suggest that a non-uniform heat conduction might give a precise description of the heat transfer through the concrete-slab thickness.

These last remarks have allowed us to highlight the key elements involved in the energy charge-discharge process in our experimental platform: the indoor air, the concrete slab (as the thermal mass), the glazed-facade, the airflow rate, and the ceiling, in terms of heat transfer.

Nevertheless, the characterization of the thermal aspects of the experimental platform should also consider the heat transfer associated with the exchanges in mass (air) between the indoor and outdoor environments. This consideration requires the knowledge of the natural airflow rate within the platform. Thus, we address the following chapter to characterize the ventilation airflow rate.

Furthermore, this characterization has endorsed the consideration of including, later in the modeling, the key elements mentioned here before. Also, to consider not to include the direct solar radiation in the modeling of the heat transfer in the concrete slab.

Chapter 3

Characterization of the natural ventilation airflow rate

Scope

This chapter is dedicated to characterizing the natural ventilation airflow rate in the platform, in terms of air change rate per hour (*ach*). This characterization aims to determine an expression relating the net *ach* as a function of the wind speed and direction, and the indoor-outdoor temperature difference. To do this, direct airflow simulations were performed for a single-zone model of the platform via network airflow models in CONTAM, to account for wind and temperature effects on the net *ach*. Air leakages are also included. These simulations require the knowledge of the airflow characteristics of the openings and leakages, i.e., discharge coefficient, airflow rate coefficient, flow exponent and effective area. These characteristics were estimated using experimental data from airtightness tests. Since these tests allow us to determined an expression for the discharge coefficient that depends on the pressure difference, pressure measurements were carried out to observe the pressure levels attained in the platform. Finally, the distribution of the air-leakage is studied for two particular cases, and the combined effects of wind and temperature are also studied.

3.1 Initial considerations and airflow pattern recognition

After assessing the experimental and modeling techniques that have been developed and implemented for the determination of the natural airflow rate (cf. §1.1.3, p.14), and since we are interested in taking into account those with deep consideration of the physical phenomena, the most attractive options are CFD simulations, heavy instrumentation, or both. Since the computation time expend by CFD simulations can become excessively large very promptly, such modeling techniques are rendered as inconvenient. Complicated and expensive experimental methods such as tracer gas, particle image velocimetry, or heavy instrumentation in terms of airspeed measurements using complex algorithms as in [19, 33, 98], are neither suitable nor accessible techniques for our particular case. The reasons are attributed to the non-generic distribution and the number of natural ventilation openings in our platform.

At first sight, the most plausible appears to be the implementation of empirical modeling techniques, specifically using airflow path with the electrical analogy, because these models do not require heavy experimental equipment or simulation tools, or both, and their use is largely acceptable among this field of study. However, an essential obstacle for such models is the precise knowledge of the airflow path within the building. In this matter, instead of assuming a hypothetical airflow path, several small flags were installed at all the openings, as well as, at other parts within the platform, to identify visually (video recording) any possible airflow patterns. Though this could only be performed for one facade at a time, the behavior of the flags showed airflow patterns that could only be taken into account when performing numerical modeling techniques as CFD. For instance, let us look at some screenshots from a 17 mins video recorded on May 15th, 2017 starting at 11 h, shown in figure 3.1 (a)-(c), and figure 3.1 (e) (f). During this recording, only the openings at the South facade and shed-roof remained open. In figure 3.1 (a), the flags on the openings at the South facade appear to be in a steady state (no air current appears to be detected by the flags), represented by the yellow arrow (reference state). In figure 3.1 (b), all four flags appear to be tilted inwardly (airflow entering the platform, green arrows). Based on the wind direction during the recording (cf. figure 3.1 (c), top right corner: blue line), the behavior in figure 3.1 (b) is expected, and can be easily considered in the airflow path electrical analogy modeling. On the other hand, in figure 3.1 (c), the flag on the bottom right opening appears to be tilted inwardly, and the flag on the bottom left opening appears to be tilted outwardly, while both flags on the top openings appear to be steady. The behavior of the bottom openings might be expected regarding the wind direction. However, the behavior of the top openings with respect to those of the bottom might be unexpected when only considering the wind direction. Also, accounting for this particular behavior in the airflow path electrical analogy modeling, might not be convenient. In such cases, stochastic studies on airflow pattern recognition might lead to determine the most likely airflow path to happen, before considering the implementation of such models. Only as an illustrative purpose, in figure 3.1 (d), the flags appear to be tilted outwardly (airflow leaving the platform, green arrows); another behavior easily to account for in airflow path models.

Therefore, this airflow pattern recognition, rather simple, led us to consider another modeling method. In this regard, the choice of airflow network models seems the most suitable option, since a deep consideration of the physical laws is taken into account. However, instead of solving the sys-

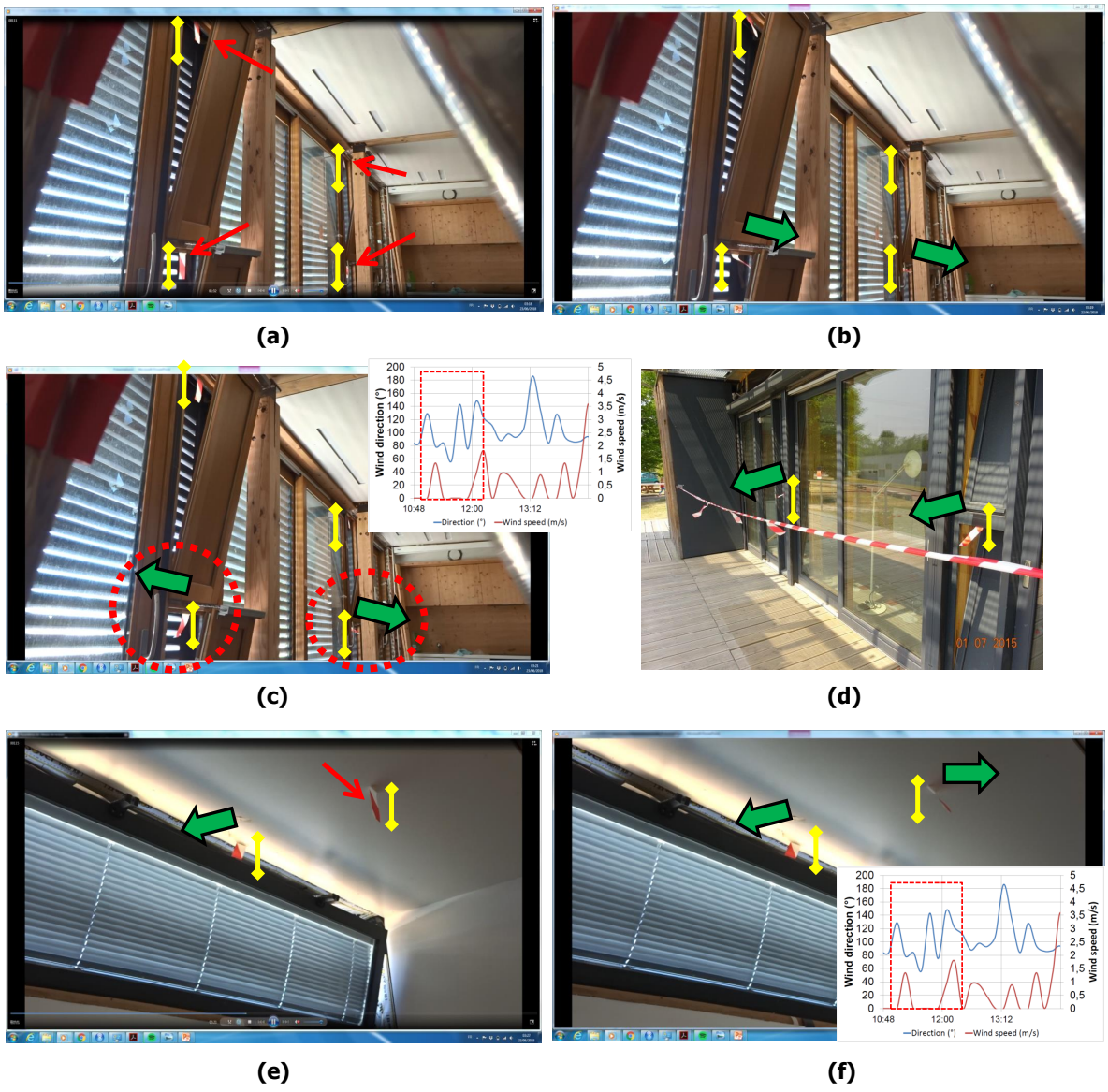

Figure 3.1: Screenshots from a 17 mins video for airflow pattern recognition: a reference of the flags in steady position (yellow arrows) and flow direction indicated by the flags (green arrows). At the South facade: (a) all flags motionless, (b) all flags tilted inwardly, (c) both upper flags motionless while both lower flags tilted outwardly (left) and inwardly (right), (d) all flags tilted outwardly. At the shed-roof: (e) left flag tilted outwardly while right flag steady, (f) left flag tilted outwardly while right flag tilted inwardly.

tem of equations that might result from the implementation of such model, CONTAM software was decided to be employed. This software allows to perform transient airflow simulations, and includes several kinds of airflow models; having different options for air-leakages and openings. Also, as it employs the Newton-Raphson numerical method, low errors are to be expected in the numerical solution [28].

3.2 Modeling of the natural airflow rate in the platform

The natural airflow rate in the platform, as a function of wind and thermal buoyancy effects, is proposed to be determined using the airflow simulation software CONTAM. This software is, dedicated to performing airflow simulations by solving the flow conservation equation, in either steady and transitory conditions, coupled with Bernoulli's equation, without accounting for any heat exchanges inside the given building (convection, radiation, conduction). The simulation calculates the pressure difference and airflow rate at every opening in the building, along with the flow direction. Also, the airflow rate of a specific zone of the building can be calculated.

The interest in the implementation of this software lays especially in the possibility to determine simple expressions linking the wind and thermal buoyancy effects individually to the natural airflow rate in the platform. Here, the natural airflow rate will be represented in the form of air change per hour or *ach*, since it is a standard way to refer to the ventilation airflow rate when considering natural ventilation in buildings.

Since this software allows to design the given enclosure only by visualizing the top view, some modifications are made to the geometry of the platform. The modeling process is presented in figure 3.2. The actual geometry of the platform (physical domain) with a total volume of approximately 210 m^3, a floor surface of 67 m^2, a maximum height of 4,9 m with respect to the ground, and two sets of openings, facing north, at different distances from the south facade, is reduced to a simple geometry (domain modeling) where those two sets of openings are confined at the same facade, reducing the total volume to 158 m^3, with a floor surface of 46 m^2.

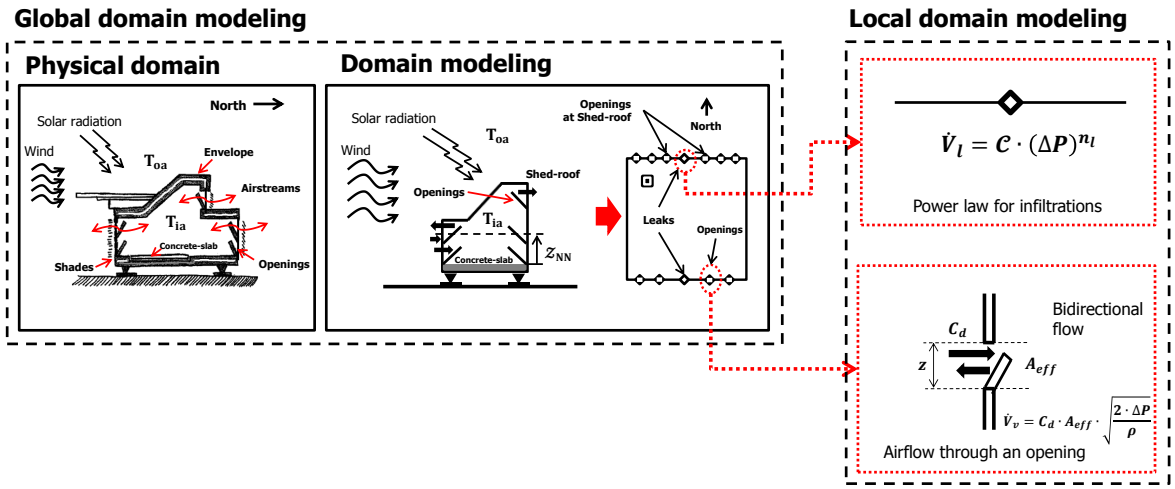

Figure 3.2: Schematic of the modeling process employed. Global domain modeling: Physical or real domain, and single-zone model in CONTAM (domain modeling). Local domain modeling: airflow models chosen for openings and infiltrations.

Here, the two different heights of the south and north facades are distinguished on the software with their corresponding heights: 3,7 m and 4,9 m, respectively with respect to the ground. To do this, we followed the next six steps to design the model on CONTAM:

(1) A single-zone enclosure represented by four walls

After drawing the four walls of the enclosure, on the *project configuration properties* window, in the *sketchpad dimensions* label, the width, and height are set to 70 and 66 cells with a *scaling factor* of 0,1 m, to account for the real dimensions in meters of the zone limited by the south facade and the shed-roof (a 7 x 6,6 m surface area). Then, on the *zone properties* window, a *normal-zone type* is created inside the four walls, where the volume of the enclosure is included. Finally, the temperature and pressure are set to vary instead of remain constant, and no *temperature schedule* is considered. To account for the height of the enclosure, on the *level data* window, the *distance to level above* is set to 3,47 m which is the height from the floor of the platform to its highest point.

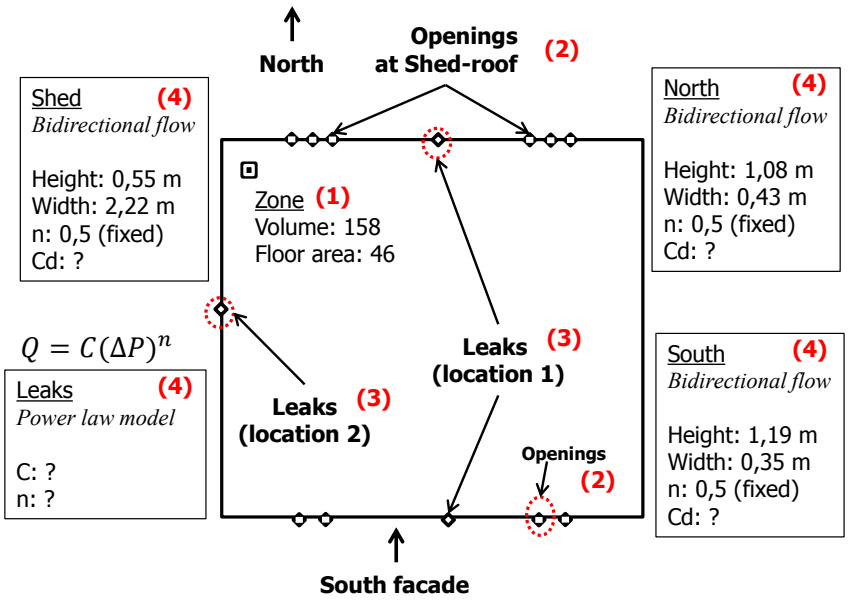

Figure 3.3: Schematic showing the steps in the construction of the single-zone model on CONTAM: (1) single-zone area and volume, (2) location of the natural ventilation openings (South, North, shed-roof), (3) location of air-leakages (location 1 and location 2), (4) Airflow models selection for the openings and leakages.

(2) Location of the natural ventilation openings

The openings or as the software called them, *airflow paths*, are created onto the walls of the enclosure (cf. fig. 3.2, domain modeling box on the right-hand side). Four *airflow paths* are created onto the wall facing south (bottom wall) and six onto the wall facing north (top wall). As two of the openings at the south facade are located above the other two, the relative elevation of these openings is set at 1,2 m in the *flow path* label on the *airflow path properties* window. In the same label, the location of the opening is terminated by setting the value of the x coordinate to their real relative distance on the facade, and finally, no limitations for pressure or flow capacity are considered for each opening.

(3) Location of the air-leakages

The location or distribution of the air infiltrations on the envelope is a delicate topic due to the imprecisions that might arise when estimating the airflow rate through modeling techniques [20, 32]. According to the CETE de Lyon in its report regarding the generalities and sensitization of the enve-

lope airtightness in buildings [21], the regions most likely to attend air-leakages are: (*i*) facades and floors, (*ii*) external furnishings, (*iii*) electrical equipment, and (*iv*) traps and elements crossing the walls. Therefore, the following two scenarios figured as the most likely locations and should be analyzed:

a. The infiltrations are equally distributed on the facades containing the natural ventilation openings: the location of the infiltrations is fixed at half of each facade height.

b. The infiltrations are not equally distributed and an *in situ* identification of their location is required: with the intention to recovery the tightness of the platform envelope, an *in situ* identification process has shown that the majority of the air-leakage are located behind the kitchen (at the West facade) (cf. §3.3.1).

Both scenarios can be simulated on CONTAM without complications (refer to §3.4 for results).

(4) Airflow models for the openings and infiltrations

For each *airflow path* created, a *flow element* is required by the software. Therefore, by accessing the *flow element* label on the *airflow path properties* window and then selecting *new element*, the *airflow path* can be created by choosing the appropriated *airflow element model*. This *airflow element model* describes the airflow through the opening. In our case, a *one-way flow using power law models* in the form of $Q = C(dP)^n$ is chosen for the *airflow paths* symbolizing the air leakages and infiltrations; a *two-way flow models* in the form of one opening is chosen for the *airflow paths* symbolizing the natural ventilation openings.

Regarding the air leakages and infiltrations, the dimensions of the orifices are generally small and often unmeasurable, which a priori justify the assumption of only admitting a unidirectional flow.

Regarding the natural ventilation openings, the *airflow element model* chosen is based on previous studies done by [19, 27, 36, 70], which analyses have allowed us to realize that the total opening size created by the four openings at the South or North facades of our platform, might match the same considerations. This remark leads to consider the possibility of the establishment of a neutral plane with a starting height $\mathscr{Z}_{NN}$ (cf. eq. 1.1.2.1, p.14) crossing the upper openings at the South or North facades as shown in figure 3.4 (a).

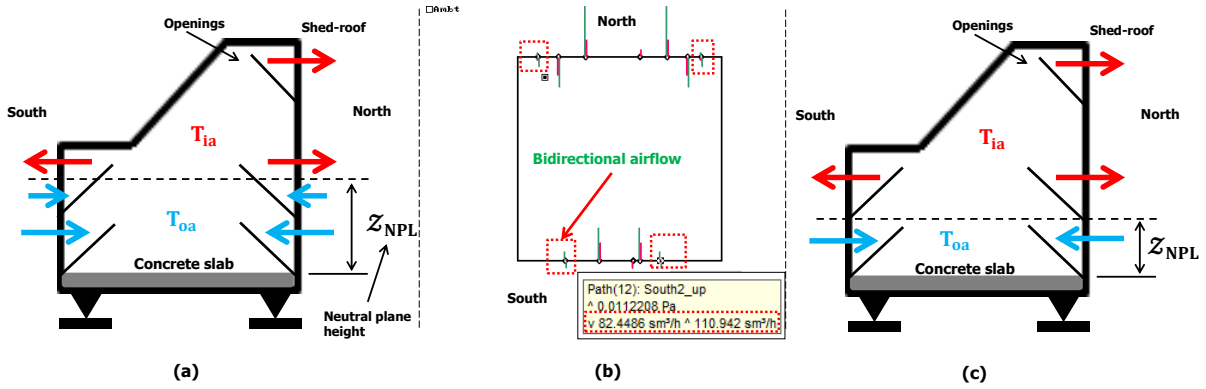

Figure 3.4: Considerations for a bidirectional flow: (a) when the NPL crosses an opening, (b) CONTAM simulation results for temperature difference only, (c) when the NPL does not cross any opening.

Here, if the situation shown in figure 3.4 (a) applies, the upper openings at the South facade might experience a bidirectional flow (blue and red arrows). In fact, evidence of this bidirectional flow can

also be highlighted by the simulation results from CONTAM as shown in figure 3.4 (b) inside red dotted squares (airflows are represented by green lines). This behavior can be explained by the total opening area created by the four openings at the South facade and the four lower openings at the North facade. Individually they do not meet the requirements to consider them as large openings (where bidirectional flows are most likely to occur), but together they behave as a large opening. Note that this consideration might be rendered moot when including wind effects, which might break the neutral plane established.

Furthermore, this before also leads to consider the following two inquiries: (1.) does the neutral plane remained at this fixed position during the entire opening period? (cf. fig. 3.4 (a)) Or (2.) does the neutral plane behave as a moving boundary implying that stack ventilation occurs? (for instance, starting as in figure 3.4 (c), then moving up to location as in figure 3.4 (a), and continuing). CONTAM does seem to account for inquiry (2.), since it is allowed to perform transient simulations. However, a dimensionless analysis implementing the Froude number can help to determine the moments when wind effects become strong enough to break this neutral plane (NPL) established [71]. The analysis presented in chapter 2 implies that inquiry (2.) should be considered, since most days presented absence of wind.

Finally, by choosing a *two-way flow model*, CONTAM only allows the user to provide the opening dimensions, as well as, the value of the corresponding discharge coefficient C_d (where the default value is set to 0,78). The flow exponent n is fixed at a value of 0,5 (theoretical value established by Bernoulli's law); refer to §1.1.3.1 for definitions. In turn, the methodology to determine the value of the discharge coefficient and the flow exponent, is presented later in §3.3.

(5) Accounting for wind and thermal buoyancy effects

Wind effects are taking into account by an expression relating the relative dynamic pressure at the building height with the wind speed. The following equation computes the relative wind pressure at each facade:

$$P(t) = \frac{1}{2} \cdot \rho \cdot \mathcal{V}_{met}^2(t) \cdot C_f \cdot C_p(\phi_{WS}) \qquad [\text{Pa}] \tag{3.1}$$

where $\mathcal{V}_{met}$ represents the wind speed measured at a free height of 10 m by a meteorological station. The coefficient C_f, named *wind speed modifier*, considers the effects of the terrain where the building is installed regarding elevation and roughness, as follows:

$$C_f = \frac{\mathcal{V}_f^2}{\mathcal{V}_{met}^2} = A_o^2 \cdot \left[\frac{\mathscr{Z}_f}{\mathscr{Z}_{met}}\right]^{2\cdot\gamma} \qquad [-] \tag{3.2}$$

where $\mathcal{V}_f$ represents the wind speed at the facades height $\mathscr{Z}_f$ containing openings, and $\mathscr{Z}_{met}$ is the height where the meteorological station measures the wind speed. The factor A_o and exponent γ depend on the terrain type as shown in table 3.1.

A view of the terrain where our platform was installed, is presented in figure 3.5. From figure 3.5 (a), it can be inferred that the terrain surrounding the platform does not fit the characteristics of an urban terrain type, according to [101]; in this regard, a suburban terrain type seems an adequate classification for our case, and it will be considered in the simulations. The resulting C_f values for North and South

Table 3.1: Terrain type coefficients for the wind speed modifier [28].

Terrain type	Factor (A_o)	Exponent (γ)
Urban	0,35	0,40
Suburban	0,60	0,28
Airport	1,00	0,15

facades are presented in table 3.2.

Finally, in equation 3.1 the coefficient $C_p(\phi_{Wf})$ represents the external pressure coefficient which depends on the relative wind direction ϕ_W with respect to the azimuth angle of the facade ϕ_f, as: $\phi_{Wf} = \phi_W - \phi_f$.

The effects of thermal buoyancy are taken into account on the software by allowing to differentiate the temperature inside and outside of the zone. The transient conditions are considered by enabling the variation of the air density with temperature, but the air temperature of each zone is considered uniform throughout its volume.

Table 3.2: Resulting values of C_f for the *wind speed modifier* using equation 3.2.

Parameter	North	South
Facade height ($\mathscr{L}_f$) [m]	4,9	3,7
C_f	0,2414	0,2063

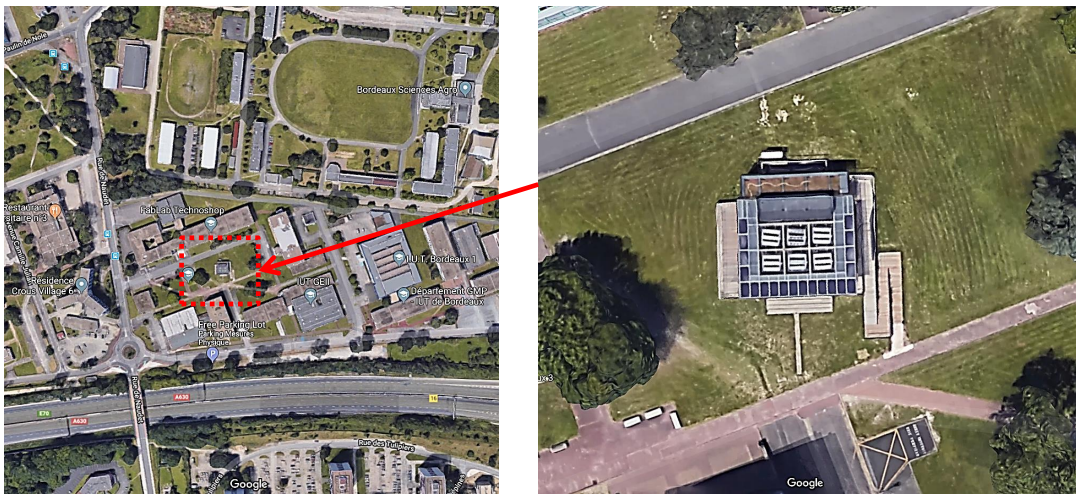

(a) **(b)**

Figure 3.5: (a) Surrounding around the platform, and (b) image of the platform [41].

(6) Estimation of external pressure coefficients

The values of this coefficient C_p are determined by following the standard EN 1991-1-4:2005 (Euro code 1). For this, the experimental platform is considered as a parallelepiped as shown in figure 3.6 (red boxes). Since the computation of C_p assigned to each facade depends on the ratio h/d (notation used in the standard), the C_p values attributed to the windward and leeward facades with openings (North and South) are $+0{,}76$ and $-0{,}42$, respectively. This values were obtained by interpolation (cf. table 3.3, values in red color). In the standard, the distance h is the height from the ground to the high-

est point of the building, and d is the length of the facade longitudinal to the wind direction (cf. fig. 3.6).

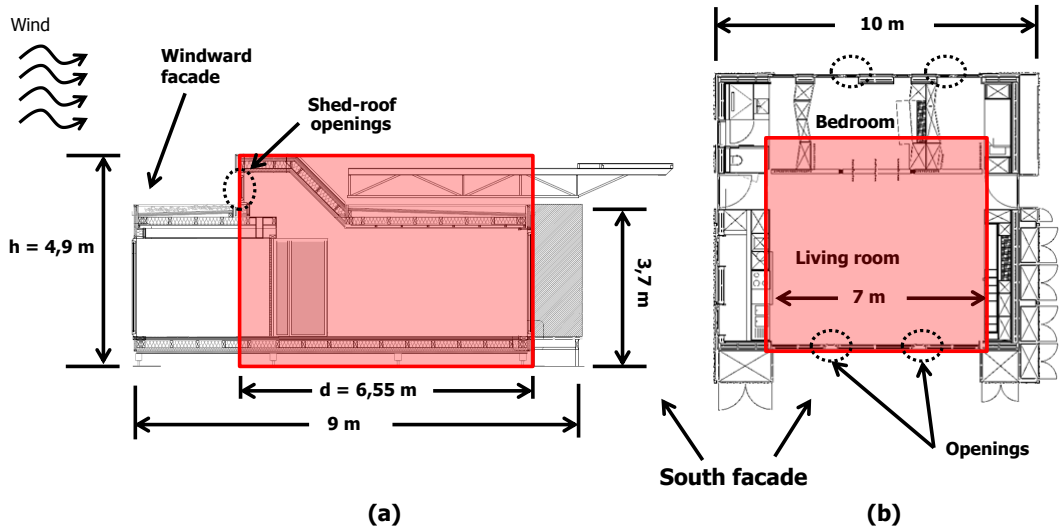

Figure 3.6: Building morphology approximation implemented in the estimation of the external pressure coefficients (red boxes): (a) West view, and (b) Top view.

Table 3.3: Recommended external pressure coefficient values for rectangular vertical walls.

			$C_{pe,10}$				
		h/d	A	B	C	D	E
b	6,55 m						
d	7,00 m	1				+0,8	−0,5
e	6,55 m	0,6986	−1,2	−0,8	−0,5	+0,76	−0,42
h	4,89 m	≤0,25				+0,8	−0,5
C_p				−0,856		+0,76	−0,42

For the C_p values attributed to the facades longitudinal to the wind direction (perpendicular to the windward facade), the norm recommends three different regions with different C_p values, depending on the distance away from the windward facade. The C_p values assigned for each of these regions are listed in table 3.3 under A, B and C, namely −1,2, −0,8 and −0,5, respectively. Since there are no openings at the West and East facades, the need of knowing the C_p value for these facades is unimportant when either the North or South facades are windward facades. When either the East or West facades are windward facades, the C_p values of the facades longitudinal to the wind direction (North or South) are important since they contain the openings. In this case, to compute the C_p values for the longitudinal facades, we calculate an average C_p value by weighting the C_p values of each region as follows (no interpolation is needed):

$$\overline{C_p} = \frac{e/5}{d} \cdot [C_{p_A}] + \frac{4 \cdot e/5}{d} \cdot [C_{p_B}] + \frac{d-e}{d} \cdot [C_{p_C}] \qquad [-] \tag{3.3}$$

Therefore, for the case where the North facade is the windward facade, the C_p values are assigned as follows: +0,76 for 0° and 360°; −0,856 for 90° and 270°; and −0,42 for 180° (the leeward facade). For intermediate angles, on CONTAM, the user has the option to choose between linear or polynomial

interpolation on the *wind pressure profile* window; a polynomial interpolation have been chosen here, refer to figure 3.7.

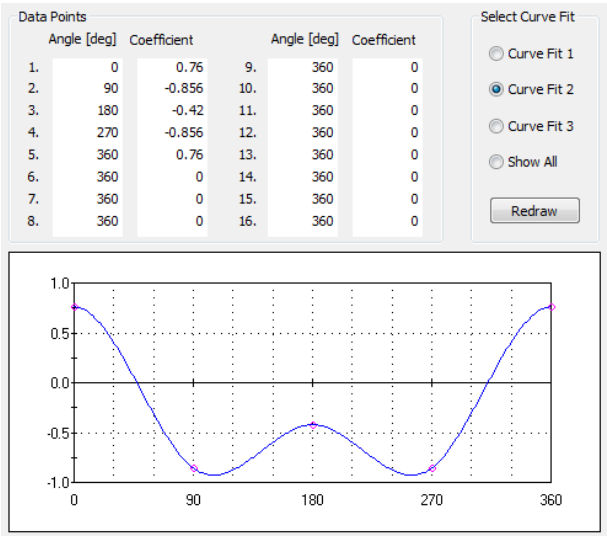

Figure 3.7: External pressure coefficient C_p profile used on the simulations.

(7) Airflow simulations on CONTAM

The airflow simulations can be performed by either considering weather data from an Energy Plus file-type or manually changing the values of both the indoor and outdoor temperatures, and wind speed and direction, on the *Edit weather data: weather and wind parameters* window. To account separately for the influence of wind and thermal buoyancy effects on the airflow rate (in the form of *ach*), we followed the procedure illustrated in figure 3.8:

a) Airflow rate due to wind effects only: In order to isolate the influence of wind effects on the *ach*, both the indoor (T_{ia}) and outdoor (T_{oa}) air temperature are set to have the same value, and the simulations are performed by varying the wind speed (V) and direction (ϕ_W), arbitrarily. The wind speed from 1 to 10 $m \cdot s^{-1}$; keeping the wind direction at a constant angle, and this was performed for different angle values, from 0 to 360°. Since the resulting *ach* only depends on wind speed and direction, we referred to this air change per hour as ach_W.

b) Airflow rate due to thermal buoyancy effects only: For isolating the effects of thermal buoyancy on the *ach*, the wind speed is set to zero. Then, the simulations are performed by varying the indoor and outdoor air temperatures arbitrarily within the temperature range encountered in the measurement campaigns. We referred to the resulting air change per hour due only to thermal buoyancy as $ach_{\Delta T}$.

In summary:
In order to perform the airflow simulation on CONTAM, the following requirements are still needed:

1. The airflow characteristics of both the openings and the tightness of the building envelope.
2. the location of the air infiltrations/leakages.

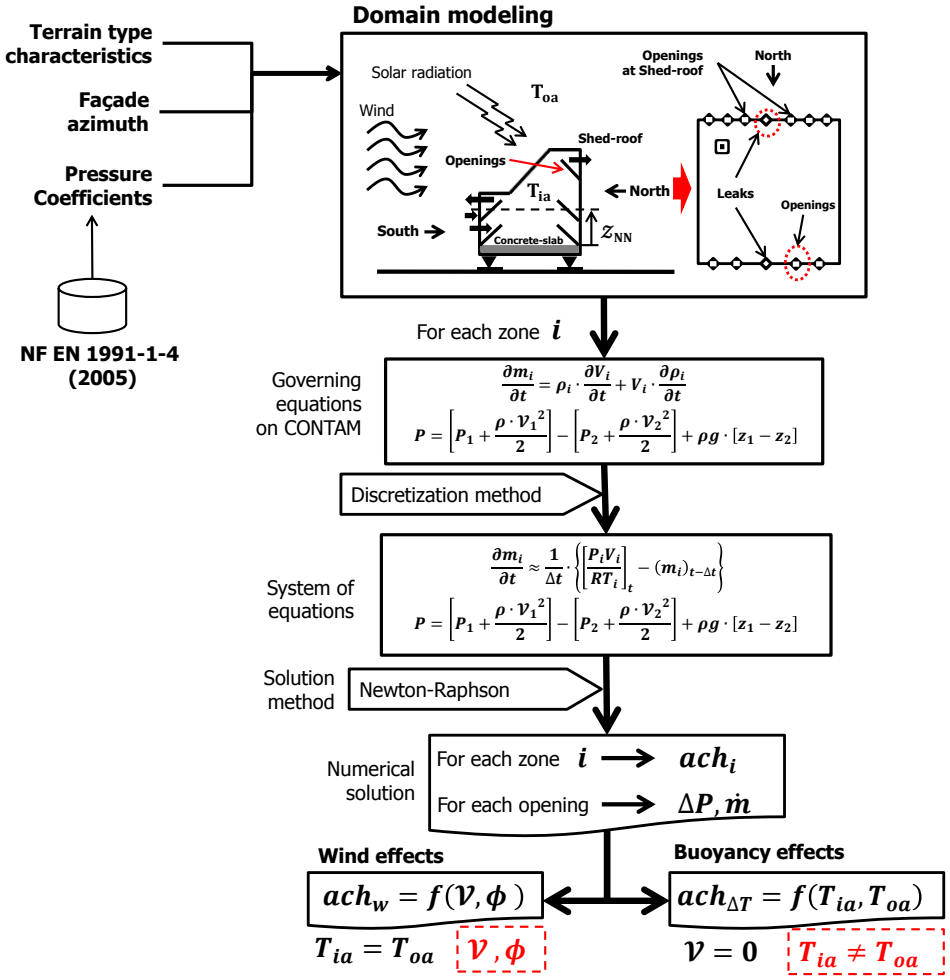

Figure 3.8: Schematic of the simulation process employed.

3.3 Airflow characteristics of the openings

In order to determine the airflow characteristics of the air-leakage and openings, to complete the *airflow model* on the software, airtightness tests (also known as blower door tests or fan pressurization tests) are implemented. For the air-leakage (openings closed), the airtightness tests are performed following the procedure recommended by the standard NF EN 13829. For the openings, we proposed to follow the same procedure as for the latter, but with the openings opened (similar to [55]).

We decided to characterize the airflow capacity of the platform openings in terms of discharge coefficient and airflow rate, instead of using the values reported in the literature (cf. §1.1.3.1). The reason lays in the morphology of the openings in the platform, which are equipped with a high tightness level (cf. fig. 3.9).

3.3.1 Recovery of the envelope tightness and airtightness tests

Since the platform had been affected due to various phases of assembly and transport, its envelope was carefully examined by pressurizing the platform with the ventilator and using the smoke pencil

(a) (b)

Figure 3.9: Tightness of the openings: (a) South, and (b) North facades.

to identify the regions most likely to attend air-leakages, based on [21]. Before this, all air-conducts related to the mechanical ventilation and PCM system were sealed (cf. fig. 3.10 (a)-(b)).

After identification, polyurethane foam in aerosol (with a traction resistance up to 175 kPa and density of 1,09 $g \cdot cm^{-3}$) and the "special tightness adhesive", were employed to close the big holes and to reinforce the joinery (cf. fig. 3.10 (c)-(f)). Consecutively, airtightness test were performed to see how each hole sealed and joinery reinforced, reduces the air-leakage rate, and evaluate if it met the regulated air-leakage rate (cf. fig. 3.12, and table 3.4). It appears that only around 27% of the air-leakage were reduced by performing the actions in table 3.4. Finally, after these actions, the majority of the air-leakages were identified to be located at the West facade due several electrical networks (cf. fig. 3.10 (e)); location of part of the home automation system.

(a) (b) (c) (d) (e) (f)

Figure 3.10: Sealing of air-conducts related to the mechanical ventilation and PCM system (a)-(b), indicated by red arrows. Reinforcement of joinery (c)-(d), red rectangles. Sealing holes due to electrical networks and water system (e)-(f), indicated by red arrows.

(1) Airtightness tests with openings closed

Considering that the outdoor conditions can strongly influence the variability of the outcome of each test, two measurement campaigns were carried out in 2015 and 2016 to repeat the tests as many as possible. In 2015, 34 tests were performed in ten different days from June 17th to October 30th, e.g.,

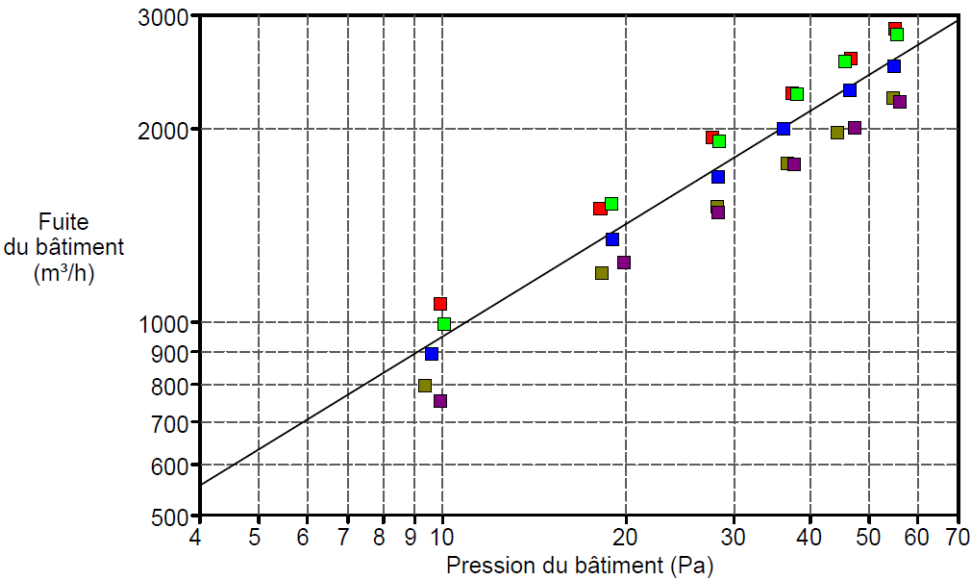

Figure 3.11: Airtightness tests results performed on June 15th, 2015.

Table 3.4: *ach* results from airtightness tests performed on June 15th, 2015.

Test n°	Color code	ach_{50}* $[h^{-1}]$	Action
1	Red	13,07	After blocking all mechanical ventilation conducts
2	Green	12,99	After sealing the bedroom window-door (cf. fig.3.10 (c))
3	Blue	12,53	After sealing big holes found in electrical networks and hot water system (cf. fig.3.10 (e)-(f))
4	Olive	12,09	After sealing door joinery (cf. fig.3.10 (d))
5	Purple	11,72	After sealing the kitchen extractor

**ach* at a pressure difference of 50 Pa.

on June 17th, the air-leakage test was performed three times. In 2016, ten tests were performed in six different days from September 20th to October 11th. The experimental plan implemented for airtightness tests was the protocol recommended by the standard NF EN 13829; experimental results are presented latter in §3.4.

(2) Airtightness tests with openings opened

Part of the tests performed during the measurement campaigns consisted of opening a set of openings and performing the same test as for the case of openings closed. In this case, depending on the opening configuration one blower door could not achieve the pressure difference levels recommended by the standard, and thus, two blower doors were implemented simultaneously, as shown in figure 3.12. For this the software TECLOG was used.

3.3.2 Discharge coefficient of the openings

For the determination of the discharge coefficient, the following expression arises by equalizing the theoretical and empirical definitions of the airflow capacity of an opening (cf. eq.1.6 and eq.1.7

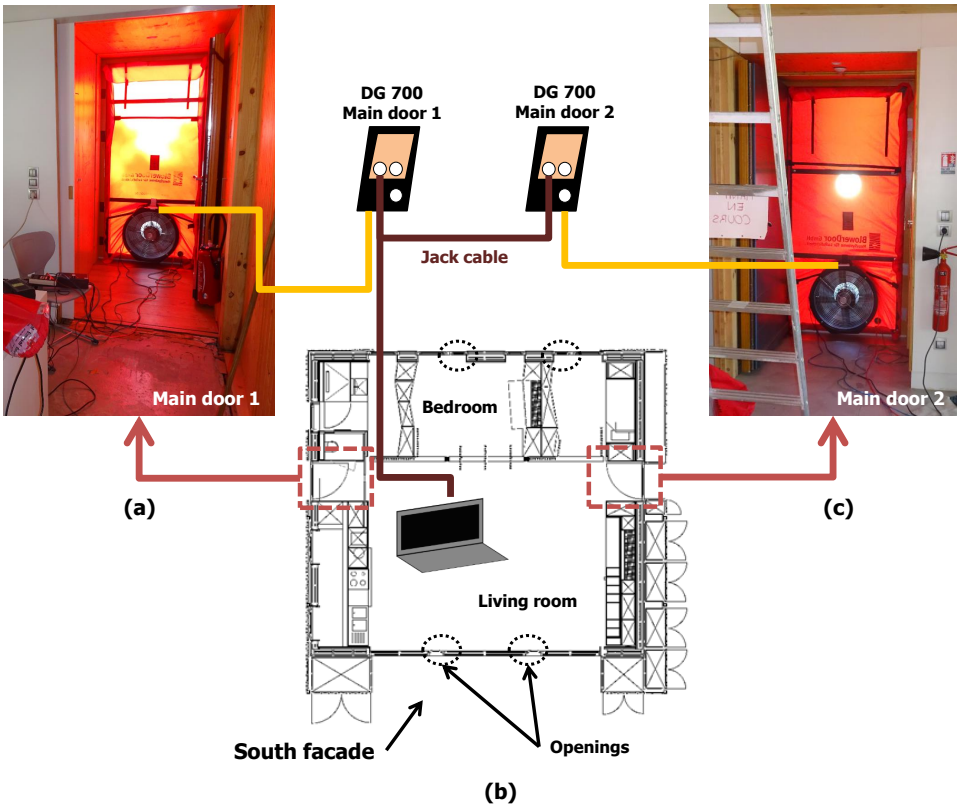

Figure 3.12: Experimental set-up for airtightness tests with openings opened. (a) Blower door installed at the West door. (b) Location of both blower doors. (c) Blower door installed at the East door.

(pp.15-15), respectively):

$$C_d\left(\Delta P\right) = \frac{\mathscr{C}}{S_{eff}} \cdot \left[\frac{\rho}{2}\right]^{1/2} \cdot \left[\Delta P\right]^{n-1/2} \qquad [-] \tag{3.4}$$

where, S_{eff} represents the effective area of the opening and is calculated for the tilted window type using equation 1.9 (p.18), by knowing the opening dimensions and their opening-angle. In our case, the latter is equal to 20°, which corresponds to the maximum opening-angle of all the openings in the platform. A similar expression for C_d can be obtained by the definition given in [47], but it involves other characteristics of the openings in addition to those in equation 3.4. Therefore, we only require the value of the airflow rate coefficient $\mathscr{C}$ and the flow exponent n, for each opening to determine an expression of their corresponding discharge coefficient as a function of the pressure difference.

Finally, since equation 3.4 depends on the pressure difference, it is condensed to the following expression in order to evaluate the discharge coefficient at each pressure difference to decide whether an average value can be used or not, over the working pressure levels:

$$C_{d_v}\left(\Delta P\right) = \mathscr{C}_{d_v} \cdot \left[\Delta P\right]^{n_{d_v}} \qquad [-] \tag{3.5}$$

where, as example for the openings at the South facade, $\mathscr{C}_{d_{south}}$ is equal to $\frac{\mathscr{C}_{south}}{S_{eff_{south}}} \cdot \left[\frac{\rho}{2}\right]^{1/2}$, and the exponent $n_{d_{south}}$ is equal to $n_{south} - 1/2$.

3.3.3 Identification of $\mathscr{C}$ and n for each opening

Here, the subscript "v" will be used to refer to the openings and "l" to refer to the air-leakage or infiltrations, i.e., $\mathscr{C}_{south}$ and n_{south} for the opening at the south facade, $\mathscr{C}_{north}$ and n_{north} for the opening at the north facade, and $\mathscr{C}_{shed}$ and n_{shed} for the opening at the shed-roof. In order to identify the values of $\mathscr{C}$ and n for the openings, the following is considered for processing the results from the airtightness tests with openings opened:

- The air-leakage are present in every test.
- The openings at the South and North facades are programmed by default to open and close all four simultaneously. On the other hand, the two openings at the shed-roof can both be opened simultaneously or individually. Therefore, the coefficient $\mathscr{C}_{South}$ includes all four openings; this coefficient must be divided by four to know the value of only one opening.

Then, with the airtightness tests results, an expression similar to equation (1.7) (p.15) is obtained by fitting a power law regression to the airflow rate results with respect to the pressure difference. In general, the fitted regression for each test with openings opened, yield:

$$\dot{V}_{v+l}\left(\Delta P\right) = \mathscr{C}_{v+l} \cdot \left[\Delta P\right]^{n_{v+l}} \qquad \left[\mathrm{m^3 \cdot s^{-1}}\right] \tag{3.6}$$

where $\dot{V}_{v+l}$ represents the total airflow rate through the openings and leakages, e.g., $\dot{V}_{south+l} = \mathscr{C}_{south+l}\left(\Delta P\right)^{n_{south+l}}$, for the test where the openings at the South facade remained open. Now, the airflow rate only through the openings can be either obtained by using directly, the airflow rate measurements:

$$\dot{V}_v = \dot{V}_{v+l} - \dot{V}_l \qquad \left[\mathrm{m^3 \cdot s^{-1}}\right] \tag{3.7}$$

or by employing the fitted regression as follows:

$$\dot{V}_v\left(\Delta P\right) = \mathscr{C}_{v+l} \cdot \left[\Delta P\right]^{n_{v+l}} - \mathscr{C}_l \cdot \left[\Delta P\right]^{n_l} \qquad \left[\mathrm{m^3 \cdot s^{-1}}\right] \tag{3.8}$$

which, ultimately, corresponds to the following expression for only the openings:

$$\dot{V}_v\left(\Delta P\right) = \mathscr{C}_v \cdot \left[\Delta P\right]^{n_v} \qquad \left[\mathrm{m^3 \cdot s^{-1}}\right]. \tag{3.9}$$

3.4 Results and analysis

3.4.1 Airtightness tests and discharge coefficient identification

The linear regressions resulting after processing the data from airtightness tests, for identification of the airflow rate coefficient ($\mathscr{C}$) and flow exponent (n) of each opening with the procedure developed in §3.3.3, are grouped in table 3.5. Also, the parameters needed to identify the value of the discharge coefficients through equation 3.5, for each opening, are included (cf. table 3.5, three last rows).

Since we obtained an expression for the discharge coefficient which depends on the pressure difference (ΔP), instead of a constant value, the working pressure difference must be known in order to determine the values of the discharge coefficient. In order to have an estimate of the working range for

Table 3.5: Results of airtightness tests.

	Openings opened					
	Shed-roof	Shed-roof	North	South	South+shed	South+North+shed
Number of openings	1 (West)	2	4	4	6	10
$\mathscr{C}_l$ $\left[\mathrm{m^3{\cdot}s^{-1}{\cdot}Pa^{-n_l}}\right]$	0,0325	0,0325	0,0353	0,0358	0,0861*	0,0375
n_l	0,6560	0,6560	0,6560	0,6500	0,5800*	0,6400
R^2	0,9996	0,9997	0,9996	0,9998	0,9997	0,9991
$\mathscr{C}_{l+v}$	0,1936	0,3547	0,5906	0,7078	1,3000	1,8220
n_{l+v}	0,5500	0,5430	0,5010	0,5340	0,4151	0,4727
R^2	0,9957	0,9991	0,9996	0,9963	0,9972	0,9998
$\mathscr{C}_v$	0,1619	0,3231	0,5619	0,6744	1,2250	1,7920
n_v	0,5133	0,5241	0,5048	0,5251	0,3955	04666
R^2	0,9999	0,9999	0,9999	0,9999	0,9999	0,9999
$S_{v_{eff}}$ $\left[\mathrm{m^2}\right]$	0,4840	0,4840	0,3575	0,3473	—	—
$S_{total_{eff}}$ $\left[\mathrm{m^2}\right]$	0,4840	0,9680	1,4300	1,3890	1,2430**	2,1420**
$\mathscr{C}_{d_v}$	0,2591	0,3051	0,3792	0,4081	—	—
n_{d_v}	0,0133	0,0241	0,0048	0,0251	—	—
R^2	0,9884	0,9992	0,9972	0,9997	—	—

*The values of $\mathscr{C}_l$ and n_l changed due to a malfunction of the openings at the North facade.
**Using the Canadian convention EqLA (Equivalent Leakage Area): pressure difference of 10 Pa with a dicharge coefficient of 0,6 (hole with sharp edges).

ΔP, the pressure difference was measured at two points during a short period (from July 9$^{\text{th}}$ to 11$^{\text{th}}$); the values encountered are shown in figure 3.13 (a). Also in this figure, the following is presented:

(a) The pressure measurements at two point in the platform, where P1 is located at the South facade (green line), and the P2 is located at the North facade (red line).
(b) Location of these measurement , P1 and P2.
(c) A zone presenting an absence of wind.
(d) Another zone presenting an absence of wind.
(e) An schematic of the platform, where the prevalent wind direction is indicated (250°).
(f) The corresponding wind speed (red) and wind direction (blue).

The corresponding wind speed and direction from the meteorological station and the location of the two points of measurement are also presented in this figure (cf. fig. 3.13 (b) and (f). During these measurements, only the openings at the South and shed-roof were functional.

The behavior of both P1 and P2 are in agreement with the dynamics of the wind speed and direction; the levels of P1 and P2 encountered might seem rather high for typical values encountered *in situ* measurements. However, similar pressure levels were encountered when performing wind tunnel tests for similar wind speed levels [98]. Nevertheless, we used these pressure ranges to evaluate the discharge coefficients.

The resulting airflow rates through the openings (cf. eq. 3.9) and their discharge coefficient (cf. eq. 3.5), for the pressure ranges, are presented in figures 3.14 and 3.15, respectively. In these figures, the results of both parameters, are presented for each group of openings: the set of four openings at the South facade (black lines), the set of four opening at the North facade (red lines), and the set of two openings at the shed-roof (blue lines).

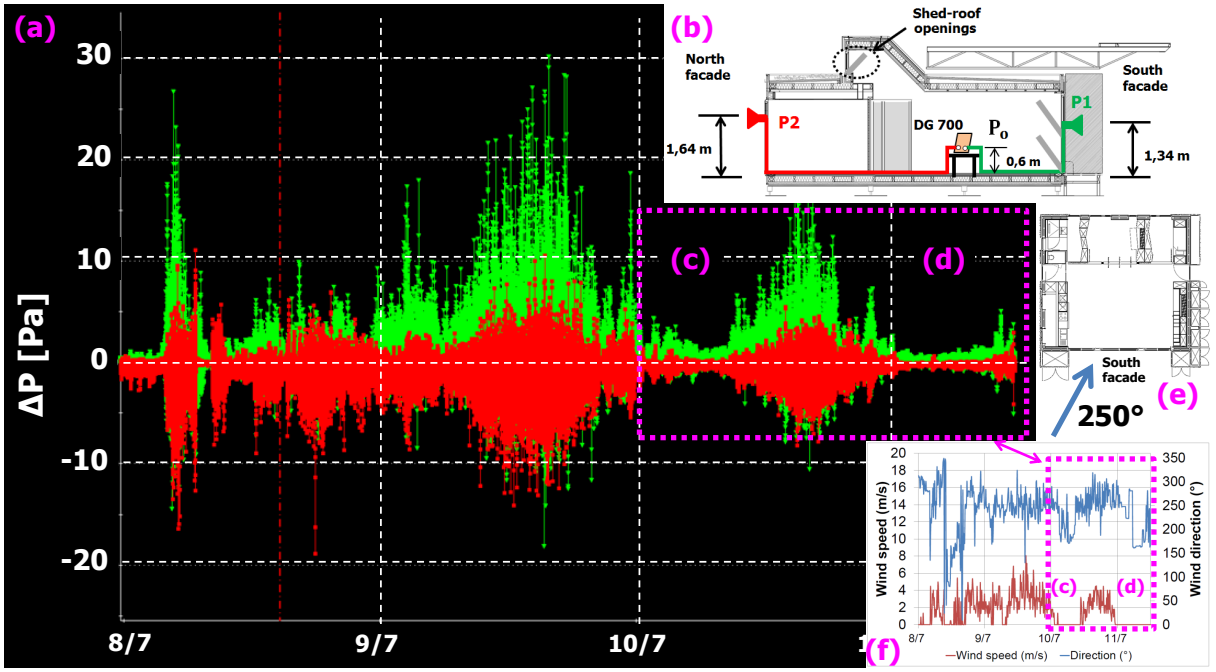

Figure 3.13: (a) Pressure measurements performed on July 8th - 11th, 2017: at one point on the South (P1, green) and North (P2, red) facades with respect to the indoor environment (P_o). (b) Experimental set-up and points of measurements (P1, P2, P_o). (c)-(d) Moments of absence of wind. (e) A schematic representation of a wind direction of 250°. (f) Corresponding wind speed (dark red) and direction (blue).

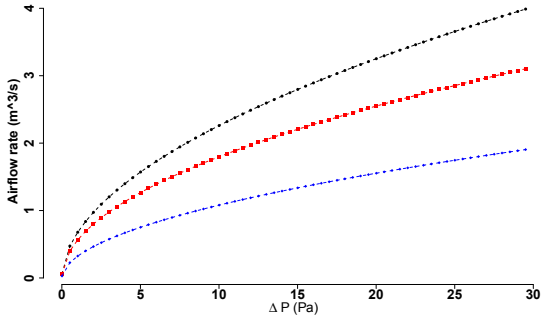

Figure 3.14: Airflow rate for each group of openings: South facade (black circles), North facade (red squares), and shed-roof (blue rhombuses).

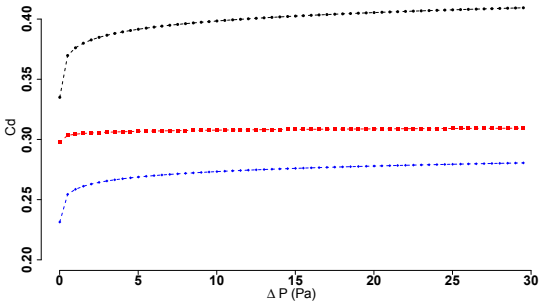

Figure 3.15: Values of discharge coefficient for each group of openings: South facade (black circles), North facade (red squares), and shed-roof (blue rhombuses).

The interest of showing the airflow rate for each set of openings is merely for comparison purposes with what has been found in the literature for the same type of openings. Let's take figure 1.1 for instance, the airflow rate is reported as a function of the opening degree in centimeters: 200 $m^3 \cdot h^{-1}$ for an opening degree of 12 cm. In our case, the opening degrees are: 16 cm for the openings at the shed-roof, 22 cm for those at the South facade, and 23 cm for those at the North facade. We can infer from this figure, that each of our openings must bare an airflow capacity larger than 200 $m^3 \cdot h^{-1}$ at least. In figure 3.14, it can be observe that the airflow capacity of each set of openings is larger than 200 $m^3 \cdot h^{-1}$ (0,056 $m^3 \cdot s^{-1}$). Note that the values in this figure correspond to a set of openings; for one opening, the values must be divided by the total number of openings: for one opening at the South

facade yields about 900 $m^3 \cdot h^{-1}$ at a ΔP of about 2,5 Pa.

Regarding the discharge coefficients presented in figure 3.15, their values do not appear to change significantly within the pressure range. In fact, their mean values result in 0,40±0,01 for the openings at the South facade; 0,31±0,002 for the openings at the North facade; and around 0,28±0,01 for the openings at the shed-roof. These values are similar to those found by [25, 24], but they are rather low, in comparison with those largely accepted in the literature, of around 0,6 - 0,7 for a similar type of openings [36, 50]. This difference (about 38%) might be explained by: (*i*) the tightness of the openings itself (cf. fig.3.9), or (*ii*) by the obstructions within the airflow path between the fan and the opening when performing the airtightness tests.

For the case (*i*), the tightness might increase the friction losses, and thus, yield a decrement in the discharge coefficient. For the case (*ii*), if the obstruction is a contributing factor to reducing the discharge coefficient, the corresponding loss coefficient values should be encountered in a decrementing order as follows: the openings at the shed-roof, then those at the North facade, and finally, those at the South facade. The more obstructions, the more significant the pressure losses. The same can not be stated for the tightness of each opening since it appears to be the same level of tightness for all the openings.

Then, if we compute the loss coefficients for each opening by introducing the values of the discharge coefficient encountered and the corresponding fully and effective opening areas into equation 1.8 (p.18), result in: 74,81 for the openings at the shed-roof; 17,06 for those at the North facade; and 7,55 for those at the South facade. These values are in agreement with the explanation given for the case (*ii*). The same equation was employed in [98], where, with a total and effective opening area of 1,82 and 0,377, respectively, the loss coefficient resulted in 28,9 with a discharge coefficient of 0,67. Unfortunately, no other experiments have been performed in order to support statements (*i*) and (*ii*).

In summary:
Performing *in situ* airtightness tests for the estimation of the friction characteristics of openings, might not be the most suitable choice due to the presence of internal obstructions, such as furniture, partition-walls, doors, among others. However, the implementation of these tests for the estimation of the airflow capacity in terms of airflow rate levels appears to agree with the values reported in the literature.

3.4.2 Comparison of the air change rate per hour using airtightness tests

Since the only indicator of the natural air change rate per hour (*ach*) we have is the ach_{50}, which only gives values for the infiltration rate, in this section we compare our results with a similar research work. To do this, we first compute the ach_{50} for each of the opening configurations presented in table 3.5, for either the case of openings opened or closed. For the case of opening closed, we only took the $\mathscr{C}_l$ and n_l values reported for the "South+shed" column in table 3.5 (0,08611 and 0,58), because this was the current infiltration rate state. For the case of openings opened, we took $\mathscr{C}_v$ and n_v (openings opened only, no leakages).

Table 3.6: Natural airflow rate (*ach*) with the standard.

	ach_l with openings closed (leakages) $[h^{-1}]$			
ach_l at 50 Pa	18,97			
ach_l according to K-P model*	0,95			
ach_l according to NF EN 12831:2004	0,76			
	ach_v with openings opened (with leakages) $[h^{-1}]$			
	Shed-roof	Shed-roof	North	South
Openings	1 (West)	2	4	4
ach_v at 50 Pa	27,48	57,02	92.25	119,86
ach_v according to K−P model*	1,37	2,85	4,61	6,00

*Refer to equation 1.12 on page 19.

Second, we use the K-P model (cf. eq. 1.12, p.19) to determine both the *ach* with openings closed and opened. The results are presented here after in table 3.6. The last row of this table presents the resulted *ach* for a specific opening configuration. Third, we compare these results with the values reported by R. Jack *et. al* [55] as shown in figure 3.16.

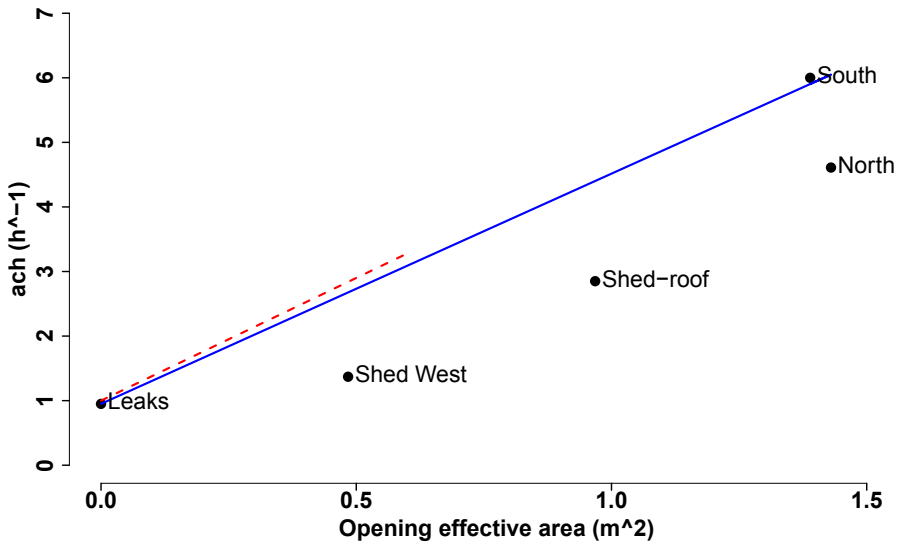

Figure 3.16: *ach* results from the K−P model as a function of the opening effective-area: work of [55] (red dashed line), and from our airtightness tests (black dots).

In figure 3.16, it can be observe that the greater the opening area, the greater the *ach* value, as expected. However, it can be observe that the configuration "South+shed" appears to have a smaller opening area than the "South" opening configuration.

3.4.3 Airflow simulation results

An schematic of the single-zone model constructed on CONTAM is presented in figure 3.17, where the air-leakages are equally distributed at the facades with openings (a), and at the West facade (b), respectively.

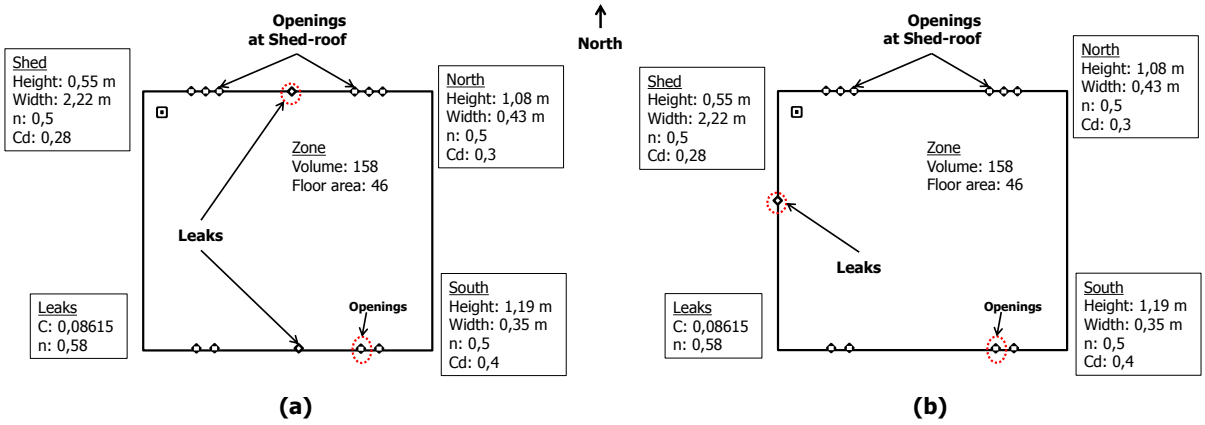

Figure 3.17: Schematic of the single-zone model employed in the simulations with leakages: (a) equally distributed at the facades with openings, (b) at the West facade only.

3.4.3.1 Air change per hour due to thermal buoyancy effects only

The simulation results for the air change per hour due to thermal buoyancy only $ach_{\Delta T}$ are presented in figure 3.18, for the case of air-leakage only (blue line), openings at the South and shed-roof opened with no leakages (red line), and all openings opened with no leakages (black line). The results are presented with respect to the indoor-outdoor temperature difference range employed in the simulations.

From these results, an expression relating the $ach_{\Delta T}$ and ΔT directly, can be obtained by fitting a power law regression as follows:

$$ach_{\Delta T} = \mathscr{A} \cdot \left| \frac{T_{ia} - T_{oa}}{T_{oa}} \right|^{x} \qquad \left[\mathrm{h}^{-1}\right] \tag{3.10}$$

where the values of $\mathscr{A}$ and x depend on the opening configuration. The values obtained for different configurations are presented in table 3.7. The interest of such expression lays in the facility to determine the value of $ach_{\Delta T}$ without repeating the simulations. The resulting regression models are in agreement with the theoretical description of the airflow rate due to a temperature difference (cf. eq. 1.3). These results are important since no knowledge of the airflow path is needed, and the simulation accessibility is very high.

Table 3.7: Regression results for $ach_{\Delta T}$ as a function of temperature.

	Leaks Equally distributed			Leaks at the West facade		
Openings opened	$\mathscr{A}$ $[\mathrm{h}^{-1}]$	Exponent x	R^2	$\mathscr{A}$ $[\mathrm{h}^{-1}]$	Exponent x	R^2
None (leakages)	4	0,5847		0*	—	
South + shed-roof	63	0,5019		63	0,5019	
South + shed-roof + North	103	0,5017	0,9999	103	0,5017	0,9999
South + shed-roof ($C_d = 0{,}7$)	130	0,5024		130	0,5024	
South + shed-roof + leaks	67	0,5051		66	0,5040	

*Due to the air-leakage model in CONTAM, which only admits unidirectional flow.

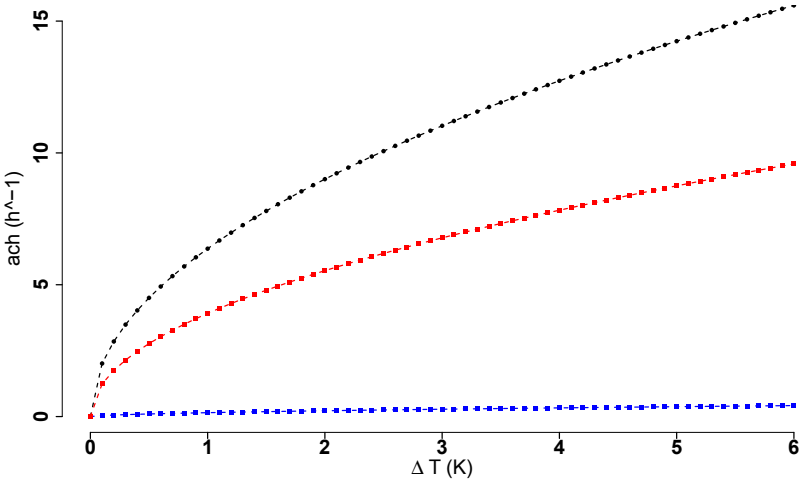

Figure 3.18: Resulting *ach* due to thermal buoyancy only ($ach_{\Delta T}$): air-leakages only (blue line), openings at the South and shed-roof opened with no leakages (red line), and all openings opened with no leakages (black line).

3.4.3.2 Air change per hour due to wind effects only

The simulation results for the air change per hour due to wind effects only ach_W are presented in figures 3.19-3.21.

a) With leakages equally distributed at the facades with openings:

In figure 3.19, the resulting ach_W for the case of air-leakage only (openings closed) with respect to the wind speed are presented for different wind directions. In figure 3.20, the resulting ach_W for the case of openings opened with no leakages with respect to the wind speed are presented for different wind directions.

Similarly, a linear regression can be obtained for the resulting *ach* as a function of the wind speed, as follows:

$$ach_W = \mathscr{B}(\phi_W) \cdot \mathscr{V}_{met}^{y} \qquad \left[\mathrm{h}^{-1}\right] \tag{3.11}$$

where y depends on the opening configuration: leaks only (cf. table 3.8) or openings with no leaks ($y = 1$). $\mathscr{B}$ is the slope of each line in figures 3.19 and 3.20, which value depends on the wind direction ϕ_W, and also, on the opening configuration. By plotting each slope $\mathscr{B}(\phi_W)$ with respect to ϕ_W, results in the points presented in figure 3.21. The blue squares represent the different slopes from figure 3.19 (air-leakages), and the red squares represent the slopes from figure 3.20.

This behavior, exhibit by $\mathscr{B}(\phi_W)$, can be approximated by a Fourier's series regression (cf. fig. 3.21, dashed lines). A three cycles Fourier's series was encountered to fit this behavior at less than 5% of relative error, resulting in:

$$\begin{aligned}\mathscr{B}(\phi_W) = {} & A + B \cdot \cos[\omega \cdot \phi_W] + C \cdot \sin[\omega \cdot \phi_W] + D \cdot \cos[2 \cdot \omega \cdot \phi_W] + E \cdot \sin[2 \cdot \omega \cdot \phi_W] \\ & + F \cdot \cos[3 \cdot \omega \cdot \phi_W] - G \cdot \sin[3 \cdot \omega \cdot \phi_W] \qquad \left[\mathrm{h}^{-1} \cdot \mathrm{m}^{-y} \cdot \mathrm{s}^{y}\right]\end{aligned} \tag{3.12}$$

where the values of the coefficients A to G and ω, are presented in table 3.8. Note that only these

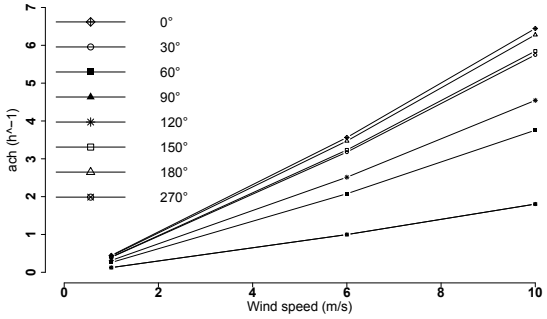

Figure 3.19: Wind results of simulations with leakages equally distributed at the facades with openings for different wind direction: leakages only.

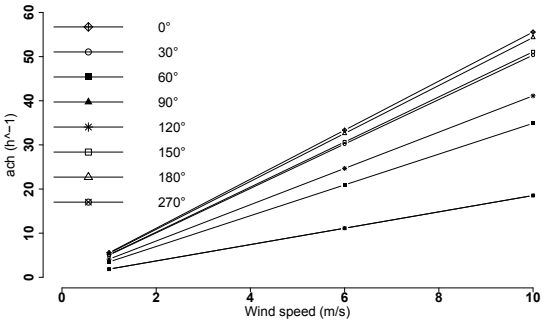

Figure 3.20: Wind results of simulations with leakages equally distributed at the facades with openings for different wind direction: South + shed only, no leakages.

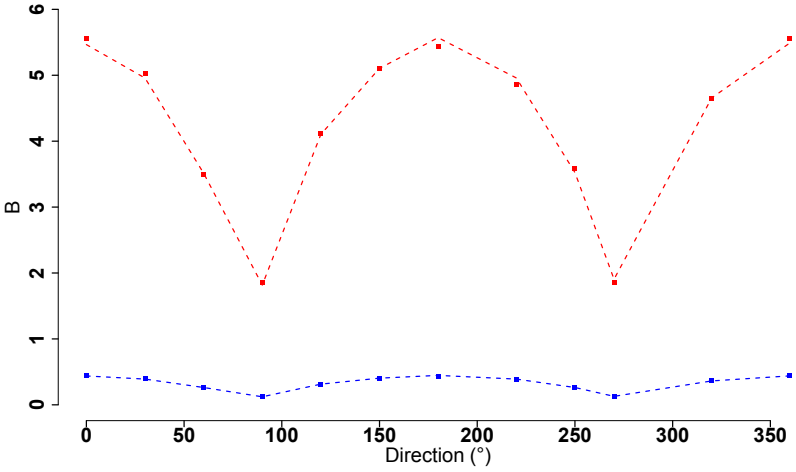

Figure 3.21: Results of $\mathcal{B}(\phi_W)$ for different wind direction and fitted Fourier's regression: Openings south + shed without leakages (red) and Infiltrations only (blue).

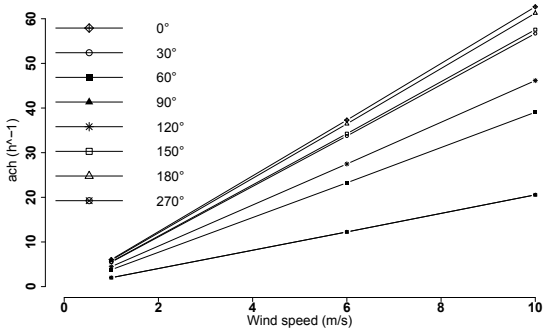

Figure 3.22: Wind results of simulations with leakages equally distributed at the facades with openings for different wind direction: South + shed + leakages.

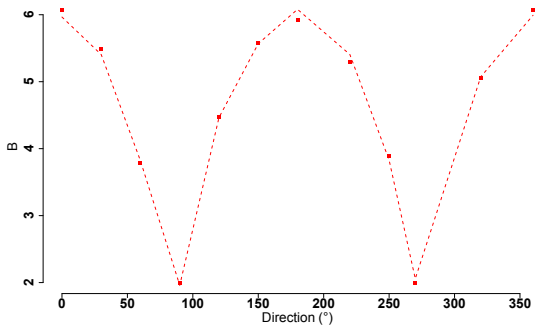

Figure 3.23: Results of $\mathcal{B}(\phi_W)$ for different wind direction and fitted Fourier's regression: Openings south + shed + leakages.

values are presented for the opening configuration South+shed-roof since they were the only functional openings during the measurement campaigns, as mentioned earlier.

Regarding the resulting ach_W for the two locations of air-leakages, the value of $\mathscr{B}(\phi_W)$ for "South + shed + leaks" (cf. table 3.8), appears to have only a slight difference. Also, a slight difference is presented between $\mathscr{B}(\phi_W)$ for the case of "South+shed+leaks" (at the West facade) and "South+shed" (no leakages).

This differences indicate that the consideration of either the case of openings opened **without leaks** or the case of openings opened **with leaks** at the West facade, will not have a significant influence in the resulting net ach_W. However, having the leaks equally distributed at the facades with openings slightly increases the net ach_W, and this for openings at the South and North facades. The results for the leaks located at the West facade are presented in the following.

Table 3.8: Resulting values for $\mathscr{B}(\phi_W)$.

	Leaks Equally distributed								
Openings	y	A	B	C	D	E	F	G	ω
Leakages	1,16	0,328	0,1367	-0,0415	-0,0398	0,0237	0,0129	-0,01702	0,03307
South + shed	1,00	4,234	1,5620	-0,4756	-0,4890	0,2869	0,1585	-0,2150	0,03305
South + shed + leaks	1,00	4,611	1,7160	-0,5226	-0,5343	0,3139	0,1732	-0,2344	0,03305
	Leaks at the West facade								
South + shed + leaks	1,00	4,471	1,6380	-0,5668	-0,4582	0,2971	0,1191	-0,23430	0,03272

b) With leakages located at the West facade:

The simulation results for the ach_W as a function of the wind speed and the coefficient $\mathscr{B}$ as a function of the wind direction are presented in figures 3.24 and 3.25, respectively. It can be observe, that in figures 3.25 and 3.24, and 3.26 and 3.25, that only a slight difference is presented for ach_w and $\mathscr{B}$, respectively as mentioned before.

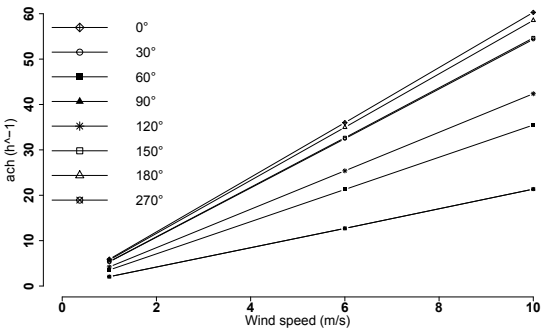

Figure 3.24: Wind results of simulations with leakages at the West facade for different wind direction: South + shed + leakages.

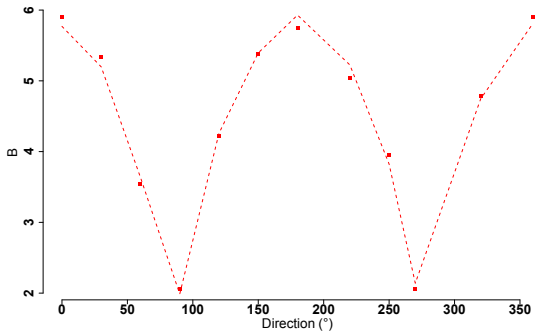

Figure 3.25: Results of $\mathscr{B}(\phi_W)$ with leakages at the West facade for different wind direction and fitted Fourier's regression: Openings south + shed + leakages.

Similar behavior as in figures 3.21, 3.25 and 3.29, has been reported in the literature [37, 61, 62], specifically, in [62] (cf. fig. 1.18, p.21). However, the applicability of obtaining the regression models presented here before (cf. eqs. 3.10-3.12), is rather less complicated than those propose by other researchers [62,

97].

In summary:
The location of the air-leakages has no apparent influence on the results given by the CONTAM software.

3.4.3.3 Consistency of airflow simulation results

This section is dedicated to give explanation about the correlations draw from the simulation results. For instance, take expression (3.10); a similar expression can be easily conceived by replacing equation (1.3) into equation (1.6), and assuming Boussinesq's approximation. The difficulty lays in the determination of the airflow rate coefficient $\mathscr{C}$, since the common expressions for the effective area reported in the literature does not applied for out platform due to the required knowledge of the airflow paths [2]. On the contrary, the determination of the airflow flow exponent might not be complicated, since for the case of openings opened only (no leaks) the expected value of n is 0,5. For the case of leaks only (openings closed), the value of n remained unknown without performing experiments.

Regarding equation (3.11) can be easily identified by replacing equation (1.2) on page 12 into equation (1.5) on page 15. Here, the difficulty also lays in the determination of the coefficient $\mathscr{C}$, since it depends on the airflow path and on the wind direction. The flow exponent n, for the case of openings opened only, the expected value is one; for the case of opening closed, the value of y is two times the value of n ($y = 2 \cdot n$), but also the n value can only be determined by experimental techniques.

3.4.3.4 Combined effects: assistance and opposition

In order to understand the superposition of both effects (wind and buoyancy), airflow simulations were performed by maintaining constant one effect and varying the other. For instance, figure 3.26 presents the resulting net *ach* value for a wind speed of 1 m·s^{-1} ($\mathscr{V}_{met} = 1$ m·s^{-1}) at different temperature differences and different wind directions. For the temperature differences, the outdoor air temperature was varied; maintaining the indoor air temperature constant at 22 °C.

In this figure, it can be observe that for a wind direction within the first and fourth quadrant (namely $90° > \phi_W > 270°$), the *ach* value appears to decrease first and then increase, where the threshold appears to be a temperature difference (ΔT) depending on the direction: 2 K for 0° and 20°, 1 K for 60°, 1 K for 320°. For wind directions greater than or equal to 90°, this behavior disappears. Such behavior is consistent with the case where the wind effect opposes and assists a stack ventilation strategy (cf. fig. 1.6, p.15). Thus, the behavior for wind directions between 0° and 90° indicates that wind and buoyancy effects oppose to each other; for wind directions greater than or equal to 90°, both effects assist each other.

This can be explained by assuming plausible airflow path, for instance, since the indoor air temperature is higher than than the outdoor air, the airflow path established should be: outdoor air enters the building from the lower openings and leaves the building through the upper openings. In this case, the only lower openings opened are at the South facade, because at the North facade, only the openings at the shed-roof are opened. Therefore, for a wind direction of between 0° (wind towards the South pole),

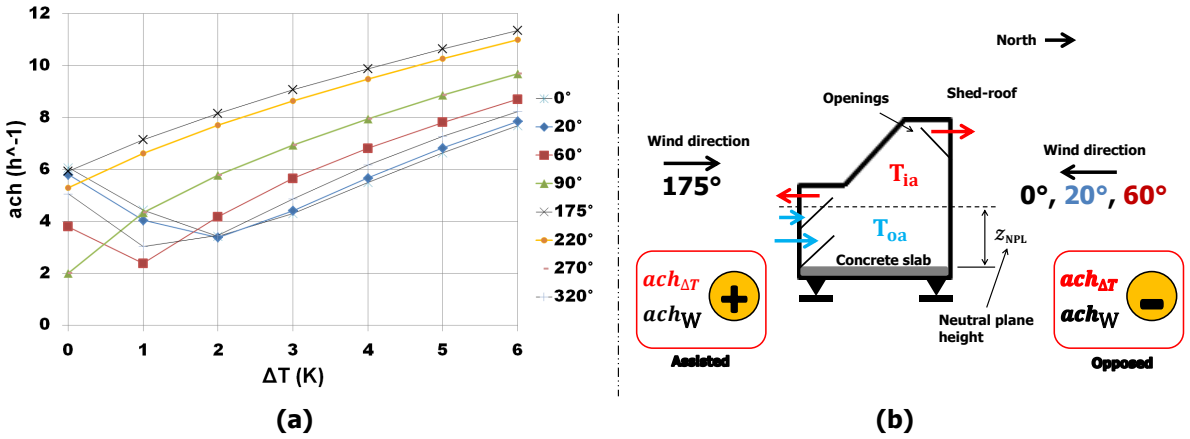

Figure 3.26: (a) Simulation results when combining wind an buoyancy effects, for a constant wind speed of 1 $m{\cdot}s^{-1}$ and different wind directions. Indoor temperature was fixed at 22 °C, while the outdoor temperature was decreased from 22 to 16 °C. (b) Illustration of the situations presented here at the right-hand side of this figure, for three four wind direction; showing the opposing and the assisting of both effects.

the wind encounters the outgoing flow through the openings at the shed-roof (windward facade), and thus, both flows are opposed to each other, decreasing the net airflow rate in the building. Conversely, for an opposite wind direction, say 180 °, the wind encounters the outgoing flow at the upper openings at the South facade (windward facade) and the ingoing flow at the lower openings. For this case, it appears that the net airflow rate is assisted, which indicates that the wind reinforces the ingoing flow due to buoyancy effects. Additionally, for wind direction of 90° or 270°, a assisting effect is expected, since the wind encounters outgoing flow through four upper openings, and thus, enhancing the net airflow rate (cf. fig. 3.26).

3.5 Concluding remarks on the airflow characteristics of the platform and perspectives

The undertaken work in this chapter was devoted to characterizing the natural airflow rate in the platform via airflow simulation on CONTAM. This characterization aimed to determine an expression relating the net *ach* as a function of the wind speed and direction, and the indoor-outdoor temperature difference. Thus, we can retain the following remarks:

- For the buildings or enclosures, where the airflow path is difficult to be determined due to a large number of openings, focusing on estimating the net airflow rate by using network airflow models, can lead to avoiding unnecessary difficulties.
- The assumption of air-leakage equally distributed at the facades with openings seems to be appropriate, instead of identifying them first by performing airtightness tests with the smoke pencil, when focusing on the global effect of wind and buoyancy via the net air change rate.
- Performing *in situ* airtightness tests for the estimation of the friction characteristics of openings, might not be the most suitable choice due to the presence of internal obstructions, such as furniture, partition-walls, doors, among others. However, the implementation of these tests for the

estimation of the airflow capacity in terms of airflow rate levels appears to agree with the values reported in the literature.

- Finally, from the airflow simulations for the combined wind and buoyancy effects, these effects appear to oppose to each other only in a specific range of wind direction.

At the moment, we may conclude that the real value of the natural air change rate in the platform remains uncertain. However, since our results have been compared with values reported in the literature, we may state that the values encountered may be a reasonable estimation of this parameter when an annual-averaged value is needed.

Moreover, the last part of this chapter has shown that we are not yet capable of reporting an expression that combines both wind and buoyancy effects directly, since: The net value of *ach* does not appear to be a simple addition when both effects are assisted, nor a simple subtraction when both effects are opposed. Therefore, an expression able to superpose both effects is still needed. In order to choose from the superposition models reported in the literature and to avoid any possible overestimation or underestimation of the *ach* value, it is necessary to determine its real value. For the latter, we are able to identify the value of *ach* by employing the heat flux and temperature measurements performed during the measurement campaigns (presented in chapter 2), and a global energy balance in the indoor air. The first part of the following chapter is dedicated to identify and compare the *ach* value.

Chapter 4

Identification of a thermal model to describe the behavior of the platform

Scope

This chapter is dedicated to constructing a thermal model with the aim of describing the behavior of the platform. This behavior is represented by three main elements: the indoor air temperature, the natural ventilation airflow rate, and the concrete-slab surface temperature. These three main elements are represented, respectively, through an energy balance for the indoor air, a semi-empirical expression for the natural airflow rate, and a non-uniform conduction heat transfer model for the concrete slab. The two first elements were identified together over experimental data. The last element was chosen after comparing the case of uniform and non-uniform heat conduction.

Such thermal model is wanted to contemplate the following aspects:

- To account, as much as possible, for the physical sense.
- To describe the thermal behavior accurately.
- To be able to adapt itself when the opening configuration strategy changes.

Thus, it is decided to implement a semi-empirical modeling approach by taking into account all analyses, data, and hypotheses, presented in previous chapters. Hereafter, we will refer to this model as the "coupled model."

4.1 Identification of a thermal behavior model for the indoor air using experimental data

4.1.1 Energy balance for the indoor air

The thermal behavior of the indoor air is modeled by following the energy balance equation of a fixed control volume in the case of an open thermodynamic system. This control volume (CV) is set to represent the entire volume of the experimental platform as a single-zone (cf. fig. 4.1). This assumption might be justified by the fact that all internal partition-walls and doors remained open during the measurement campaigns.

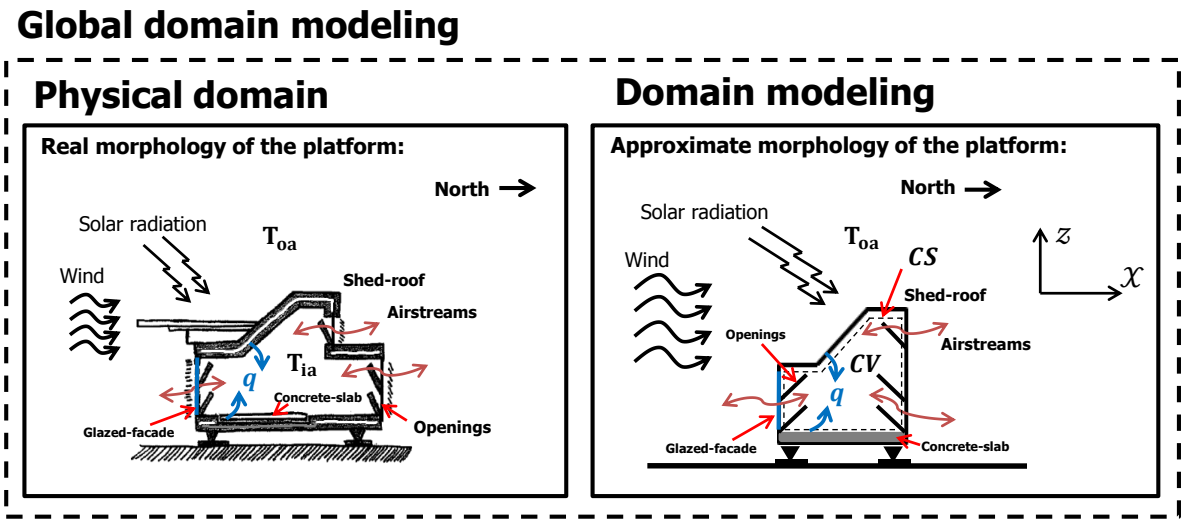

Figure 4.1: Schematic of the platform employed in the modeling. Left-hand side: physical domain (real domain). Right-hand side: domain modeling (approximation of the real domain). Airstreams (brown arrows), convective heat exchanges (blue arrows).

The "control surfaces" (CS) of this control volume (CV) consist of two types of thermodynamic boundaries: impermeable and permeable; this way to distinguish the type of boundary is introduced to separate the boundaries where heat and mass transfer are allowed (permeable) from those where only heat transfer is allowed (impermeable) [108]. The elements of the envelope: ceiling, floor, and walls (including windows) and natural ventilation openings (only when close), are considered as impermeable control surfaces (ICS). The natural ventilation openings, only when open, are considered as permeable control surfaces (PCS). A schematic representation of the exchanges in mass and heat between the indoor air volume and these CS is presented in figure 4.1.

Theoretically, since we consider a fixed control volume, the changes in the enthalpy of the indoor air can be written as follows [108]:

$$\left[\frac{\mathrm{d}\mathscr{H}(t)}{\mathrm{d}t}\right]_{CV} = \frac{\mathrm{d}}{\mathrm{d}t}\left[\oint_{CS}\overrightarrow{q(t)}\circ\overrightarrow{dS}\right] + \Phi_{gen}(t) + \sum_{in}\dot{m}_{in}(t)\cdot\left[\mathscr{H}(t) + \frac{\mathscr{V}(t)^2}{2} + g\cdot\mathscr{Z}\right]_{in} - \sum_{out}\dot{m}_{out}(t)\cdot\left[\mathscr{H}(t) + \frac{\mathscr{V}(t)^2}{2} + g\cdot\mathscr{Z}\right]_{out} \quad [\mathrm{W}] \tag{4.1}$$

where $\mathcal{H}(t)$ given in J represents the enthalpy. On the right-hand side of equation 4.1, the first term represents the heat exchanged between the impermeable control surfaces and the indoor air in the form of convection. This heat exchanged is represented by q(t) in J·m^{-2} (cf. fig. 4.1, blue lines). A power generation term Φ_{gen} in W represents any heat source within the CV, e.g., occupancy, lights, household appliances. The last two terms in equation 4.1 represent the heat exchanged with the airflow entering and leaving the control volume, respectively, where $\dot{m}(t)$, $\mathcal{V}(t)$, g, and $\mathcal{Z}$, represent the mass flow, the relative airstream speed, the gravitational constant, and the relative height of the airstream source, respectively.

Equation 4.1 can be simplified, after examine some considerations (explained hereafter), as follows:

$$\begin{aligned}\rho(T_{ia}) \cdot V_{ia} \cdot c_p(T_{ia}) \cdot \frac{\mathrm{d}T_{ia}(t)}{\mathrm{d}t} = {} & h'_{C_D}(t) \cdot S_D \cdot [T_{S_D}(t) - T_{ia}(t)] \;+\; h'_{C_P}(t) \cdot S_P \cdot [T_{S_P}(t) - T_{ia}(t)] \\ & + \; h'_{C_g}(t) \cdot S_g \cdot \left[T_{S_g}(t) - T_{ia}(t)\right] \\ & + \; V_{ia} \cdot \frac{ach(t)}{3600} \cdot \left[\rho(T_{oa}) \cdot c_p(T_{oa}) \cdot T_{oa}(t)\right] \\ & - \; V_{ia} \cdot \frac{ach(t)}{3600} \cdot \left[\rho(T_{ia}) \cdot c_p(T_{ia}) \cdot T_{ia}(t)\right] \qquad [\mathrm{W}]\end{aligned} \tag{4.2}$$

where the mass and specific heat capacity of the indoor air is represented by $\rho(T_{ia}) \cdot V_{ia}$ and $c_p(T_{ia})$, respectively, which together represent the heat capacity of the indoor air volume. The temperatures of the indoor and outdoor air are represented by $T_{ia}(t)$ and $T_{oa}(t)$, respectively. The surface temperature of the floor concrete-slab, ceiling and glazed-facade are represented by $T_{S_D}(t)$, $T_{S_P}(t)$, and $T_{S_g}(t)$, respectively; those surfaces in contact with the indoor air. Finally, the convective heat transfer coefficient is represented by $h_C(t)$. Also, in equation 4.2, the resulting net airflow rate, due to the airstreams entering and leaving the control volume through the permeable control surfaces, is represented by the term $ach(t) \cdot V_{ia}/3600$ in m^3·s^{-1}, where $ach(t)$ is the air change rate per hour in h^{-1}, V_{ia} is the indoor air volume, and the factor $1/3600$ is for dimension agreement, which converts the magnitude hours into seconds. Finally, the heat transfer associated with the airstreams entering and leaving the CV, are represented by $\rho(T_{oa}) \cdot c_p(T_{oa}) \cdot T_{oa}(t)$ and $\rho(T_{ia}) \cdot c_p(T_{ia}) \cdot T_{ia}(t)$, respectively.

In order to simplify equation 4.1 into equation 4.2, the following considerations were taken into account, along with the hypothesis in table 4.1:

(a) No heat generation within the platform is considered since it remained unoccupied during all measurement campaigns (cf. table 4.1, hyp. n°3).

(b) The indoor air behaves as an ideal gas (cf. table 4.1, hyp. n°4). This hypothesis might be justified to be retained by the working temperature ranges in our experiments. Also, based on this hypothesis, the sensible part of the enthalpy can be expressed in terms of the specific heat capacity c_p and temperature [12].

(c) The assumption of a uniform temperature was retained, regarding the most frequent vertical temperature gradient encountered in our experimental results, between the air near the shed-roof and the air near the floor, of about 0,47 °C (cf. §2.6.2.3). Therefore, in equation 4.2, T_{ia} represents the temperature of the entire indoor air volume (cf. Table 4.1, hyp. n°5), and this

temperature is the one measured at the center of the platform at 1,70 m above the floor (cf. fig. 2.14, p.52).

(d) Stack ventilation occurs at a uniform indoor and outdoor air temperatures, which is in agreement with the previous consideration and the natural airflow rate characterization presented in chapter 3.

(e) The heat transfer through infiltrations and leakages are taking into account indirectly in the term $ach(t)$, also via the natural air flow rate characterization in chapter 3.

(f) The indoor furniture is considered to be in thermal equilibrium with the air (cf. table 4.1, hyp. n°6), as well as, any internal partition-walls, doors, and shelves, thus being always at temperature T_{ia}.

Table 4.1: Hypotheses employed in the modeling of the heat transfer in the platform.

N°	Hypotheses/Assumptions	Notation	Justification
1)	Single-zone approximation	–	For simplification
2)	Internal energy depends only on the enthalpy term	$\mathscr{E} = f(\mathscr{H})$	For simplification
3)	No internal heat generation	$\Phi_{gen} = 0$	Unoccupied building
4)	Ideal gas approximation and only sensible heat is considers	$\Delta\mathscr{H} = \rho \cdot V \cdot c_p \cdot \Delta T$	Working temperature range in experiments
5)	Indoor air uniform in temperature	$\Delta T_{ia}(x, y, z) = 0$	For simplification
6)	Furniture, partition-walls and doors are in thermal equilibrium with the indoor air	$\varphi_{furniture_{(\lambda,C,R)}} = 0$	For simplification
7)	Physical properties are constant with temperature, except for ρ and c_p	$\mathscr{P}(\Delta T) = 0$	Working temperature range in experiments
8)	The air density depends on the temperature	$\rho(T) = \frac{101325}{287 \cdot T}$	Expression for temperature dependence
9)	Solar radiation reaching the indoor environment is negligible	$\varphi_{iSWL} \sim 0$	Window shades closed and experimentation
10)	The air specific heat depends on the temperature	$c_p(T) = \frac{1009-1003}{350-293} \cdot [T - 293] + 1003$	

Regarding the term relating the convective heat transfer in equation 4.1, it was decided to consider the convective heat transfer between the indoor air and the floor, ceiling and glazed-facade surfaces, individually in three terms, as in equation 4.2. The reason lays in hyp. n°5 (cf. table 4.1) or consideration (c) here above, where this assumption leads to recompute the convective heat transfer coefficient at each surface presented earlier in figures 2.43-2.45 (which we named h_C). In these figures the coefficient h_C was computed using the air temperature measured at 10 cm (recall the "measurement device"). However, to consider hypothesis n°5 (cf. table 4.1), it is necessary to compute this coefficient using the air temperature measured at 1,70 m above the floor instead (refer to remark (c) here before). This convective coefficient will be named here as h'_C and is defined as follows:

$$h'_{C_{S_i}} = \frac{\varphi_{C_{S_i}}}{T_{ia} - T_{S_i}} \qquad \left[\mathrm{W{\cdot}m^{-2}{\cdot}K^{-1}}\right] \tag{4.3}$$

where S_i represents any of the three surfaces: floor, ceiling and glazed-facade. Thus, the convective coefficient for each surface is represented, respectively, by: h'_{C_D}, h'_{C_P}, and glazed-facade (h'_{C_g}). The resulting convective coefficients are presented in figures 4.2, 4.3, and 4.4: for the opening configurations n°1, n°2, and n°3, respectively. Recall here, that the temperature of the glazed-facade surface T_{S_g} was not measured for configuration n°2, as mentioned in chapter 2. Thus, it will not be shown hereafter in figure 4.3.

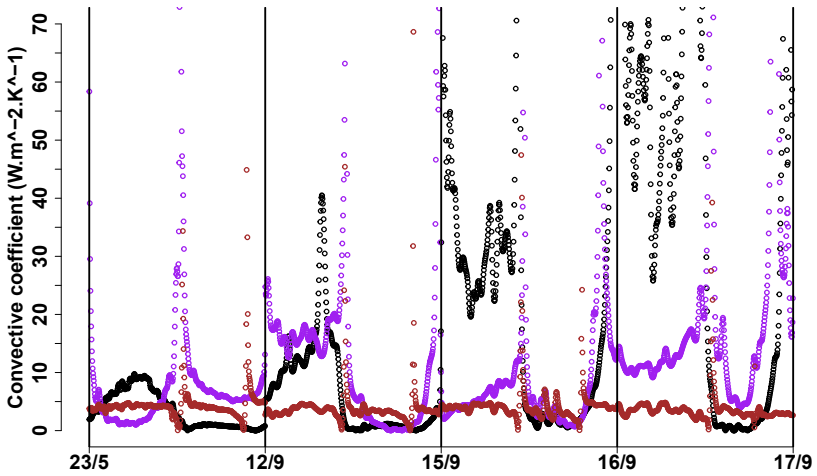

Figure 4.2: For config. n°1: floor h'_{C_D} (black), ceiling h'_{C_P} (purple), and glazed-facade h'_{C_g} (brown).

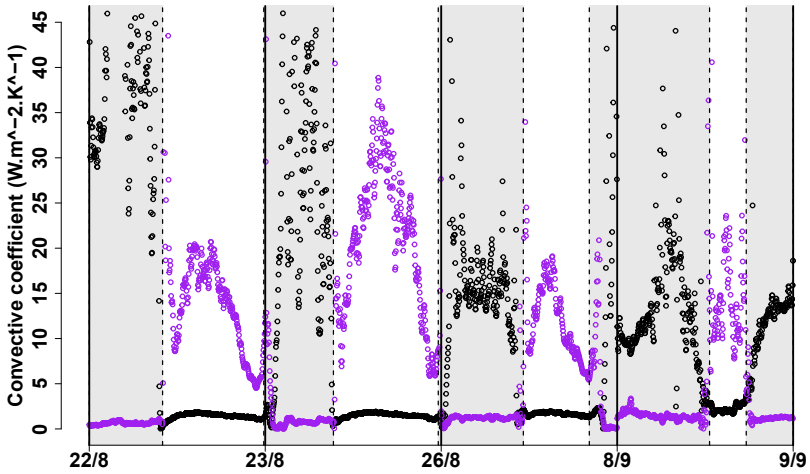

Figure 4.3: For config. n°2: floor h'_{C_D} (black), and ceiling h'_{C_P} (purple).

For configurations n°2 and n°3 (cf. figs. 4.3 and 4.4), a significant difference in the behavior of h'_C can be observed for daytime and nighttime periods. For instance, in figure 4.3, the values of h'_C for the floor (h'_{C_D}, black dots) are larger than the values for the ceiling (h'_{C_P}, purple dots), and this during nighttime (gray zones, openings opened). The opposite is observed during the daytime (white zones, openings closed): h'_{C_P} presents larger values than h'_{C_D}. The same can be said for the daytime and nighttime in figure 4.4. On the other hand, in figures 4.4 and 4.4, it can be observed that h'_{C_g} for the glazed-facade (brown dots) presents similar behavior during the daytime and nighttime, and its values appear to be

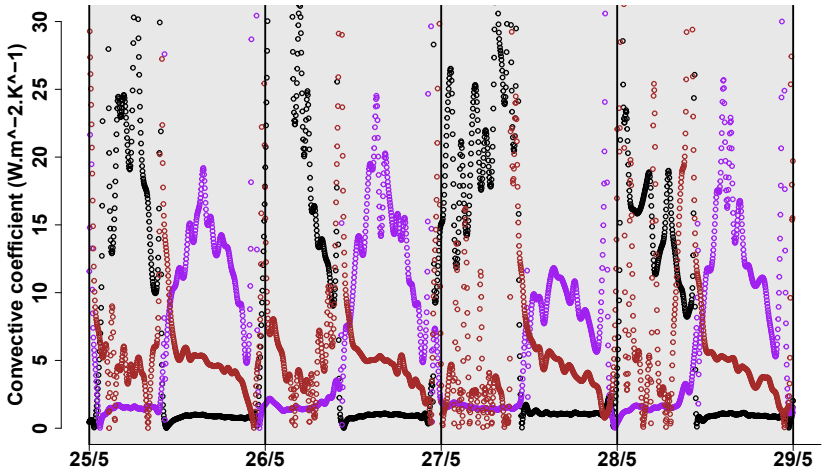

Figure 4.4: For config. n°3: floor h'_{C_D} (black), ceiling h'_{C_P} (purple), and glazed-facade h'_{C_g} (brown).

the same for each days. This before leads to state the following remarks:

- During nighttime, when the openings are opened, h'_{C_D} is larger enough with respect to h'_{C_P}, that the effect of the latter becomes imperceptible or, even yet, negligible.
- During the daytime, when the openings are either closed or opened, h'_{C_P} is larger enough with respect to h'_{C_D}, that the effect of the latter also becomes imperceptible or, even yet, negligible.

However, for configuration n°1 in figure 4.2, it seems that a similar remark, as those mentioned above, regarding the behavior of the floor and ceiling, can only be said for the first day (May 23rd), but not for the others. This might be explained by the fact that the temperature levels encountered in mid-September were not of typical summertime temperature values; unfortunately configuration n°1 was not implemented in any other time. The temperature of the glazed-facade surface is of interest because results showed that, it always presents the highest temperature values in comparison with the floor and ceiling surfaces (cf. §2.5.3, p.69). Thus, the analysis above leads to retain the following:

In summary:
It is necessary to account for the convective heat transfer individually for each surface: a vertical wall, a horizontal wall at the bottom (floor), and a horizontal wall at the top (ceiling). The most important vertical wall seems to be the glazed-facade, due to its thermal behavior and contact with the indoor air.

At this point, by using experimental data, equation 4.2 can only be solved for configurations n°1 and n°3 since the glazed-facade surface temperature was not measured for configuration n°2. For the latter it is necessary to represent the glazed-facade temperature surface T_{S_g} in a way as to include experimental data. For this, we propose to represent T_{S_g} in terms of the surrounding surface temperatures (SST) measured on the floor surface. An average value of SST can be obtained by approximating its value using the definition of the mean radiant temperature (MRT). The definition of MRT is based on a weighted-superposition to the fourth power, as follows [51, 100]:

$$T^4_{surr}(t) \approx \mathcal{F}_{P\to D} \cdot T^4_{S_P}(t) + \mathcal{F}_{g\to D} \cdot T^4_{S_g}(t) + \mathcal{F}_{w\to D} \cdot T^4_{S_w}(t) \qquad \left[\mathrm{K}^4\right] \tag{4.4}$$

$$\mathscr{F}_{P\to D} + \mathscr{F}_{g\to D} + \mathscr{F}_{w\to D} = 1 \qquad [-] \tag{4.5}$$

where T_{surr} represents the mean radiant temperature. The subscript w represents the rest of the vertical walls surrounding the floor concrete-slab other than the glazed-facade. Note here, that equation 4.4 only holds for a long-wavelength environment. The coefficients $\mathscr{F}_{P\to D}$, $\mathscr{F}_{g\to D}$ and $\mathscr{F}_{w\to D}$, represent the diffuse view factor, respectively, between the following surfaces: ceiling, glazed-facade and remain walls; and the floor surface. Then, by equating together, equations 4.4 and 4.5, the following expression can be obtained for the temperature of the glazed-facade surface T_{S_g}:

$$T_{S_g}(t) \approx \frac{1}{\mathscr{F}_{g\to D}} \sqrt[4]{T^4_{surr}(t) - \mathscr{F}_{P\to D}\cdot T^4_{S_P}(t) - \left[1 - \mathscr{F}_{P\to D} - \mathscr{F}_{g\to D}\right]\cdot T^4_{S_w}(t)} \qquad [\mathrm{K}]\,. \tag{4.6}$$

The vertical walls, other than the glazed-facade, are considered to be in thermal equilibrium with the indoor air, and thus, they are assumed as to have the same temperature as the indoor air: $T_{S_w} \approx T_{ia}$.

4.1.2 Estimation of the natural airflow rate via heat flux and temperature measurements

At the end of chapter 3, the searching for an expression able to relate both the wind and buoyancy effects showed that when both effects are considered simultaneously, the resulting value of net *ach* appears not to be a simple superposition of both individual effects, e.g., addition or subtraction. Thus, an expression able to relate both effects is still necessary to determine the value of *ach*, for the case when neither effects dominate. For such a case, various superposition models (empirical and theoretical) have been reported in the literature [76, 59, 92, 104, 105, 45]. Despite that these models have been determined for simple opening configurations, we decided to evaluate them with the intention of choosing a model for *ach*, relating both effects, that can estimate the real value of the *ach* in our platform.

However, to evaluate which of the reported models fit the best to our particular case, the real value of *ach* should be known to avoid any overestimations or underestimations of this parameter. To do this, the value of *ach* was determine indirectly through the energy balance considered before (cf. eq. 4.2). From this energy balance, we can draw an expression for the *ach* in terms of the internal convective heat exchanges, as follows:

$$\begin{aligned} ach(t) = \frac{3600}{V_{ia}\cdot\left[\rho(T_{oa})\cdot c_p(T_{oa})\cdot T_{oa}(t) - \rho(T_{ia})\cdot c_p(T_{ia})\cdot T_{ia}(t)\right]} \Big\{ & \rho(T_{ia})\cdot V_{ia}\cdot c_p(T_{ia})\cdot \frac{\mathrm{d}T_{ia}(t)}{\mathrm{d}t} \\ & - h'_{C_D}(t)\cdot S_D\cdot\left[T_{S_D}(t) - T_{ia}(t)\right] - h'_{C_P}(t)\cdot S_P\cdot\left[T_{S_P}(t) - T_{ia}(t)\right] \\ & - h'_{C_g}(t)\cdot S_g\cdot\left[T_{S_g}(t) - T_{ia}(t)\right]\Big\} \qquad \left[\mathrm{h}^{-1}\right] \end{aligned} \tag{4.7}$$

where the variable $T_{S_g}(t)$ is replaced by equation 4.6. Note that, since equation 4.7 carries the experimental error from each of the variables, the resulting *ach* might present inconsistencies, e.g., negative values. Consequently, the absolute value of *ach* will be presented. Hereafter, we will referred to it as ach_{φ_C} since this *ach* is determined from the convective heat exchanges. The resulting ach_{φ_C} is presented in figures 4.5-4.7 (blue dots), for each opening configuration: n°1 (close-close), n°2 (open-close),

n°3 (open-open), respectively. In addition, each figure include the following:

- The corresponding air change rate per hour due to buoyancy effects only $ach_{\Delta T}$ (red dots), using equation 3.10 (p.118). This can help us to evaluate the accuracy of the airflow simulations in the moments of absence of wind.
- The corresponding air change rate per hour due to wind effects only ach_W (yellow dots), using equation 3.11 (p.119). This can help us to evaluate the accuracy of the airflow simulations in the moments when wind effects dominates.
- The value of the air change rate per hour estimated by a theoretical superposition model such as $ach_n = [ach^n_{\Delta T} + ach^n_W]^{1/n}$, with $n = 2$ [76] (green line).
- The value of the air change rate per hour estimated by an empirical superposition model such as $ach_m = \left[ach^{1/m}_{\Delta T} + ach^{1/m}_W\right]^{1/m}$, with $m = 2$ (purple line).
- The value of the air change rate per hour estimated by the K-P model (ach_{K-P}), using equation 1.12 (p.19) (cyan horizontal line).
- The corresponding indoor and outdoor temperature measurements (brown dashed line and dots, respectively, with axis on the right-hand side).

Variables in equation 4.7

Desired variable (unknown): ach.
Data from experiments: T_{ia}, T_{S_D}, T_{S_P}, T_{oa}, T_{surr}, h'_{C_D}, h'_{C_P}, h'_{C_g}.

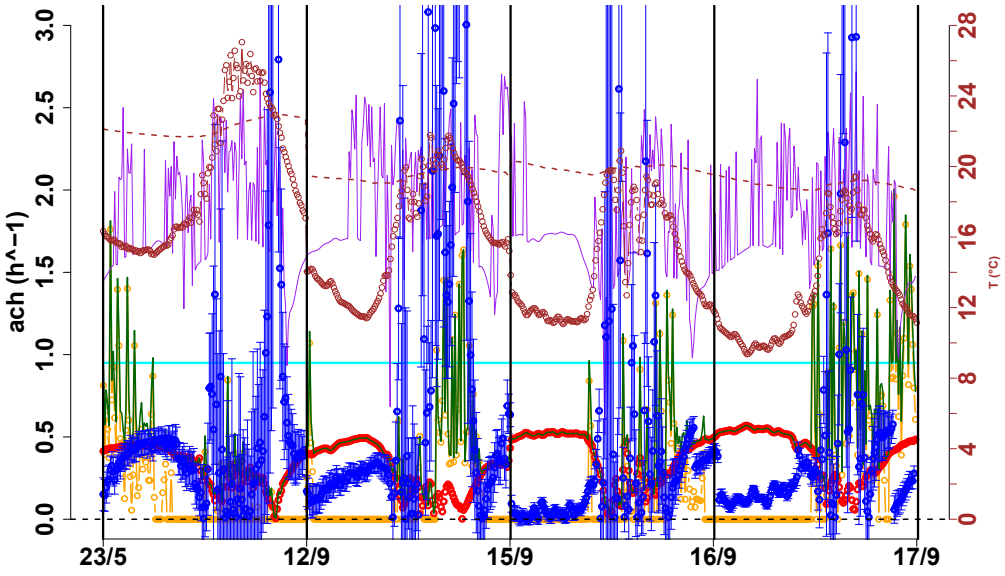

Figure 4.5: Resulting air change rate per hour for config. n°1: ach_{φ_C} (blue), $ach_{\Delta T}$ (red), ach_W (yellow), $ach_{n=2}$ (green), ach_{K-P} (cyan), and $ach_{m=2}$ (purple). The corresponding temperature measurements: indoor air (brown dashed line) and outdoor air (brown circles).

In figures 4.5-4.7, it can be observed that as the indoor air temperature (brown dashed line) approaches the outdoor air temperature (brown dots), the resulting ach_{φ_C} (blue dots) presents a rather

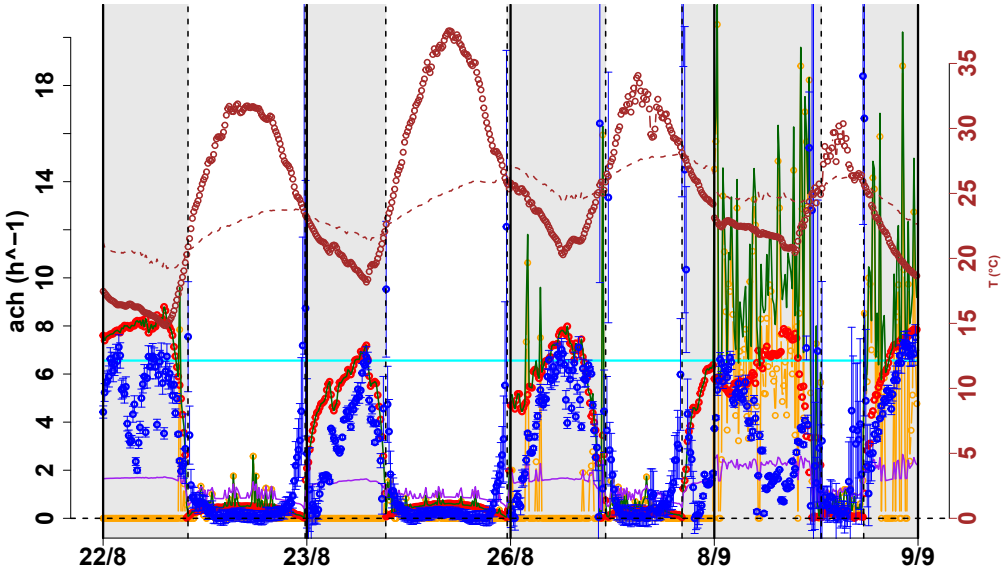

Figure 4.6: Resulting air change rate per hour for config. n°2: ach_{φ_C} (blue), $ach_{\Delta T}$ (red), ach_W (yellow), $ach_{n=2}$ (green), ach_{K-P} (cyan), and $ach_{m=2}$ (purple). The corresponding temperature measurements: indoor air (brown dashed line) and outdoor air (brown circles).

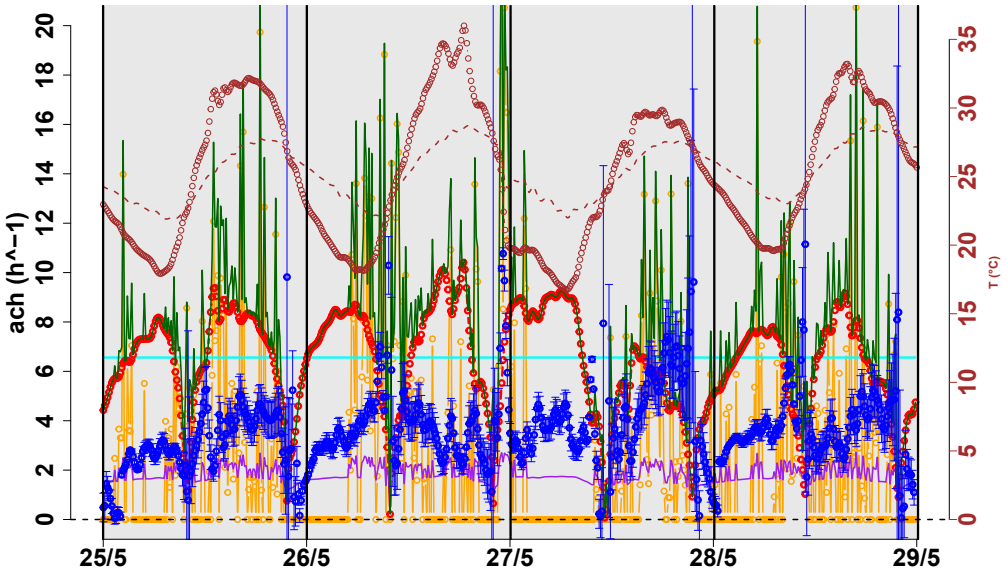

Figure 4.7: Resulting air change rate per hour for config. n°3: ach_{φ_C} (blue), $ach_{\Delta T}$ (red), ach_W (yellow), $ach_{n=2}$ (green), ach_{K-P} (cyan), and $ach_{m=2}$ (purple). The corresponding temperature measurements: indoor air (brown dashed line) and outdoor air (brown circles).

behavior where the values attained by ach_{φ_C} might become unrealistic. Unrealistic values because they do not appear to agree with the prevailing behavior presented during the moments where both temperatures are significantly far away from each other, e.g., nighttime and daytime. This asymptotic behavior can be caused by the enthalpy difference in the denominator of equation 4.7; as this difference becomes small the value of ach_{φ_C} (blue dots) might reach rather improbable values.

Moreover, in each figure, it can be observed that considering either the wind effects (yellow line) alone or the buoyancy effects alone (red dots), leads to an overestimation of ach_{φ_C} (blue dots). The superposition model $ach_{n=2}$ (green line) and the ach_{K-P} model (cyan line), also seems to overestimate the value of ach_{φ_C}. Conversely, the superposition model $ach_{m=2}$ overestimates the value of ach_{φ_C} for configuration n°1, but underestimates it for configuration n°2 and n°3. Table 4.2 summarizes the results of this comparison. The reasons of such overestimations may lay in the following aspects:

- The airflow simulations performed on CONTAM might overestimate the value of ach_W, due to the approximations regarding the wind effects, e.g., the value of the pressure coefficients, the wind profile power law, among others. But also, because both buoyancy and wind effects are opposed. For the cases of absence of wind, the value of $ach_{\Delta T}$ might overestimate the value of ach_{φ_C}, since neither any internal heat exchanges (convection with walls) nor thermal stratification is considered on CONTAM.
- The overestimation and underestimation of ach_{φ_C} by the models ach_n and ach_m, maybe because these models account for a situation where either wind and buoyancy are always assisted or always opposed, but not both interchangeably.
- The overestimation by the model ach_{K-P} maybe because it is said to give the annual-averaged value of the natural air change rate per hour.

Table 4.2: Comparison between air change rate models.

Model	**Notation**	**Remarks regarding ach_{φ_C}**
Buoyancy effects alone	$ach_{\Delta T}$	overestimation
Wind effects alone	ach_W	overestimation
K−P model [93]	ach_{K-P}	overestimation
Superposition as ach_n [76] for $n = 2, 3, 5, 10$	$ach_n = [ach_{\Delta T}^n + ach_W^n]^{1/n}$	overestimation
Superposition as ach_m for $m = 2$	$ach_m = \left[ach_{\Delta T}^{1/m} + ach_W^{1/m}\right]^{1/m}$	overestimation and underestimation

In summary:
It appears that none of the models fit the values of ach_{φ_C} for each configuration, and thus, other expression for determine the net *ach* should be proposed.

4.1.3 Identification of Model A for all opening configuration

Now, let us propose a "Model A" consisting of equations 4.2 and 4.6, where the natural airflow rate or air change per hour *ach* in the platform, is considered to be a product superposition of wind and buoyancy effects, as shown in equation 4.8.

Here in equation 4.8, the expressions for both buoyancy (red box) and wind (yellow box) effects were presented in chapter 3 (cf. eqs. 3.10-3.11, pp.118-119). Then, the coefficients C_l, C_v, a_l, a_v, b_l and b_v, will be determined by solving Model A for T_{ia}, finding the values that minimizes the $RMSE$ value between T_{ia} model and T_{ia} measured. This was done by trial and error. Only one set of values

$$
\textbf{Model A}\begin{cases}
\textbf{1)}\quad \rho(T_{ia})\cdot V_{ia}\cdot c_p(T_{ia})\cdot \dfrac{\mathrm{d}T_{ia}(t)}{\mathrm{d}t} = h'_{C_D}(t)\cdot S_D\cdot\left[T_{S_D}(t)-T_{ia}(t)\right] \;+\; h'_{C_P}(t)\cdot S_P\cdot\left[T_{S_P}(t)-T_{ia}(t)\right] \\
\qquad\qquad + \; h'_{C_g}(t)\cdot S_g\cdot\left[T_{S_g}(t)-T_{ia}(t)\right] \\
\qquad\qquad + \; V_{ia}\cdot\dfrac{ach(t)}{3600}\cdot\left[\rho(T_{oa})\cdot c_p(T_{oa})\cdot T_{oa}(t)-\rho(T_{ia})\cdot c_p(T_{ia})\cdot T_{ia}(t)\right] \\
\textbf{2)}\quad T_{S_g}(t) = \frac{1}{\mathscr{F}_{g\to D}}\sqrt[4]{T^4_{surr}(t)-\mathscr{F}_{P\to D}\cdot T^4_{S_P}(t)-\left[1-\mathscr{F}_{P\to D}-\mathscr{F}_{g\to D}\right]\cdot T^4_{ia}(t)}-273,15 \\
\textbf{3)}\quad ach(t) = \begin{cases}
C_l\cdot\left[4\cdot\left|\dfrac{T_{ia}(t)-T_{oa}(t)}{T_{oa}(t)}\right|^{0,58}\right]^{a_l}\cdot\left[\mathscr{B}_l(\phi_W)\cdot\mathscr{V}^{1,16}_{met}(t)\right]^{b_l}; \text{when NV openings closed} \\
C_l\cdot\left[4\cdot\left|\dfrac{T_{ia}(t)-T_{oa}(t)}{T_{oa}(t)}\right|^{0,58}\right]^{a_l}: \text{If } \mathscr{V}_{met}(t)=0; \text{when NV openings closed} \\
C_v\cdot\left[\mathscr{A}\cdot\left|\dfrac{T_{ia}(t)-T_{oa}(t)}{T_{oa}(t)}\right|^{1/2}\right]^{a_v}\cdot\left[\mathscr{B}_v(\phi_W)\cdot\mathscr{V}_{met}(t)\right]^{b_v}; \text{when NV openings opened} \\
C_v\cdot\left[\mathscr{A}\cdot\left|\dfrac{T_{ia}(t)-T_{oa}(t)}{T_{oa}(t)}\right|^{1/2}\right]^{a_v}: \text{If } \mathscr{V}_{met}(t)=0; \text{when NV openings opened}
\end{cases}
\end{cases}
\tag{4.8}
$$

Color-box code: Buoyancy effect (red) and wind effect (yellow).

is wanted for these coefficients that fit the best all three configurations. The reason of performing the identification by adjusting Model A to best fit T_{ia} (model) with T_{ia} (measured), lays in the reliability of the air temperature measurement.

4.1.3.1 Selecting a dataset for the identification process

A dataset of consecutive days is chosen for the identification process. For such dataset, the experimental results from configurations n°2 and n°3 can be employed. These two datasets allow us to evaluate Model A for accuracy. On the other hand, the dataset of experimental results from configuration n°1, allows us to evaluate Model A in terms of adaptability, in addition to accuracy, since this configuration was not tested for consecutive days. The adaptability of the model can also be highlighted, by evaluating its accuracy under different opening configurations.

Moreover, in addition to the criteria presented in chapter 1 in table 1.2 (p.24), the convective heat flow terms for the floor, ceiling, and the storage term on equation (4.2) will be computed using experimental results for each configuration (cf. figs. 4.8-4.10). In this way, we are also able to judge the numerical results by the accuracy of describing each of these terms. In other words, the model should also describe the magnitudes for each term in equation 4.2 in order to be retained.

In figures 4.8-4.10, it can be observed that the convective heat flow at the ceiling (blue line) appears to be one of the most important terms, i.e., presents large heat flow values with respect to the other terms, during the daytime (negative values), whether the openings are kept closed (see figure 4.8 on 23/5, and figure 4.9 (daytime)) or kept opened (cf. fig.4.10). Conversely, during nighttime, the most important term appears to be the convective heat flow at the floor concrete-slab (red line). Note that in figure 4.8, this before does not applied from 12/9 to 17/9, as explained before.

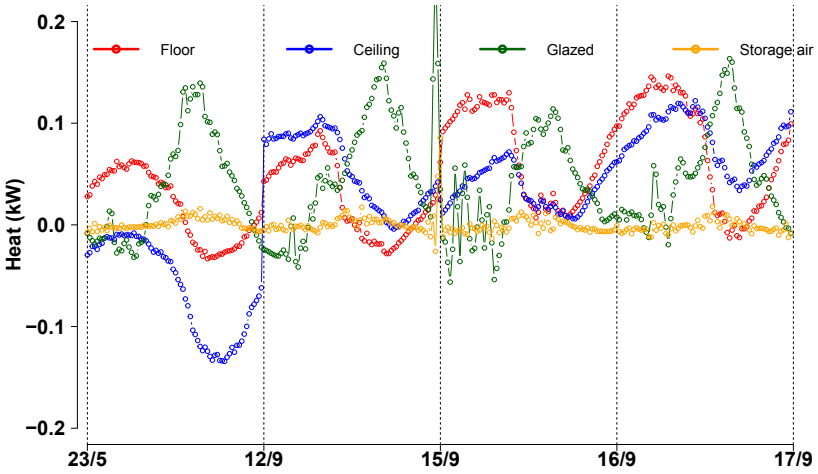

Figure 4.8: For config. n°1. Convective heat flow for the floor (red),ceiling (blue), glazed-facade (green), and storage term (yellow), from the point of view of the air (negative values correspond to a discharge).

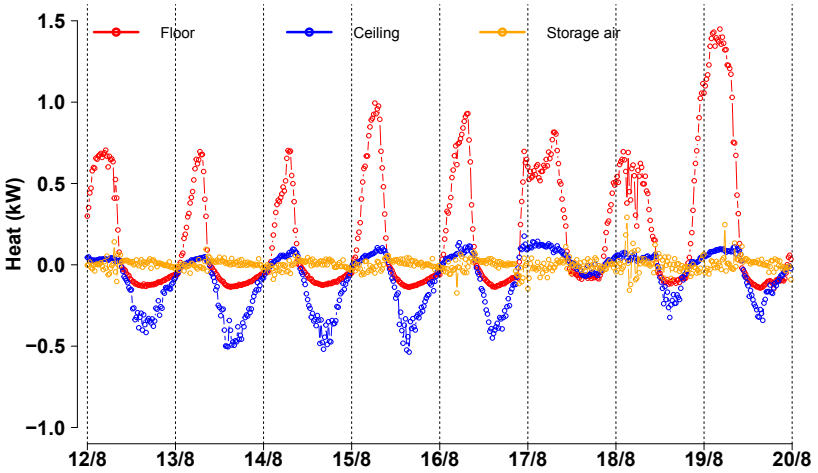

Figure 4.9: For config. n°2. Convective heat flow for the floor (red) and ceiling (blue), and storage term (yellow), from the point of view of the air (negative values correspond to a discharge).

4.1.3.2 Discussion and evaluation of the results from the identification process of Model A

The equations of the model were solved using the software **R** with the package *dsolve*. The time step employed was the same as the meteorological station sample rate: one time-iteration every ten minutes, and the method chosen for the numerical solution was "*Radau*" (implicit Runge-Kutta), which is a fifth order solution method. The values of the constant parameters and coefficients employed in Model A, are presented in table 4.3.

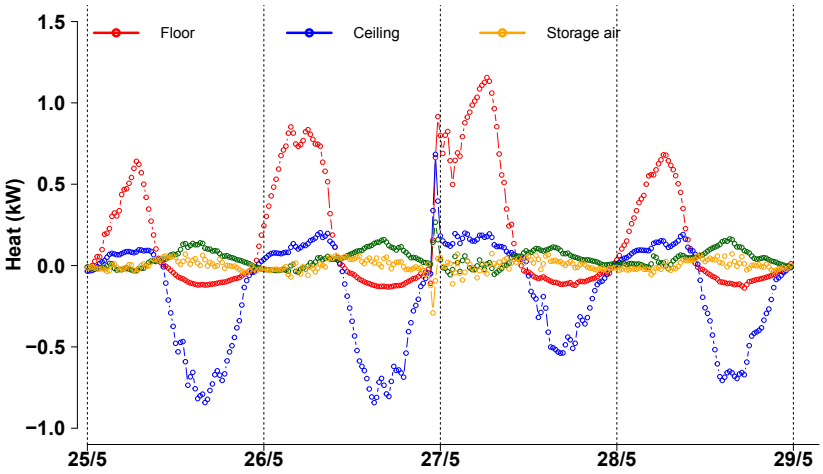

Figure 4.10: For config. n°3. Convective heat flow for the floor (red),ceiling (blue), glazed-facade (green), and storage term (yellow), from the point of view of the air (negative values correspond to a discharge).

Table 4.3: Set of parameters for Model A.

Parameters	V_{ia}	S_D	S_P	S_g	$\mathcal{F}_{P\to D}$	$\mathcal{F}_{g\to D}$	$\mathcal{F}_{w\to D}$	h'_{C_g}	$\mathcal{A}$
Dimensions	$[m^3]$	$[m^2]$	$[m^2]$	$[m^2]$	$[-]$	$[-]$	$[-]$	$[W{\cdot}m^{-2}{\cdot}K^{-1}]$	$[h^{-1}]$
Values	158*	46*	58*	17,4*	0,37**	0,14**	0,49	4,5***	67 (*)

* Dimensions of the single-zone model.
** $\mathcal{F}_{P\to D}$ and $\mathcal{F}_{g\to D}$ were calculated by abacuses reported in [118]; $\mathcal{F}_{w\to D}$ obtained by superposition.
*** From experimental data.
(*) From airflow simulations for $ach_{\Delta T}$ (cf. table 3.7, p.118).

Variables in Model A

Desired variable (unknown): T_{ia}, ach.
Data from experiments: T_{S_D}, T_{S_P}, T_{oa}, T_{surr}, h'_{C_D}, h'_{C_P}, h'_{C_g}.
Data from meteorological station: $\mathcal{V}_{met}$, ϕ_W.

The solution of Model A, for each opening configuration (cf. table 2.6, p.65), is presented in figures 4.11-4.16, where a histogram is included to show the distribution of the absolute error of T_{ia} model ($|error| = |value_{measured} - value_{simulated}|$). The computation time (or running time) expended to solve the model for each configuration was about 18 s, where a low computation time was expected since most variables in Model A were taken from experimental data. Thereby, each figure presents the following:

- **(a)** a comparison of the indoor air temperature T_{ia} between the model (red line) and experimental data (black circles), along with the absolute error (brown line),
- **(b)** the resulting heat flow terms in equation 4.2 using T_{ia} from the model: floor (red), ceiling (blue), glazed-facade (green), energy storage in air (yellow), and ventilation (purple),
- **(c)** the resulting air change rate per hour (ach) from the model solution (black dotted line).

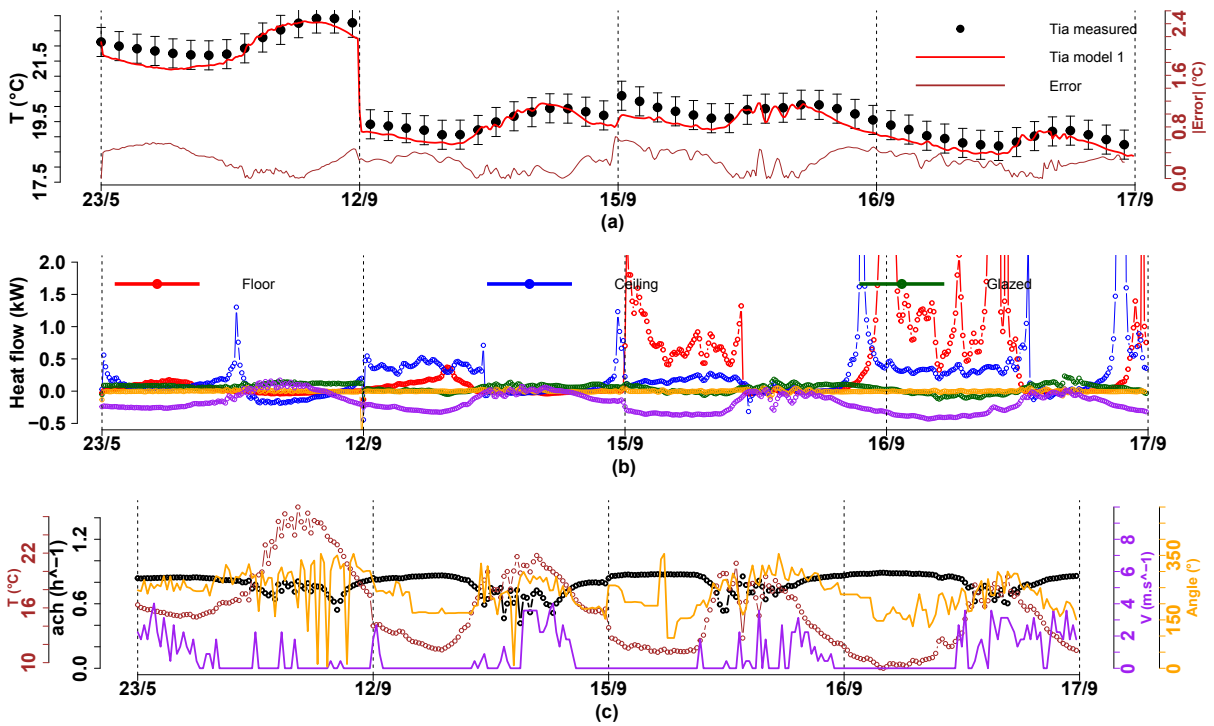

Figure 4.11: Numerical results for config. n°1: **(a)** T_{ia} model (red line), T_{ia} measured (black dots), and absolute error (brown line); error bars $\pm$0,48 °C. **(b)** Heat flows: floor (red), ceiling (blue), glazed-facade (green), energy storage in air (yellow), and ventilation (purple). **(c)** *ach* (black), $\mathcal{V}_{met}$ (purple) and ϕ_W (yellow), and T_{oa} (brown).

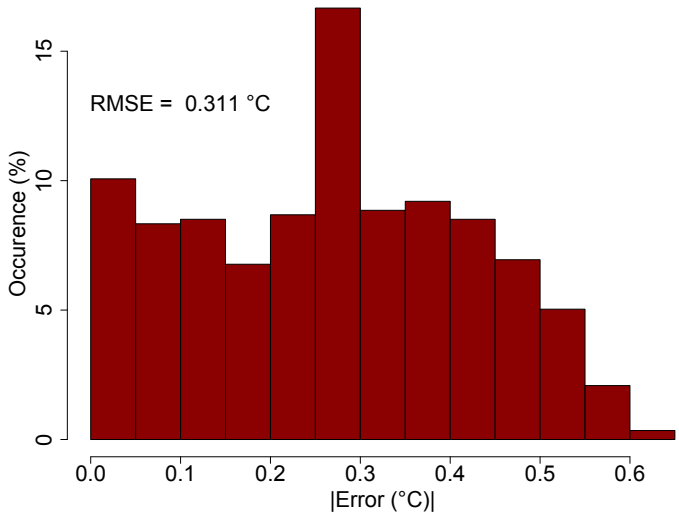

Figure 4.12: For config. n°1. Associated error distribution for T_{ia} in fig.4.11 (a), and the $RMSE$ value.

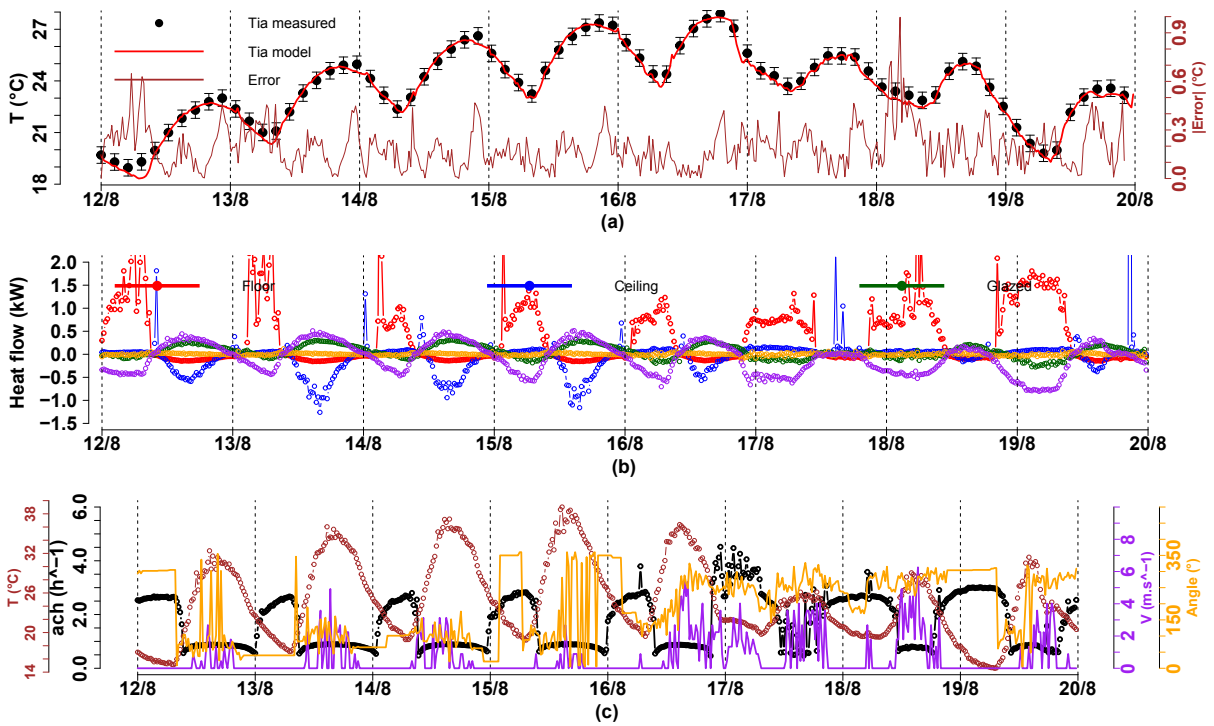

Figure 4.13: Numerical results for config. n°2: **(a)** T_{ia} model (red line), T_{ia} measured (black dots), and absolute error (brown line); error bars $\pm$0,48 °C. **(b)** Heat flows: floor (red), ceiling (blue), glazed-facade (green), energy storage in air (yellow), and ventilation (purple). **(c)** *ach* (black), $\mathcal{V}_{met}$ (purple) and ϕ_W (yellow), and T_{oa} (brown).

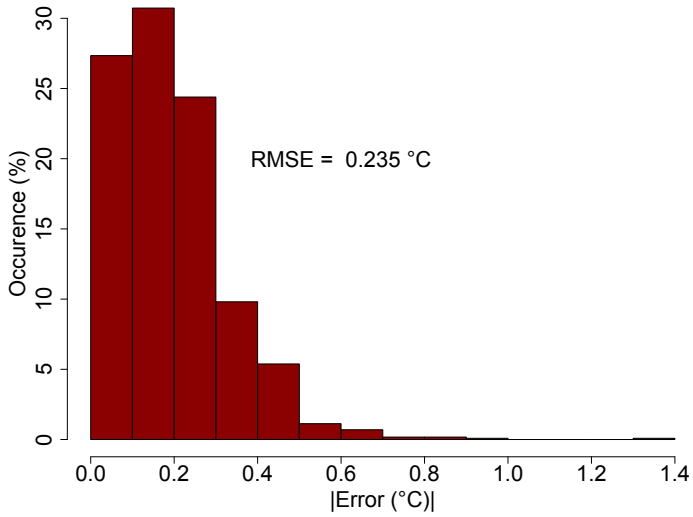

Figure 4.14: For config. n°2. Associated error distribution for T_{ia} in fig.4.13 (a), and the $RMSE$ value.

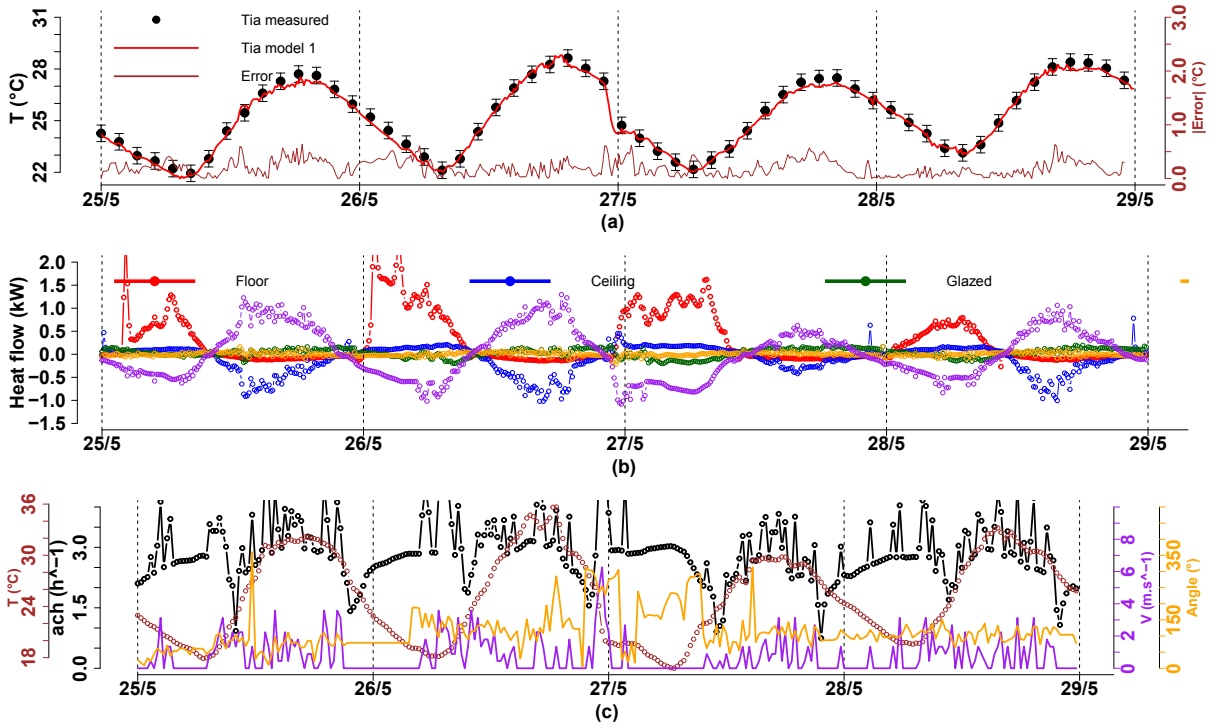

Figure 4.15: Numerical results for config. n°3: **(a)** T_{ia} model (red line), T_{ia} measured (black dots), and absolute error (brown line); error bars ±0,48 °C. **(b)** Heat flows: floor (red), ceiling (blue), glazed-facade (green), energy storage in air (yellow), and ventilation (purple). **(c)** *ach* (black), $\mathcal{V}_{met}$ (purple) and ϕ_W (yellow), and T_{oa} (brown).

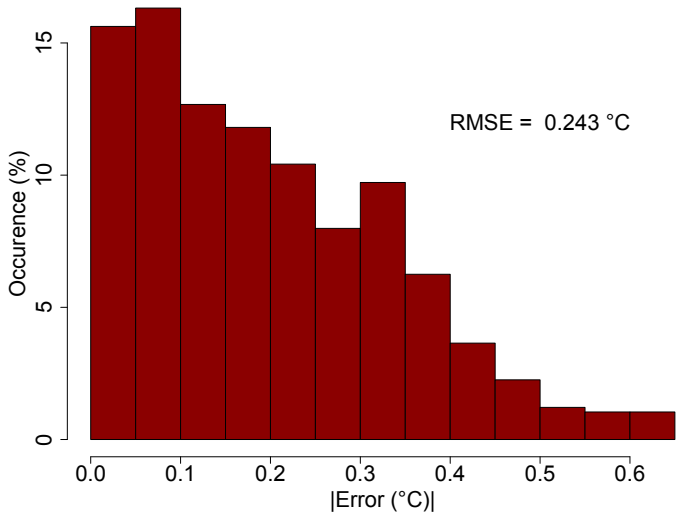

Figure 4.16: For config. n°3. Associated error distribution for T_{ia} in fig.4.15 (a), and the $RMSE$ value.

Table 4.4: Identified set of values for *ach* expression in Model A (cf. eq. 4.8).

	Best values for all configurations								Wind direction ϕ_W	
Config. n°	C_l	C_v	a_l	a_v	b_l	b_v	$RMSE^*$ [°C]	$\overline{\lvert error \rvert}^*$ [°C]	Most frequent	Average
1							0,31	0,27		
2	1	1	0,2	0,5	0	0,2	0,24	0,19	91°	175°
3							0,24	0,19		
	Best values for each configurations alone								Wind direction ϕ_W	
Config. n°	C_l	C_v	a_l	a_v	b_l	b_v	$RMSE^*$ [°C]	$\overline{\lvert error \rvert}^*$ [°C]	Most frequent	Average
1	0,1	0	0,2	0	0	0	0,12	0,10	245°	232°
2	1	1	0,1	0,4	0,2	0,1	0,20	0,16	289 °	185°
3	0	1	0	0,5	0	0,2	0,24	0,19	87°	114°

*Between the model and experimental data for T_{ia}; only two significant figures to agree with the uncertainty in our temperature measurements.

(A) Accuracy and adaptability to different opening configurations regarding the indoor air temperature

The identified values are presented in table 4.4. For the results of model A, regarding the behavior (or dynamics) of T_{ia} (cf. figs. 4.11 (a), 4.13 (a) and 4.15 (a), red line), satisfactory results are obtained since the values of the absolute error are very low (brown line), where the maximum $RMSE$ value is 0,31 °C for configuration n°1 (cf. figs. 4.11 (a) and 4.12).

The adaptability of Model A can be highlighted regarding the changing of the opening configuration since the $RMSE$ converges to similar values on each configuration: 0,31 °C for config. n°1; 0,24 °C for config. n°2; and 0,24 °C for config. n°3. This indicates that model A works best for describing a night ventilation strategy, such as configuration n°2 (cf. fig.4.13 (a)). Additionally, its adaptability is also highlighted in configuration n°1 (cf. fig.4.11 (a)), since the dataset implemented, is not from consecutive days as in configurations n°2 and n°3. Thereby, the following remarks can be said about the performance of model A in terms of dynamics and accuracy, for each configuration:

- For the case where the openings remained close, as in figure 4.11 (entire day) and in figure 4.13 (daytime only): model A appears to accurately describe the behavior of T_{ia} in regard to the $RMSE$ value, and the average absolute error; an average absolute error around 0,27 °C and 0,19 °C for configs. n°1 and n°2, respectively.
- For the case where the openings remained opened, as in figure 4.13 (nighttime only) and in figure 4.15 (entire day): model A appears to describe more accurately the behavior of T_{ia} (with respect to the case of openings closed) in regard to the $RMSE$ value, and the average absolute error; an average absolute error around 0,19 °C, for configuration n°3, respectively.
- Finally, a slight phase shift appears to be presented between T_{ia} model and T_{ia} measured, and is longer in the daytime than in nighttime.

However, the results from identification in table 4.4, show that the best values for all configurations are not the best values for each configuration alone, apart from configuration n°3. For instance, the

best values for configuration n°2 that minimizes the $RMSE$ value for T_{ia}, are different. Moreover, the best values for configuration n°1, indicates that the ventilation term in equation 4.2 does not seem to be significant ($C_l = 0{,}1$). This may imply that the infiltrations are very low, which may seem contradictory with the values found for configuration n°2 ($C_l = 1$). Nevertheless, in configuration n°2, both strategies (openings opened and closed) are tested, whereas in configuration for n°1 there is only one strategy (openings closed).

Furthermore, the identified superposition model for *ach*, implies that wind effects does not influence at all or there was a prevalence absence of wind, for the case of openings closed ($b_l = 0$). The latter is highlighted in figure 4.17; expected for weather conditions in the summertime.

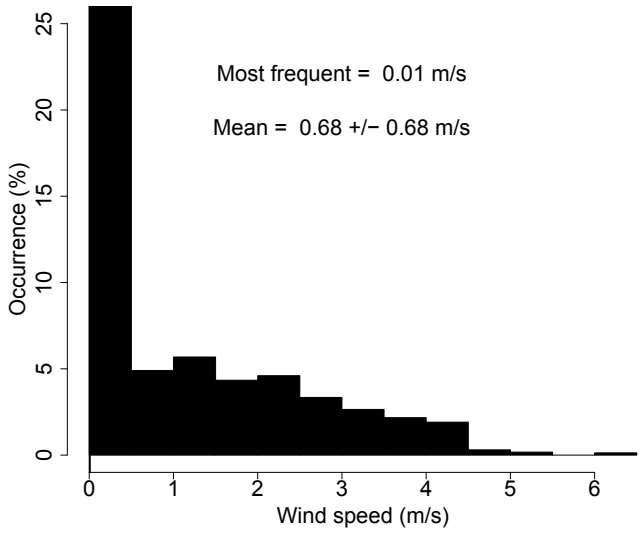

Figure 4.17: Wind speed occurrence distribution during the measurement campaigns for each opening configuration; a total of 2304 samples.

Likewise, this statement seems to hold also for the case of openings opened during the daytime in configuration n°3, even with a strong presence of wind all along this measurement campaign (cf. fig. 4.15 (c)). From this analysis, we may conclude that the values of the exponents, clearly respond to the most frequent or dominant situation taking place. However, these low exponent values may be subjected to the superposition arrangement (the product of $ach_{\Delta T}$ and ach_W), and that the coefficients C_l and C_v were fixed to one in the identification process for all configurations.

(B) Accuracy and adaptability to different opening configurations regarding the convective heat flow terms

Regarding the results for the convective heat flows and energy storage terms in equation 4.2: for configuration n°1, the behavior of the heat flows in figure 4.11 (b) appear to be similar to those in figure 4.8. However, the magnitude of the floor slab (red) and ceiling (blue) terms not always agreed. For configuration n°2 (comparing figures 4.9 and 4.13 (b)), a clear overestimation in the floor slab term is presented (red line) for only two of the days (nighttime of 12/8 ad 13/8), and this, also in the ceiling term only for three of the days (daytime 13/8, 14/8 and 15/8). For configuration n°3, comparing figure 4.10 and 4.15 (b), the model presents an overestimation in the floor slab (red) and ceiling (blue) terms for

three days out of four days in nighttime. In turn, the ceiling term (blue) in figure 4.15 (b), shows strong agreement with the values in figure 4.10, except for the 27/5 which is underestimated in the daytime.

(C) Accuracy and adaptability to different opening configurations regarding the air change rate per hour

The resulting air change rate per hour *ach* (black dotted line) for each configuration is shown in figures 4.18-4.20, respectively, where $ach_{\Delta T}$ (red line), ach_W (yellow line), ach_{K-P} (cyan line), and ach_{φ_C} (blue line) are included. Hereafter, we will refer to the identified superposition model for *ach* as "$ach_{(\Delta T \text{x} W)}$."

At first sight, it appears that $ach_{(\Delta T \text{x} W)}$ (black dotted line) is only in agreement with the *ach* experimentally determined (named ach_{φ_C}) for configuration n°3 in figure 4.20. For configuration n°1 (cf. fig. 4.18), the value of $ach_{(\Delta T \text{x} W)}$ clearly overestimates the value of ach_{φ_C}. For configuration n°2 (cf. fig. 4.19), the value of $ach_{(\Delta T \text{x} W)}$ appears to underestimate the value of ach_{φ_C} by approximately 0,5 times, during the nighttime, but both behaviors appear to be similar. On the contrary, the value of $ach_{(\Delta T \text{x} W)}$ appears to overestimate the value of ach_{φ_C} by 2 times, during the daytime for configuration n°2. For the latter, the behavior of $ach_{(\Delta T \text{x} W)}$ is clearly inversely proportional to ach_{φ_C}.

All different behaviors for each configuration might be explained by the values of the identified coefficients presented in table 4.4. Only for configuration n°3 the same values were identified to be the same, when alone as when being together with all the configurations. In this case, both the behavior and magnitude of $ach_{(\Delta T \text{x} W)}$ and ach_{φ_C} appear to be the same. However, the values of the identified coefficients presented in table 4.4 changed for the other two configurations n°1 and n°2, which might indicate that both wind and buoyancy are not assisted with the same force.

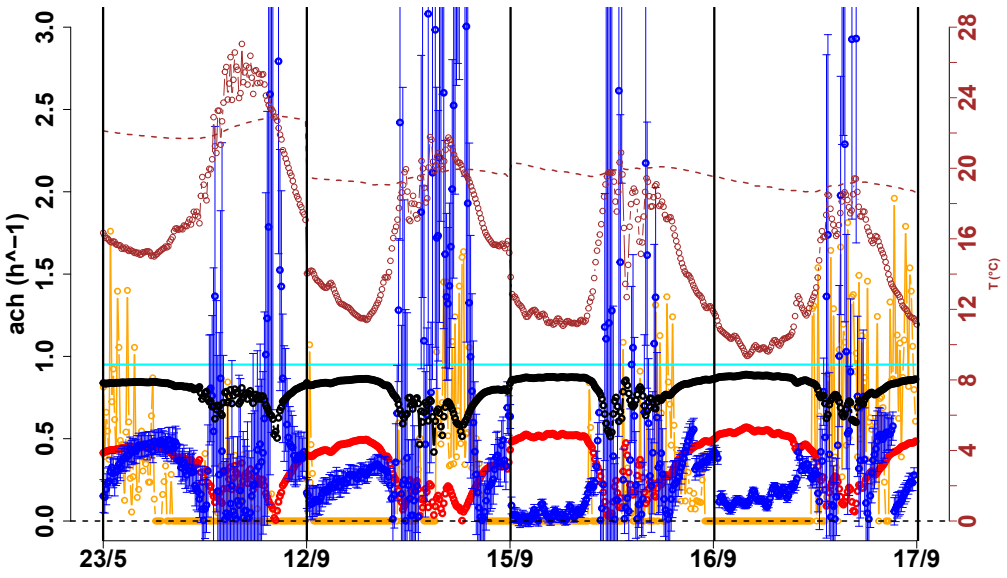

Figure 4.18: Resulting air change rate per hour for config. n°1: $ach_{(\Delta T \text{x} W)}$ (black), ach_{φ_C} (blue), $ach_{\Delta T}$ (red), ach_W (yellow), and ach_{K-P} (cyan). The corresponding temperature measurements: indoor air (brown dashed line) and outdoor air (brown circles).

(D) Assessment of the identified natural airflow model

Finally, we want to highlight the apparent relationship between the identified values of the exponents

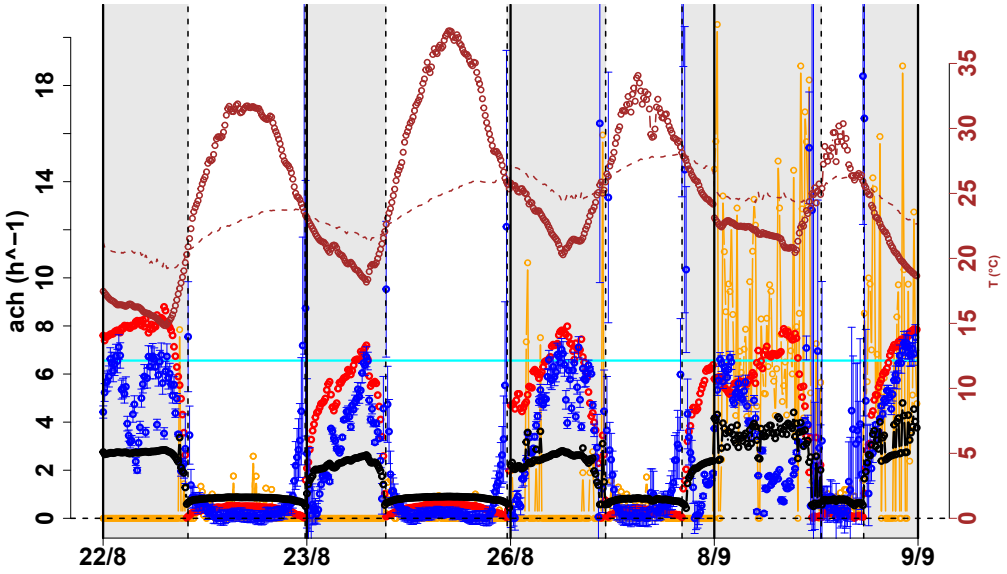

Figure 4.19: Resulting air change rate per hour for config. n°2: $ach_{(\Delta T \text{x} W)}$ (black), ach_{φ_C} (blue), $ach_{\Delta T}$ (red), ach_W (yellow), and ach_{K-P} (cyan). The corresponding temperature measurements: indoor air (brown dashed line) and outdoor air (brown circles).

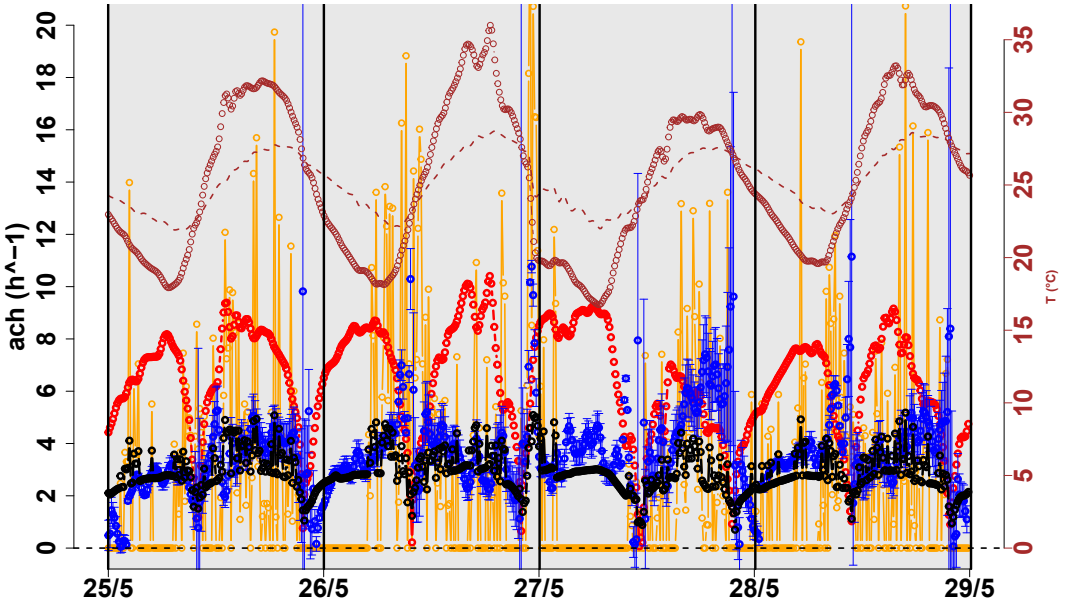

Figure 4.20: Resulting air change rate per hour for config. n°3: $ach_{(\Delta T \text{x} W)}$ (black), ach_{φ_C} (blue), $ach_{\Delta T}$ (red), ach_W (yellow), and ach_{K-P} (cyan). The corresponding temperature measurements: indoor air (brown dashed line) and outdoor air (brown circles).

a_l, a_v, b_l and b_v in $ach_{(\Delta T \text{x} W)}$, and the wind direction ϕ_W. The first hint of such relationship appears to be between the sign of the exponents and the most frequent wind direction. For instance, observe the signs of the exponents with the best values identified for all configuration (cf. table 4.4): all have a positive value ($a_l = 0{,}2$; $a_v = 0{,}5$; $b_v = 0{,}2$). Now, the most frequent wind direction encountered is

91° after analyzing all data collected for the wind direction (cf. fig. 4.21).

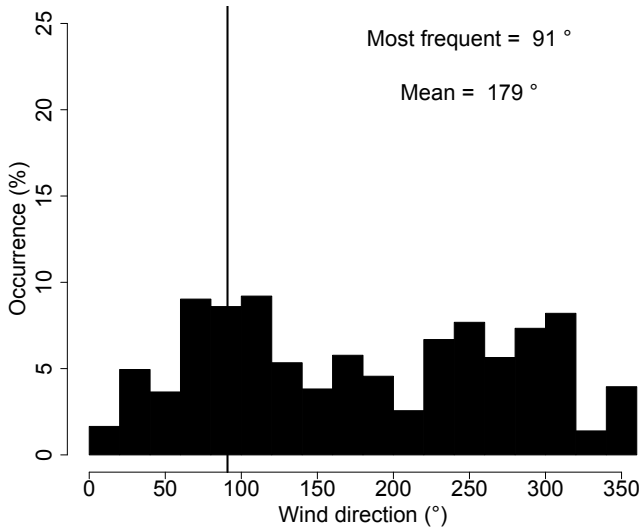

Figure 4.21: Wind direction occurrence distribution during the measurement campaigns for each opening configuration; a total of 2304 samples.

Then, if we recall the characterization of the natural airflow rate presented in chapter 3, it indicated that for a wind direction between 90° and 270° (namely 90°$> \phi_W >$270°), wind and buoyancy effects first oppose, then are assisted depending on the temperature difference level (cf. fig. 3.26, p.123). For other wind directions, both effects are assisted. Therefore, with this recall in mind, since the most frequent wind direction was encountered to be 91° (cf. table 4.4), both wind and buoyancy effects are expected to be assisted. This agrees with the positive values of the exponents ($a_l = 0{,}2$; $a_v = 0{,}5$; $b_v = 0{,}2$). This agreement is also encountered for configurations n°1 and n°2, respectively:

- $a_l = 0{,}2$ and $\phi_W = 245°$.
- $a_l = 0{,}1$; $a_v = 0{,}4$; $b_l = 0{,}2$; $b_v = 0{,}1$ and $\phi_W = 289°$.

A physical explanation for this, was given in §3.4.33.4.3.4 (p.122). On the other hand, for configuration n°3 the most frequent wind direction encountered is 87°, although this angle is near 91°, an exponent with a negative value might be expected. However, every exponent resulted to be positive: $a_v = 0{,}5$; $b_v = 0{,}2$. A better relationship between ... might be identified if the moments were the openings remained close are separated from the moments were they remained open, and also, if separating the daytime from nighttime.

4.1.3.3 Physical significance of the identified superposition natural airflow model $ach_{(\Delta T \mathbf{x} W)}$

A superposition model $ach_{(\Delta T \mathrm{x} W)}$ in the form of $C \cdot ach_{\Delta T}^{a} \cdot ach_{W}^{b}$ was inspired by the usual way that heat transfer phenomena is accounted for in convective heat transfer (for instance: $\mathcal{N}u = C' \cdot \mathcal{R}e^{n} \cdot \mathcal{P}r^{m}$). Likewise, if a similar expression is chosen for ach, the phenomena involved in natural ventilation might also be accounted for. A difference and limitation may lay regarding dimensions, since the coefficient C should have dimensions such as $\mathrm{h}^{a} \cdot \mathrm{h}^{b} \cdot \mathrm{h}^{-1}$, which does not have a physical meaning. However, regardless of the heat transfer phenomena studied, the value of the exponents (associated to a specific phenomena, e.g., $\mathcal{R}e$ for force convection and $ach_{\Delta T}$ for air movement due to

thermal buoyancy) gives indications about how strong is the phenomenon (the value of the exponent), and if such phenomenon opposes to another (the sign of the exponent: if negative, decreases, and if positive, increases). This last remark is essential to the physical significance of the identified model $ach_{(\Delta T \text{x} W)}$.

Finally, the superposition model $ach_{(\Delta T \text{x} W)}$ can be expressed in a dimensionless form, by the following analysis. Recalling the expression for the superposition model:

$$ach = C \cdot ach_{\Delta T}^{a} \cdot ach_{W}^{b} \qquad \left[\text{h}^{-1}\right] \tag{4.9}$$

where the expression of $ach_{\Delta T}$ and ach_{W} were presented in chapter 3 (cf. eqs. 3.10-3.11). By replacing these two expressions into equation 4.9, yields:

$$ach = \left[C \cdot \mathscr{A}^{a} \cdot \mathscr{B}^{b}\right] \cdot \left|\frac{T_{ia} - T_{oa}}{T_{oa}}\right|^{0,5 \cdot a} \cdot \mathscr{V}_{met}^{b} \qquad \left[\text{h}^{-1}\right] \tag{4.10}$$

Now, multiplying the entire previous equation by $1/\mathscr{V}_{f}^{b}$, using the expression for the *wind speed modifier* C_h (cf. eq. 3.2, p.105), and equating expression 4.10, yields:

$$\frac{ach}{C \cdot \mathscr{A}^{a} \cdot \mathscr{B}^{b} \cdot \mathscr{V}_{f}^{b}} = \left|\frac{T_{ia} - T_{oa}}{T_{oa}}\right|^{0,5 \cdot a} \cdot \left[\frac{1}{\sqrt{C_h}}\right]^{b} \qquad [-] \tag{4.11}$$

where the left-hand side term is a variation of the dimensionless flow rate number $\mathcal{F}$ [19]:

$$\mathcal{F} = \left|\frac{T_{ia} - T_{oa}}{T_{oa}}\right|^{0,5 \cdot a} \cdot \left[\frac{1}{C_h}\right]^{-0,5 \cdot b} \qquad [-] \tag{4.12}$$

to which, we can give a more practical expression in terms of $\mathscr{V}_{met}$, to be:

$$\mathcal{F} = \frac{ach}{C \cdot \mathscr{A}^{a} \cdot \mathscr{B}^{b} \cdot \left[\mathscr{V}_{met} \cdot \sqrt{C_h}\right]^{b}} \qquad [-]\,. \tag{4.13}$$

In addition, an expression can be given to $\mathscr{A}$ and $\mathscr{B}$, based on the equations presented in chapter 1, as follows for $\mathscr{A}$ (when considering small openings):

$$\mathscr{A} = 3600 \cdot \frac{\left(C_d \cdot S_{eff}\right)_{eq}}{V_{ia}} \cdot \sqrt{2 \cdot g \cdot \mathscr{Z}} \qquad \left[\text{h}^{-1}\right] \tag{4.14}$$

and for $\mathscr{B}$:

$$\mathscr{B} = 3600 \cdot \frac{\left(C_d \cdot S_{eff}\right)_{eq}}{V_{ia}} \cdot \sqrt{\Delta C_p} \qquad \left[\text{s}\cdot\text{h}^{-1}\cdot\text{m}^{-1}\right] \tag{4.15}$$

where the term $\left(C_d \cdot S_{eff}\right)_{eq}$ is the equivalent airflow resistance for any given airflow path within the building.

In summary:
From the analysis above, Model A appears to be accurately and adaptable enough for describing the thermal behavior of the indoor air temperature, which indicates that wind and buoyancy effects are most probably to be assisted by each other, due to the most frequent wind direction encountered; in agreement with what has been reported in §3.4.3(D). However, the identified values in table 4.4 also depends on the accuracy of the first two equations in Model A, which is why the necessity of them to be consistent with the thermal characterization of the platform. In this regard, an analysis of the error of Model A due to the numerical solution method employed and the uncertainty of the experimental data introduce should be performed to assess its reliability.

4.2 Choice of a thermal behavior model for the thermal mass

As shown before, one of the most important terms in equation 4.2 is the convective heat flow at the floor concrete-slab. In order to reduce the experimental data required to run the model, the following is intended to choose a conduction heat transfer model to describe the surface temperature of the floor concrete-slab. Despite the values of Biot's number found in chapter 2 regarding the concrete-slab for each configuration (values around 0,1), the Biot's number critical value (Bi $\ll$ 0,1) suggests that uniform conduction heat transfer might not occur through the slab thickness. However, a "Model B" is proposed to consider both uniform and no-uniform conduction heat transfer. Thus, we introduced a Model B1 which considers uniform conduction heat transfer via a lumped-capacitance model, and a Model B2 which considers non-uniform conduction heat transfer via a space discretization over the slab thickness using finite difference. Both models are solved using experimental data. Finally, the model that describes more accurately the behavior of the floor surface temperature will be coupled with the Model A.

4.2.1 Lumped-capacitance approximation

The assumption of uniform conduction heat transfer through the concrete-slab thickness implies that all temperature gradients are null or negligible, and thus, the entire slab is considered to have a uniform temperature. This assumption is often called "the lumped-capacitance model approximation" [119], and it is merely defined by an energy balance of the superficial heat exchanges between the slab and its environment, similar to equation 4.2, as follows:

$$\rho_D \cdot e_D \cdot c_{p_D} \cdot \frac{\mathrm{d}T_D(t)}{\mathrm{d}t} = h'_{C_D}(t) \cdot [T_{ia}(t) - T_D(t)] \;+\; \varepsilon_D \cdot \sigma \cdot \left[T^4_{surr}(t) - T^4_D(t)\right] \qquad [\mathrm{W}] \tag{4.16}$$

where the subscript D refers to the floor concrete-slab, and the consideration of one temperature T_D is sufficient to agree with the lumped-capacitance approximation. The concrete slab thickness is represented by e_D, and its emissivity by ε_D. The term on the left-hand side of equation 4.16 represents the sensible energy storage term. The two terms on the right-hand side represent the convective heat flow exchanged with the indoor air, and the long wavelength radiative heat transfer exchanged between the surrounding surfaces. Based on the analysis presented in §2.6.1.6 (p.79), any other form of radiative

heat transfer, i.e., short wavelength, is neglected. Also, despite the several layers included in the floor slab (cf. fig. 4.22), only the concrete layer will be considered for the modeling and computation.

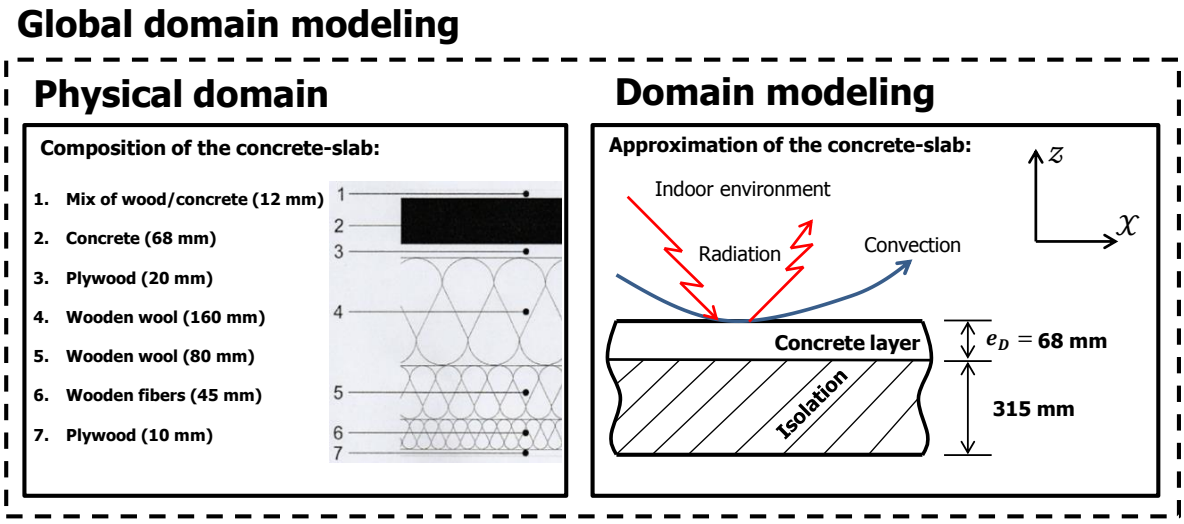

Figure 4.22: Schematic employed in the modeling of the heat transfer through the concrete-slab.

4.2.2 Spatial discretization via finite differences

The physical domain to be discretized is presented in figure 4.22, where the top surface of the concrete slab is submitted to convective and radiative heat exchanges with the indoor environment only. The bottom surface of the concrete layer is considered to be isolated, as well as its other ends in the XY plane. For this, following the finite difference method, the concrete-slab thickness is divided into several N small control volumes (CV_N) as showed in figure 4.23 with a thickness of Δz, where each CV_N is considered to be at a uniform temperature T_{D_N}, represented by a single point N ("node") located at the center of the control volume.

Therefore, the classic transitory one-dimensional heat conduction equation in cardinal coordinates can be written by using the finite difference method for spatial discretization only [118], as follows:

$$\rho_D \cdot \Delta z \cdot c_{p_D} \cdot \frac{\mathrm{d}T_{D_N}(t)}{\mathrm{d}t} = \frac{T_{D_{N-1}}(t) - 2 \cdot T_{D_N}(t) + T_{D_{N+1}}(t)}{\Delta z} \qquad [\mathrm{W}] \tag{4.17}$$

where T_{D_N} represents the temperature of the node N. The temperatures $T_{D_{N-1}}$ and $T_{D_{N+1}}$, when analyzing node N, represent the temperature of the nodes before and after, or in our case, the nodes above and below node N in the z-direction, respectively. The distance Δz is calculated by dividing the considered thickness e_D with a desired number of nodes M.

The boundary conditions of our modeling domain can be written for the top node ($N = 1$) or CV_1 (submitted to convection an radiation heat transfer), being at temperature T_{D_1}, where the CV_1 has a

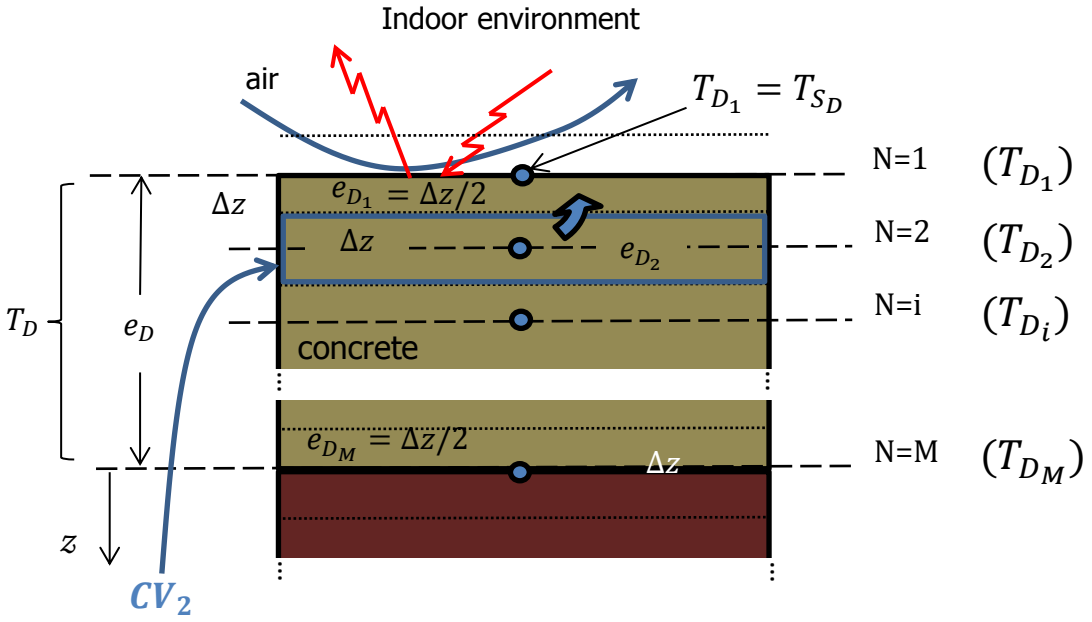

Figure 4.23: Schematic of the method employed in the discretization of the concrete-slab thickness.

thickness of half Δz, as follows:

$$\rho_D \cdot \frac{\Delta z}{2} \cdot c_{p_D} \cdot \frac{dT_{D_1}(t)}{dt} = h'_{C_D}(t) \cdot [T_{ia}(t) - T_{D_1}(t)] + \varepsilon_D \cdot \sigma \cdot \left[T^4_{surr}(t) - T^4_{D_1}(t)\right] + \lambda_D \cdot \frac{T_{D_2} - T_{D_1}}{\Delta z} \quad [\mathrm{W}] \tag{4.18}$$

where λ_D represents the thermal conductivity of the concrete slab, considered to have a constant value through the slab. The last term on the right-hand side of equation 4.18 represents the conductive heat flux from the CV_2 to the CV_1.

The boundary condition for the bottom node $N = M$ or CV_M, can be written as follows:

$$\rho_D \cdot \frac{\Delta z}{2} \cdot c_{p_D} \cdot \frac{dT_{D_M}(t)}{dt} = \lambda_D \cdot \frac{T_{D_{M-1}} - T_{D_M}}{\Delta z} \quad [\mathrm{W}]\,. \tag{4.19}$$

For the intermediate control volumes, i.e., CV_2 to CV_{M-1}, the heat conduction equation is the same as equation 4.17.

4.2.3 Choice of a Model B for all opening configuration

Model B1 with the lumped-capacitance approximation, and Model B2 with the discretization of the concrete slab, have been defined here before. The dataset for the comparison process and validation criteria is the same as described in §4.1.3.1 (p.135). The method for solving Model B is the same as for Model A. However, since we employed our experimental data only (no meteorological data), the time step chosen is of one iteration every minute. The values employed, for Models B1 and B2, are presented in table 4.5.

Variables in Model B1 and B2

Desired variables (unknowns): T_D, T_{D_1} and T_{D_M}.
Data from experiments: T_{ia}, T_{surr}, h'_{C_D}.

Table 4.5: Set of parameters for Model B.

Parameters	e_D	c_{p_D}	S_D	ρ_D	ε_D	M	Δz	λ_D
Dimensions	[mm]	$[\mathrm{J{\cdot}kg^{-1}{\cdot}K^{-1}}]$	$[\mathrm{m^2}]$	$[\mathrm{kg{\cdot}m^{-3}}]$	[−]	[−]	[mm]	$[\mathrm{W{\cdot}m^{-1}{\cdot}K^{-1}}]$
Values	68**	1000*	46**	2300*	0,95*	64***	1,06	1,8*

* Standard physical properties for concrete [1].
** Geometrical parameters of the concrete layer.
*** Retained total number of nodes; no significant difference found for a larger number of nodes.

4.2.3.1 Discussion and evaluation of results from Model B1 and B2

The solution of Model B1, for configuration n°2 only (cf. table 2.6, p.65), is presented in figures 4.24 and 4.25. In the latter, a histogram is included to show the distribution of the absolute error between the model and measurement. The computation time (or running time) expended to solve the model for each configuration was less than a minute. Figure 4.24 presents the following two plots:

(a) A comparison of the surface temperature of floor concrete-slab T_{S_D} between the model (yellow and red lines) and experimental data (blue circles), along with the absolute error (brown line) at every instant. This error is calculated between the temperature T_{S_D} measured (blue dots) and the model (red line). Also, the results of model B1 using $h'_{C_{D-TEM}}$ (yellow line, named TS_D model 1), and model B1 using $h'_{C_{D-FGT}}$ (red line, named TS_D model 2). For this Model, $T_{S_D} \equiv T_D$.

(b) The resulting heat flow on the floor for each term in equation 4.16 using T_{S_D} from the model: Convection (red), radiation (dark green), energy storage term (black).

Figure 4.24 (a) shows the results from Model B1, when using $h'_{C_{D-TEM}}$ (yellow line) and $h'_{C_{D-FGT}}$ (red line). The values of the former are computed with the heat flux measurement from thermoelectric modules (TEM), and the values of the latter are computed with the heat flux measurement from Captec heat flux meters (FGT), which was encountered to be around half of the value from the thermoelectric modules (cf. Appendix A.3). Note here that this was also found by Yang [113] as presented previously at the end of §1.4.2.2. Moreover, in figure 4.24 (a), it can be observed that the red line reproduces more accurately the behavior of T_{S_D} (blue circles) in comparison with the yellow line. Where the latter slightly underestimates the temperature during nighttime.

The resulting mean absolute error between the blue circles and the red line is 0,14 °C (brown line), with a $RMSE$ value of 0,18 °C (cf. fig. 4.25). The $RMSE$ value is about 0,24 when using $h'_{C_{D-TEM}}$. This implies that the overestimation caused by the thermoelectric modules in the estimated convective heat flux appears to have an impact (a difference of about 0,06 in terms of $RMSE$) on the prediction of the surface temperature of the concrete slab. Although, the importance of this impact is rather subjected to the application and purpose of the model, the value of $h'_{C_{D-FGT}}$ or just $h'_{C_D}/2$ will be employed in the next simulations.

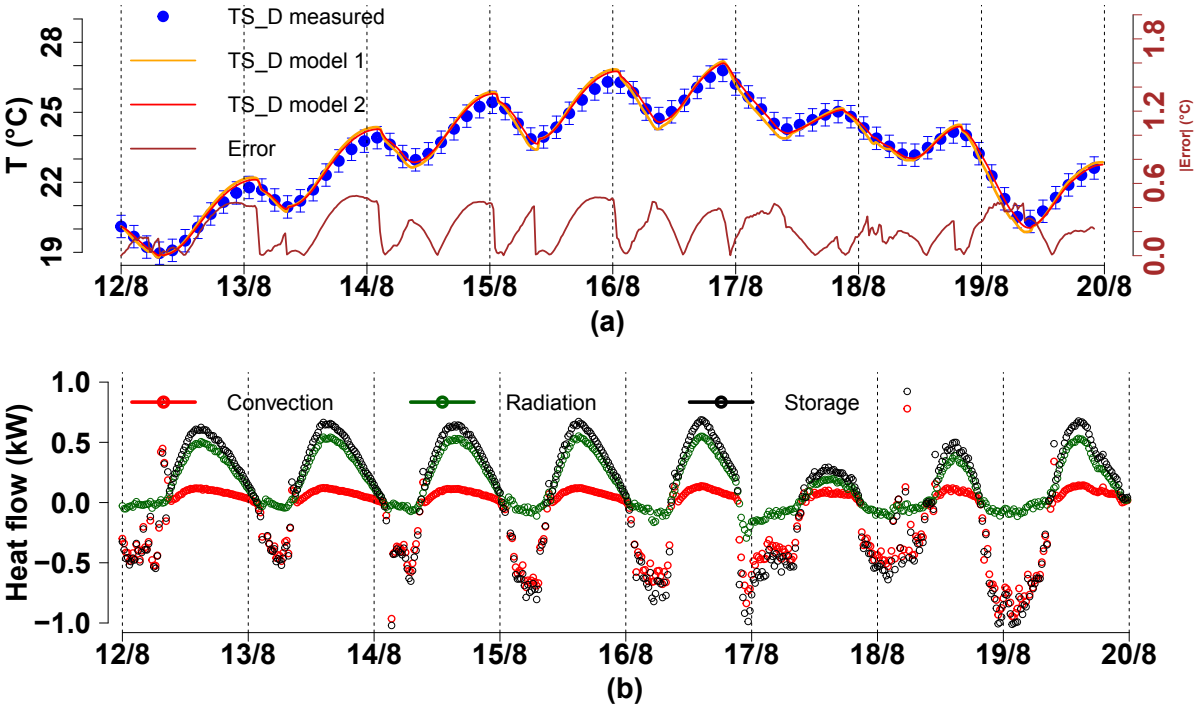

Figure 4.24: Model B1 for config. n°2. (a) concrete-slab surface temperature measured (blue dots), T_D model with $h'_{C_{D-TEM}}$ (yellow line, TD_S model 1), and T_D model with $h'_{C_{D-FGT}}$ (red line, TD_S model 2). Absolute error (brown) between red line and blue dots, and error bars $\pm$0,48 °C. Recall that: $T_{S_D} \equiv T_D$. (b) Terms on equation 4.16, from the point of view of the surface (negatives values correspond to a discharge).

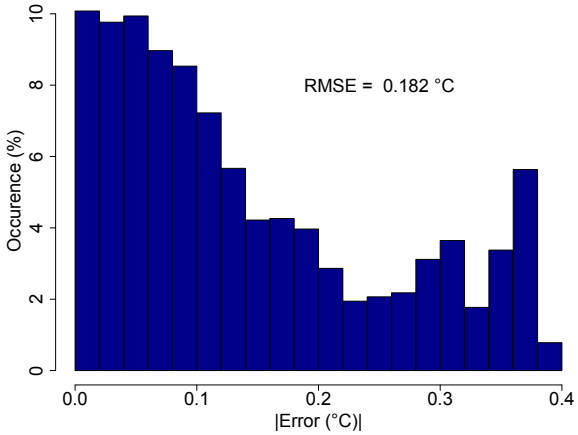

Figure 4.25: Associated error distribution for T_{S_D} in fig. 4.24 (a), and the $RMSE$ value.

The solution of Models B2, also for configuration n°2 only, is presented in figures 4.26 and 4.27. The computation time (or running time) expended to solve the model for each configuration was also less than a minute. Figure 4.26 presents the following:

(a) a comparison of the surface temperature of floor concrete-slab T_{S_D} between the model (yellow and red lines) and experimental data (blue circles), along with the absolute error (brown line) at every instant. This error is calculated between the temperature T_{S_D} measured (blue) and the

model (red). We present two "sub-models" for T_{S_D}: one with $h'_{C_{D-TEM}}$ (yellow line, named TS_D model 1), and another with $h'_{C_{D-FGT}}$ (red line, named TS_D model 2).

(b) the resulting heat flow on the floor for each term in equation 4.16 using T_{S_D} from the model: Convection (red), radiation (dark green), energy storage term (black).

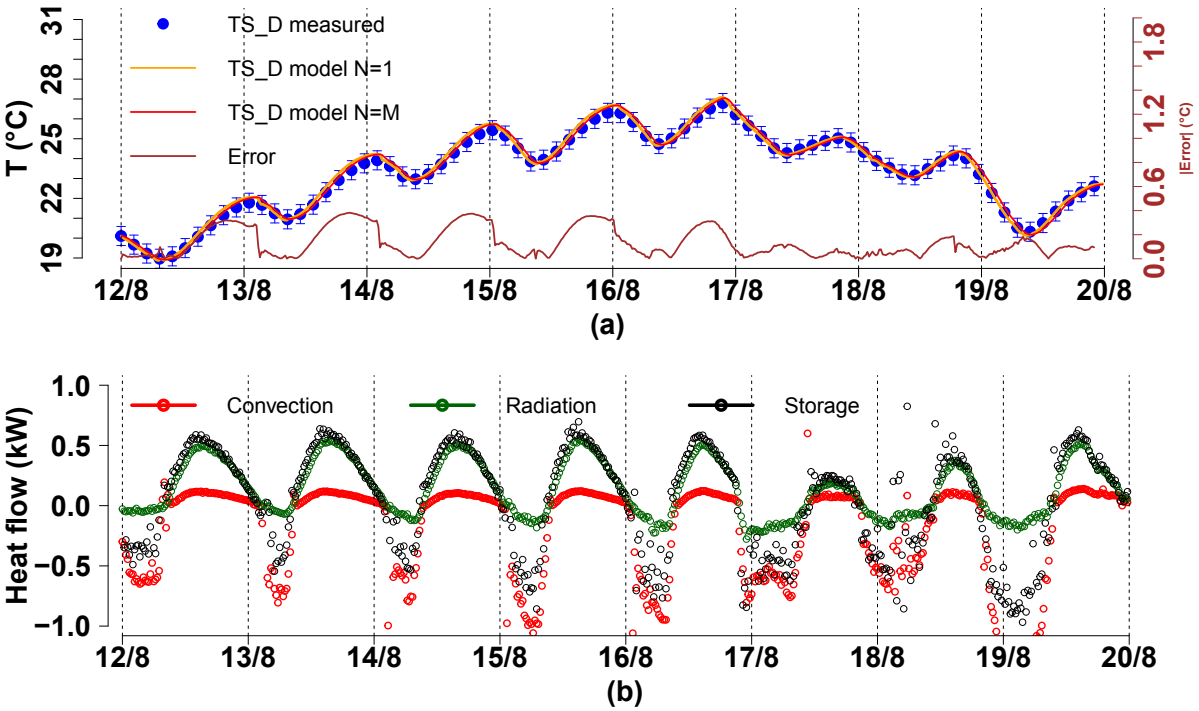

Figure 4.26: Model B2 for config. n°2. (a) Temperatures of the top node (yellow line, TD_S model N=1) and bottom node (red line, TD_S model N=M). Absolute error (brown) between top node and blue dots, and error bars ±0,48 °C. (b) heat flow terms on equation 4.17, from the point of view of the surface (negatives values correspond to a discharge).

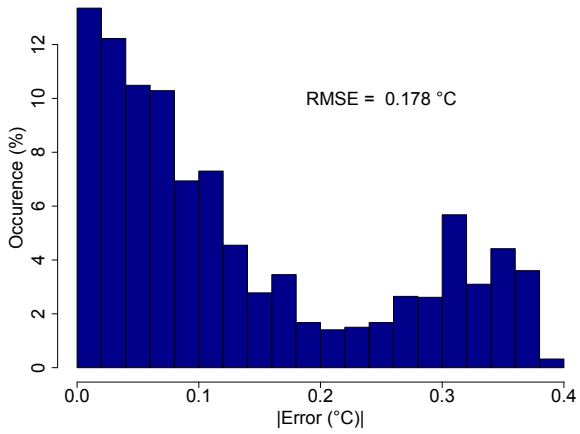

Figure 4.27: Associated error distribution for T_D in fig. 4.26 (a), and the $RMSE$ value.

Therefore, figure 4.26 (a) shows the results of Model B2 using $h'_{C_D}/2$ only. In this figure, the temperature results for the top (N=1, yellow line) and bottom (N=M, red line) nodes are presented, where a

difference of about 0,07 °C was encountered between these nodes. Finally, better results were encountered for model B2 regarding the $RMSE$ value 0,18 °C (cf. fig. 4.27).

Finally, lower $RMSE$ values were encountered, when employing a larger value of Δz and holding the total number of nodes, for any given number of nodes chosen. In other words, a slightly bigger thickness than the real value, gives better results in terms of dynamics and errors.

In summary:
Although not big differences are encountered between Models B1 and B2 in terms of $RMSE$ and dynamics, the best representation of T_{S_D} appears to be achieved by Model B2. This indicates that considering a no-uniform conduction heat transfer through the slab thickness leads to better prediction of its thermal behavior (also suggested by the values of Biot's number encountered). Despite lower $RMSE$ values were encountered when employing a bigger value for the concrete slab thickness (e_D), this was rejected due to the inconsistency with the real physical domain.

4.3 A complete model for describing the coupling between the energy charge-discharge of the thermal mass and natural ventilation

4.3.1 Evaluation of the model with data inside the identification process

Now, by merging Model B2 with Model A, the temperature measurement of the concrete-slab surface is no longer needed, and the coupling between the energy charge-discharge of the thermal mass and natural ventilation is completed. This model is summarized in equation 4.20 and we will refer to it as "the coupled model."

The numerical results of "the coupled model" are presented in figures 4.28-4.31, for configuration n°2 only. The computation time expended was about 13 minutes.

Variables in "the coupled model"

Desired variables (unknowns): T_{ia}, T_{S_D}, T_D, ach.
Data from experiments: T_{oa}, T_{surr}, T_{S_P}, h'_{C_P}, h'_{C_D}, h'_{C_g}.
Data from meteorological station: $\mathcal{V}_{met}$, ϕ_W.

The coupled model

$$
\begin{cases}
\textbf{1)} \quad \rho(T_{ia}) \cdot V_{ia} \cdot c_p(T_{ia}) \cdot \dfrac{\mathrm{d}T_{ia}(t)}{\mathrm{d}t} = h'_{C_D}(t) \cdot S_D \cdot \left[T_{S_D}(t) - T_{ia}(t)\right] + h'_{C_P}(t) \cdot S_P \cdot \left[T_{S_P}(t) - T_{ia}(t)\right] \\
\qquad\qquad + h'_{C_g}(t) \cdot S_g \cdot \left[T_{S_g}(t) - T_{ia}(t)\right] \\
\qquad\qquad + V_{ia} \cdot \dfrac{ach(t)}{3600} \cdot \left[\rho(T_{oa}) \cdot c_p(T_{oa}) \cdot T_{oa}(t) - \rho(T_{ia}) \cdot c_p(T_{ia}) \cdot T_{ia}(t)\right] \\
\textbf{2)} \quad \rho_D \cdot \Delta z \cdot c_{p_D} \cdot \dfrac{\mathrm{d}T_{D_N}(t)}{\mathrm{d}t} = \dfrac{T_{D_{N-1}}(t) - 2 \cdot T_{D_N}(t) + T_{D_{N+1}}(t)}{\Delta z} \\
\quad \text{with} \quad \rho_D \cdot \dfrac{\Delta z}{2} \cdot c_{p_D} \cdot \dfrac{\mathrm{d}T_{D_1}(t)}{\mathrm{d}t} = h'_{C_D}(t) \cdot \left[T_{ia}(t) - T_{D_1}(t)\right] + \varepsilon_D \cdot \sigma \cdot \left[T^4_{surr}(t) - T^4_{D_1}(t)\right] + \lambda_D \cdot \dfrac{T_{D_2} - T_{D_1}}{\Delta z} \\
\quad \text{and} \quad \rho_D \cdot \dfrac{\Delta z}{2} \cdot c_{p_D} \cdot \dfrac{\mathrm{d}T_{D_M}(t)}{\mathrm{d}t} = \lambda_D \cdot \dfrac{T_{D_{M-1}} - T_{D_M}}{\Delta z} \\
\textbf{3)} \quad T_{S_g}(t) = \frac{1}{\mathcal{F}_{g \to D}} \sqrt[4]{T^4_{surr}(t) - \mathcal{F}_{P \to D} \cdot T^4_{S_P}(t) - \left[1 - \mathcal{F}_{P \to D} - \mathcal{F}_{g \to D}\right] \cdot T^4_{ia}(t)} - 273,15 \\
\textbf{4)} \quad ach(t) = \begin{cases}
C_l \cdot \left[4 \cdot \left| \dfrac{T_{ia}(t) - T_{oa}(t)}{T_{oa}(t)} \right|^{0,58}\right]^{a_l} \text{; when NV openings closed} \\
C_v \cdot \left[\mathcal{A} \cdot \left| \dfrac{T_{ia}(t) - T_{oa}(t)}{T_{oa}(t)} \right|^{1/2}\right]^{a_v} \cdot \left[\mathcal{B}_v(\phi) \cdot \mathcal{V}_{met}(t)\right]^{b_v} \text{; when NV openings opened} \\
C_v \cdot \left[\mathcal{A} \cdot \left| \dfrac{T_{ia}(t) - T_{oa}(t)}{T_{oa}(t)} \right|^{1/2}\right]^{a_v} \text{: If } \mathcal{V}_{met}(t) = 0 \text{; when NV openings opened}
\end{cases}
\end{cases}
\tag{4.20}
$$

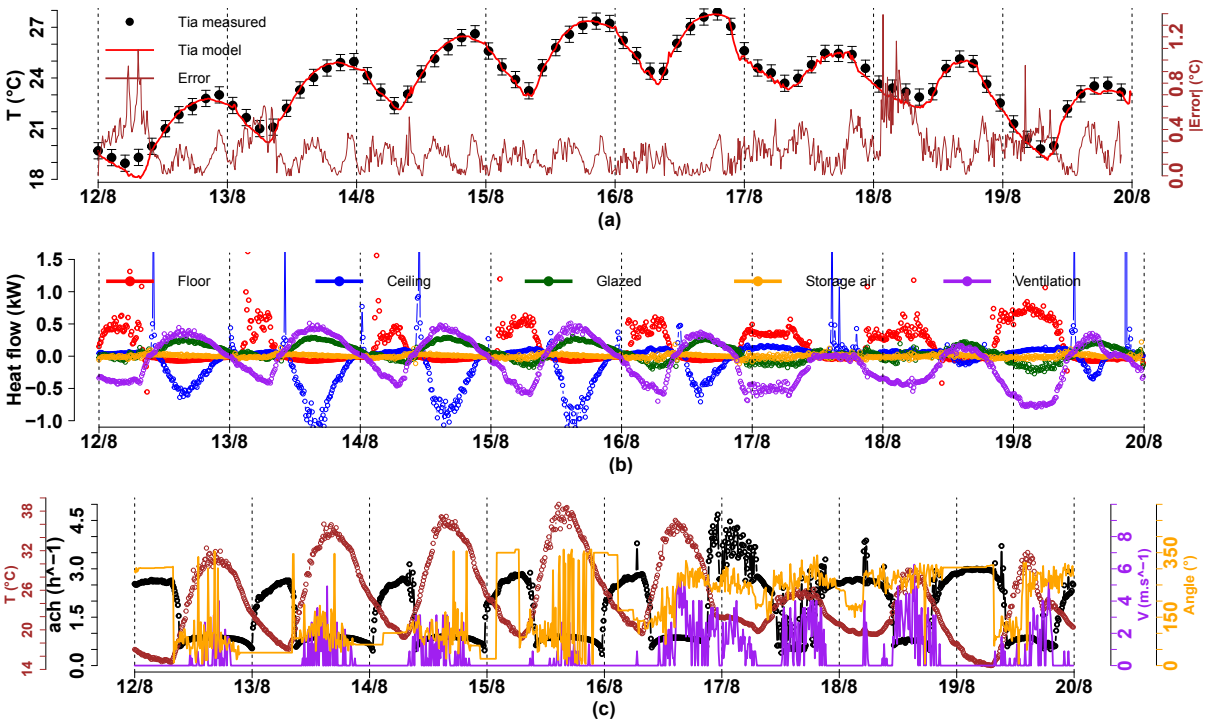

Figure 4.28: Results for config. n°2: (a) T_{ia} model (red line), T_{ia} measured (black dots), and absolute error (brown line). (b) Heat flows: floor (red), ceiling (blue), glazed-facade (green), energy storage in air (yellow), and ventilation (purple). (c) *ach* (black), $\mathcal{V}_{met}$ (purple) and ϕ_W (yellow), and T_{oa} (brown).

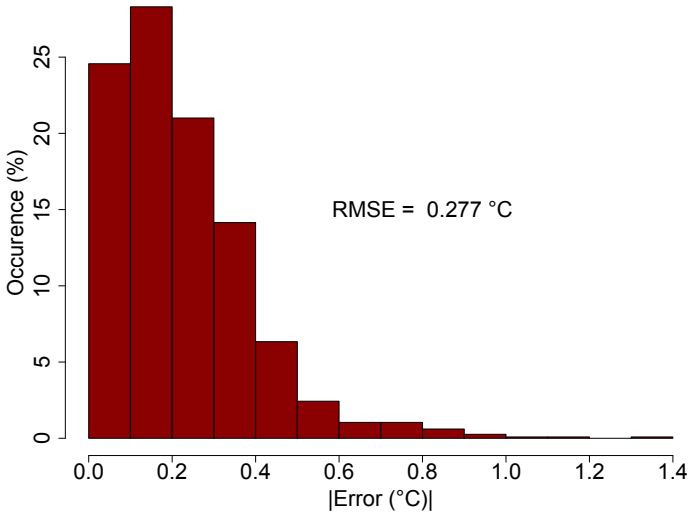

Figure 4.29: Associated error distribution for fig. 4.28 (a), and the $RMSE$ value.

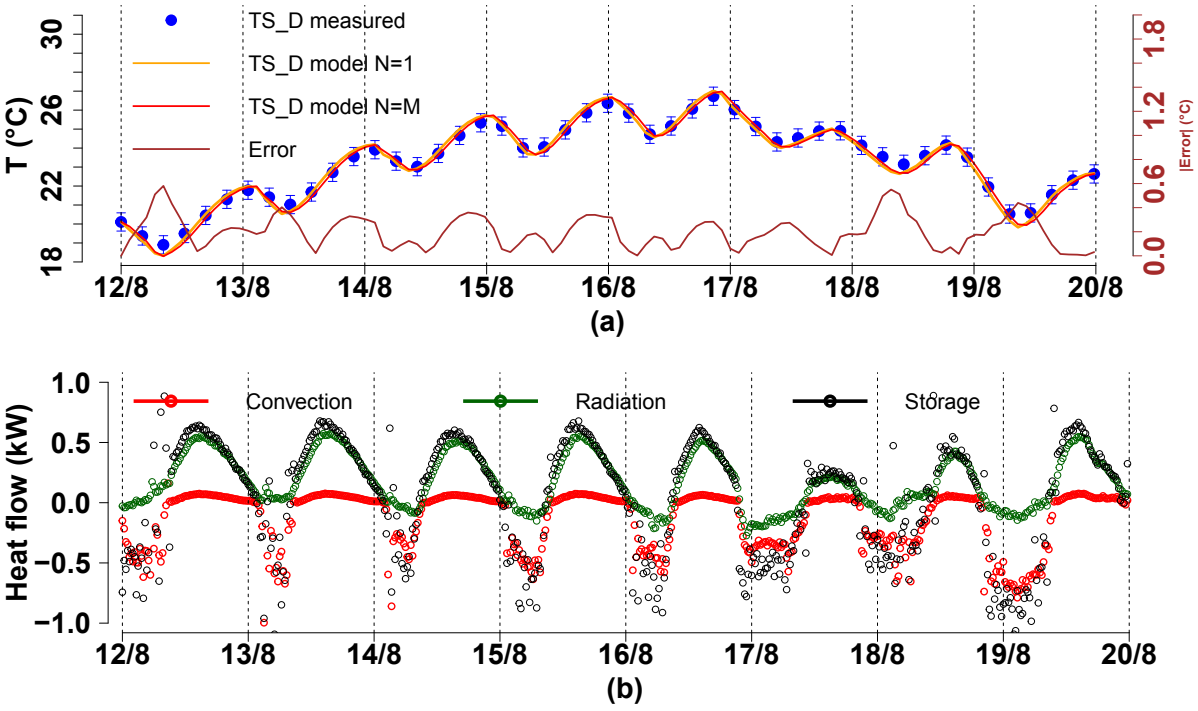

Figure 4.30: Results for config. n°2. (a) Temperatures of the top node (yellow line, TD_S model N=1) and bottom node (red line, TD_S model N=M). Absolute error (brown) between red line and blue dots, and error bars $\pm$0,48 °C. (b) heat flow terms, from the point of view of the surface (negatives values correspond to a discharge).

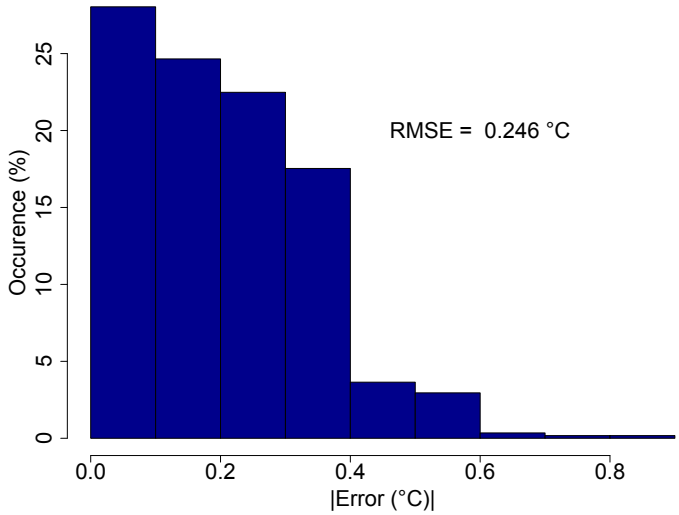

Figure 4.31: Associated error distribution for fig. 4.30 (a), and the $RMSE$ value.

The accuracy of coupling Model B2 to Model A appears to be slightly reduced for the description of both T_{ia} and T_{S_D} simultaneously, in comparison with the results from both models alone (cf. figs. 4.14 and 4.27) in terms of $RMSE$ values:

- $RMSE$ values for T_{ia} of 0,24 and 0,28 °C, from Model A and "the coupled model", respectively.
- $RMSE$ values for T_{S_D} of 0,18 and 0,25 °C, from Model B and "the coupled model", respectively.

Regarding the heat flow terms, the resulting convective heat flow for the concrete slab in both figures 4.28 (b) (red) and 4.30 (b) (red), appear to agree with each other regarding the magnitudes, and also with the convective heat flow determined experimentally presented in figure 4.9 (red). Conversely, the resulting convective heat flow term for the ceiling in figure 4.28 (b) (blue), appears to overestimate this value for only three days (13/8 - 15/8) in comparison with figure 4.9 (blue).

Regarding the air change rate per hour, the resulting *ach* values in figure 4.28 (c) (black), can not be compared directly with the values in figure 4.19 (black), since the experimental data employed is not from the same days. However, similar values are encountered between them.

Despite the accuracy encountered with the "the coupled model", a model with the least variables from experimental data or none not all, would be required for forecasting the thermal behavior of the platform under different outdoor conditions and different natural ventilation scenarios (other than those implemented during out measurement campaigns). In this matter, there are five variables in the models that are taken from the measurement campaigns: T_{surr}, T_{S_P}, h'_{C_P}, h'_{C_D}, h'_{C_g}. Until now, a constant value was employed for h'_{C_g} for all the models before, which indicates that the model is not particularly sensible to values admitted for this variable. Therefore, it can be said that only four variables, which values are taken from the measurement campaigns, remained: T_{surr}, T_{S_P}, h'_{C_P}, h'_{C_D}.

4.3.2 Evaluation of the model with data outside the identification process

The coupled model was also tested using data from outside the identification process. The only data remaining from the measurement campaigns with typical summertime weather conditions, for consecutive days, was for configuration n°2: from July 27$^{\text{th}}$ to 29$^{\text{th}}$. The numerical results are presented

in figures 4.32-4.35. As expected, the accuracy of the model is reduced: a $RMSE$ value of 0,53 °C and 0,43 °C, for T_{ia} and T_{S_D}, respectively.

Variables in "the coupled model" tested with data outside identification

Data from experiments: T_{oa}, T_{surr}, T_{S_P}, h'_{C_P}, h'_{C_D}.
Data from meteorological station: $\mathcal{V}_{met}$, ϕ.
Coefficients in *ach* **model:** same as in table 4.4 for all configurations.

One of the leading causes for the accuracy reduction is that, for this dataset, the most frequent wind direction was approximately 300°. From the analysis in chapter 3, for such wind direction, it is expected that wind and buoyancy effects would oppose to each other, and since the values for the exponents have been fixed to be the same as before (cf. table 4.4), the $ach_{\Delta T x W}$ model for this case is not fully consistent with the phenomena involved; despite the $RMSE$ values, which might be acceptable depending on the application.

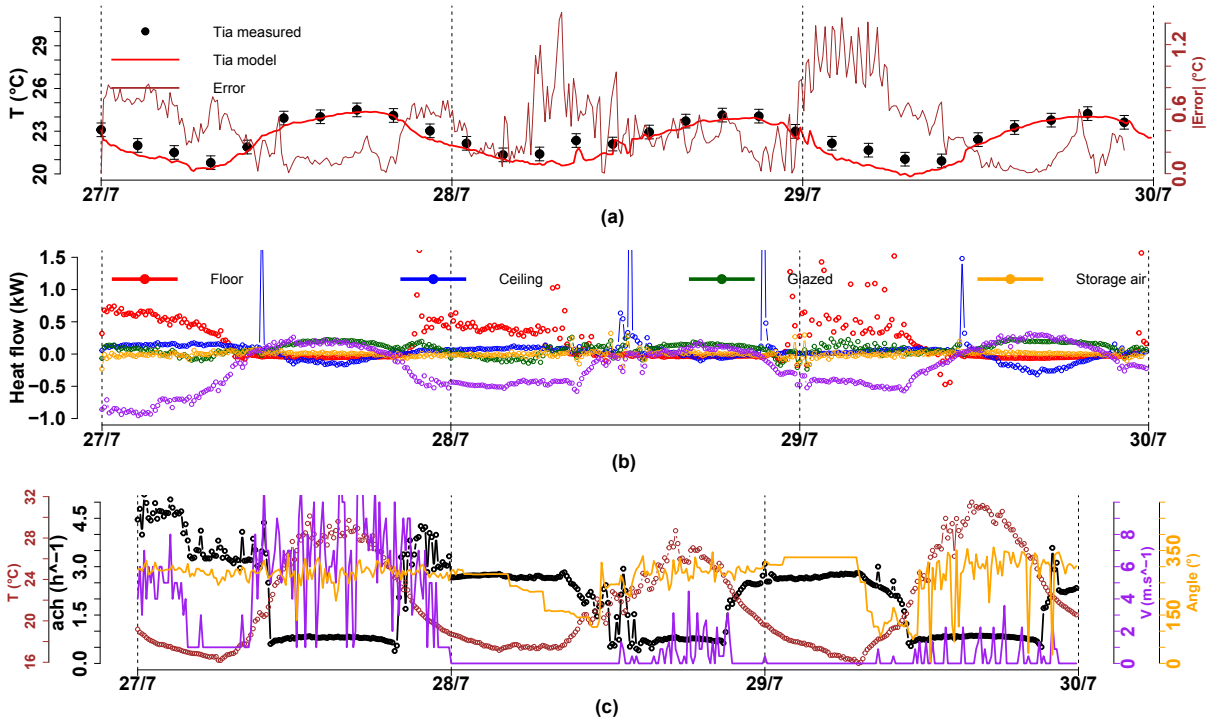

Figure 4.32: Results for config. n°2 (data not part of identification): (a) T_{ia} model (red line), T_{ia} measured (black dots), and absolute error (brown line). (b) Heat flows: floor (red), ceiling (blue), glazed-facade (green), energy storage in air (yellow), and ventilation (purple). (c) *ach* (black), $\mathcal{V}_{met}$ (purple) and ϕ_W (yellow), and T_{oa} (brown).

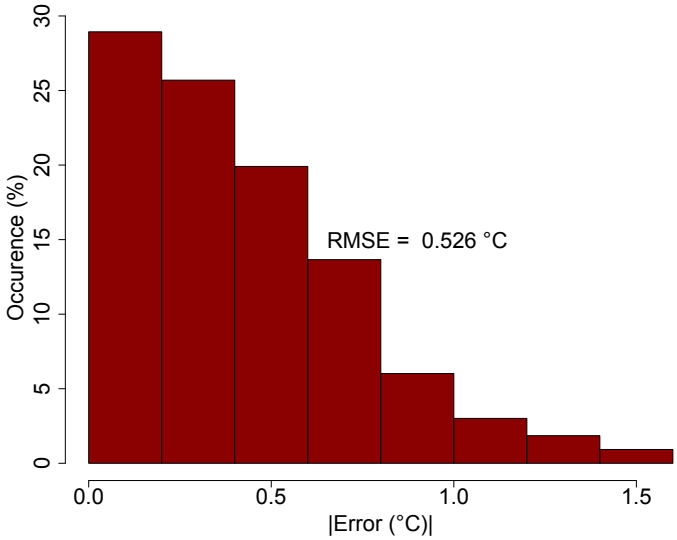

Figure 4.33: For config. n°2 (data not part of identification). Associated error distribution for fig. 4.32 (a), and the $RMSE$ value.

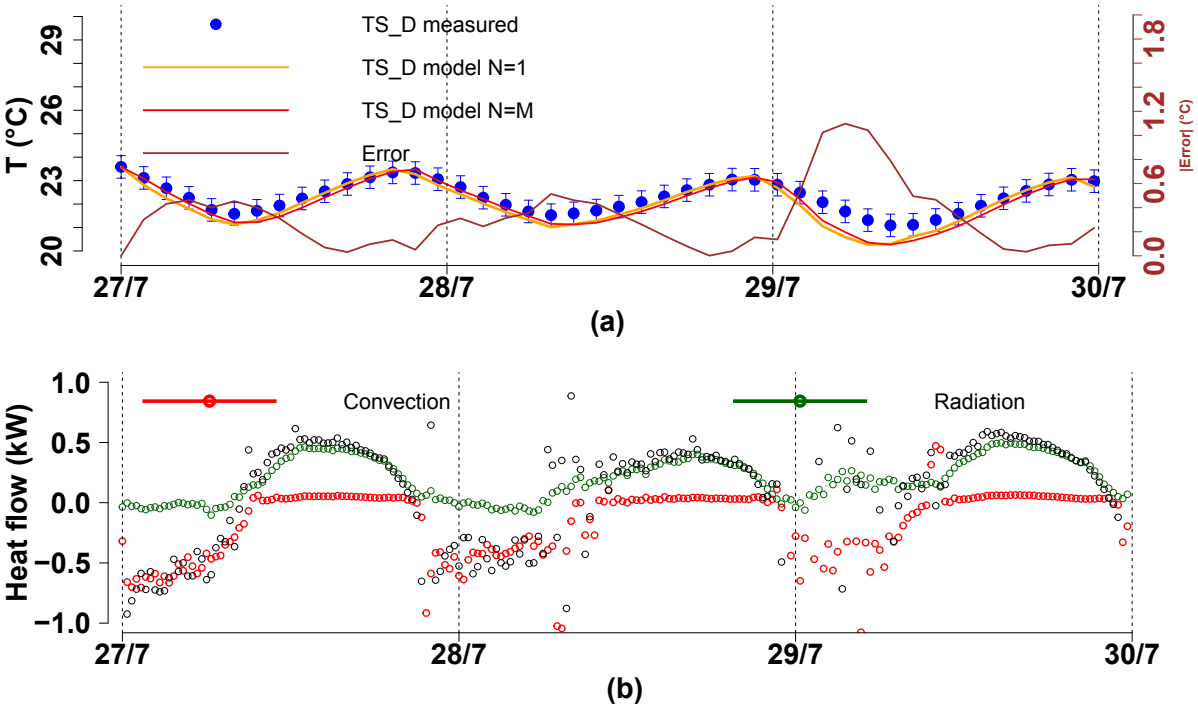

Figure 4.34: Results for config. n°2 (data not part of identification). (a) Temperatures of the top node (yellow line, TD_S model N=1) and bottom node (red line, TD_S model N=M). Absolute error (brown) between red line and blue dots, and error bars $\pm$0,48 °C. (b) heat flow terms, from the point of view of the surface (negatives values correspond to a discharge).

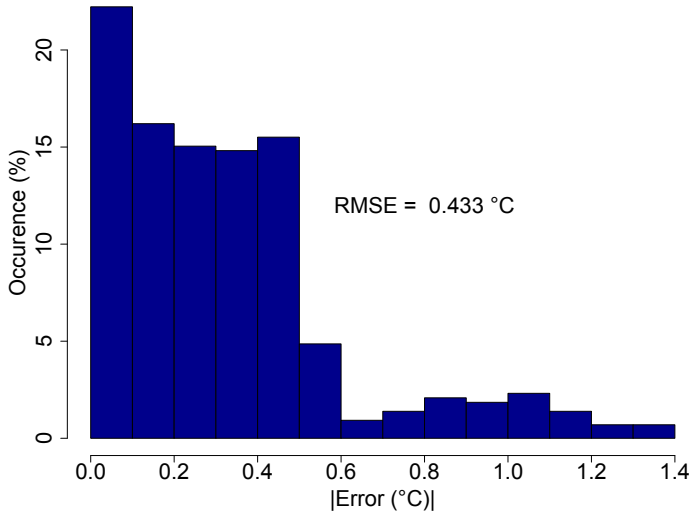

Figure 4.35: For config. n°2 (data not part of identification). Associated error distribution for fig. 4.34 (a), and the $RMSE$ value.

4.4 Concluding remarks

In this chapter, we had addressed the problem of identifying a thermal model that describes the behavior of the platform. At the moment, the identified model (namely the "coupled model") seems to thoroughly describe the behavior of the indoor air temperature and the surface temperature of the concrete slab, for the measurement campaigns implemented in the identification process. However, this model still employs experimental data as inputs (other than those from the meteorological station): the convective heat transfer coefficient at the floor and ceiling surfaces, the mean radiant temperature, and the ceiling surface temperature. The couple model can be represented in a simple schematic by highlighting the three main elements (indoor air, airflow rate, concrete-slab), and the components that are still needed (in purple):

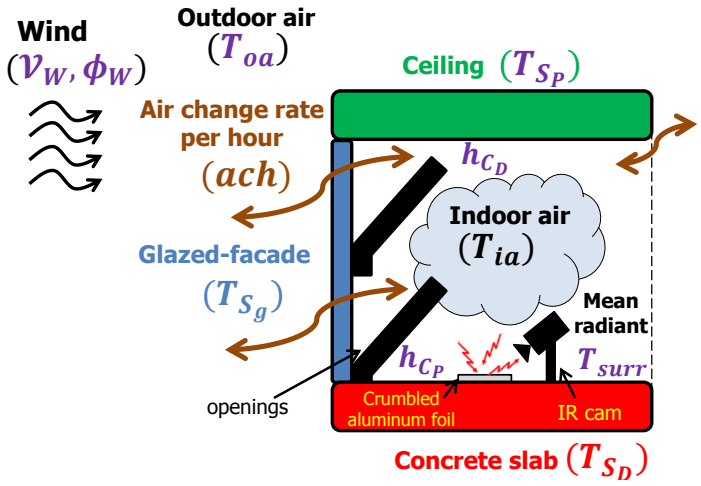

Nevertheless, this identification has allowed us to notice the following:

- It is necessary to account, separately, for the convective heat exchanged between the indoor air and the floor and ceiling, apart from the vertical walls.
- The consideration of only two capacities seems to be enough for a good description of the thermal behavior. However, in this case, since a small number of parameters is involved in the model, this model is more sensitive to all those parameters, and thus, they need to be represented attentively. Moreover, the fact that only two thermal capacitances, in any given coupled model with natural ventilation, are enough to well described the behavior of the indoor air temperature of the platform is in agreement with the models reported in the literature concerning the coupling of natural ventilation with the thermal mass.
- The value of the exponents' signs in the superposition model for *ach* is related to the phenomena involved, i.e., buoyancy and wind forces are assisted or opposed to each other, being strongly dependent on the wind direction. Such phenomena encourage to find an expression that can link both parameters directly.
- The determination of the net *ach*, indirectly, via an energy balance with heat flux and temperature measurements, arises as a suitable identification methodology for cases where costs reduction is far more important than accuracy requirements, in comparison to other experimental techniques.

Nevertheless, it has been demonstrated that instead of focusing on the local effects of wind and buoyancy, the natural airflow rate can be well estimated by focusing only on the global influence of both effects.

General conclusion and future work

Recapitulation of the undertaken work

Throughout this study, we are interested in characterizing the thermal and airflow aspects of an experimental platform, which stands as a prototype of Plus Energy House (PEH), to identify a thermal model that describes its behavior under typical weather conditions of southwest France in the summertime.

For this model, based on the literature review concerning the theoretical study on the coupling between natural ventilation and the thermal mass, we have been interested in only account for the heat transfer in two elements: the indoor air and the thermal mass (assumed to be concentrated in the floor concrete-slab). Also, in addition to these two elements, a third element was included in the model: the natural ventilation airflow rate.

A difference between our modeling choice and those found in the literature, lays in consideration of the following aspects:

- The incorporation of the mean radiant temperature of the indoor environment of the platform.
- The prevalence necessity of accounting for the convective heat exchanges between the indoor air ventilated-volume, and the surfaces of the floor concrete-slab, the ceiling, and the glazed-facade, separately, in the representation of the heat transfer in the indoor air. Apart from the ventilation and energy storage terms.
- The temperature dependence of the air density and specific heat capacity.
- The accounting for both wind and thermal buoyancy effects via a product superposition model for the ventilation airflow rate.
- Time-dependent convective heat transfer coefficients.

Such considerations are based on the characterization of both, the energy charge and discharge processes, and the natural ventilation airflow rate within the platform.

As a result, the identified thermal behavior model, the “couple model”, accounts for the heat transfer in the three main elements mentioned earlier by:

- An energy balance for the indoor air, complemented with the representation of the mean radiant temperature as the weighted sum of the absolute temperature of the surrounding surfaces.
- The representation of the concrete-slab temperature through a non-uniform conduction heat transfer approximation, via the finite differences discretization method.
- A superposition model, for the ventilation airflow rate, that allows to accounting individually for the effects of wind and thermal buoyancy.

Moreover, concerning this last element, the ventilation airflow rate, a particularity was observed in the superposition model: the sign of the exponents might need to be adjusted depending on the wind direction. However, the relationship between the magnitude of these coefficients/exponents and the dominance of wind and buoyancy effects is still unknown. Other superposition models found in the literature have been proven not to be suitable, since they were developed for simple airflow path/patterns, in simple natural ventilation strategies such as single-sided, cross and stack ventilation, with a reduced number of openings. Thus, network airflow models were implemented via direct airflow simulations through the software CONTAM, because the knowledge of an airflow path/pattern is not necessary. Also, because of the number and distribution (location) of the openings in our experimental platform, which might be judged as rather complicated for a one-story building of 70 m^2. These airflow simulations considered the following: the location of the air-leakage within the platform, a single-zone model, and transient conditions with no consideration of any contaminants and humidity.
In this regard, the characterization of the airflow rate in the platform included the *in situ* estimation of the airflow capacity of the openings and their friction characteristics via the discharge coefficient.

Finally, the thermal characterization of the platform has also contributed to promoting the implementation of thermoelectric modules, as an alternative to conventional heat flux meters, for estimating the convective and radiative heat exchanges in the building domain. The most attractive characteristic to consider the implementation lays in the following aspects:

- Budget, since the cost of thermoelectric modules, is around ten times lower than the cost of conventional heat flux meters, such as Captec®.
- Sensitivity/accuracy/size, since thermoelectric modules generate a higher electric potential than conventional heat flux meters, for the same device size. This higher potential can allow a more accurate estimation of the heat flux measured with the same measuring system (sensor + acquisition system). This accurate estimation might be essential for measuring weak heat flux levels in passive environments.

Specific remarks from chapter one

In this chapter, we have covered the basics for comprehending the natural ventilation concept. We have briefly reviewed the experimental and modeling techniques already implemented for past researchers, in the estimation of the ventilation airflow rate due to the wind and thermal buoyancy effects. Also, a brief reviewed of the experimental and modeling techniques concerning the heat flux measurement and the estimation of the convective and radiative heat flux, have been presented. These literature review has allowed noticing the following remarks:

- The coupling between natural ventilation and the thermal mass of a building can be studied by only considering two simple energy balances, one on the indoor air and another on the thermal mass, and the equation for the ventilation airflow rate.
- The location of the air-leakage/infiltrations must be analyzed attentively, to avoid overestimation or underestimation of the air-leakage rate.
- The use of flat-plate heat flux meters arises as a good experimental technique for estimating the

convective heat exchanges, and more importantly, thermoelectric modules are considerably more attractive than conventional heat flux meters regarding their sensitivity.

Regarding this last remark, in the studies reviewed, the implementation of the heat flux meters differed in geometry and arrangement, i.e., black and shiny sensors installed with one of their sides always in contact [23, 29] and installed with a separation between them [63, 109, 113]. The selection of the heat flux meter depends mainly on the heat flux levels to be measured, the accuracy wanted in the heat flux measured and the measuring system employed in the measurement.

Regarding the experimental and modeling techniques for estimating the ventilation airflow rate, a limitation arises in their applicability to our specific case, since:

- The experimental techniques require heavy instrumentation (often expensive) of the openings in terms of airspeed and pressure measurements (local), being the ones that could lead to a better understanding of the phenomena involved in the ventilation process.
- The modeling techniques such as CFD requires large computation time depending on the computer power and the models itself. The models based on empirical observations require the knowledge of the airflow patterns within the building.

Thus, the modeling technique more suitable for our case seems to be the implementation of network airflow models via direct airflow simulations performed by software such as CONTAM, since the knowledge of the airflow patterns is not required.

The more suitable experimental technique seems to be the airtightness tests since it allows us to obtain empirical expressions relating the ventilation airflow directly to the pressure difference in the building for both cases: infiltrations (openings closed) and openings opened. Also, the location of the leakages can be identified without complications, and this technique has the potential to estimate *in situ* the airflow capacity and friction characteristics of the openings.

Specific remarks from chapter two

The exhaustive experimental study presented in chapter two has allowed characterizing, in detail, the thermal aspects of the experimental platform, suggesting the following major points:

- It is not enough to take the convective coefficients as constant values when the openings are open. It would be necessary to model or to identify them in another way.
- The convection inside the platform does not appear to have a dominant nature, natural or forced, both may occur when the openings are open.
- The direct solar radiation does not heat directly the indoor environment of the platform.
- The most representative measuring location on the slab surface is between the two groups of openings and in the middle of the platform, close to the south facade.
- It is necessary to take into account the convective effects on the slab surface, on the ceiling, and on the glazed-facade individually, due to their behavior.
- It is clear that there are some vertical walls that contribute the most to the heating of the indoor air; taking them all when describing the indoor air heat gains might lead to overestimations.
- The vertical thermal stratification of the indoor air within the platform, can be neglected regarding the thermal comfort of the indoor environment. However, regarding buoyancy driven

ventilation, it is suggested that neglecting these thermal gradients may be a suitable choice for larger values of $\mathcal{F}r$ number, than the ones encountered.

- The values of $\mathcal{B}i$ number encountered suggest that a non-uniform heat conduction might give a precise description of the heat transfer through the concrete-slab thickness.

These last remarks have allowed us to highlight the key elements involved in the energy charge-discharge process in our experimental platform: the indoor air, the concrete slab (as the thermal mass), the glazed-facade, the airflow rate, and the ceiling, in terms of heat transfer.

Nevertheless, the characterization of the thermal aspects of the experimental platform should also consider the heat transfer associated with the exchanges in mass (air) between the indoor and outdoor environments. This consideration requires the knowledge of the natural airflow rate within the platform. Thus, we address the following chapter to characterize the ventilation airflow rate.

Furthermore, this characterization has endorsed the consideration of including, later in the modeling, the key elements mentioned here before. Also, to consider not to include the direct solar radiation in the modeling of the heat transfer in the concrete slab.

Specific remarks from chapter three

The undertaken work in this chapter was devoted to characterizing the natural airflow rate in the platform via airflow simulation on CONTAM. This characterization aimed to determine an expression relating the net *ach* as a function of the wind speed and direction, and the indoor-outdoor temperature difference. Thus, we can retain the following remarks:

- For the buildings or enclosures, where the airflow path is difficult to be determined due to a large number of openings, focusing on estimating the net airflow rate by using network airflow models, can lead to avoiding unnecessary difficulties.
- The assumption of air-leakage equally distributed at the facades with openings seems to be appropriate, instead of identifying them first by performing airtightness tests with the smoke pencil, when focusing on the global effect of wind and buoyancy via the net air change rate.
- Performing *in situ* airtightness tests for the estimation of the friction characteristics of openings, might not be the most suitable choice due to the presence of internal obstructions, such as furniture, partition-walls, doors, among others. However, the implementation of these tests for the estimation of the airflow capacity in terms of airflow rate levels appears to agree with the values reported in the literature.
- Finally, from the airflow simulations for the combined wind and buoyancy effects, these effects appear to oppose to each other only in a specific range of wind direction.

At the moment, we may conclude that the real value of the natural air change rate in the platform remains uncertain. However, since our results have been compared with values reported in the literature, we may state that the values encountered may be a reasonable estimation of this parameter when an annual-averaged value is needed.

Moreover, the last part of this chapter has shown that we are not yet capable of reporting an expression that combines both wind and buoyancy effects directly, since: The net value of *ach* does not appear to be a simple addition when both effects are assisted, nor a simple subtraction when both effects are

opposed. Therefore, an expression able to superpose both effects is still needed. In order to choose from the superposition models reported in the literature and to avoid any possible overestimation or underestimation of the *ach* value, it is necessary to determine its real value. For the latter, we are able to identify the value of *ach* by employing the heat flux and temperature measurements performed during the measurement campaigns (presented in chapter 2), and a global energy balance in the indoor air. The first part of the following chapter is dedicated to identify and compare the *ach* value.

Specific remarks from chapter four

In this chapter, we had addressed the problem of identifying a thermal model that describes the behavior of the platform. At the moment, the identified model (namely the "coupled model") seems to thoroughly describe the behavior of the indoor air temperature and the surface temperature of the concrete slab, for the measurement campaigns implemented in the identification process. However, this model still employs experimental data as inputs (other than those from the meteorological station): the convective heat transfer coefficient at the floor and ceiling surfaces, the mean radiant temperature, and the ceiling surface temperature. The couple model can be represented in a simple schematic by highlighting the three main elements (indoor air, airflow rate, concrete-slab), and the components that are still needed (in purple):

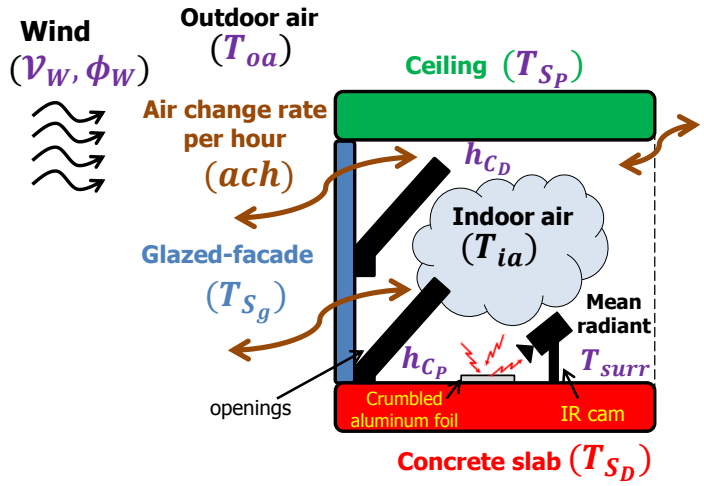

Nevertheless, this identification has allowed us to notice the following:

- It is necessary to account, separately, for the convective heat exchanged between the indoor air and the floor and ceiling, apart from the vertical walls.
- The consideration of only two capacities seems to be enough for a good description of the thermal behavior. However, in this case, since a small number of parameters is involved in the model, this model is more sensitive to all those parameters, and thus, they need to be represented attentively. Moreover, the fact that only two thermal capacitances, in any given coupled model with natural ventilation, are enough to well described the behavior of the indoor air temperature of the platform is in agreement with the models reported in the literature concerning the coupling of natural ventilation with the thermal mass.
- The value of the exponents' signs in the superposition model for *ach* is related to the phenomena

involved, i.e., buoyancy and wind forces are assisted or opposed to each other, being strongly dependent on the wind direction. Such phenomena encourage to find an expression that can link both parameters directly.

- The determination of the net *ach*, indirectly, via an energy balance with heat flux and temperature measurements, arises as a suitable identification methodology for cases where costs reduction is far more important than accuracy requirements, in comparison to other experimental techniques.

Nevertheless, it has been demonstrated that instead of focusing on the local effects of wind and buoyancy, the natural airflow rate can be well estimated by focusing only on the global influence of both effects.

Future work

The experimental and modeling study developed/implemented throughout the present work has allowed us to conceive some of the subsequent activities in different research areas:

(1) Thermal characterization:

The fact that the discharge process of the indoor ceiling surface is not done by convection nor by radiation leads to reconsider our initial hypothesis of the concrete-slab as the most important element in the platform. Thus, if neither the convective nor the radiative heat exchanges discharge the ceiling to the indoor environment, the ceiling would be discharged by conduction through its thickness towards the roof surface. Such a case brings us to consider its specific thermal behavior in the coupled model.

(2) Airflow characterization:

The apparent relationship between the exponents (values and signs) in the product superposition model for the net air change rate per hour and the wind direction, leads to perform further analysis aiming to find an expression that can describe this relationship.

(3) Metrology:

The apparent overestimation of the convective heat transfer coefficient (h_C) by the thermoelectric modules, in comparison with Captec heat flux meters, also lead to perform further analysis with the objective of finally validating such devices in the estimation of the convective heat flux, and thus, the convective heat transfer coefficient.

(4) Forecasting and control:

The construction of a forecasting model able to accurately predict the behavior of the platform, in order to develop control systems that can supervise the opening-closing of the natural ventilation openings along with the home automation system, to reduce air conditioning usage.

Motivation for accomplishing the future work

The craving of the settlement of a unified methodology that proportions the sufficient knowledge about the airflow characteristics of a building, in order to master the natural ventilation concept applied to such building, for boosting the thermal comfort and for reducing the usage of air conditioning systems.

Associated publications

Proceedings in conferences

1) Stockage/déstockage d'énergie sensible et ventilation naturelle en bâtiment : une approche expérimentale à l'échelle 1. Nominated to the Biot-Fourier price. In: Congrès SFT 2016 - Toulouse, France [22].
2) Experimental study of a natural ventilation strategy in a full-scale enclosure under meteorological conditions: a buoyancy-driven approach. In: 6th Engineering, Science and Technology Conference (ESTEC) 2017 - Ciudad de Panama, Panama [7].
3) Evaluation expérimentale d'une stratégie domotique de pilotage des éléments mobiles : vers un contrôle semi-passif simple du confort d'été en BEPos. In: Congrès SFT 2018 - Pau, France [6].
4) Influence des effets du vent et du tirage thermique sur le taux de renouvellement de l'air d'un bâtiment ventilé naturellement : estimations par simulation aéraulique directe et par validation expérimentale d'une modélisation thermique. In: Conférence IBPSA 2018 - Bordeaux, France [8].
5) Statistical analysis of architectural features effects on indoor environmental conditions in a Plus Energy House prototype. In: Passive and Low Energy Architecture (PLEA) - Hong kong, December 2018. Accepted as long paper [9].

Oral presentation in conferences

1) Stockage/déstockage d'énergie sensible et ventilation naturelle en bâtiment : une approche expérimentale à l'échelle 1. Nominated to the Biot-Fourier price. In: Congrès SFT 2016 - Toulouse, France [22].
2) Experimental study of a natural ventilation strategy in a full-scale enclosure under meteorological conditions: a buoyancy-driven approach. In: 6th Engineering, Science and Technology Conference (ESTEC) 2017 - Ciudad de Panama, Panama [7].
3) Influence des effets du vent et du tirage thermique sur le taux de renouvellement de l'air d'un bâtiment ventilé naturellement : estimations par simulation aéraulique directe et par validation expérimentale d'une modélisation thermique. In: Conférence IBPSA 2018 - Bordeaux, France [8].

Bibliography

[1] Marc Abadie et al. *Energétique des bâtiments et simulation thermique*. Paris: Eyrolles, 2015. ISBN: 978-2-212-14275-4.

[2] Francis Allard. *Natural ventilation in buildings: A design handbook*. James and James - UK (Science publisher), 1998. ISBN: 1-873936-72-9.

[3] K.T. Andersen. *Naturlig ventilation i erhvervsbygninger, By og Byg*. Statens Byggeforskningsinstitutt - Hørsholm, 2002.

[4] K. A. Antonopoulos and E. P. Koronaki. "Effect of indoor mass on the time constant and thermal delay of buildings". In: *International Journal of Energy Research* 24.5 (2000), pp. 391–402. DOI: 10.1002/(SICI)1099-114X(200004)24:5<391::AID-ER585>3.0.CO;2-L. URL: https://onlinelibrary.wiley.com/doi/abs/10.1002/%28SICI%291099-114X%28200004%2924%3A5%3C391%3A%3AAID-ER585%3E3.0.CO%3B2-L.

[5] ASHRAE. *Handbook - Fundamentals*. American Society of Heating, Refrigeration and Air-Conditioning Engineers, 2009.

[6] Miguel Chen Austin et al. "Evaluation expérimentale d'une stratégie domotique de pilotage des éléments mobiles : vers un contrôle semi-passif simple du confort d'été en BEPos". In: *Congrès SFT 2018 - Pau, France*. 2018, pp. 762 –769. URL: http://www.sft.asso.fr/actes-2018.html.

[7] Miguel Chen Austin et al. "Experimental study of a natural ventilation strategy in a full-scale enclosure under meteorological conditions: a buoyancy-driven approach". In: *6th Engineering, Science and Technology Conference - Panama 2017 (ESTEC 2017)*. 2017, pp. 657 –667. DOI: 10.18502/keg.v3i1.1469. URL: https://knepublishing.com/index.php/KnE-Engineering/article/view/1469/3542.

[8] Miguel Chen Austin et al. "Influence des effets du vent et du tirage thermique sur le taux de renouvellement de l'air d'un bâtiment ventilé naturellement : estimations par simulation aéraulique directe et par validation expérimentale d'une modélisation thermique". In: *Conférence IBPSA France – Bordeaux*. 2018, pp. 13 –21. URL: http://ibpsa.fr/index.php?option=com_jdownloads&Itemid=53&view=viewcategory&catid=81.

[9] Miguel Chen Austin et al. "Statistical analysis of architectural features effects on indoor environmental conditions in a Plus Energy House prototype". In: *Passive and Low Energy Architecture (PLEA) - Hong Kong*. Accepted as long paper. December 2018.

[10] Boussad Azerou. "Conception, réalisation et mise en œuvre de fluxmètre thermiques passif et dynamique à base de couches minces". Université de Nantes. PhD thesis. 2013, 1 vol. (142 p.)

[11] C.A. Balaras and A.A. Argiriou. “Infrared thermography for building diagnostics”. In: *Energy and Buildings* 34 (2002), pp. 171 –183.

[12] Adrian Bejan. *Convection Heat Transfer*. John Wiley and Sons, Inc., 2013. ISBN: 978-0-470-90037-6. DOI: 10.1002/9781118671627.

[13] Annamaria Belleri, Roberto Lollini, and Spencer M. Dutton. “Natural ventilation design: An analysis of predicted and measured performance”. In: *Building and Environment* 81 (2014), pp. 123 –138. ISSN: 0360-1323. DOI: https://doi.org/10.1016/j.buildenv.2014.06.009. URL: http://www.sciencedirect.com/science/article/pii/S0360132314001954.

[14] Aaron David Bernstein. *Natural Science for practical use in every household*. CHR. Schmidt, New York, 1869. ISBN: 978-1298544254.

[15] Thomas Berthou. “Développement de modèles de bâtiment pour la prévision de charge de climatisation et l’élaboration de stratégies d’optimisation énergétique et d’effacement”. Ecole national supérieure des mines de Paris. PhD thesis. 2013, 228 p.

[16] P Blondeau, M Spérandio, and F Allard. “Night ventilation for building cooling in summer”. In: *Solar Energy* 61.5 (1997), pp. 327 –335. ISSN: 0038-092X. DOI: https://doi.org/10.1016/S0038-092X(97)00076-5. URL: http://www.sciencedirect.com/science/article/pii/S0038092X97000765.

[17] AuthorEnrico Bonilauri. *What’s the “time constant” of a building?* Oct. 2015. URL: https://emu.systems/2015/10/19/whats-the-time-constant-of-a-building/ (visited on 06/10/2018).

[18] E. Burleson. *Paris Agreement and Consensus to Address Climate Challenge*. 2016.

[19] Marcello Caciolo. “Analyse expérimentale et simulation de la ventilation naturelle mono-façade pour le rafraîchissement des immeubles de bureaux”. Ecole nationale supérieure des mines de Paris. PhD thesis. 2010, 221 p.

[20] G. Carpentier and J. Uyttenbroeck. *La ventilation des bâtiments en relation avec la consommation d’énergie pour le chauffage*. Rapport III - Commission des communautés européennes, 1978.

[21] R. Carrié et al. *Perméabilité à l’air de l’enveloppe des bâtiments - Généralités et sensibilisation*. CETE de Lyon, Département Villes et Territoires, Groupe Habitat Urbanisme Construction, October 2006. URL: https://centrevaldeloire.coachcopro.com/media/download/8392.

[22] Miguel Chen Austin et al. “Stockage/déstockage d’énergie sensible et ventilation naturelle en bâtiment : une approche expérimentale à l’échelle 1”. In: *Congrès SFT 2016*. 2016. URL: http://www.sft.asso.fr/document.php?pagendx=12939.

[23] Yassine Cherif et al. “Superficial heat transfer by forced convection and radiation in a horizontal channel”. In: *International Journal of Thermal Sciences* 48.9 (2009), pp. 1696 –1706. ISSN: 1290-0729. DOI: https://doi.org/10.1016/j.ijthermalsci.2009.01.017. URL: http://www.sciencedirect.com/science/article/pii/S1290072909000258.

[24] Y-H. Chiu and D.W. Etheridge. “External flow effects on the discharge coefficients of two types of ventilation opening”. In: *Journal of Wind Engineering and Industrial Aerodynamics* 95.4 (2007), pp. 225 –252. ISSN: 0167-6105. DOI: https://doi.org/10.1016/j.jweia.2006.06.013. URL: http://www.sciencedirect.com/science/article/pii/S0167610506000857.

[25] D. Costola and D.W. Etheridge. “Unsteady natural ventilation at model scale—Flow reversal and discharge coefficients of a short stack and an orifice”. In: *Building and Environment* 43.9 (2008), pp. 1491 –1506. ISSN: 0360-1323. DOI: https://doi.org/10.1016/j.buildenv.2007.08.005. URL: http://www.sciencedirect.com/science/article/pii/S0360132307001618.

[26] D. Cóstola, B. Blocken, and J.L.M. Hensen. “Overview of pressure coefficient data in building energy simulation and airflow network programs”. In: *Building and Environment* 44.10 (2009), pp. 2027 –2036. ISSN: 0360-1323. DOI: https://doi.org/10.1016/j.buildenv.2009.02.006. URL: http://www.sciencedirect.com/science/article/pii/S0360132309000444.

[27] E. Dascalaki et al. “On the combination of air velocity and flow measurements in single-sided natural ventilation configurations”. In: *Energy and Buildings* 24 (1996), pp. 155–165.

[28] William S. Dols and Brian J. Polidoro. *CONTAM User Guide and Program Documentation Version 3.2*. National Institute of Standards and Technology (NIST), September 4, 2015. DOI: 10.6028/NIST.TN.1887. URL: https://www.nist.gov/publications/contam-user-guide-and-program-documentation-version-32.

[29] Imen Douiri. “Instrumentation dun four pilote pour la cuisson de genoise”. Ecole Nationale Superieure des Industries Agricoles et Alimentaires. PhD thesis. 2007, 1 vol. (148 p.) URL: http://theses.fr/2007AGPT0085.

[30] Mohamed El Harzli. “Etude et réalisation d’un nouveau capteur de rayonnement thermique : Application à la detection du rayonnement provenant de sources lointaines”. Université des sciences et technologies de Lille. PhD thesis. 1993, 1 vol. (180 p.)

[31] Steven J. Emmerich, W. Stuart Dols, and James W. Axley. *Natural Ventilation Review and Plan for Design and Analysis Tools*. National Institute of Standards and Technology (NIST), 2001.

[32] D.W. Etheridge and P. Phillips. *The prediction of ventilation rates in houses and the implications for energy conservation*. C.I.B. S17 Meeting - Holzkirchen, 1977.

[33] Ghjuvan Antone Faggianelli. “Rafraîchissement par la ventilation naturelle traversante des bâtiments en climat méditerranéen”. Université de Corse - Pascal Paoli. PhD thesis. 2014, 213 p.

[34] Joel H. Ferziger and Milovan Peric. *Computational Methods for Fluid Dynamics*. Springer-Verlag Berlin Heidelberg NewYork, 2005, pp. 14–15. ISBN: 3-540-42074-6.

[35] D. Feuermann and W. Hawthorne. "On the potential and effectiveness of passive night ventilation cooling". In: *Solar Energy for the 21st Century, proceedings of the 1991 Congress of ISES - Denver, CO, August 19th - 23rd*. 1991.

[36] F. Flourentzou, J. Van der Maas, and C.-A. Roulet. "Natural ventilation for passive cooling: measurement of discharge coefficients". In: *Energy and Buildings* 27 (1998), pp. 283–292.

[37] Roberto Z. Freire, Marc O. Abadie, and Nathan Mendes. "Single-sided natural ventilation driven by wind pressure and temperature difference". In: *Energy and Buildings* 62 (2013), pp. 222 –229.

[38] Antonio Gagliano et al. "Influence of Natural Ventilation on the Thermal Behavior of a Massive Building". In: *Energy Procedia* 78 (2015). 6th International Building Physics Conference, IBPC 2015, pp. 1287 –1292. ISSN: 1876-6102. DOI: https://doi.org/10.1016/j.egypro.2015.11.142. URL: http://www.sciencedirect.com/science/article/pii/S1876610215018743.

[39] C. Ghiaus and F. Allard. *Natural Ventilation in the Urban Environment: Assessment and Design*. Earthscan, 2005, pp. 72–73. ISBN: 1-84407-129-4.

[40] B. Givoni. *Man, Climate and Architecture*. Architectural Science Series. Applied Science Publ., 1976.

[41] *Google Maps*. en-FR. URL: https://www.google.fr/maps/44.7912247,-0.6117142,60m/data=!3m1!1e3 (visited on 06/22/2018).

[42] Mario Grosso. "Wind pressure distribution around buildings: a parametrical model". In: *Energy and Buildings* 18.2 (1992), pp. 101 –131. ISSN: 0378-7788. DOI: https://doi.org/10.1016/0378-7788(92)90041-E. URL: http://www.sciencedirect.com/science/article/pii/037877889290041E.

[43] Gwenan-ingénierie. *Déphasage et amortissement*. fr-FR. June 2012. URL: http://www.eztimat.com/2012/06/06/les-infos-utiles/ (visited on 03/01/2018).

[44] Katarzyna Gładyszewska-Fiedoruk and Andrzej Gajewski. "Effect of wind on stack ventilation performance". In: *Energy and Buildings* 51 (2012), pp. 242 –247. ISSN: 0378-7788. DOI: https://doi.org/10.1016/j.enbuild.2012.05.007. URL: http://www.sciencedirect.com/science/article/pii/S0378778812002629.

[45] Sherman Max H. "Superposition in Infiltration Modeling". In: *Indoor Air* 2.2 (1992), pp. 101–114. DOI: 10.1111/j.1600-0668.1992.04-22.x. URL: https://onlinelibrary.wiley.com/doi/abs/10.1111/j.1600-0668.1992.04-22.x.

[46] J. Hauke and T. Kossowski. "Comparison of values of Pearson's and Spearman's correlation coefficients on the same sets of data". In: *Quaestiones geographicae* 30(2) (2011), pp. 87 –93. DOI: 10.1.1.466.4196.. URL: http://citeseerx.ist.psu.edu/viewdoc/download?doi=10.1.1.466.4196&rep=rep1&type=pdf.

[47] K. Sheshagiri Hebbar, K. Sridhara, and P. A. Paranjpe. “Performance of conical jet nozzles in terms of discharge coefficient”. In: *Journal of the aeronautical society of India* 22.1 (1969), pp. 4 –9.

[48] Johan Hedbrant. “On the thermal inertia and time constant of singl-family houses”. Institute of Technology - Linköpings Universitet, Sweden. PhD thesis. 2001, No.887 (128 p.) ISBN: 91-7373-045-9.

[49] Per Heiselberg, Kjeld Svidt, and Peter V. Nielsen. “Characteristics of airflow from open windows”. In: *Building and Environment* 36.7 (2001). Ventilation for Health and Substainable Environment, pp. 859 –869. ISSN: 0360-1323. DOI: https://doi.org/10.1016/S0360-1323(01)00012-9. URL: http://www.sciencedirect.com/science/article/pii/S0360132301000129.

[50] Per Kvols Heiselberg, Kjeld Svidt, and Peter Vilhelm Nielsen. “Windows: measurements of air flow capacity”. In: *Indoor Environmental Engineering* R0040.115 (2000).

[51] Philippe Herin. “Conception et caractérisation de capteurs de flux radiatif et convectif : application aux mesures « in situ »”. Université de Lille Flandres Artois. PhD thesis. 1988, 1 vol. (144 p.)

[52] J. M. HOLFORD and A. W. WOODS. “On the thermal buffering of naturally ventilated buildings through internal thermal mass”. In: *Journal of Fluid Mechanics* 580 (2007), 3–29. DOI: 10.1017/S0022112007005320.

[53] G.R. Hunt and P.F. Linden. “The fluid mechanics of natural ventilation-displacement ventilation by buoyancy-driven flows assisted by wind”. In: *Building and Environment* 34 (1999), pp. 707–720.

[54] International Energy Agency (IEA). *Key World Energy Statistics 2017*. 2017. URL: https://webstore.iea.org/key-world-energy-statistics-2017.

[55] Richard Jack et al. “Quantifying the Effect of Window Opening on the Measured Heat Loss of a Test House”. In: *International SEEDS Conference 2015: Sustainable Ecological Engineering Design for Society - Leeds Beckett University*. 2015, pp. 183 –196. DOI: 10.1007/978-3-319-32646-7_13.

[56] John D. Anderson Jr. *Fundamentals of Aerodynamics*. Architectural Science Series. McGraw Hill - 5th edition, 2011. ISBN: 978-0-07-339810-5.

[57] Albert Judet and Bernard Sesolis. *Aéraulique : Principes de l’aéraulique appliqués au génie climatique*. Collection des guides thématiques de l’AICVF, PYC édition, 1991, pp. I, 221. ISBN: 2-85330-106-0.

[58] Tommy Kleiven. “Natural Ventilation in Buildings - Architectural concepts, consequences and possibilities”. Norwegian University of Science and Technology. PhD thesis. 2003, 305 p.

[59] J.H. Klems. “Methods of estimating air infiltration through windows”. In: *Energy and Buildings* 5.4 (1983), pp. 243 –252. ISSN: 0378-7788. DOI: https://doi.org/10.1016/0378-7788(83)90012-9. URL: http://www.sciencedirect.com/science/article/pii/0378778883900129.

[60] M. Krzaczek, J. Florczuk, and J. Tejchman. “Field investigations of stack ventilation in a residential building with multiple chimneys and tilted window in cold climate”. In: *Energy and Buildings* 103 (2015), pp. 48 –61. ISSN: 0378-7788.

[61] Tine Steen Larsen, Per Kvols Heiselberg, and T. Sawachi. “Analysis and Design of Single-Sided Natural Ventilation”. In: *The 4th International Symposium on Heating, Ventilation and Air-Conditioning - China*. Vol. 1. 2003, pp. 159–163.

[62] T.S. Larsen and P. Heiselberg. “Single-sided natural ventilation driven by wind pressure and temperature difference”. In: *Energy and Building* 40.6 (2008), pp. 1031 –1040.

[63] S. Lassue, B. Duthoit, and P. Théry. “A Convective and Radiative Flux Sensor for Designing Thermal Comfort Controllers”. In: *Indoor Environment* 1.5 (1992), pp. 293–299. DOI: 10.1177/1420326X9200100507. eprint: https://doi.org/10.1177/1420326X9200100507. URL: https://doi.org/10.1177/1420326X9200100507.

[64] S. LASSUE et al. “CONTRIBUTION TO THE EXPERIMENTAL STUDY OF NATURAL CONVECTION BY HEAT FLUX MEASUREMENT AND ANEMOMETRY USING THERMOELECTRIC EFFECTS”. In: *Experimental Heat Transfer, Fluid Mechanics and Thermodynamics 1993*. Ed. by M.D. Kelleher et al. Elsevier Series in Thermal and Fluid Sciences. Amsterdam: Elsevier, 1993, pp. 831 –838. ISBN: 978-0-444-81619-1. DOI: https://doi.org/10.1016/B978-0-444-81619-1.50101-5. URL: http://www.sciencedirect.com/science/article/pii/B9780444816191501015.

[65] S. Lassue et al. “Mesures fluxmétriques et notion d’impédance thermique appliquées à la caractérisation d’une paroi de bâtiment soumise à des sollicitations naturelles”. In: *Materials and Structures* 29.4 (1996), pp. 219–225. ISSN: 1871-6873. DOI: 10.1007/BF02485943. URL: https://doi.org/10.1007/BF02485943.

[66] Stephane Lassue. “Analyse des échanges radiatifs et convectifs à la surface d’une paroi opaque : application à la commande optimale du système habitat”. Université de Lille Flandres Artois. PhD thesis. 1989, 1 vol. (174 p.)

[67] A. Le Mounier, B. Delinchant, and S. Ploix. *Rapport sur les algorithmes d’estimation paramétrique en ligne pour caractériser les paramètres d’enveloppe, les paramètres des appareils électriques et les paramètres des fonctions de satisfaction représentatives des attentes de confort des occupants*. Tech. rep. Livrable 3.3.2 du projet PRECCSION, 2013.

[68] Thananchai Leephakpreeda. “Applications of thermoelectric modules on heat flow detection”. In: *ISA Transactions* 51.2 (2012), pp. 345 –350. ISSN: 0019-0578. DOI: https://doi.org/10.1016/j.isatra.2011.11.003. URL: http://www.sciencedirect.com/science/article/pii/S0019057811001303.

[69] E. Legloanec et al. “Non-intrusive thermal measurement methods adapted to painted cave walls”. In: *QIRT 2014*. 2014. DOI: 10.21611/qirt.2014.192.

[70] Rong Li, Adrian Pitts, and Yuguo Li. “Buoyancy-driven natural ventilation of a room with large openings”. In: *IBPSA 2007: Building Simulation*. 2007.

[71] P.F. Linden. “The fluid mechanics of natural ventilation”. In: *Annu. Rev. Fluid Mech* 31 (1999), pp. 201–238.

[72] Alexandre Madeleine. “Projet SUMBIOSI - Domotique/Pilotage/Métrologie”. Ecole Nationale Supérieure d’Arts et Métiers - ParisTech. MA thesis. 2012, 70 p.

[73] Max D. Morris. “Factorial sampling plans for preliminary computational experiments”. In: *Technometrics* 33.2 (1991). American Statistical Association, pp. 161 –174. DOI: 10.2307/1269043. URL: https://www.jstor.org/stable/1269043.

[74] Peter V. Nielsen et al. “Characteristics of buoyant flow from open windows in naturally ventilated rooms”. In: *ROOMVENT 2000, 7th International conference on air distribution in rooms UK*. Vol. 2. 2000, pp. 825–830.

[75] Hervé Oiry. “Etude thermique àpprofondie d’un fluxmètre à gradient tangentiel”. Université de Nantes. PhD thesis. 1985, 1 vol. (122 p.)

[76] Ivan Oropeza-Perez, Poul Alberg Østergaard, and Arne Remmen. “Model of natural ventilation by using a coupled thermal-airflow simulation program”. In: *Energy and Buildings* 49 (2012), pp. 388 –393. ISSN: 0378-7788. DOI: https://doi.org/10.1016/j.enbuild.2012.02.039. URL: http://www.sciencedirect.com/science/article/pii/S0378778812001314.

[77] Liliane Oter-Duthoit. “Application des méthodes de la théorie des systèmes à la simulation de l’évolution des flux thermiques sur les faces dd’entrée et de sortie d’une parois multicouche”. Université des sciences et technologies de Lille. PhD thesis. 1985, 1 vol. (105 p.)

[78] A.H.C. Van Paassen, S.H. Liem, and B.P. Gröninger. “Control of Night Cooling with Natural Ventilation: Sensitivity Analysis of Control Stratégies and Vent Openings”. In: *19th Annual AIVC Conference, Ventilation and cooling - Oslo, 28-30 septembre*. 1998.

[79] Luis David Patiño López. “Caractérisation des propriétés thermoélectriques des composants en régime harmonique : Techniques et Modélisation”. Université de Bordeaux 1. PhD thesis. 2004, 101 p.

[80] R. Pelletret et al. “Modelling of large openings”. In: *AIVC 21th Conference, Air Movement and Ventilation Control within Buildings - Ottawa Canada*. 1991.

[81] K. A. Randolph and L. L. Myers. *Basic Statistics in Multivariate Analysis*. Oxford University Press New York, 2013. ISBN: 978-0-19-976404-4.

[82] Thomas Recht et al. “Analyse de la fiabilité de COMFIE par comparaison à des mesures: Application à un bâtiment passif”. In: *Conférence IBPSA France-Arras-2014*. 2014.

[83] Alain Ricaud and Ismaël Lokhat. *Construire une maison à énergie positive*. Dunod Paris, 2010, p. 186. ISBN: 978-2-10-054902-3.

[84] Jesús Girón Rodríguez. “Implantation de la domotique sur SUMBIOSI”. ENSEIRB-MATMETCA. MA thesis. 2012, 70 p.

[85] Fabien Rouault. “Système intégré de rafraîchissement d’air pour le bâtiment à base de matériaux à changement de phase”. Ecole Nationale Supérieure d’Arts et Métiers - ParisTech. PhD thesis. 2014, 178 p.

[86] Claude-Alain Roulet. *Santé et qualité de l’environnement intérieur dans les bâtiments*. PPUR - Science et ingénierie de l’environnement, 2010, pp. 226–227. ISBN: 9782880747930.

[87] P.G. Rousseau and E.H. Mathews. “A new integrated design tool for naturally ventilated buildings”. In: *Energy and Buildings* 23.3 (1996). PLEA ’94 International Conference, pp. 231 –236. ISSN: 0378-7788. DOI: https://doi.org/10.1016/0378-7788(95)00948-5. URL: http://www.sciencedirect.com/science/article/pii/0378778895009485.

[88] Jérémy Rouxel. “Projet SUMBIOSI”. Université de Bordeaux - IUT. MA thesis. 2012, 38 p.

[89] D.M. Rowe, ed. *CRC Handbook of Thermoelectrics*. Boca Raton, Florida: CRC Press, 1995. ISBN: 9780849301469.

[90] R. Schumacker and S Tomek. *Understanding Statistics Using R*. Springer New York Heidelberg Dordrecht London, 2013. ISBN: 978-1-4614-6226-2.

[91] Paul-Antoine Serrault. “Intégration et Pilotage d’un système de refroidissement d’air à Matériaux à Changement de Phase dans un bâtiment à énergie positive : le cas de Sumbiosi”. Ecole Nationale Supérieure d’Arts et Métiers - ParisTech. MA thesis. 2014, 53 p.

[92] C.Y. Shaw. “Wind and temperature induced pressure differentials and an equivalent pressure difference model for predicting air infiltration in schools”. In: *ASHRAE Transactions* 86 (1980). NRCC 18633, pp. 268 –279.

[93] Max H. Sherman. “Estimation of infiltration from leakage and climate indicators”. In: *Energy and Building* 10 (1987), pp. 81–86.

[94] Ebrahim Solgi et al. “A literature review of night ventilation strategies in buildings”. In: *Energy and Buildings* 173 (2018), pp. 337 –352. ISSN: 0378-7788. DOI: https://doi.org/10.1016/j.enbuild.2018.05.052. URL: http://www.sciencedirect.com/science/article/pii/S0378778818307850.

[95] Alain Sommier et al. “Characterization of sponge cake baking in an instrumented pilot oven”. In: *International Journal of Food Studies* 1 (2012), pp. 144 –158. DOI: 10.7455/ijfs/1.2.2012.a5.

[96] Louis Stephan. “Modélisation de la Ventilation Naturelle pour l’Optimisation du Rafraîchissement Passif des Bâtiments”. Université Savoie Mont Blanc. PhD thesis. 2010.

[97] M.V. Swami and S. Chandra. “Correlations for pressure distribution of buildings and calculation of natural-ventilation airflow”. In: *ASHRAE Transactions* 94.4 (1988), pp. 244 –266.

[98] Renate Teppner et al. “Air change rates driven by the flow around and through a building storey with fully open or tilted windows: An experimental and numerical study”. In: *Energy and Buildings* 76 (2014), pp. 640 –653. ISSN: 0378-7788. DOI: https://doi.org/10.1016/j.enbuild.2014.03.004. URL: http://www.sciencedirect.com/science/article/pii/S0378778814002199.

[99] Pierre Thureau. “Fluxmètres thermiques”. In: *Techniques de l’ingénieur Mesure des grandeurs thermophysiques* base documentaire : TIB544DUO.ref. article : r2900 (1996). fre. eprint: basedocumentaire:TIB544DUO.. URL: https://www.techniques-ingenieur.fr#.

[100] Barbara E Tredre. “Assessment of mean radiant temperature in indoor environments”. In: *British Journal of Industrial Medicine* 22.1 (1965), pp. 58–66. DOI: PMID:14261707. URL: http://www.ncbi.nlm.nih.gov/pmc/articles/PMC1008216/.

[101] *Urban vs Suburban vs Rural - Difference*. URL: https://difference.guru/difference-between-urban-suburban-and-rural/ (visited on 05/28/2018).

[102] Hugo Viot et al. “Fast on-Site Measurement Campaigns and Simple Building Models Identification for Heating Control”. In: *Energy Procedia* 78 (2015). 6th International Building Physics Conference, IBPC 2015, pp. 812 –817. ISSN: 1876-6102. DOI: https://doi.org/10.1016/j.egypro.2015.11.107. URL: http://www.sciencedirect.com/science/article/pii/S1876610215018391.

[103] Christian Vultaggio. “Les méthodes de la théorie du signal appliquées à l’analyse des transferts thermiques sur la surface d’une paroi opaque en régime variable”. Université de Lille Flandres Artois. PhD thesis. 1987, 1 vol. (124 p.)

[104] I. S. Walker and D. J. Wilson. “Field Validation of Algebraic Equations for Stack and Wind Driven Air Infiltration Calculations”. In: *HVAC&R Research* 4.2 (1998), pp. 119–139. DOI: 10.1080/10789669.1998.10391395. eprint: https://www.tandfonline.com/doi/pdf/10.1080/10789669.1998.10391395. URL: https://www.tandfonline.com/doi/abs/10.1080/10789669.1998.10391395.

[105] I.S. Walker and D.J. Wilson. “Evaluating models for superposition of wind and stack effect in air infiltration”. In: *Building and Environment* 28.2 (1993). Special Issue Thermal Experiments in Simplified Buildings, pp. 201 –210. ISSN: 0360-1323. DOI: https://doi.org/10.1016/0360-1323(93)90053-6. URL: http://www.sciencedirect.com/science/article/pii/0360132393900536.

[106] G. N. Walton. “Airflow and multiroom thermal analysis”. In: *ASHRAE transactions* 88 (1982), pp. 78 –91.

[107] Bo Wang. “Interaction between wind-driven and buoyancy-driven natural ventilation”. In: *13th Conference of International Building Performance Simulation Association - Chambéry France August 26-28*. 2013.

[108] Kenneth Jr. Wark and Donald E. Richards. *Termodinámica*. Vol. 6th edition in Spanish. McGraw-Hill - Interamericana de España S.A.U., 2001. ISBN: 0-07-068305-0.

[109] Tingting Wu. “Formalisme des impedances thermiques généralisées. Application à la caractérisation thermique de parois de bâtiments”. Université d’Artois. PhD thesis. 2011, p. 217.

[110] Tingting Wu et al. “Thermal characteristics in situ monitoring of detached house wall constituted by raw clay”. In: *European Journal of Environmental and Civil Engineering* 14.5 (2010), pp. 653–667. DOI: 10.1080/19648189.2010.9693252. eprint: https://doi.org/10.1080/19648189.2010.9693252. URL: https://doi.org/10.1080/19648189.2010.9693252.

[111] Jimmy Yam, Yuguo Li, and Zuohuan Zheng. “Nonlinear coupling between thermal mass and natural ventilation in buildings”. In: *International Journal of Heat and Mass Transfer* 46.7 (2003), pp. 1251 –1264. ISSN: 0017-9310. DOI: https://doi.org/10.1016/S0017-9310(02)00379-4. URL: http://www.sciencedirect.com/science/article/pii/S0017931002003794.

[112] Dong Yang and Yuanhao Guo. “Fluctuation of natural ventilation induced by nonlinear coupling between buoyancy and thermal mass”. In: *International Journal of Heat and Mass Transfer* 96 (2016), pp. 218 –230. ISSN: 0017-9310. DOI: https://doi.org/10.1016/j.ijheatmasstransfer.2016.01.017. URL: http://www.sciencedirect.com/science/article/pii/S0017931015312369.

[113] Yingying Yang. “Innovative non-destructive methodology for energy diagnosis of building envelope”. Universite de Bordeaux. PhD thesis. 2017, 1 vol. (148 p.)

[114] Zhiqiang (John) Zhai, Mohamed El Mankibi, and Amine Zoubir. “Review of Natural Ventilation Models”. In: *Energy Procedia* 78 (2015). 6th International Building Physics Conference, IBPC 2015, pp. 2700 –2705. ISSN: 1876-6102. DOI: https://doi.org/10.1016/j.egypro.2015.11.355. URL: http://www.sciencedirect.com/science/article/pii/S1876610215020871.

[115] Zhiqiang (John) Zhai et al. “Review of natural ventilation models”. In: *International Journal of Ventilation* 15.3-4 (2016), pp. 186–204. DOI: 10.1080/14733315.2016.1214390. eprint: https://doi.org/10.1080/14733315.2016.1214390. URL: https://doi.org/10.1080/14733315.2016.1214390.

[116] Junli Zhou et al. “Coupling of thermal mass and natural ventilation in buildings”. In: *Energy and Buildings* 40.6 (2008), pp. 979 –986. ISSN: 0378-7788. DOI: https://doi.org/10.1016/j.enbuild.2007.08.001. URL: http://www.sciencedirect.com/science/article/pii/S0378778807002083.

[117] Ch. Zürcher and T. Frank. *Physique du bâtiment - Construction et énergie*. vdf Hochschulverlag AG and der ETH Zürich, 2014, p. 348. ISBN: 978-3-7281-3445-5.

[118] Y. A. Çengel. *Heat Transfer: A Practical Approach*. McGraw-Hill, 2003, pp. 584–585. ISBN: 9780072458930.

[119] M. Necati Özisik. *Heat conduction*. Vol. Second edition. John Wiley and Sons, Inc., 1993. ISBN: 0-471-53256-8.

[120] M. Necati Özisik. *Heat Transfer: A Basic Approach*. McGraw-Hill, 1985, p. 431. ISBN: 0-07-047982-8.

List of Figures

i Image of the experimental platform, Sumbiosi: South-facade view. . . . viii
ii Image of the experimental platform, Sumbiosi: North-facade view. . . . viii
iii Echanges radiatifs et convectifs sur le dispositif de mesure destiné à observer et quantifier le stockage/déstockage. . . . ix
iv Instrumentation de l'ensemble de la surface de dalle : représentation schématique (a) et dispositif de mesure pour observer le stockage/déstockage (b). . . . x
v Résultats de la densité du flux thermique pour la configuration 2. En surface de dalle : échanges radiatifs (orange) et convectifs (noir). En surface du plafond : échanges radiatifs (vert) et convectifs (violet). Vitesse d'air en surface de dalle (rouge foncé, axe à droite). Moments d'ouverture des ouvrants (zones grises). . . . xii
vi Résultats du modèle pour une configuration 2. A gauche : température d'air intérieur mesurée (noir) et simulée (rouge), température de surface de dalle mesurée (bleu) et simulée (orange premier nœud et vert dernier nœud). A droite : taux de renouvellement de l'air (noir) et températures d'air intérieur et extérieur (rouge). . . . xv
1 2015 world total primary energy production according to IEA [54]. . . . 1
2 Objectives in energy consumption of the regulation RT 2020 in France. . . . 1
3 Overview of the physical phenomena: (a) charge process, (b) discharge process, and (c) physical phenomena. . . . 3
4 Image of the experimental platform, Sumbiosi: South-facade view. . . . 4
5 Image of the experimental platform, Sumbiosi: North-facade view. . . . 4
6 Schematic of the architectural plan of the experimental platform: (a) West view and (b) top view. Values of the global heat transfer coefficients for external walls of the platform (dotted lines). . . . 4

1.1 Influence factors and relations in the air movement domain inside and around the building [117]. . . . 8
1.2 Cooling potential due to nighttime ventilation technique [2]. . . . 10
1.3 The natural ventilation concept. . . . 12
1.4 Representation of wind forces (a), and pressure distribution induced by wind (b) [58]. . . . 12
1.5 Air movement due to buoyancy forces: (a) small openings, (b) one large lower opening [70]. . . . 13
1.6 Stack ventilation with: (a) assisting winds, and (b) opposing winds [58]. . . . 15
1.7 Airflow capacity of bottom and side hung windows depending on the opening degree [57]. . . . 16
1.8 Variation of the airflow capacity of bottom and side hung windows as a function the indoor-outdoor temperature [57]. . . . 16

1.9 Values of discharge coefficient obtained by [36]. . . . 16
1.10 Values of discharge coefficient obtained by [49]. . . . 17
1.11 Values of stack discharge coefficients for inward and outward flow in still air [25]. . . . 17
1.12 Values of stack discharge coefficients for inward and outward flow with wind [25]. . . . 17
1.13 (a) Influence of wind on the efficiency of stack ventilation. (b) Air change rates in the investigated rooms as the function of the wind velocity [44]. . . . 20
1.14 Comparisons between the experi-mental and simulation results performed into the PowerDomus software for the wind tunnel case [37]. . . . 20
1.15 Measured and calculated volume flow rates: Warren & Parkins (black thin line), De Gids & Phaff (black dotted line, ΔT = 0 °C), and De Gids & Phaff (black thick line, ΔT = 5 °C) [61]. . . . 20
1.16 Results of the blower door tests with window opening from [55]. . . . 20
1.17 Averaged facade pressure coefficient as a function of azimuth angle [87]. . . . 21
1.18 Fitted regression model over experimental data of a coefficient regarding wind effects as a function of the incident angle [62]. . . . 21
1.19 Example of a network airflow modeling applied to a multi-zone building [39]. . . . 22
1.20 Comparison of the temperature of the outdoor and indoor environments: thermal lag and damping factor [43]. . . . 23
1.21 Schematic of the model [116]. . . . 26
1.22 Schematic of the models for two cases: (*a*) the indoor thermal mass is not in equilibrium with the indoor air, and (*b*) both are in equilibrium [111]. . . . 27
1.23 Schematic of the model [112]. . . . 27
1.24 Experimental set-up: (*a*) Sketch, (*b*) inside the ventilated enclosure showing the heat source E and the thermal mass (steel balls), and (*c*) temperature and airspeed probes. [112]. . . . 28
1.25 Experimental and theoretical results for the ventilation flow rate ($\dot{V}$) and the indoor air temperature (T_i) when $T_o = 33 + 7 \cdot \cos\left(4{,}09\text{x}10^{-4} \cdot t - \pi\right)$ [112]. . . . 29
1.26 Structure of Captec® heat flux meter: (a) Composition, and (b) transversal side view with heat flux lines [23]. . . . 30
1.27 General structure of a Peltier module [89]: (a) a singular TEM, and (b) two multistage TEM configurations. . . . 31
1.28 Experimental set-up in [51, 66]: (1) Air conditioning central, (2) Radiant panels, (3) a 12 cm heavyweight concrete wall, (4) air temperature probe, (5) room temperature probe, (6) a lightweight wall (isolation-wood), designed heat flux meters. . . . 32
1.29 Proportional controller converted into a room temperature programmable device (a), and a schematic of the experimental room (b). . . . 33
1.30 Experimental set-up in Douiri 2007 [29]: Heat flux meters installed inside the oven. . . . 33
1.31 Experimental set-up in [23]: Heat flux meters black and shiny, installed inside the heat exchanger (a). . . . 33
1.32 Experimental set-up in [109]: Heat flux meters installed at the (a) front and (b) rear faces of an external wall in a real residential building. . . . 34

1.33 Experimental set-up in [68]: (a) installation on the rear face of a wall, and (b) for measuring solar radiation heat flux. . . . 34
1.34 Experimental set-up in [113]: (a) heat flux (Peltier or TEM and Captec) and temperature sensors installed on the wall front face (laboratory case), and (b) heat flux (Captec) and temperature sensors installed on the wall front face (in situ case). . . . 35
1.35 Results for laboratory case: (a) Convective coefficient estimated for the TEM (black) and FGT (blue); coefficient estimated by correlation (red). (b) Surface temperatures: FGT (black), black TEM (red), shiny (TEM) blue. (c) Resulting convective heat flux for the black TEM (black), shiny TEM (red), and FGT (green) [113]. . . . 37
1.36 Schematic of the radiative heat flux designed by [30]. . . . 38
1.37 Simulation results in steady state conditions [51]. (a) In the case of a shiny heat flux meter place on a concrete wall submitted to: (1) $\varphi_R = 20\ \mathrm{W{\cdot}m^{-2}}$, (2) $\varphi_R = 20\ \mathrm{W{\cdot}m^{-2}}$ and $\varphi_C = 4 \cdot [20 - T_s]\ \mathrm{W{\cdot}m^{-2}}$. (b) In the case of a shiny heat flux meter place on a polystyrene wall submitted to the same heat fluxes as in case (a): (3) and (4), respectively. 38
1.38 Schematic representation of the resistive circuit when a heat flux meter is installed [51]. 38
1.39 Schematic of the calibration apparatus employed for the zero-flux technique [110]. . . . 40

2.1 Image of Sumbiosi current state (a). Architectural features: floor concrete-slab (b), and programmable solar shades and natural ventilation openings (inside red squares) at the South glazed-facade (c)-(d), (e) at the shed-roof and (f) at the North facade. . . . 44
2.2 Illustration of the platform employing its architectural features: passive energy storage in summer daytime (a), and semi-passive energy discharge in summer nighttime (b). . . . 45
2.3 Images of the natural ventilation openings: (a) at the South facade, (b) at the North facade, (c) at the shed-roof, and (d) between the living room and bed room. . . . 46
2.4 Domains and variables for the experimental approach. Top: inputs and outputs studied regarding the building domain (in italic letter). Bottom: inputs and outputs studied regarding the thermal mass domain (in red). . . . 46
2.5 A representation of the convective and radiative heat exchanges over a “measurement device” containing a couple of black and shiny thermoelectric modules, and two thermocouples to measure the air and surface temperatures. . . . 48
2.6 Instrumentation of the concrete-slab surface: (a) distribution of the “measurement devices”, anemometers location (blue circles), and IR camera view section (purple square), (b) an image of the “measurement devices” near to the South facade openings. . . . 48
2.7 Image of the installation for airspeed measurement near the concrete-slab surface. . . . 49
2.8 Location of the “measurement devices” at the ceiling and the glazed-facade (blue boxes): (a) West-side view and (b) top view. . . . 49
2.9 Image of the measurement zone on the ceiling surface. . . . 50
2.10 Image of the measurement zone on the glazed-facade surface. . . . 50
2.11 Image of the installation for temperature measurement: (a) indoor air and (b) outdoor air. 50

2.12 Experimental set-up for infrared measurements. On the left-hand side: Infrared camera. On the right-hand side: A fully crumbled aluminum foil (isotropic and diffuse reflector), a black foil placed on the concrete-slab surface (reference). 51
2.13 Image of the meteorological station. 51
2.14 Distribution of supplementary thermocouples for air temperature measurements inside the platform (in yellow). 52
2.15 Images of a shiny thermoelectric module: (a) width, (b) thickness, and (c) a thermoelectric module installed with the silicon trail. 53
2.16 A cross-section schematic representation and images of the calibration set-up, (a) and (b) respectively. 54
2.17 Electrical response of the black coated thermoelectric module N^{o}8 after correction, when applying a heat load of 20 W·m^{-2}, along with the uncertainty of the voltmeter NI 9205. 54
2.18 Linear regression fitted to the electrical response of the black coated thermoelectric module n^{o}8, after correction, confronted with the heat loads applied, to determine the sensitivity value. 55
2.19 Variation in the uncertainty δ_φ in the heat flux measurement of the TEM N^{o}8: when using $\overline{\delta_\mathcal{K}}$ (in red) and when using $\delta_\mathcal{K}$ depending on the heat flux applied (in blue). . . . 58
2.20 Thermocouples measurement when having the bath at 9, 89 °C, before correction. . . 59
2.21 Thermocouples measurement when having the bath at 9, 89 °C, after correction. . . . 59
2.22 Schematic of a surface i submitted to superficial heat transfer. 59
2.23 Flowchart of the automation strategy for the natural ventilation openings during the measurement campaign in 2016. 65
2.24 For config. n°1: Outdoor temperature (black solid line, left axis), indoor temperature (black dashed line, left axis), mean radiant temperature (red dashed line, left axis), wind direction (yellow, right axis), wind speed (purple, right axis), direct solar radiation (brown circles, left axis). Moments where openings remained opened (gray zones). . . . 67
2.25 For config. n°2: Outdoor temperature (black solid line, left axis), indoor temperature (black dashed line, left axis), mean radiant temperature (red dashed line, left axis), wind direction (yellow, right axis), wind speed (purple, right axis), direct solar radiation (brown circles, left axis). Moments where openings remained opened (gray zones). . . . 67
2.26 For config. n°3: Outdoor temperature (black solid line, left axis), indoor temperature (black dashed line, left axis), mean radiant temperature (red dashed line, left axis), wind direction (yellow, right axis), wind speed (purple, right axis), direct solar radiation (brown circles, left axis). Moments where openings remained opened (gray zones). . . . 68
2.27 For config. n°1: Convective heat flux for the floor (black line), the ceiling (purple line), and for the glazed-facade (brown line). Moments where openings remained opened (gray zones). 69
2.28 For config. n°2: Convective heat flux for the floor (black line), and the ceiling (purple line). Moments where openings remained opened (gray zones). 70

2.29 For config. n°3: Convective heat flux for the floor (black line), the ceiling (purple line), and for the glazed-facade (brown line). Moments where openings remained opened (gray zones). 70
2.30 For config. n°1. Air temperatures (lines with small circles) measured at the: floor (black), ceiling (purple), and glazed-facade (brown). Indoor air (black dashed line) and mean radiant temperature (red dashed line). Surface temperatures (solid lines) measured at the: floor (black), ceiling (purple), and glazed-facade (brown). Moments where openings remained opened (gray zones). 72
2.31 For config. n°2. Air temperatures (lines with small circles) measured at the: floor (black), and ceiling (purple). Indoor air (black dashed line) and mean radiant temperature (red dashed line). Surface temperatures (solid lines) measured at the: floor (black), and ceiling (purple). Moments where openings remained opened (gray zones). 72
2.32 For config. n°3. Air temperatures (lines with small circles) measured at the: floor (black), ceiling (purple), and glazed-facade (brown). Indoor air (black dashed line) and mean radiant temperature (red dashed line). Surface temperatures (solid lines) measured at the: floor (black), ceiling (purple), and glazed-facade (brown). Moments where openings remained opened (gray zones). 73
2.33 For config. n°1: Radiative heat flux for the floor (black line), the ceiling (purple line), and for the glazed-facade (brown line). Moments where openings remained opened (gray zones). 73
2.34 For config. n°2: Radiative heat flux for the floor (black line), and the ceiling (purple line). Moments where openings remained opened (gray zones). 74
2.35 For config. n°3: Radiative heat flux for the floor (black line), the ceiling (purple line), and for the glazed-facade (brown line). Moments where openings remained opened (gray zones). 74
2.36 Correlation plot based on the Pearson coefficient for experimental results from no-windy nighttime: the sample size resulted in 196. 78
2.37 Correlation plot based on the Pearson coefficient for experimental results from windy and sunny daytime: the sample size resulted in 271. 78
2.38 Correlation results for no-windy nighttime with Spearman's coefficient. 81
2.39 Correlation results for sunny and windy daytime with Spearman's coefficient. 82
2.40 For each day in config. n°1, results of the convective heat flux vs air-surface temperature difference: floor (black), ceiling (purple), and glazed-facade (brown). 83
2.41 For each day in config. n°2, results of the convective heat flux vs air-surface temperature difference: floor (black), ceiling (purple), and glazed-facade (brown). 84
2.42 For each day in config. n°3, results of the convective heat flux vs air-surface temperature difference: floor (black), ceiling (purple), and glazed-facade (brown). 84
2.43 For each day in config. n°1, results of the convective heat transfer coefficient using equation 2.24: floor (black), ceiling (purple), and glazed-facade (brown). 85
2.44 For each day in config. n°2, results of the convective heat transfer coefficient using equation 2.24: floor (black), and ceiling (purple). 85

2.45 For each day in config. n°3, results of the convective heat transfer coefficient using equation 2.24: floor (black), ceiling (purple), and glazed-facade (brown). 86
2.46 $\mathcal{B}i$ at the floor surface for config. n°2 87
2.47 $\mathcal{N}u$, $\mathcal{R}e$ and $\mathcal{G}r$, at the floor surface for config. n°2 87
2.48 $\mathcal{B}i$ at the floor surface for config. n°3 87
2.49 $\mathcal{N}u$ and $\mathcal{G}r$ at the floor surface for config. n°3 87
2.50 For config. n°2: $\mathcal{R}i$ number (black circles), and $\mathcal{F}r$ number (brown circles). Horizontal lines: both $\mathcal{R}i$ critical values (black solid lines), and both $\mathcal{F}r$ critical values (black dashed lines). $\mathcal{F}r = 0$: absence of wind. 89
2.51 Air temperature vertical distribution within the platform. Air at the shed-roof (red circles). Indoor air (black dashed line). Floor: air (black circles), surface (black solid line). Ceiling: air (purple circles), surface (purple solid line). Air temperature differences: indoor-outdoor (green), ceiling-indoor (yellow), indoor-floor (blue), ceiling-floor (brown), and shed-floor (red). 90
2.52 Occurrence distribution of the air temperature difference between the shed and the floor (a vertical distance of around 3,5 m). Data employed: measurement campaign carried out in 2016; a total of 51398 samples. 91
2.53 Experimental set-up implemented during the measurement campaign of 2015. 91
2.54 Total heat flux (φ_b) distribution over the floor concrete-slab surface during the discharge period from the measurement campaign of 2015. 92
2.55 Thermograms of indoor surfaces of the envelope: (a) South facade, (b) concrete-slab and surroundings, (c) North facade, (d) shed-roof, (e) East door. 93
2.56 Outdoor (black line) and indoor (red line) air temperatures of the entire measurement campaign carried out during the summertime in 2016. 95
2.57 Degrees of discomfort time of days whose T_{op} is greater than $T_{comfort_{max}}$. 95
2.58 Left axis: T_{ia} to 1,70 m, black line. T_{ia} at 0,10 m, dotted with balls. Right axis: 1,70 m air velocity, black dotted line. Air velocity at 0,10 m, black line. 96
2.59 Left axis: T_{ia} black line. T_{surr} black line with "+". T_{op} dotted line in blue. Axis on the right: Air velocity, black dotted line. All measurements made at 1,70 m height. 96

3.1 Screenshots from a 17 mins video for airflow pattern recognition: a reference of the flags in steady position (yellow arrows) and flow direction indicated by the flags (green arrows). At the South facade: (a) all flags motionless, (b) all flags tilted inwardly, (c) both upper flags motionless while both lower flags tilted outwardly (left) and inwardly (right), (d) all flags tilted outwardly. At the shed-roof: (e) left flag tilted outwardly while right flag steady, (f) left flag tilted outwardly while right flag tilted inwardly. 101
3.2 Schematic of the modeling process employed. Global domain modeling: Physical or real domain, and single-zone model in CONTAM (domain modeling). Local domain modeling: airflow models chosen for openings and infiltrations. 102

3.3 Schematic showing the steps in the construction of the single-zone model on CONTAM: (1) single-zone area and volume, (2) location of the natural ventilation openings (South, North, shed-roof), (3) location of air-leakages (location 1 and location 2), (4) Airflow models selection for the openings and leakages. 103
3.4 Considerations for a bidirectional flow: (a) when the NPL crosses an opening, (b) CONTAM simulation results for temperature difference only, (c) when the NPL does not cross any opening. 104
3.5 (a) Surrounding around the platform, and (b) image of the platform [41]. 106
3.6 Building morphology approximation implemented in the estimation of the external pressure coefficients (red boxes): (a) West view, and (b) Top view. 107
3.7 External pressure coefficient C_p profile used on the simulations. 108
3.8 Schematic of the simulation process employed. 109
3.9 Tightness of the openings: (a) South, and (b) North facades. 110
3.10 Sealing of air-conducts related to the mechanical ventilation and PCM system (a)-(b), indicated by red arrows. Reinforcement of joinery (c)-(d), red rectangles. Sealing holes due to electrical networks and water system (e)-(f), indicated by red arrows. 110
3.11 Airtightness tests results performed on June 15th, 2015. 111
3.12 Experimental set-up for airtightness tests with openings opened. (a) Blower door installed at the West door. (b) Location of both blower doors. (c) Blower door installed at the East door. 112
3.13 (a) Pressure measurements performed on July 8th - 11th, 2017: at one point on the South (P1, green) and North (P2, red) facades with respect to the indoor environment (P_o). (b) Experimental set-up and points of measurements (P1, P2, P_o). (c)-(d) Moments of absence of wind. (e) A schematic representation of a wind direction of 250°. (f) Corresponding wind speed (dark red) and direction (blue). 115
3.14 Airflow rate for each group of openings: South facade (black circles), North facade (red squares), and shed-roof (blue rhombuses). 115
3.15 Values of discharge coefficient for each group of openings: South facade (black circles), North facade (red squares), and shed-roof (blue rhombuses). 115
3.16 *ach* results from the K—P model as a function of the opening effective-area: work of [55] (red dashed line), and from our airtightness tests (black dots). 117
3.17 Schematic of the single-zone model employed in the simulations with leakages: (a) equally distributed at the facades with openings, (b) at the West facade only. 118
3.18 Resulting *ach* due to thermal buoyancy only ($ach_{\Delta T}$): air-leakages only (blue line), openings at the South and shed-roof opened with no leakages (red line), and all openings opened with no leakages (black line). 119
3.19 Wind results of simulations with leakages equally distributed at the facades with openings for different wind direction: leakages only. 120
3.20 Wind results of simulations with leakages equally distributed at the facades with openings for different wind direction: South + shed only, no leakages. 120

3.21 Results of $\mathscr{B}(\phi_W)$ for different wind direction and fitted Fourier's regression: Openings south + shed without leakages (red) and Infiltrations only (blue). 120
3.22 Wind results of simulations with leakages equally distributed at the facades with openings for different wind direction: South + shed + leakages. 120
3.23 Results of $\mathscr{B}(\phi_W)$ for different wind direction and fitted Fourier's regression: Openings south + shed + leakages. 120
3.24 Wind results of simulations with leakages at the West facade for different wind direction: South + shed + leakages. 121
3.25 Results of $\mathscr{B}(\phi_W)$ with leakages at the West facade for different wind direction and fitted Fourier's regression: Openings south + shed + leakages. 121
3.26 (a) Simulation results when combining wind an buoyancy effects, for a constant wind speed of 1 m·s^{-1} and different wind directions. Indoor temperature was fixed at 22 °C, while the outdoor temperature was decreased from 22 to 16 °C. (b) Illustration of the situations presented here at the right-hand side of this figure, for three four wind direction; showing the opposing and the assisting of both effects. 123

4.1 Schematic of the platform employed in the modeling. Left-hand side: physical domain (real domain). Right-hand side: domain modeling (approximation of the real domain). Airstreams (brown arrows), convective heat exchanges (blue arrows). 126
4.2 For config. n°1: floor h'_{C_D} (black), ceiling h'_{C_P} (purple), and glazed-facade h'_{C_g} (brown). . 129
4.3 For config. n°2: floor h'_{C_D} (black), and ceiling h'_{C_P} (purple). 129
4.4 For config. n°3: floor h'_{C_D} (black), ceiling h'_{C_P} (purple), and glazed-facade h'_{C_g} (brown). . 130
4.5 Resulting air change rate per hour for config. n°1: ach_{φ_C} (blue), $ach_{\Delta T}$ (red), ach_W (yellow), $ach_{n=2}$ (green), ach_{K-P} (cyan), and $ach_{m=2}$ (purple). The corresponding temperature measurements: indoor air (brown dashed line) and outdoor air (brown circles). 132
4.6 Resulting air change rate per hour for config. n°2: ach_{φ_C} (blue), $ach_{\Delta T}$ (red), ach_W (yellow), $ach_{n=2}$ (green), ach_{K-P} (cyan), and $ach_{m=2}$ (purple). The corresponding temperature measurements: indoor air (brown dashed line) and outdoor air (brown circles). 133
4.7 Resulting air change rate per hour for config. n°3: ach_{φ_C} (blue), $ach_{\Delta T}$ (red), ach_W (yellow), $ach_{n=2}$ (green), ach_{K-P} (cyan), and $ach_{m=2}$ (purple). The corresponding temperature measurements: indoor air (brown dashed line) and outdoor air (brown circles). 133
4.8 For config. n°1. Convective heat flow for the floor (red),ceiling (blue), glazed-facade (green), and storage term (yellow), from the point of view of the air (negative values correspond to a discharge). 136
4.9 For config. n°2. Convective heat flow for the floor (red) and ceiling (blue), and storage term (yellow), from the point of view of the air (negative values correspond to a discharge). 136
4.10 For config. n°3. Convective heat flow for the floor (red),ceiling (blue), glazed-facade (green), and storage term (yellow), from the point of view of the air (negative values correspond to a discharge). 137

4.11 Numerical results for config. n°1: **(a)** T_{ia} model (red line), T_{ia} measured (black dots), and absolute error (brown line); error bars ±0,48 °C. **(b)** Heat flows: floor (red), ceiling (blue), glazed-facade (green), energy storage in air (yellow), and ventilation (purple). **(c)** *ach* (black), $\mathcal{V}_{met}$ (purple) and ϕ_W (yellow), and T_{oa} (brown). 138
4.12 For config. n°1. Associated error distribution for T_{ia} in fig.4.11 (a), and the $RMSE$ value. 138
4.13 Numerical results for config. n°2: **(a)** T_{ia} model (red line), T_{ia} measured (black dots), and absolute error (brown line); error bars ±0,48 °C. **(b)** Heat flows: floor (red), ceiling (blue), glazed-facade (green), energy storage in air (yellow), and ventilation (purple). **(c)** *ach* (black), $\mathcal{V}_{met}$ (purple) and ϕ_W (yellow), and T_{oa} (brown). 139
4.14 For config. n°2. Associated error distribution for T_{ia} in fig.4.13 (a), and the $RMSE$ value. 139
4.15 Numerical results for config. n°3: **(a)** T_{ia} model (red line), T_{ia} measured (black dots), and absolute error (brown line); error bars ±0,48 °C. **(b)** Heat flows: floor (red), ceiling (blue), glazed-facade (green), energy storage in air (yellow), and ventilation (purple). **(c)** *ach* (black), $\mathcal{V}_{met}$ (purple) and ϕ_W (yellow), and T_{oa} (brown). 140
4.16 For config. n°3. Associated error distribution for T_{ia} in fig.4.15 (a), and the $RMSE$ value. 140
4.17 Wind speed occurrence distribution during the measurement campaigns for each opening configuration; a total of 2304 samples. 142
4.18 Resulting air change rate per hour for config. n°1: $ach_{(\Delta T x W)}$ (black), ach_{φ_C} (blue), $ach_{\Delta T}$ (red), ach_W (yellow), and ach_{K-P} (cyan). The corresponding temperature measurements: indoor air (brown dashed line) and outdoor air (brown circles). 143
4.19 Resulting air change rate per hour for config. n°2: $ach_{(\Delta T x W)}$ (black), ach_{φ_C} (blue), $ach_{\Delta T}$ (red), ach_W (yellow), and ach_{K-P} (cyan). The corresponding temperature measurements: indoor air (brown dashed line) and outdoor air (brown circles). 144
4.20 Resulting air change rate per hour for config. n°3: $ach_{(\Delta T x W)}$ (black), ach_{φ_C} (blue), $ach_{\Delta T}$ (red), ach_W (yellow), and ach_{K-P} (cyan). The corresponding temperature measurements: indoor air (brown dashed line) and outdoor air (brown circles). 144
4.21 Wind direction occurrence distribution during the measurement campaigns for each opening configuration; a total of 2304 samples. 145
4.22 Schematic employed in the modeling of the heat transfer through the concrete-slab. . . 148
4.23 Schematic of the method employed in the discretization of the concrete-slab thickness. 149
4.24 Model B1 for config. n°2. (a) concrete-slab surface temperature measured (blue dots), T_D model with $h'_{C_{D-TEM}}$ (yellow line, TD_S model 1), and T_D model with $h'_{C_{D-FGT}}$ (red line, TD_S model 2). Absolute error (brown) between red line and blue dots, and error bars ±0,48 °C. Recall that: $T_{S_D} \equiv T_D$. (b) Terms on equation 4.16, from the point of view of the surface (negatives values correspond to a discharge). 151
4.25 Associated error distribution for T_{S_D} in fig. 4.24 (a), and the $RMSE$ value. 151
4.26 Model B2 for config. n°2. (a) Temperatures of the top node (yellow line, TD_S model N=1) and bottom node (red line, TD_S model N=M). Absolute error (brown) between top node and blue dots, and error bars ±0,48 °C. (b) heat flow terms on equation 4.17, from the point of view of the surface (negatives values correspond to a discharge). . . . 152
4.27 Associated error distribution for T_D in fig. 4.26 (a), and the $RMSE$ value. 152

4.28 Results for config. n°2: (a) T_{ia} model (red line), T_{ia} measured (black dots), and absolute error (brown line). (b) Heat flows: floor (red), ceiling (blue), glazed-facade (green), energy storage in air (yellow), and ventilation (purple). (c) ach (black), $\mathcal{V}_{met}$ (purple) and ϕ_W (yellow), and T_{oa} (brown). 154
4.29 Associated error distribution for fig. 4.28 (a), and the $RMSE$ value. 155
4.30 Results for config. n°2. (a) Temperatures of the top node (yellow line, TD_S model N=1) and bottom node (red line, TD_S model N=M). Absolute error (brown) between red line and blue dots, and error bars $\pm$0,48 °C. (b) heat flow terms, from the point of view of the surface (negatives values correspond to a discharge). 155
4.31 Associated error distribution for fig. 4.30 (a), and the $RMSE$ value. 156
4.32 Results for config. n°2 (data not part of identification): (a) T_{ia} model (red line), T_{ia} measured (black dots), and absolute error (brown line). (b) Heat flows: floor (red), ceiling (blue), glazed-facade (green), energy storage in air (yellow), and ventilation (purple). (c) ach (black), $\mathcal{V}_{met}$ (purple) and ϕ_W (yellow), and T_{oa} (brown). 157
4.33 For config. n°2 (data not part of identification). Associated error distribution for fig. 4.32 (a), and the $RMSE$ value. 158
4.34 Results for config. n°2 (data not part of identification). (a) Temperatures of the top node (yellow line, TD_S model N=1) and bottom node (red line, TD_S model N=M). Absolute error (brown) between red line and blue dots, and error bars $\pm$0,48 °C. (b) heat flow terms, from the point of view of the surface (negatives values correspond to a discharge). 158
4.35 For config. n°2 (data not part of identification). Associated error distribution for fig. 4.34 (a), and the $RMSE$ value. 159
A.1 NIST polynomials [**NI_1**]. 199
A.2 Thermocouple type T errors when using a NI 9213 [**NI_1**]. 199
A.3 The temperature distribution for both measurements, the Bath and the thermocouples, along with the bias errors respect to a real temperature value and the random errors. . 200
A.4 The temperature distribution for both measurements, the Bath and the thermocouples, after corrections are applied. 200
A.5 Thermocouples calibration rig. 201
A.6 Thermocouples inside the thermostatic Bath. 202
A.7 Thermocouples temperature measurement behavior when having the bath at $9,89$ °C. T Bath in red (with error bars) and the mean temperature in black. 203
A.8 Both axis in (°C). The upper plot: Regression between the Bath temperature and TC32 measurement. The lower plot: Residuals values on predicting T_{Bath} using TC32 measurement. 204
A.9 Thermocouples temperature measurement behavior after corrected using expression 22, when having the bath at $9,89$ °C. T Bath in red (with error bars) and the mean temperature in black. 205

A.10 Thermocouples measurement behavior when having the bath at 14,71 °C (at the left side) and 19,75 °C (at the right side). T_{Bath} in red (with error bars) and the mean temperature in black. 210
A.11 Thermocouples measurement behavior when having the bath at 24,79 °C (at the left side) and 29,09 °C (at the right side). T_{Bath} in red (with error bars) and the mean temperature in black. 210
A.12 Thermocouples measurement behavior when having the bath at 34,78 °C (at the left side) and 39,72 °C (at the right side). T_{Bath} in red (with error bars) and the mean temperature in black. 210
A.13 Image of the experimental set-up: sensors submitted to a non-direct solar radiation environment during the summertime (case 1). 212
A.14 Image of the experimental set-up: sensors submitted to a direct solar radiation environment during the wintertime (case 2). 212
A.15 Temperature measurements from black (black dashed line) and shiny (red dotted line) thermoelectric modules for case 1. Temperature difference (brown line, axis at the right). 213
A.16 Occurrence distribution of the temperature difference between black and shiny thermoelectric modules for case 1. 213
A.17 Temperature measurements from black (black dashed line) and shiny (red dotted line) thermoelectric modules for case 2. Temperature difference (brown line, axis at the right). 214
A.18 Occurrence distribution of the temperature difference between black and shiny thermoelectric modules for case 2. 214
A.19 F.1. Schematic of the experimental set-up installed in November 2016, and their location inside the PEH: (a) Location 1 used from 2/11 to 7/11 and from 18/11 to 21/11, and (b) location 2 used from 22/11 to 25/11. 217
A.20 Images of the experimental set-up installed in November 2016, and their location inside the PEH: (a) Location 1 used from 2/11 to 7/11 and from 18/11 to 21/11, and (b) location 2 used from 22/11 to 25/11. 217
A.21 On location 1. Convection heat flux from TEM measurements (black dots) and from FGT measurements (red dots). Difference between both (green lines, axis at the right). . 218
A.22 On location 1. Convection heat flux from TEM measurements against FGT measurements (red dots). Blue line: linear regression fixed at the origin. 219
A.23 On location 2. Convection heat flux from TEM measurements (black dots) and from FGT measurements (red dots). Blue zone: the natural ventilation openings remained opened. 219
A.24 On location 2. Convection heat flux from TEM measurements against FGT measurements (red dots). Blue line: linear regression fixed at the origin. 219

List of Tables

1.1 Strengths and weaknesses of different forecasting model techniques [15]. 25
1.2 Criteria for model validation [67]. 25

2.1 Sensitivity values of Captec® heat flux meters. 52
2.2 Response of the TEM N°8 to different heat loads. 55
2.3 Uncertainties of the instruments for the calibration procedure. 57
2.4 Components in the uncertainty of the sensitivity $\mathcal{K}$. 57
2.5 Hypotheses and assumptions for data processing 62
2.6 Configurations of the openings on each measurement campaign in summertime. 65
2.7 Constant parameters employed in the dimensionless numbers. 87
2.8 Dimensionless numbers evaluated at the concrete-slab surface for each configuration. . 87

3.1 Terrain type coefficients for the wind speed modifier [28]. 106
3.2 Resulting values of C_f for the *wind speed modifier* using equation 3.2. 106
3.3 Recommended external pressure coefficient values for rectangular vertical walls. 107
3.4 *ach* results from airtightness tests performed on June 15th, 2015. 111
3.5 Results of airtightness tests. 114
3.6 Natural airflow rate (*ach*) with the standard. 117
3.7 Regression results for $ach_{\Delta T}$ as a function of temperature. 118
3.8 Resulting values for $\mathcal{B}(\phi_W)$. 121

4.1 Hypotheses employed in the modeling of the heat transfer in the platform. 128
4.2 Comparison between air change rate models. 134
4.3 Set of parameters for Model A. 137
4.4 Identified set of values for *ach* expression in Model A (cf. eq. 4.8). 141
4.5 Set of parameters for Model B. 150
A.1 Temperature setpoints 201
A.2 Maximum deviation values among thermocouples at each setpoint 202
A.3 Raw thermocouples measurement results at each setpoint 203
A.4 Maximum deviation values among thermocouples at each setpoint, after applying the correction 205
A.5 Regression coefficients values for expression 22. 206
A.6 Temperature measurements of each thermocouple with their standard deviation 208
A.7 Properties of the thermoelectric modules and conventional heat flux meters. 216
B.1 Meteorological conditions from ENSAM in 2016. 220

Appendices

A Calibration and metrology

A.1 Experimental report: Calibration of thermocouples

Abstract: Several thermocouples type T (with a temperature accuracy ± 1 °C, according to the manufacturer) were calibrated using a thermostatic bath (LAUDA RE 415, temperature stability of $\pm 0,01$ °C with temperature accuracy of $\pm 0,3$ °C and $\pm 0,5\%$ of the relative temperature, assured by an integrated PT100) and the NI 9213 acquisition card (measurement sensitivity of $\pm 0,02$ °C with a measurement error of $\pm 0,8$ °C for our temperature ranges). The goal is to increase the accuracy of our thermocouples by correcting our measurement system (thermocouple + acquisition) with a more accurate instrument (the thermostatic Bath). As results showed, the thermocouples maximum deviation to one another before correction, when measuring the temperature of a stable medium (water in this case) it does not exceed the $0,3$ °C. After correction, the maximum deviation does not exceed the $0,07$ °C. Their stability is $\pm 0,02$ °C with 95 % of confidence. Following the ASME international journal of heat transfer Policy, on reporting uncertainties in experimental results, our best estimation on reporting the temperature overall uncertainty is presented at the end of this document.

Nomenclature

TCX	Thermocouple number X	
$\overline{T}$	Time average temperature	°C
T	Temperature	°C
T^*	Estimated temperature	°C
u	To represent uncertainty	
e	To represent error	
ζ	Random error	
β	Systematic error	

1. Introduction

The well-known thermocouple calibration process can be resume as finding the regression function that relates the temperature measured by the thermocouple and its tension response, and the determination of the calibration process uncertainties. To well estimate a temperature measurement using

thermocouples, several phases regarding its tension response must be accomplished. A simple explanation would be as follows:

1.1. Technical data of the measuring system

As said before, several phases are needed to estimate a temperature measurement using thermocouples, these phases could be described as: first, since thermocouples tension responses are as low as the electric noise that can be encountered in the environment medium, a tension signal amplification phase must be applied [1]. Second, once the signal is amplified, comes the filtration phase to reduce as much as possible the electric noise due to signal amplification process. Also, when connecting the thermocouple to an acquisition system, care should be taken concerning the connection terminals. The terminals must be electrically insulated. The third phase includes two steps: the cold junction compensation and the tension-temperature regression; as it is well known that the thermocouple response is proportional to the Seebeck coefficient and the temperature, the tension signal measured would not be a linear function of the temperature. Nowadays, many standards give us the regression between the temperature and the tension delivered by a thermocouple (i.e., NIST standards). In these standards, the polynomial coefficients for all types of thermocouples that exists are given, and because of the nonlinear response of the thermocouple, the polynomials errors is also given. This phase is called linearization (see figure A.1). These polynomial coefficients are determined within a range of temperature, depending on the operation range of the thermocouple. Also, the coefficients depend on the junction compensation of the thermocouple. The polynomials coefficients given by the NIST are determined using a cold junction compensation (maintaining the reference junction to zero degrees celcius) [1].

All the signal processing required for converting the thermocouple response in a temperature measurement causes systematic errors. Errors that will always be there when performing a temperature measurement with a specific data acquisition system. Unfortunately, the error caused by the acquisition system does not account the thermocouple uncertainty or accuracy itself. The thermocouple accuracy is bound to the purity of the materials employed in its fabrication process.

In our experiments, the NI 9213 acquisition card and the Labview software have been used. The signal processing is already integrated into the National Instrument acquisition system. As so, the error committed when estimating a temperature measurement is given in the NI 9213 technical data. In our particular case, thermocouples type T have been used. The measurement errors, when using the NI 9213, are shown in figure A.2. As said, in addition to this error, comes the error of the thermocouple itself. Our thermocouples were acquired from the company TC Direct [2]. These thermocouples are second class thermocouples type T; this class gives us the thermocouple accuracy after it is manufactured under a specific standard. TC Direct follows the NF EN 60584-2 (or IEC 584.2) standard when manufacturing thermocouples, as so the accuracy on our thermocouples is ± 1 °C (this value is also mentioned in [3]). There two most common thermocouple classes and if they are not specified as first class thermocouple, they are of second class. Consistent with our case.

	Type de thermocouple					
	E	J	K	R	S	T
Plage	**0 à 1000° C**	**0 à 760° C**	**0 à 500° C**	**–50 à 250° C**	**–50 à 250° C**	**0 à 400° C**
a_0	0,0	0,0	0,0	0,0	0,0	0,0
a_1	1,7057035E–2	1,978425E–2	2,508355E–2	1,8891380E–1	1,84949460E–1	2,592800E–2
a_2	– 2,3301759E–7	–2,001204E–7	7,860106E–8	–9,3835290E–5	–8,00504062E–5	–7,602961E–7
a_3	6,5435585E–12	1,036969E–11	–2,503131E–10	1,3068619E–7	1,02237430E–7	4,637791E–11
a_4	–7,3562749E–17	–2,549687E–16	8,315270E–14	–2,2703580E–10	–1,52248592E–10	–2,165394E–15
a_5	–1,7896001E–21	3,585153E–21	–1,228034E–17	3,5145659E–13	1,88821343E–13	6,048144E–20
a_6	8,4036165E–26	–5,344285E–26	9,804036E–22	–3,8953900E–16	–1,59085941E–16	–7,293422E–25
a_7	–1,3735879E–30	5,099890E–31	–4,413030E–26	2,8239471E–19	8,23027880E–20	
a_8	1,0629823E–35		1,057734E–30	–1,2607281E–22	–2,34181944E–23	
a_9	–3,2447087E–41		–1,052755E–35	3,1353611E–26	2,79786260E–27	
a_{10}				–3,3187769E–30		
Erreur	±0,02° C	±0,05° C	±0,05° C	±0,02° C	±0,02° C	±0,03° C

Figure A.1: NIST polynomials [**NI_1**].

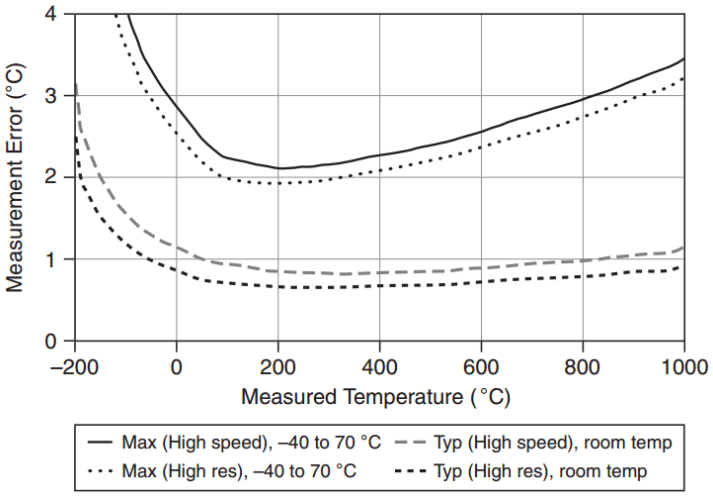

Figure A.2: Thermocouple type T errors when using a NI 9213 [**NI_1**].

1.2 Thermocouple calibration

The process of performing the junction metal-alloy, could affect the thermocouple measurement. This effect can be observed if the thermocouples (let's say 32) are immersed in a very stable temperature fluid. It would be observed that thermocouple's temperature measurements are not quite the same, even if they were of the same type or were manufactured together. Here this effect would be named as thermocouples natural deviation. This before could cause large errors in the estimation of a temperature difference, because when subtracting two measurements, the result could lays inside the range of the two thermocouples natural deviation relative to each other. This, would not be the real value of the temperature difference, thus, this must be corrected before performing any temperature difference.

As in our particular case, we are also interested in the estimation of temperature differences. As

so, the aforementioned in the previous paragraph, was conducted using a thermostatic bath (model: LAUDA RE 415) with a temperature stability of $\pm 0,01$ °C, and an accuracy of $\pm 0,3$ °C and $\pm 0,5\%$ °C of the relative temperature, assured by an integrated PT100 sensor [4]. The procedure will be described in the next section.

Furthermore, we are also interested in reducing the bias error of our thermocouples. The thermostatic bath could help us to accomplish this before, as it has a smaller bias error value than our measuring system (thermocouple + acquisition system). As the technical data of the thermocouples and acquisition system subject the bias error may lays within a range of $\pm 1,8$ °C in the worst case scenario, but it should be noted that it will not necessarily be exactly 1,8 °C. Here we proposed an experimental procedure to attempt to reduce this error interval or uncertainty, as shown graphically in figures A.3 and A.4. In the first picture, the bias (β) and random (ζ) errors in the temperature estimation of both the thermostatic bath and our thermocouples (accounting the acquisition system). The second picture shows what we are trying to accomplish: made the thermocouples measurement bias error to be equal to that of the Bath temperature.

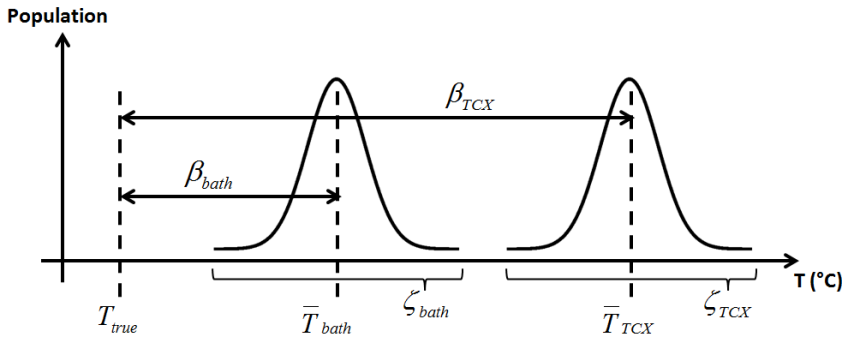

Figure A.3: The temperature distribution for both measurements, the Bath and the thermocouples, along with the bias errors respect to a real temperature value and the random errors.

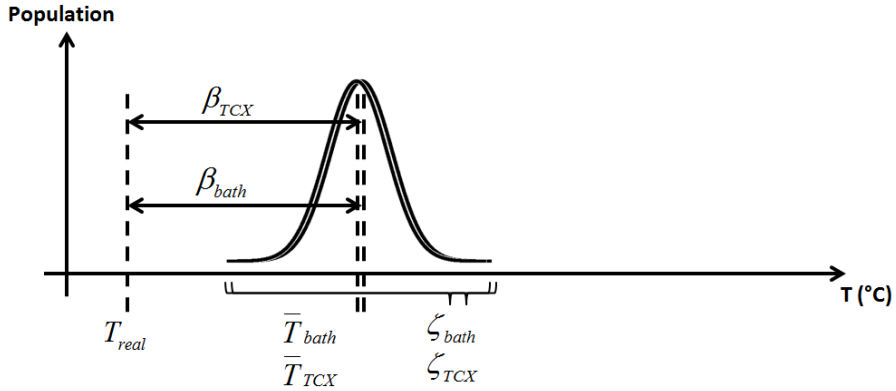

Figure A.4: The temperature distribution for both measurements, the Bath and the thermocouples, after corrections are applied.

2. Experimental procedure

2.1. In a steady-state medium

In order to observed and quantify the thermocouples natural deviation, they were immersed into the bath filled with water in two groups of 16 (32 thermocouples in total) along with a NTC probe, as shown in figure A.6 in appendix. Seven different temperature setpoints (see Table A.1, first and second columns from left to right) were set, in order to observe their stability, deviation to one another and to the bath temperature. Also, the average temperature of all thermocouples wanted to be observed. The weirdness in the bath temperature values is because the bath temperature was adjusted so that the NTC temperature matches the setpoints values. Lately, it was found that the Bath temperature sensor is more accurate that the NTC probe [3], as so the NTC measurements were discarded. After the bath reached the setpoint (now, referring to the middle column of Table A.1) and stabilize it, the data acquisition was started for only 28 seconds with a sample rate acquisition of 4 seconds. A repetition of this experiment might be considered. Results are presented in the following section.

Table A.1: Temperature setpoints

Setpoint (°C)	$\overline{T}_{Bath}$ (°C)	$\overline{T}_{TC}$ (°C)
10	9,89	9,58
15	14,71	14,41
20	19,75	19,46
25	24,79	24,51
30	29,09	28,83
35	34,78	34,54
40	39,72	39,51

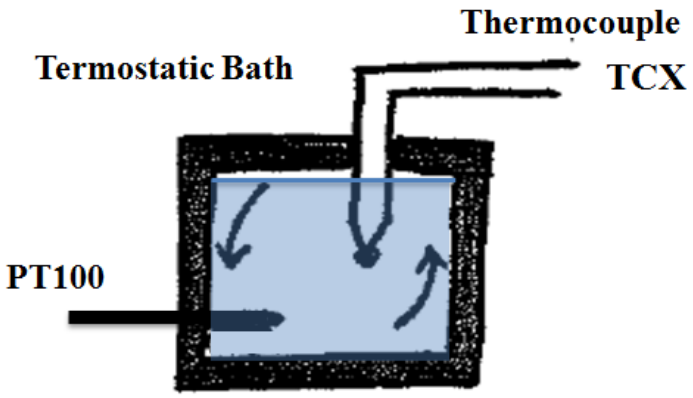

Figure A.5: Thermocouples calibration rig.

Figure A.6: Thermocouples inside the thermostatic Bath.

3. Results and data analysis

3.1. Reduction of the thermocouples deviation from the true temperature

In a steady-state medium: The thermocouples behavior at all seven temperature setpoints can be observed in figure A.7 and from figures A.10 to A.12, in appendix. The thermocouples measurement natural deviation when having the bath at $9,89$ °C could be observed in figure A.7. The maximum deviation between thermocouples is approximately $0,3$ °C. We proposed to reduce this deviation by correcting the thermocouples measurements as said in §2.1, which in other words means that we will try to find a regression function that correlates the thermocouples measurement and the Bath temperature.

Furthermore, results showed that the higher the temperature setpoint, the closer the thermocouples measurement gets to the bath temperature (see figures from A.10 to A.12 in appendix) and the maximum deviation between the thermocouples changes at each setpoint (see Table A.2), being $0,29$ °C the mean value of them all.

Table A.2: Maximum deviation values among thermocouples at each setpoint

$\overline{T}_{Bath}$ (°C)	Deviation (°C)
9,89	0,28
14,71	0,33
19,75	0,26
24,79	0,27
29,09	0,33
34,78	0,26
39,72	0,31

A slight part of the thermocouples measurements results is shown in Table A.3. The table presents the time average temperature for each thermocouple (only few of them are presented as example).

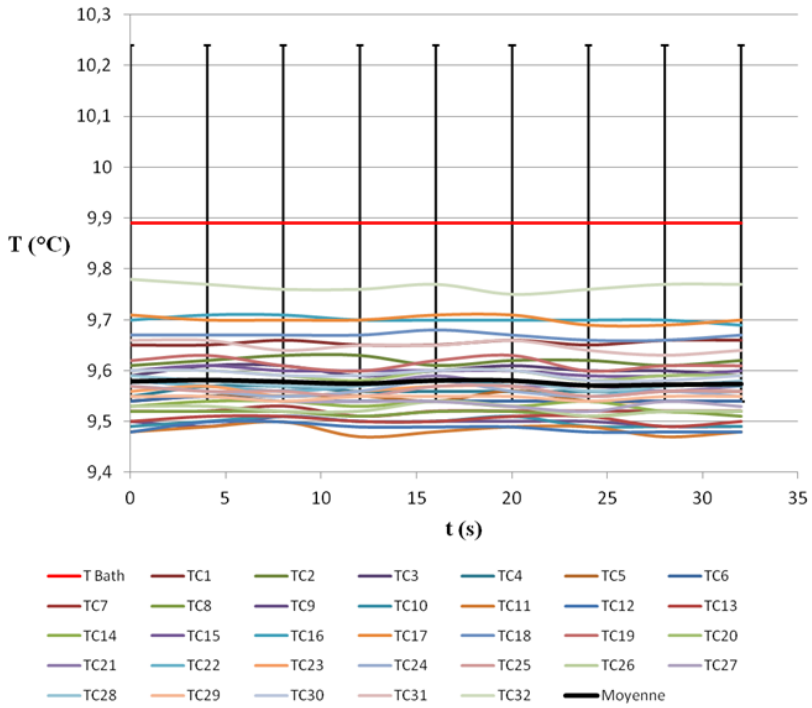

Figure A.7: Thermocouples temperature measurement behavior when having the bath at $9,89$ °C. T Bath in red (with error bars) and the mean temperature in black.

Then, the regression function is obtained by plotting the bath temperature values (values from the first column of Table A.3) versus the temperature values from each thermocouple.

Table A.3: Raw thermocouples measurement results at each setpoint

$\overline{T}_{Bath}$ (°C)	$\overline{T}_{TC}$ (°C)	$\overline{T}_{TC1}$ (°C)		$\overline{T}_{TC16}$ (°C)	$\overline{T}_{TC17}$ (°C)	$\overline{T}_{TC32}$ (°C)
9,89	9,58	9,65		9,70	9,70	9,77
14,71	14,41	14,49		14,48	14,56	14,61
19,75	19,46	19,60	...	19,57	19,55	19,62
24,79	24,51	24,63		24,62	24,60	24,67
29,09	28,83	28,92		28,94	28,97	29,03
34,78	34,54	34,67		34,70	34,65	34,71
39,72	39,51	39,60		39,65	39,65	39,71

The regression function for the thermocouple 32 is shown in figure A.8 as an example. In a general way the regression function can be written as follows:

$$\overline{T}_{Bath} = a_X \overline{T}_{TCX} + b_X \tag{21}$$

where a_X and b_X are the linear regression coefficients and the subscript X corresponds to the thermocouple number TCX. Coefficients units are: dimensionless and in degrees Celsius, respectively. Regression coefficient values are shown in Table A.5.

Expression 21 could help us to make the thermocouples measurement to be equal to the Bath temperature. We can go further and rewrite this expression as a function of time, this will help us to correct

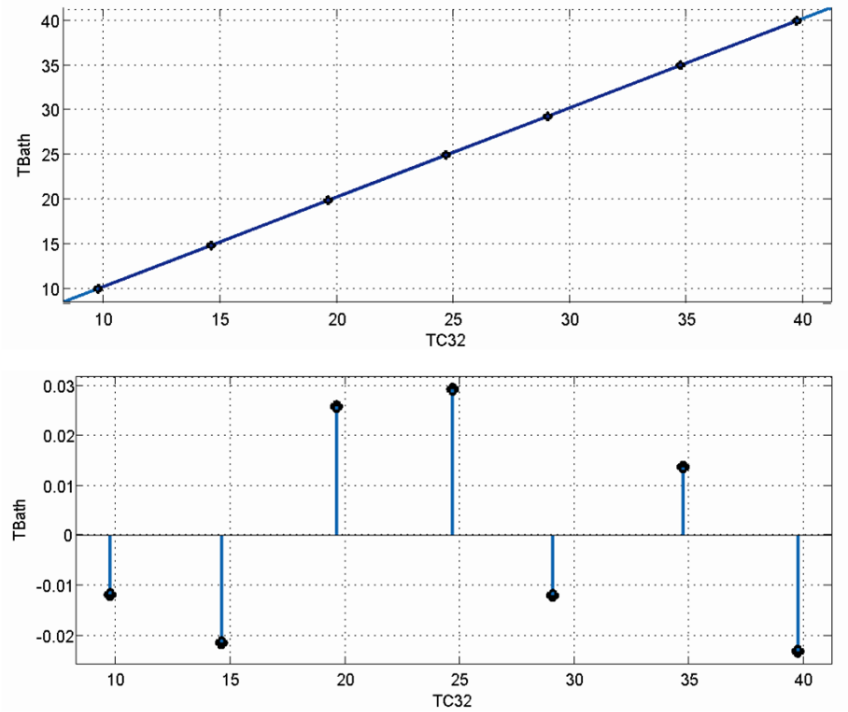

Figure A.8: Both axis in (°C). The upper plot: Regression between the Bath temperature and TC32 measurement. The lower plot: Residuals values on predicting T_{Bath} using TC32 measurement.

the thermocouple measurement at any instant. However, it is known that the correlation should have an associated error, since no regression is perfect. Thus, the regression correct the thermocouple measurement to be equal to the bath temperature at e% of error. As so, we can think of the regression as being an estimation of the Bath temperature at e% near. Then, expression 21 can be rewrite as follows:

$$T^*_{TCX}(t) = a_X T_{TCX}(t) + b_X \tag{22}$$

where T^*_{TCX} represents the estimated temperature from thermocouple X measurement. T_{TCX} is the actual thermocouple measurement.

We can test our regression function to correct our thermocouples measurements by using the results from figure A.7. The result, after applying the correction, is shown in figure A.9. Also, data showed that the maximum deviation between thermocouples at this setpoint is reduced to $0,04$ °C, which is way lower than the value presented in Table A.2: $0,28$ °C (maximum deviations values at each setpoint are presented in Table A.4). As we will see in the next section, despite the correction we just made to the temperature magnitude of our thermocouples measurement, the thermocouples random error remained the same.

Before we go to the random error analysis, the regression function error in estimating a temperature must be treated. The plots showed in figure A.8 were computed using the software Matlab and its app: curve fitting. As we can see it can also give us the residual plot, which plot the deviation of the predicted value by the regression function. So, we interpreted this plot as the error of the regression function. These residuals can be gather all together to have a unique error value instead of 7 different ones, which

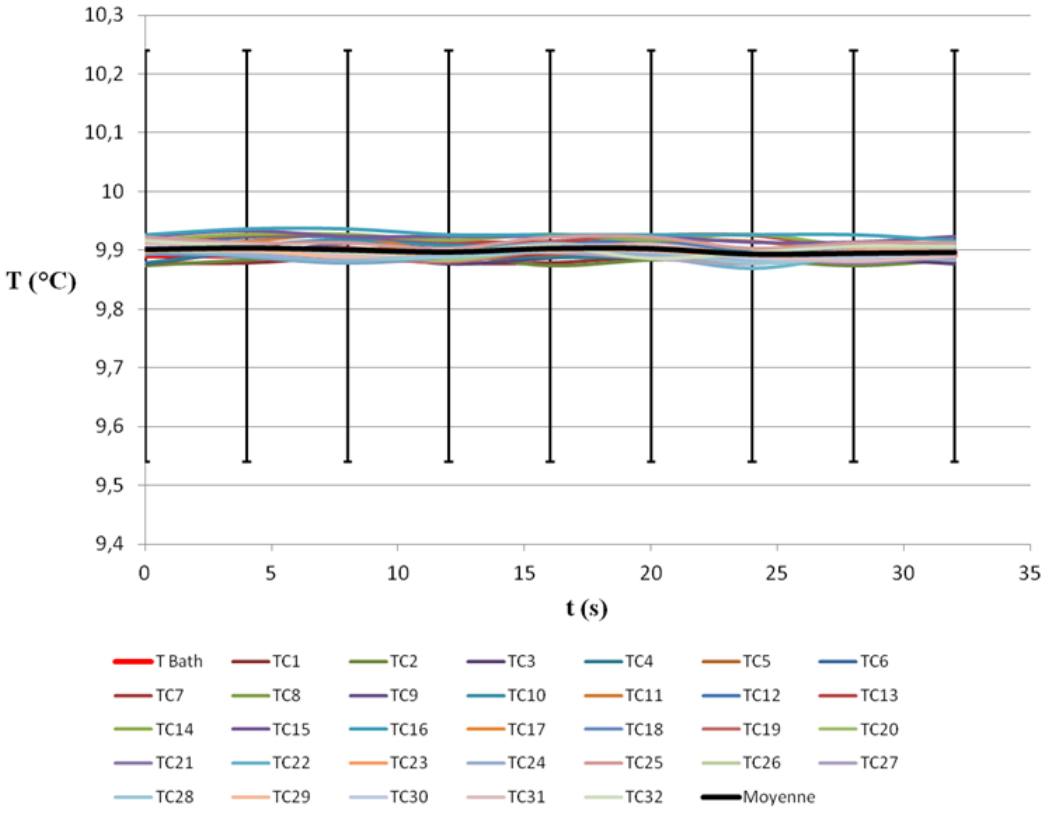

Figure A.9: Thermocouples temperature measurement behavior after corrected using expression 22, when having the bath at $9,89$ °C. T Bath in red (with error bars) and the mean temperature in black.

Table A.4: Maximum deviation values among thermocouples at each setpoint, after applying the correction

$\overline{T}_{Bath}$ (°C)	Deviation (°C)
9,89	0,04
14,71	0,07
19,75	0,07
24,79	0,06
29,09	0,05
34,78	0,04
39,72	0,04

would be convenient as we will not have to look for this plot in order to estimate the error. This unique error value is calculated by the root-mean-square error (RMSE) and luckily Matlab compute it for us. RMSE values for each regression is also showed in Table A.5. However, it does not tell us whether the error in estimation made the prediction be higher than the temperature of the bath or lower. Now, we have to decide whether this error should be considered as a bias or as a random error. Well, we can deduct that this error should be consider as part of the bias error, since it is the error that the regression commit in the process to estimate the Bath temperature from the thermocouple measurement.

Table A.5: Regression coefficients values for expression 22.

TCX	$a_X\ (-)$	$b_X\ (°C)$	$RMSE_X\ (°C)$
TC1	0,9959	0,2674	0,0238
TC2	0,9968	0,2942	0,0221
TC3	0,9974	0,3116	0,0220
TC4	0,9966	0,3601	0,0187
TC5	0,9973	0,378	0,0185
TC6	0,9976	0,3779	0,0189
TC7	0,9967	0,4058	0,0165
TC8	0,9966	0,4142	0,0164
TC9	0,997	0,4304	0,0188
TC10	0,9975	0,4315	0,0205
TC11	0,9961	0,4622	0,0161
TC12	0,9966	0,4548	0,0185
TC13	0,997	0,4433	0,0203
TC14	0,9955	0,4306	0,0196
TC15	0,9951	0,3707	0,0240
TC16	0,995	0,2742	0,0258
TC17	0,9968	0,2287	0,0318
TC18	0,9971	0,2504	0,0282
TC19	0,9966	0,3124	0,0260
TC20	0,997	0,3311	0,0240
TC21	0,9972	0,3456	0,0209
TC22	0,9969	0,3492	0,0177
TC23	0,9969	0,3662	0,0275
TC24	0,997	0,3609	0,0201
TC25	0,9973	0,378	0,0173
TC26	0,9951	0,4154	0,0193
TC27	0,9964	0,3905	0,0224
TC28	0,9985	0,3335	0,0241
TC29	0,9958	0,3896	0,0213
TC30	0,9954	0,3507	0,0235
TC31	0,9962	0,2873	0,0212
TC32	0,9967	0,1689	0,0243

3.2. Determination of the temperature stability

The stability of the temperature measurement was calculated as the standard deviation of a continue sets of measurements at a given temperature setpoint value assured by the thermostatic bath, and using a confidence interval of 95 % in a normal distribution (meaning: $1,96$ times the standard deviation value) [3]. Data showed that the majority of the thermocouples presented a standard deviation of $\pm 0,01$ °C, except for the TC10, which was $\pm 0,02$ °C (see Table A.6). Therefore, the temperature stability or random error for all thermocouples would be, $\pm 0,02$ °C (0,0196 °C), except for the TC10 which would be $\pm 0,04$ °C (0,0392 °C).

4. Conclusion

In order to conclude, our best estimation in temperature measurement for experiments replication, would be as follows:

$$T^*_{TCX} = (a_X T_{TCX} + b_X) \pm u_X \quad (^\circ C) \tag{23}$$

where u_X is as the ASME [**ASME**] subjects:

$$u_X = \sqrt{(\beta_{TCX})^2 + (\zeta_{TCX})^2} \tag{24}$$

$$\beta_{TCX} = 0,3 + 0,5\%(T^*_{TCX}) + RMSE_X \quad (^\circ C) \tag{25}$$

where ζ_{TCX} is equal to $0,02$ °C for all thermocouples, except for the TC10 which is $0,04$ °C.

If the temperature measurements are needed to be compared, using let's say the measurements from two of our thermocouples: TCX and TCY, in the same experiment. Only the random error of both thermocouples: ζ_{TCX} and ζ_{TCY}, must be used, instead of u_{TCX} and u_{TCX} (as interpreted from [5]).

A little example, in order to illustrate the use of expressions 23 to 25, is as follows: A medium is said to be at 10 ± 1 °C and let's say we measure its temperature with our thermocouple 32 (TC32). Our best estimation of the temperature of such medium, would be calculated first by using the expression 23 and the a_{32} and b_{32} values from Table A.5. This give: $10,14$ °C. Second, we have to determine the uncertainty in the temperature measured. Expressions 24 and 25 will help us to to that, given: $u_{TC32} = 0,38$ °C. Thus, our measurement would be reported as: $10,14 \pm 0,38$ °C. Finally, values are presented with 2 significant figures since the instrument we have used to calibrate our thermocouples can only display the temperature as so.

Furthermore, when temperature differences are needed to be estimated, using our thermocouples (let's say TCX and TCY), we would have that the magnitude of the difference, will be calculated as:

$$\Delta T^* = T^*_{TCX} - T^*_{TCY} \quad (^\circ C) \tag{26}$$

and the uncertainty in the temperature difference, as follows:

$$u_{\Delta T^*} = \pm (\zeta_{TCX} + \zeta_{TCY}) \quad (^\circ C) \tag{27}$$

where if the temperature difference ΔT^* encountered is lower than $u_{\Delta T^*}$, the temperatures should be considered to be equal as we cannot be more accurate in our measurement estimation.

5. References

(1) T. Ferguson. Mesurer des temperatures par thermocouples (2001).

(2) Welded Tip Fiberglass Thermocouple, available at http://www.tcdirect.fr.

(3) T. Dupuis. Pratique de la mesure en genie climatique (2015). ISBN: 978-2-10-073762-8.

(4) Lauda. Eco Silver Operating instructions manual (2014). English version.

(5) R. J. Moffat. Describing the uncertainties in experimental results (1988). Elsevier: Experimental

Thermal and Fluid Science.

(6) ASME International. Policy on reporting uncertainties in experimental measurements and results (1990). Journal of Heat Transfer.

Table A.6: Temperature measurements of each thermocouple with their standard deviation

TC1	TC2	TC3	TC4	TC5	TC6	TC7
9,65±0,01	9,62±0,01	9,60±0,01	9,56±0,01	9,54±0,01	9,54±0,00	9,52±0,00
14,49±0,01	14,45±0,01	14,42±0,01	14,38±0,01	14,36±0,01	14,35±0,01	14,34±0,01
19,60±0,01	19,56±0,01	19,53±0,01	19,49±0,01	19,45±0,01	19,44±0,01	19,43±0,01
24,63±0,01	24,58±0,01	24,54±0,01	24,52±0,01	24,48±0,01	24,47±0,01	24,47±0,01
28,92±0,01	28,87±0,01	28,83±0,01	28,81±0,01	28,76±0,01	28,75±0,01	28,76±0,01
34,67±0,01	34,61±0,01	34,57±0,01	34,55±0,01	34,51±0,01	34,49±0,01	34,50±0,01
39,60±0,01	39,55±0,01	39,51±0,01	39,49±0,01	39,45±0,01	39,44±0,01	39,45±0,01
TC9	TC10	TC11	TC12	TC13	TC14	TC15
9,50±0,01	9,50±0,01	9,48±0,01	9,49±0,01	9,50±0,01	9,53±0,01	9,60±0,01
14,30±0,01	14,30±0,01	14,28±0,01	14,28±0,01	14,29±0,01	14,32±0,01	14,38±0,01
19,40±0,01	19,38±0,01	19,38±0,01	19,37±0,01	19,37±0,01	19,41±0,01	19,47±0,01
24,43±0,01	24,41±0,01	24,42±0,01	24,41±0,01	24,41±0,01	24,46±0,01	24,52±0,01
28,72±0,01	28,70±0,02	28,72±0,01	28,72±0,01	28,71±0,01	28,78±0,01	28,85±0,01
34,47±0,01	34,45±0,02	34,47±0,01	34,46±0,01	34,46±0,01	34,52±0,01	34,60±0,01
39,41±0,01	39,40±0,02	39,41±0,01	39,40±0,01	39,41±0,01	39,47±0,01	39,54±0,01
TC17	TC18	TC19	TC20	TC21	TC22	TC23
9,70±0,01	9,67±0,01	9,61±0,01	9,59±0,01	9,57±0,01	9,57±0,01	9,56±0,01
14,56±0,01	14,54±0,01	14,48±0,01	14,45±0,01	14,43±0,01	14,43±0,01	14,42±0,01
19,55±0,01	19,53±0,01	19,47±0,01	19,45±0,01	19,43±0,01	19,43±0,01	19,41±0,01
24,60±0,01	24,58±0,01	24,54±0,01	24,51±0,01	24,51±0,01	24,51±0,01	24,48±0,01
28,97±0,01	28,94±0,01	28,89±0,01	28,86±0,01	28,83±0,01	28,84±0,01	28,82±0,01
34,65±0,01	34,61±0,01	34,57±0,01	34,54+±0,00	34,51±0,01	34,52±0,01	34,50±0,01
39,65±0,01	39,61±0,01	39,56±0,01	39,53±0,01	39,50±0,01	39,50±0,00	39,50±0,01
TC25	TC26	TC27	TC28	TC29	TC30	TC31
9,56±0,01	9,52±0,01	9,54±0,01	9,58±0,01	9,55±0,00	9,59±0,01	9,65±0,01
14,41±0,01	14,40±0,01	14,43±0,01	14,40±0,01	14,45±0,01	14,50±0,01	14,40±0,01
19,42±0,01	19,40±0,01	19,40±0,01	19,42±0,01	19,42±0,01	19,46±0,01	19,51±0,01
24,49±0,01	24,49±0,01	24,47±0,01	24,48±0,01	24,49±0,01	24,53±0,01	24,58±0,01
28,82±0,01	28,83±0,01	28,81±0,00	28,81±0,01	28,83±0,01	28,88±0,01	28,92±0,01
34,50±0,01	34,51±0,01	34,50±0,01	34,48±0,00	34,52±0,01	34,58±0,01	34,61±0,01
39,48±0,01	39,51±0,01	39,49±0,01	39,47±0,00	39,52±0,01	39,57±0,00	39,60±0,01

TC S.A., B.P. 87, 69573 DARDILLY CEDEX - FRANCE
TELEPHONE : 04 78 43 27 25 - TELECOPIEUR : 04 78 43 27 62
E-MAIL : info@tcsa.fr - SITE WEB : http://www.tcsa.fr

04 78 43 27 25

INTERNATIONAL :
TELEPHONE : +33 478 432 725
TELECOPIEUR : +33 478 432 762

THERMOCOUPLES

TYPES, CONDUCTEURS, CARACTERISTIQUES, NORMES NATIONALES ET INTERNATIONALES, TOLERANCES

CODE LITTERAL	CONDUCTEURS POSITIF	CONDUCTEURS NEGATIF	NORMALISATION DES FORCES ELECTROMOTRICES DES COUPLES THERMOELECTRIQUES La **norme européenne CEI 584.1**, basée sur l'E.I.T.90, fait référence. La plupart des normes nationales ci-dessous lui sont équivalentes:	VARIATION APPROXIMATIVE PAR DEGRE DE LA F.E.M. GENEREE, JONCTION DE REFERENCE A 0°C µV/°C à 100°C	à 500°C	à 1000°C	TENUE EN TEMPERATURE DE LA JONCTION DE MESURE NB: HORS ISOLANTS USAGE CONTINU °C	USAGE INTERMITTENT	REMARQUES
K	**NICKEL - CHROME** Ni-Cr; KP Noms déposés: Chromel, BTE, Tophel, T1, Thermo Kanthal KP	**NICKEL - ALUMINIUM** (MAGNETIQUE) Ni-Al; KN Noms déposés: Alumel, ATE, Nial, T2, Thermo Kanthal KN	NF EN 60584-1:1996 (Remplace NFC 42-321:1978) DIN EN 60584.1:1996 BS EN 60584.1:1996 ANSI/MC96.1 JISC 1602	42	43	39	0 à +1100	–180 à +1300	Nos remarques sur le comportement des thermocouples vis-à-vis des différents milieux sont valables pour les thermocouples nus, certains matériaux de gaine pouvant limiter sérieusement les performances intrinsèques des thermocouples.
T	**CUIVRE**	**CUIVRE - NICKEL** Constantan; TN Noms déposés: Constantan Cupron, CTE, Advance	NF EN 60584-1:1996 (Remplace NFC 42-321:1978) DIN EN 60584.1:1996 BS EN 60584.1:1996 ANSI/MC96.1 JISC 1602	46	–	–	–185 à +300	–250 à +400	Thermocouple très courant. Bien adapté aux milieux oxydants. Large gamme de températures.
J	**FER** (MAGNETIQUE) Fe; JP Nom déposé: Fer Armco	**CUIVRE - NICKEL** Constantan; JN Noms déposés: Constantan Cupron, CTE, Advance	NF EN 60584-1:1996 (Remplace NFC 42-321:1978) DIN EN 60584.1:1996 BS EN 60584.1:1996 ANSI/MC96.1 JISC 1602	54	56	–	+20 à +700	–180 à +750	Pour applications cryogéniques ou basses températures. Valeurs de tolérance particulièrement intéressantes.
N	**NICKEL - CHROME - SILICIUM** Nicrosil	**NICKEL - SILICIUM** Nisil	NF EN 60584-1:1996 (Remplace NFC 42-321:1978) DIN EN 60584.1:1996 BS EN 60584.1:1996 ANSI/MC96.1 JISC 1602	30	38	38	0 à +1150	–270 à +1300	Couramment utilisé dans l'industrie du plastique. Peut s'utiliser sans protection en milieu réducteur.
E	**NICKEL - CHROME** Ni-Cr; EP Noms déposés: Chromel, Tophel	**CUIVRE- NICKEL** Constantan; EN Noms déposés: Constantan Cupron, Advance	NF EN 60584-1:1996 (Remplace NFC 42-321:1978) DIN EN 60584.1:1996 BS EN 60584.1:1996 ANSI/MC96.1 JISC 1602	68	81	–	0 à +800	–40 à +900	Très stable, particulièrement à haute température. Peut atteindre 1300°C. Bonne tenue en milieu oxydant. Tenue remarquable au cyclage thermique.
R	**PLATINE - 13% RHODIUM**	**PLATINE**	NF EN 60584-1:1996 (Remplace NFC 42-321:1978) DIN EN 60584.1:1996 BS EN 60584.1:1996 ANSI/MC96.1 JISC 1602	8	10	11	0 à +1600	0 à +1700	Le thermocouple qui délivre la fém la plus élevée. Pour utilisation sous vide ou en milieu légèrement oxydant.
S	**PLATINE - 10% RHODIUM**	**PLATINE**	NF EN 60584-1:1996 (Remplace NFC 42-321:1978) DIN EN 60584.1:1996 BS EN 60584.1:1996 ANSI/MC96.1 JISC 1602	7	10	11	0 à +1550	0 à +1700	Comportement comparable au type S ci-dessous, mais tables de f.é.m. légèrement différentes. Thermocouple préféré au type S dans certains pays.
B	**PLATINE - 30% RHODIUM**	**PLATINE - 6% RHODIUM**	NF EN 60584-1:1996 (Remplace NFC 42-321:1978) DIN EN 60584.1:1996 BS EN 60584.1:1996 ANSI/MC96.1 JISC 1602	1	5	9	+100 à +1600	0 à +1800	Pour hautes températures. Résistance élevée à l'oxydation et à la corrosion. Se pollue facilement et nécessite une protection. Valeurs de tolérance particulièrement intéressantes. Souvent utilisé en étalonnage de 400 à 1000°C.
G (anciennement W)	**TUNGSTENE**	**TUNGSTENE 26% RHENIUM**	NON NORMALISE[1]	5	16	21	+20 à +2320	0 à +2600	Comportement comparable aux types R et S ci-dessus, mais tables de f.é.m. légèrement différentes. Couramment utilisé dans l'industrie du verre.
C (anciennement W5)	**TUNGSTENE 5% RHENIUM**	**TUNGSTENE 26% RHENIUM**	NON NORMALISE[1]	15	19	18	+50 à +1820	+20 à +2300	Comportement comparable au type C ci-dessous.
D (anciennement W3)	**TUNGSTENE 3% RHENIUM**	**TUNGSTENE 25% RHENIUM**	NON NORMALISE[1]	13	20	20	+20 à +2320	0 à +2600	Usage déconseillé en milieu oxydant. Les thermocouples à base de tungstène et de rhénium offrent des f.é.m. suffisamment élevées et relativement linéaires pour des mesures de haute température jusqu'à 2300°C. Bonne stabilité dans l'hydrogène, les gaz inertes et sous vide. Ne conviennent pas pour des mesures en dessous de 400°C.

CLASSES DE TOLERANCES
NORMES NF EN 60584-2:1993 OU IEC 584.2: 1982
NB: VOIR NOTES 1, 2 ET 3 EN BAS DE PAGE

	CLASSE 1	CLASSE 2	CLASSE 3
K			
Domaine	–40°C à +375°C	–40°C à +333°C	–167°C à +40°C
Valeur de tolérance	±1,5°C	±2,5°C	±2,5°C
Domaine	375°C à 1000°C	333°C à 1200°C	–200°C à –167°C
Valeur de tolérance	±0,004 · |t|	±0,0075 · |t|	±0,015 · |t|
T			
Domaine	–40°C à +125°C	–40°C à +133°C	–67°C à +40°C
Valeur de tolérance	±0,5°C	±1,0°C	±1,0°C
Domaine	125°C à 350°C	133°C à 350°C	–200°C à –67°C
Valeur de tolérance	±0,004 · |t|	±0,0075 · |t|	±0,015 · |t|
J			
Domaine	–40°C à +375°C	–40°C à +333°C	–
Valeur de tolérance	±1,5°C	±2,5°C	–
Domaine	375°C à 750°C	333°C à 750°C	–
Valeur de tolérance	±0,004 · |t|	±0,0075 · |t|	–
N			
Domaine	–40°C à +375°C	–40°C à +333°C	–167°C à +40°C
Valeur de tolérance	±1,5°C	±2,5°C	±2,5°C
Domaine	375°C à 1000°C	333°C à 1200°C	–200°C à –167°C
Valeur de tolérance	±0,004 · |t|	±0,0075 · |t|	±0,015 · |t|
E			
Domaine	–40°C à +375°C	–40°C à +333°C	–167°C à +40°C
Valeur de tolérance	±1,5°C	±2,5°C	±2,5°C
Domaine	375°C à 800°C	333°C à 900°C	–200°C à –167°C
Valeur de tolérance	±0,004 · |t|	±0,0075 · |t|	±0,015 · |t|
R			
Domaine	0°C à +1100°C	0°C à +600°C	–
Valeur de tolérance	±1,0°C	±1,5°C	–
Domaine	1100°C à 1600°C	600°C à 1600°C	–
Valeur de tolérance	±[1 +0,003 (t-1100)]°C	±0,0025 · |t|	–
S			
Domaine	0°C à +1100°C	0°C à +600°C	–
Valeur de tolérance	±1,0°C	±1,5°C	–
Domaine	1100°C à 1600°C	600°C à 1600°C	–
Valeur de tolérance	±[1 +0,003 (t-1100)]°C	±0,0025 · |t|	–
B			
Domaine	–	–	600°C à +800°C
Valeur de tolérance	–	–	±4,0°C
Domaine	–	600°C à 1700°C	800°C à 1700°C
Valeur de tolérance	–	± 0,0025 · |t|	±0,005 · |t|
G			
Domaine	–	0°C à +425°C	–
Valeur de tolérance	–	±4,5°C	–
Domaine	–	425°C à 2320°C	–
Valeur de tolérance	–	±1,0%	–
C			
Domaine	–	0°C à +426°C	–
Valeur de tolérance	–	±4,4°C	–
Domaine	–	425°C à 2320°C	–
Valeur de tolérance	–	±1,0%	–
D			
Domaine	–	0°C à +400°C	–
Valeur de tolérance	–	±0,78 mV	–
Domaine	–	400°C à 2315°C	–
Valeur de tolérance	–	±1,0%	–

1-En Europe les thermocouples G, C et D (W, W5 et W3) ne font l'objet d'aucune norme; les données que nous publions sur ces thermocouples ne sont pas officielles.

2-La tolérance est exprimée soit sous la forme d'une déviation, soit sous la forme d'une fonction de la température.

3-Les matériaux thermoélectriques sont normalement fournis pour répondre aux tolérances de fabrication spécifiées dans le tableau pour les températures supérieures à -40°C. Cependant, ces matériaux peuvent ne pas répondre aux tolérances pour les basses températures de la classe 3 pour les thermocouples type T, E, K et N. Si les thermocouples doivent satisfaire simultanément à la classe 3 et à la classe 1 ou 2, l'acheteur doit l'indiquer, une sélection des matériaux étant normalement nécessaire.

VOIR PAGE 5 LES COULEURS DE REPERAGE DES CABLES DE COMPENSATION ET D'EXTENSION

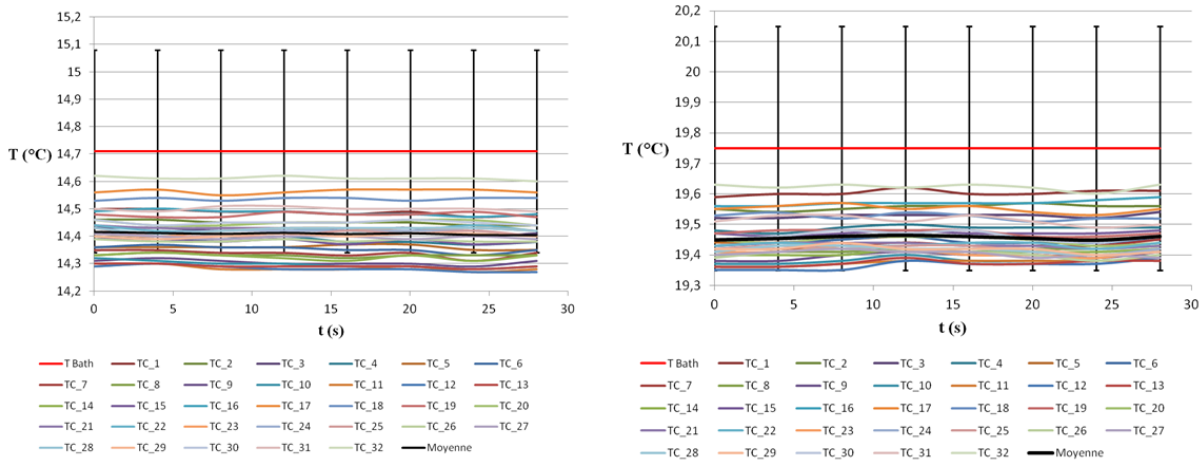

Figure A.10: Thermocouples measurement behavior when having the bath at 14, 71 °C (at the left side) and 19, 75 °C (at the right side). T_{Bath} in red (with error bars) and the mean temperature in black.

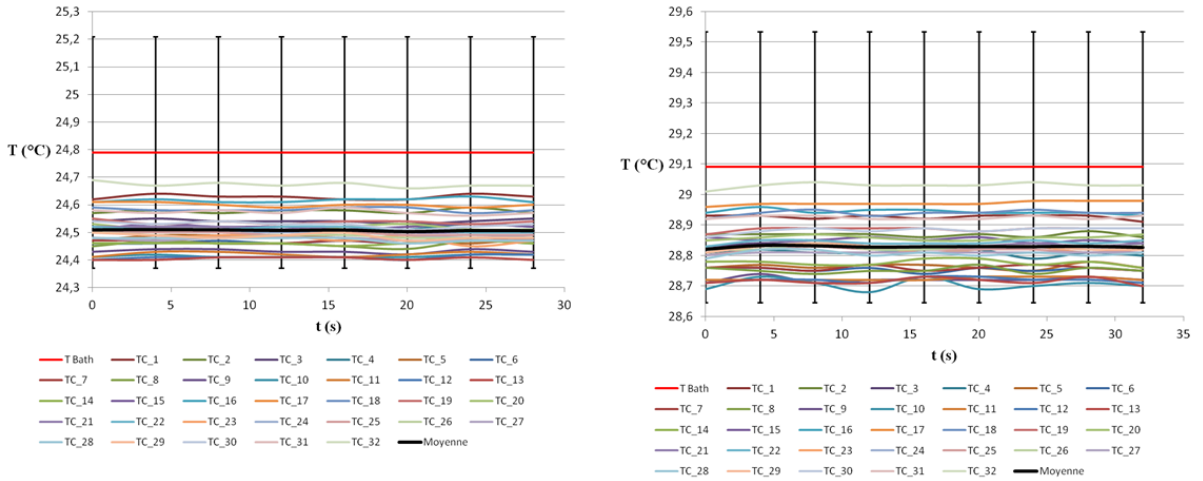

Figure A.11: Thermocouples measurement behavior when having the bath at 24, 79 °C (at the left side) and 29, 09 °C (at the right side). T_{Bath} in red (with error bars) and the mean temperature in black.

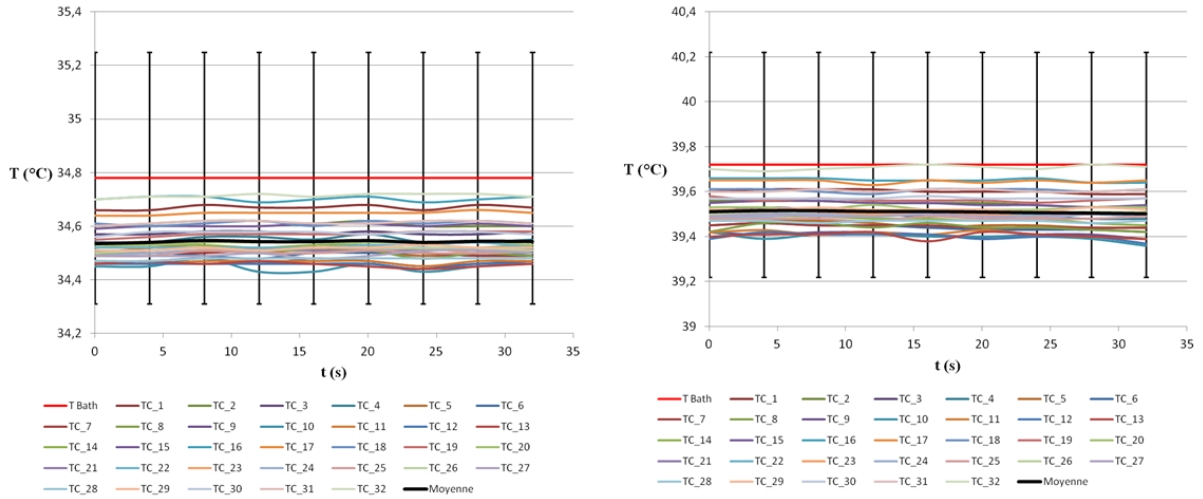

Figure A.12: Thermocouples measurement behavior when having the bath at 34, 78 °C (at the left side) and 39, 72 °C (at the right side). T_{Bath} in red (with error bars) and the mean temperature in black.

InfoZone Aide

707-4736

Identifiez-vous

0 0,00 €

Tous les produits Nos marques Nouveaux produits Mon compte Services

Nous vous proposons une offre de 500 000 produits.

Livraison gratuite dès 30€ HT d'achat en ligne.

Accueil > Chauffage, ventilation et air conditionné > Systèmes de chauffage et refroidissement électronique > Graisse thermique

Graisse thermique, Silicone, RS, 5W/m·K

Code commande RS 707-4736
Fabricant RS

21,15 €
Prix HT pour la pièce

Quantité 1	Quantité 25	Quantité 100
21,15 €	19,25 €	17,33 €

En stock pour livraison dès le lendemain

Quantité 1 Commander

Vérifier le stock en temps réel

Ajouter à une nomenclature

Documentation technique

Déclaration de conformité RoHS

Thermal Compound

Thermal Compound

Thermally Conductive Products Data Sheet

Accessoires indispensables

Clip for heatsinks
6,34 €

Aperçu

Clip for heatsinks
6,02 €

Aperçu

Détail produit

Graisse au silicone - série RS

Cette pâte de dissipateur de silicone a une durée de vie de 18 mois à compter de la date de fabrication lorsqu'elle est stockée dans le récipient d'origine non ouvert à 25° C ou à une température inférieure. Les applications incluent : composants électroniques par exemple CI, microprocesseur, MOS, LED, M/B, P/S, LCD-TV, PC portable, circuit de télécommunications, concentrateur sans fil ; module de DDRII ; applications DVD ; applications de combiné.

- Bonne conductivité thermique
- Facile à utiliser
- Stabilité élevée
- Ne durcit pas avec le temps
- Perte de poids <0,5 %
- Gravité spécifique 2,3 g/cm^3
- Température d'utilisation : -40 → +180°C
- Résistance transversale >10^{12} ohm-cm
- Dimensions du boîtier 80x80x40 mm
- Contenu du pot : 30 g

L' ensemble des produits de la Marque RS sont approuvés par les professionnels.
Notre gamme est testée par des ingénieurs pour vous donner la même qualité que les autres marques leaders et vous faire profiter des meilleurs prix..

Isolateurs thermoconducteurs (dissipateurs)

Comparer ce produit

Caractéristiques techniques

Trouver des alternatives

POur trouver un produit similaire, sélectionnez ses attributs.

Conductivité thermique	5W/m•K
Matériau	Silicone

A.2 Comparing the temperature of black and shiny thermoelectric modules

Abstract: This experimental study aims to verify if the hypothesis consisting of both thermoelectric modules having the same temperature, due to a limitation in the uncertainty of our instruments, by performing complementary measurement campaigns.

1. Experimental set-up and measurement campaigns

The experimental set-up implemented here consists of a "measurement device" installed at the most significant location, in terms of heat flux, over the floor concrete-slab surface. This "measurement device" also includes a type T thermocouple inserted into the black coated thermoelectric module. The zone where the "measurement device" is installed, was submitted to two different conditions:

- Case 1: since the window shades were kept closed, the "measurement device" is submitted to a non-direct solar radiation heat transfer, carried out during the summertime. (cf. fig. A.13).
- Case 2: since the window shades were kept opened, the "measurement device" is submitted to a direct solar radiation heat transfer, carried out during the wintertime. (cf. fig. A.14).

Figure A.13: Image of the experimental set-up: sensors submitted to a non-direct solar radiation environment during the summertime (case 1).

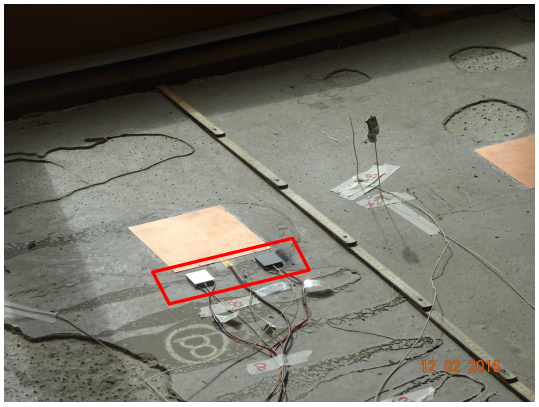

Figure A.14: Image of the experimental set-up: sensors submitted to a direct solar radiation environment during the wintertime (case 2).

2. Experimental results and analysis

The experimental results from the measurement campaigns carried out for each case, are presented hereafter.

2.1. In the summertime

Figures A.15 and A.16 present, respectively for case 1, the temperature measurements for both black (black dashed line) and shiny (red dotted line) thermoelectric modules, and a histogram to show the occurrence distribution of their temperature difference.

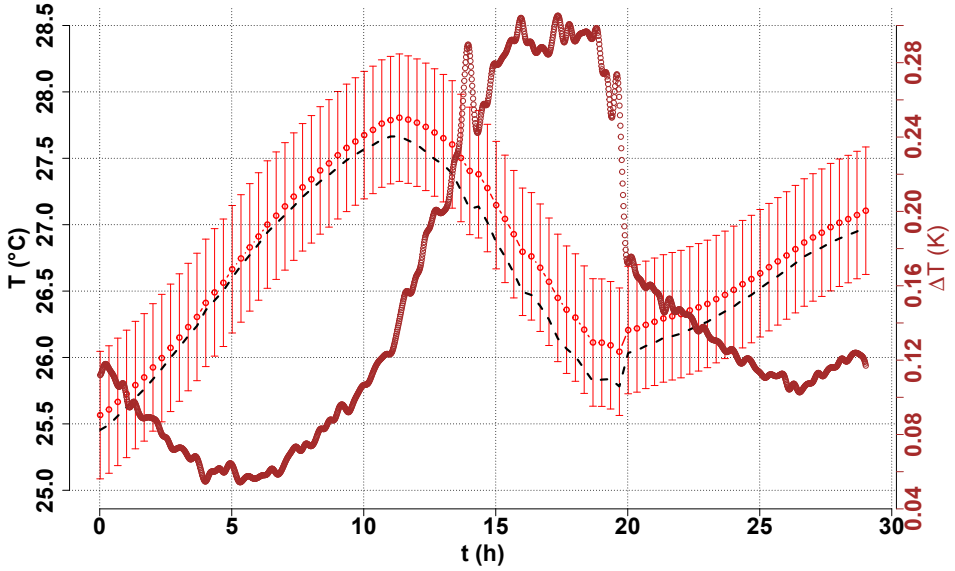

Figure A.15: Temperature measurements from black (black dashed line) and shiny (red dotted line) thermoelectric modules for case 1. Temperature difference (brown line, axis at the right).

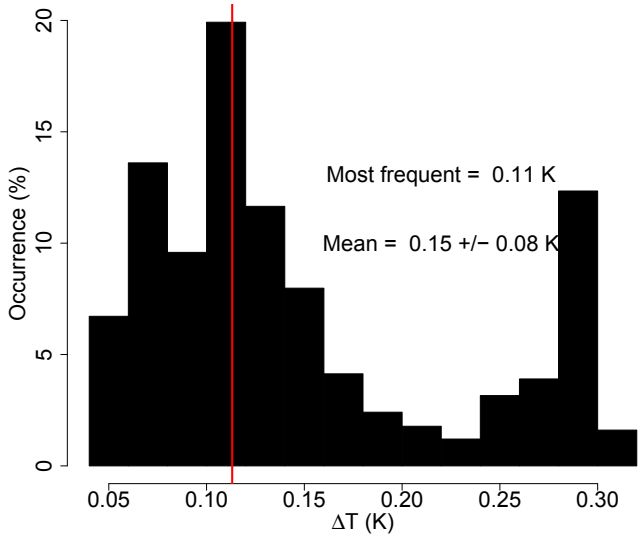

Figure A.16: Occurrence distribution of the temperature difference between black and shiny thermoelectric modules for case 1.

2.2. In the wintertime

Figures A.17 and A.18 present, respectively for case 2, the temperature measurements for both black (black dashed line) and shiny (red dotted line) thermoelectric modules, and a histogram to show the occurrence distribution of their temperature difference.

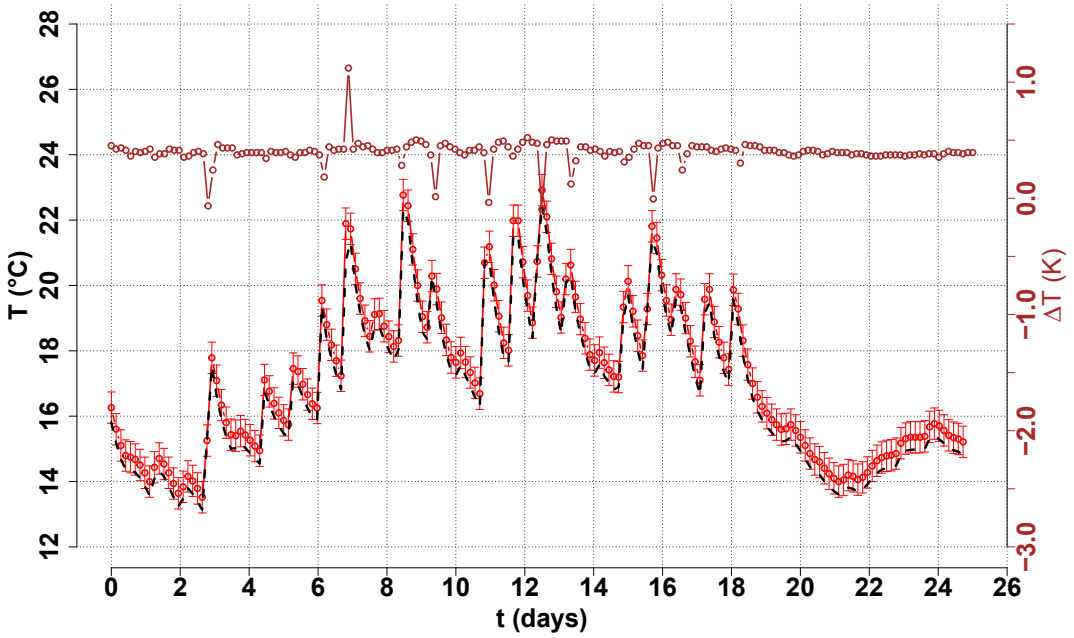

Figure A.17: Temperature measurements from black (black dashed line) and shiny (red dotted line) thermoelectric modules for case 2. Temperature difference (brown line, axis at the right).

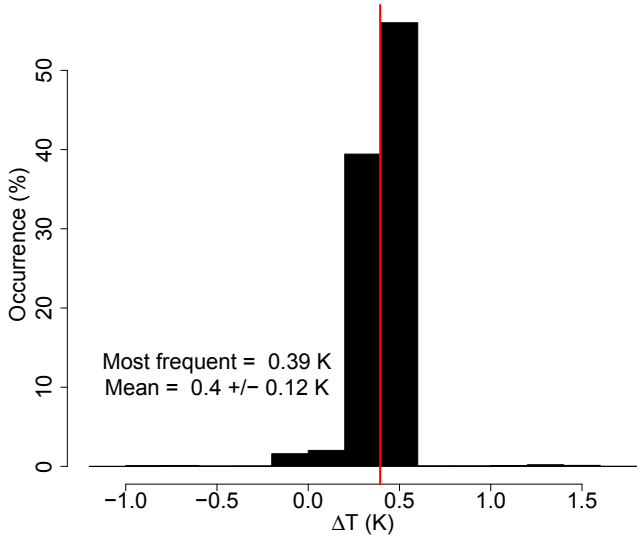

Figure A.18: Occurrence distribution of the temperature difference between black and shiny thermoelectric modules for case 2.

A.3 Assessment of thermoelectric modules as alternative to conventional heat flux meters for decoupling the superficial heat transfer

Abstract: This experimental study aims to asses the performance of thermoelectric modules (TEM) in the estimation of the convective heat flux, by comparing their measurements with conventional heat flux meters (FGT); Captec heat flux meters. In this case, a couple of black and shiny of both heat flux meters (four sensors), TEM and FGT, have been installed near each other to submit them to the same conditions. Also, these couples were installed in two different locations within the platform, in order to submit them to a no-direct solar radiation environment and a direct solar radiation environment. Regression results showed that TEM always overestimate the estimated convective heat flux by a factor of around two.

Nomenclature

FGT	Conventional heat flux meter	
TEM	Thermoelectric module	
S	Surface area	m^2
λ	Thermal conductivity	$W \cdot m^{-1} \cdot K^{-1}$
$\mathcal{K}$	Sensitivity of heat flux meters	$\mu V \cdot m^2 \cdot W^{-1}$
s	Shiny coated sensor	
b	Black coated sensor	

1. Introduction

Conventional heat flux meters are widely used for measure superficial heat flux, and as they are far expensive than thermoelectric modules, an experimental study has been conducted to compare the use of both types of heat flux sensors in the heat flux measurement. This experimental study was performed in a naturally ventilated Plus Energy House (PEH) prototype, in which only the natural ventilation semi-passive system was implemented. This system is controlled by the home automation system of the house, which controls the opening or closing of the natural ventilation openings depending on the relative conditions between the indoor and outdoor environment in regard of the thermal comfort in the summertime. However, the experimental study presented here was carried out during fall in November 2016, and the protocols for the opening and closing, of the natural ventilation openings, were chosen manually.

Until now no other research has been encountered in the literature regarding the comparison between the use of thermoelectric modules and the use of conventional heat flux meters for decoupling the convective and radiative parts in the heat flux measurement. Nevertheless, various researchers have reported perturbations induced by both types of sensors in the measured heat flux. Most of these

perturbations were encountered when comparing experimental results with simulation [51, 23, 68], and they have been given an explanation based on logic and current knowledge of the heat transfer analysis.

3. Methodology

In this experimental study, to compare the use of thermoelectric modules (TEM) over the use of conventional heat flux meters (FGT), a pair of each type of sensor was used: two thermoelectric modules and two conventional heat flux sensors. In this pair, one sensor was coated with a black-foil and the other with a shiny-foil. The properties of both types of sensors is presented in table A.7. The experimental set-up implemented here was installed on the floor concrete-slab surface in two different locations. The four sensors were installed on the floor concrete-slab surface using silicon-based thermal grease, and as the experimental set-up of the two locations slightly differed from each other, regarding the sensors arrangement, the following presents both set-ups separately.

Table A.7: Properties of the thermoelectric modules and conventional heat flux meters.

Parameters	Value
Size of the TEM [cm x cm x cm]	3 x 3 x 0,48
Surface area, S_{TEM} [m^2]	$9x10^{-4}$
Sensibility of the black TEM, $\mathcal{K}_{TEM_b}$ [$\mu V \cdot m^2 \cdot W^{-1}$]	247
Sensibility of the shiny TEM, $\mathcal{K}_{TEM_s}$ [$\mu V \cdot m^2 \cdot W^{-1}$]	267
Thermal conductivity, λ_{TEM} [$W \cdot m^{-1} \cdot K^{-1}$]	0,72
Size of the FGT [cm x cm x cm]	15 x 15 x 0,05
Surface area, S_{FGT} [m^2]	$2,25x10^{-2}$
Sensibility of the black FGT, $\mathcal{K}_{FGT_b}$ [$\mu V \cdot m^2 \cdot W^{-1}$]	128
Sensibility of the shiny FGT, $\mathcal{K}_{FGT_s}$ [$\mu V \cdot m^2 \cdot W^{-1}$]	123
Thermal conductivity, λ_{FGT} [$W \cdot m^{-1} \cdot K^{-1}$]	1

3.1. Experimental set-up: Location 1 and Location 2

The two locations where the experimental set-up was installed are presented in the following figures. Figure A.19 presents a schematic of both set-ups and figure A.20 presents an images of both set-ups To assure that the four sensors are submitted to the same conditions, they were installed close together. Note here that the experimental set-up was used first on location 1 and then was changed to location 2; they were not employed at the same time.

3.2. Protocol for the measurement campaigns

As the only functioning system of the PEH implemented in this study was the natural ventilation automated system, the experimental protocol implemented for the measurement campaigns during fall in November 2016, consisted of the following points:

1. Experimental data were collected continuously:
    - From 2/11 to 7/11, at a sample time of one minute.

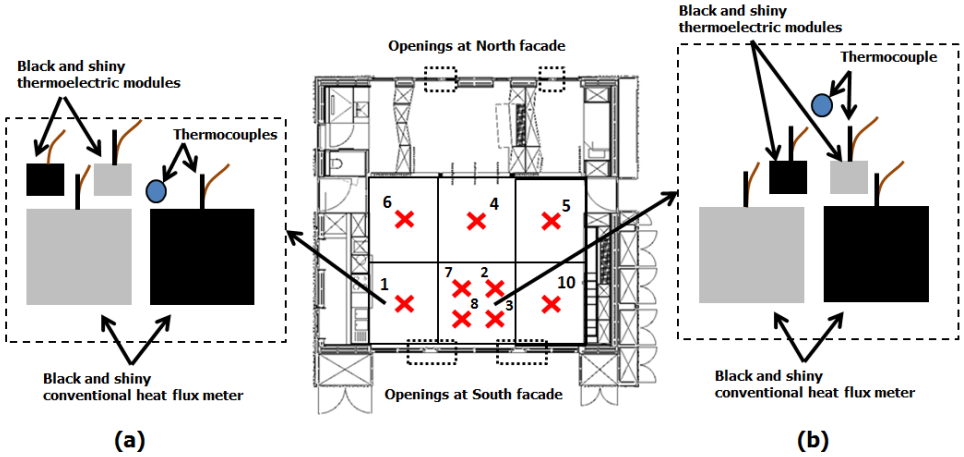

Figure A.19: Schematic of the experimental set-up installed in November 2016, and their location inside the PEH: (a) Location 1 used from 2/11 to 7/11 and from 18/11 to 21/11, and (b) location 2 used from 22/11 to 25/11.

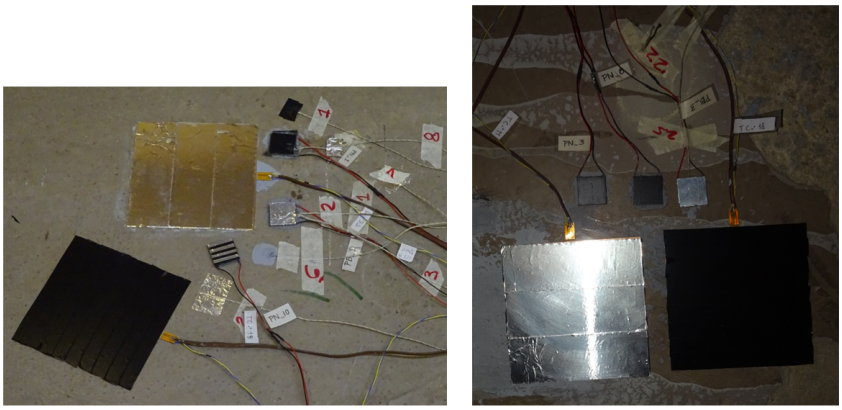

Figure A.20: Images of the experimental set-up installed in November 2016, and their location inside the PEH: (a) Location 1 used from 2/11 to 7/11 and from 18/11 to 21/11, and (b) location 2 used from 22/11 to 25/11.

- From 18/11 to 21/11, at a sample time of five seconds.
- From 22/11 to 25/11, at a sample time of one minute.

2. The solar shades were kept permanently closed during the measurement campaigns, and the natural ventilation openings were controlled manually: the opening and closing of the natural ventilation openings was performed via the user interface: a computer. Only the openings at the south facade and the Shed-roof were functional; the openings at the north facade remained closed.
3. The platform was unoccupied during the measurement campaigns, and the lights remained turned off. However, two computers remained operational; one for data collection and one for controlling the natural ventilation openings.
4. Since the inside of the platform is divided into four zones: the living room, bedroom, bathroom, and toilet; all doors dividing these zones were kept opened.

3.3. Comparison analysis

With the objective of comparing the use of both types of heat flux meters, a comparison analysis was performed regarding the following aspects:

1. The electrical response of sensors of the same surface color will be compared and confronted, where different values are expected since they are fabricated with different materials. Also, their corresponding heat flux measurement will be compared and confronted.
2. The temperature measurement from the integrated thermocouples inside both types of sensors will also be compared and confronted. These temperatures are expected two be the same, as the integrated thermocouples are meant to measure the temperature of the surface in which the heat flux meters are installed.
3. The convective and radiative heat fluxes estimated by the the measurement of both types of sensors will be also compared and confronted, using a semi-empirical model presented in §2.3.1.

4. Experimental results and analysis

Figure A.21 presents the results obtained for the estimated convective heat flux using the heat flux data collected by the black and shiny thermoelectric modules φ_{C-TEM} (black line) and using the heat flux data from the black and shiny conventional heat flux meters φ_{C-FGT} (red line). A difference can be observed at a glance in φ_C estimated by both sensors, where larger values were obtained for φ_{C-TEM}.

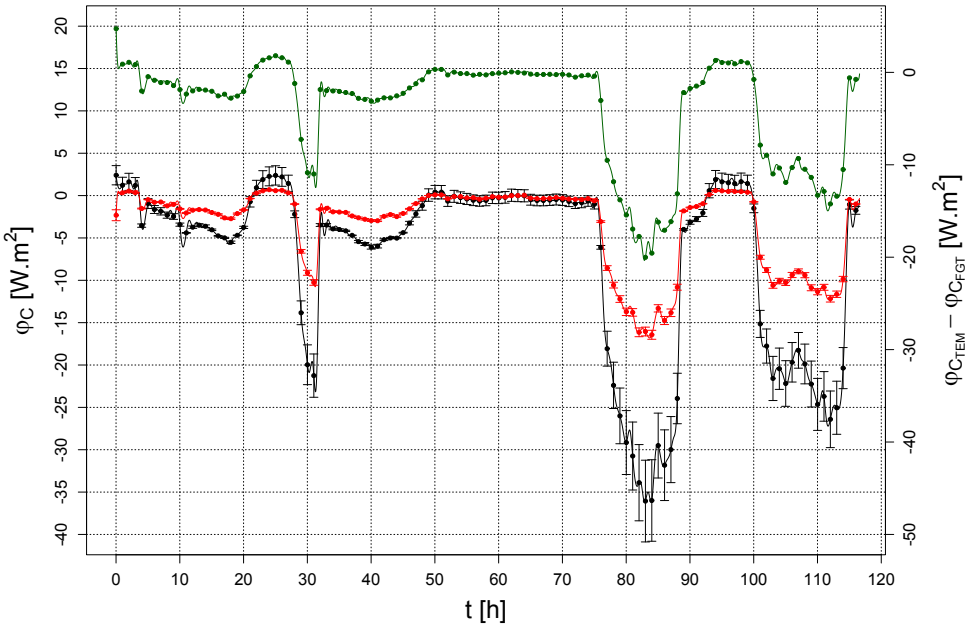

Figure A.21: On location 1. Convection heat flux from TEM measurements (black dots) and from FGT measurements (red dots). Difference between both (green lines, axis at the right).

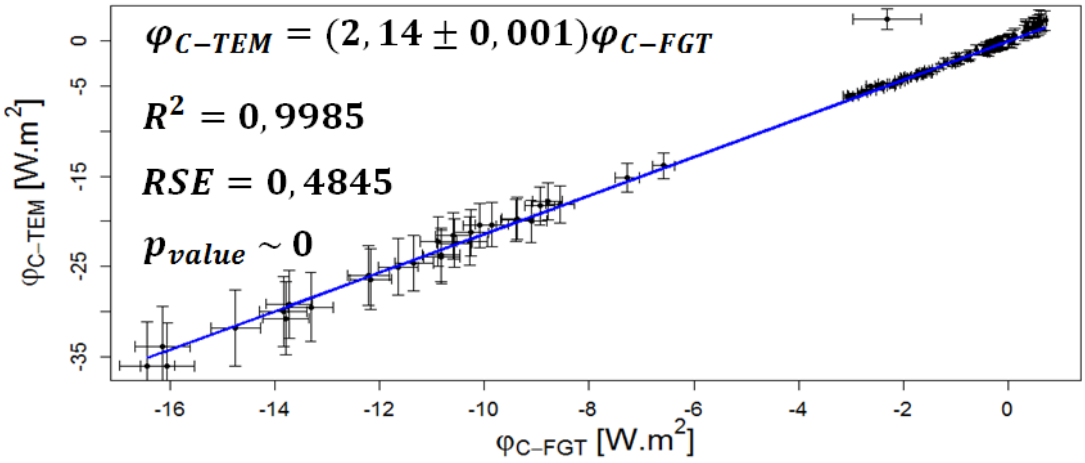

Figure A.22: On location 1. Convection heat flux from TEM measurements against FGT measurements (red dots). Blue line: linear regression fixed at the origin.

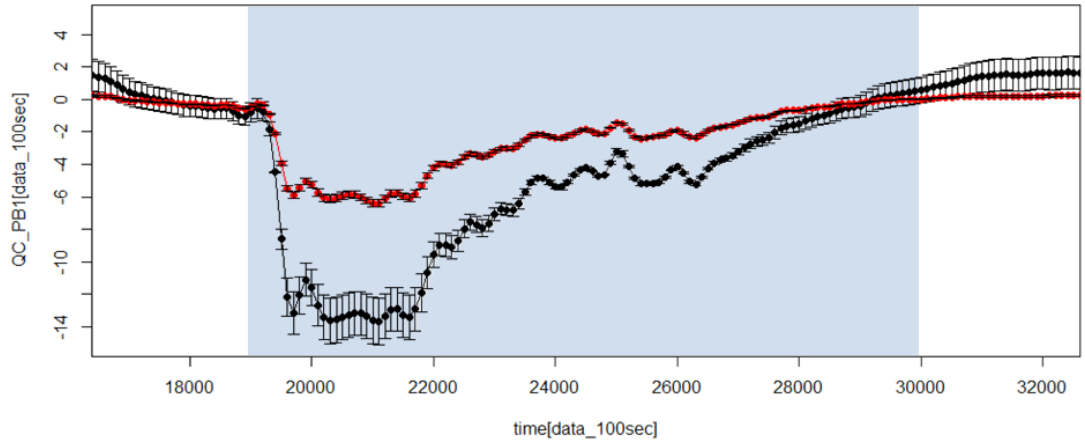

Figure A.23: On location 2. Convection heat flux from TEM measurements (black dots) and from FGT measurements (red dots). Blue zone: the natural ventilation openings remained opened.

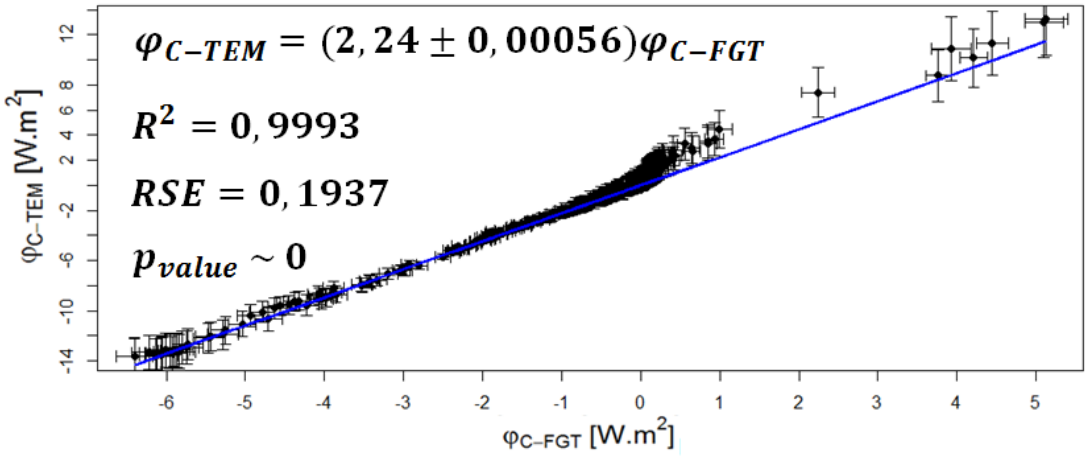

Figure A.24: On location 2. Convection heat flux from TEM measurements against FGT measurements (red dots). Blue line: linear regression fixed at the origin.

B Weather conditions from ENSAM meteorological station

Table B.1: Meteorological conditions from ENSAM in 2016.

	Opened ($T_{ia} > T_{oa}$)				Closed ($T_{ia} < T_{oa}$)			
	Mostly night				Mostly day			
Date	Clear	Cloudy	Windy	No windy	Sunny	Cloudy	Windy	No windy
27/07		*	*			*	*	
28/07	*			*		*	*	
29/07	*			*		*	*	
12/08	*			*	*		*	
13/08				*				
14/08	*			*	*		*	
15/08		*		*	*		*	
16/08		*		*	*		*	
17/08		*	*			*	*	
18/08	*			*		*	*	
19/08		*		*		*	*	
20/08		*		*		*	*	
21/08	*			*		*	*	
22/08	*			*	*		*	
23/08	*			*	*		*	
24/08	*			*		*		*
25/08	*			*	*		*	
26/08	*		*			*		*
27/08		*			*			
28/08	*					*		
29/08	*					*		
30/08		*			*			
31/08	*				*			
01/09	*				*			
02/09		*			*			
03/09	*				*			
04/09		*				*		
05/09	*					*		
06/09	*					*		
07/09		*			*			
08/09	*		*			*	*	
09/09		*				*		
10/09		*			*			
11/09	*					*		
12/09	*					*		

C Reports of airtightness tests

ESSAI DE PERMEABILITE A L'AIR DE BATIMENT

Date de l'essai : 15/06/2015
Fichier d'essai: Test2

Technicien : Miguel et Alain

Client :

Adresse du bâtiment : Sumbiosi

Débit à 50 Pascals : 2426 m³/h (+/- 2.4 %) Débit d'air
n50: 11.72 1/h Renouvellement d'air par heure
w50: 34.66 m³/(h*m² Surface au sol)

Surfaces de fuite : 1060.1 cm² (+/- 6.8 %) EqLA Canadienne @ 10 Pa ou 4.69 cm²/m² Surface d'enveloppe
599.6 cm² (+/- 11.1 %) LBL ELA @ 4 Pa ou 2.65 cm²/m² Surface d'enveloppe

q50 : 10.73 m³/(h*m² Surface d'enveloppe)

Courbe des débits de fuite: Coefficient de débit d'air (Cenv) = 250.2 (+/- 17.8 %)
Coefficient de fuite d'air (CL) = 248.4 (+/- 17.8 %)
Exposant (n) = 0.583 (+/- 0.049)
Coefficient de corrélation = 0.91510

Norme de l'essai: EN 13829
Mode de l'essai: Pressurisation
Type de méthode d'essai: A
Le contrôle a satisfait à:
Equipement: Model 4 (230V) Minneapolis Blower Door

Température intérieure :	25 °C	Volume :	207 m³
Température extérieure :	23 °C	Surface d'enveloppe :	226 m²
Pression barométrique:	101325 Pa	Surface de plancher :	70 m²
Classe de vent:	3 Petite brise	Incertitude sur les dimensions du bâtiment:	5 %
Exposition du bâtiment au vent:	Protection forte		
Type de chauffage:		Année de construction:	
Type de climatisation:			
Type de ventilation:	Aucune		

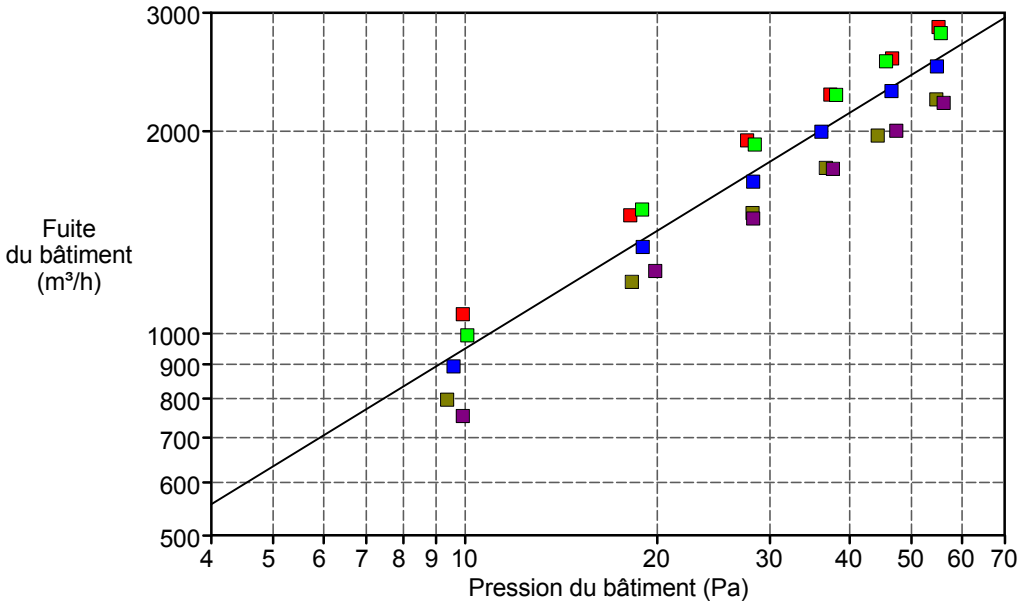

Date de l'essai : 15/06/2015 Fichier d'essai: Test2

Commentaires

Test1 : Aucun trou bouché, fenêtre chambre non réparée, bouches VMC et mcp obstruées
Test2 : fenêtre chambre bâchée
Test3 : En avoir mis de la mousse aux placard ext ouest (réseaux électrique, câble du systeme photovoltaique, systeme d'eau chaude)
Test4 : Mis du scotch noir à côté des portes vitrées et FM côté sud
Test5 : Du scotch noir mis au extrateur de la cuissine

Points de données: Dépressurisation:

Pression nominale du bâtiment (Pa)	Pression au ventilateur (Pa)	Débit nominal (m³/h)	Débit corrigé avec la température (m³/h)	% Erreur	Configuration du ventilateur
-0.2	s/o				
9.6	175.1	1063	1068	13.1	Anneau B
17.8	346.4	1492	1499	11.6	Anneau B
27.3	51.8	1929	1938	12.9	Anneau A
37.0	71.1	2257	2267	10.9	Anneau A
46.3	91.4	2555	2567	10.2	Anneau A
54.8	113.3	2842	2856	11.3	Anneau A
-0.4	s/o				
Essai 1	Pression à débit nul (Pa):	p01- = -0.4	p01+ = 0.5	p02- = -0.7	p02+ = 0.3
-0.5	s/o				
9.5	151.3	989	993	4.1	Anneau B
18.4	360.0	1521	1528	11.0	Anneau B
27.8	50.3	1901	1910	9.5	Anneau A
37.5	70.8	2253	2263	9.3	Anneau A
45.0	89.4	2528	2540	10.5	Anneau A
54.9	108.6	2784	2797	8.5	Anneau A
-0.6	s/o				
Essai 2	Pression à débit nul (Pa):	p01- = -0.6	p01+ = 0.3	p02- = -0.9	p02+ = 0.4
-0.3	s/o				
9.2	122.0	889	893	-3.6	Anneau B
18.6	278.5	1339	1345	-2.4	Anneau B
27.9	38.9	1673	1681	-3.4	Anneau A
35.8	54.9	1985	1995	-0.6	Anneau A
46.1	72.8	2283	2294	-1.4	Anneau A
54.4	86.3	2484	2495	-2.4	Anneau A
-0.4	s/o				
Essai 3	Pression à débit nul (Pa):	p01- = -0.5	p01+ = 0.1	p02- = -0.9	p02+ = 0.3
-0.1	s/o				
9.5	97.0	793	797	-12.8	Anneau B
18.4	218.6	1187	1193	-11.5	Anneau B
28.3	351.8	1504	1511	-13.0	Anneau B
36.9	42.8	1755	1763	-13.0	Anneau A
44.4	53.5	1960	1969	-12.8	Anneau A
54.8	68.7	2219	2230	-12.7	Anneau A
0.5	s/o				
Essai 4	Pression à débit nul (Pa):	p01- = -0.4	p01+ = 0.4	p02- = -0.5	p02+ = 1.0
0.0	s/o				